

University of Southampton Research Repository ePrints Soton

Copyright © and Moral Rights for this thesis are retained by the author and/or other copyright owners. A copy can be downloaded for personal non-commercial research or study, without prior permission or charge. This thesis cannot be reproduced or quoted extensively from without first obtaining permission in writing from the copyright holder/s. The content must not be changed in any way or sold commercially in any format or medium without the formal permission of the copyright holders.

When referring to this work, full bibliographic details including the author, title, awarding institution and date of the thesis must be given e.g.

AUTHOR (year of submission) "Full thesis title", University of Southampton, name of the University School or Department, PhD Thesis, pagination

UNIVERSITY OF SOUTHAMPTON

FACULTY OF NATURAL AND ENVIRONMENTAL SCIENCE

School of Ocean and Earth Science

**Freshwater fluxes and vertical mixing in the
Labrador Sea**

by

Lena M. Schulze

Thesis for the degree of Doctor of Philosophy

February 2016

UNIVERSITY OF SOUTHAMPTON
Faculty of Natural and Environmental Science
School of Ocean and Earth Science

Doctor of Philosophy

ABSTRACT

Freshwater fluxes and vertical mixing in the Labrador Sea

by Lena M. Schulze

The Labrador Sea plays an important role in the Meridional Overturning Circulation (MOC), due to the seasonal occurrence of deep convection in this region. Heat loss during mixing is balanced by heat import from the boundaries, while the seasonal freshening plays an important role in the restratification of the water column. Recent increases in freshwater input to high latitudes through accelerated rates of pack ice and glacial melt, has the potential to affect the convection in the Labrador Sea and therefore the global ocean circulation. It is more important than ever to understand the influence these changes have on the dynamics in the Labrador Sea. Understanding pathways of freshwater fluxes into the region of deep convection and the impact of storms on the mixing in the Labrador Sea will help to predict potential changes in the MOC.

To analyse recent changes in freshwater water in the Labrador Sea, an ARGO-based heat and freshwater budget of the Labrador Sea is calculated for 2002 – 2011. Over this time period a freshening of the surface waters (0 – 100 m) is observed. Between the first and second 5-year period, observations indicate a gain of 40 cm of freshwater to the surface. The surface freshening is comparable to past freshening periods associated with a reduction of deep convection (e.g. the Great Salinity Anomaly). However, the observed surface freshening is offset by subsurface warming and enhanced salinities (100 – 2000 m), distinguishing it from the past freshening periods. To investigate pathways of freshwater fluxes a particle tracking tool is used in a NEMO 1/12° ocean model. Seasonally, two peaks of freshening are observed (in spring and fall), consistent with observations. The freshening is due to the freshwater content of the coastal water along the coast of Greenland and the rate of advection of West Greenland Water. The large year-to-year variability in advection can mainly be attributed to changes in Ekman transport.

The relationship of convection to air-sea fluxes and the character of observed mixed layers in the Labrador Sea are explored by using wintertime hydrographic data from February – March 1997. The greatest number of storms occurred in December 1996 but the strongest winds and highest heat fluxes were observed in February 1997. Analysing storm tracks showed that storms in February 1997 followed more organized tracks extending from the Gulf Stream region to the Irminger Sea where they slowed and deepened. Investigation of the small scale variability within the mixed layers reveals that temperature and salinity intrusions are more common at the base of the mixed layers. During storms there were more non-density compensating intrusions present compared to the periods between storms, and the small scale variability was enhanced near the top of the mixed layers. This study underlines the importance of understanding the mechanisms through which water can reach the basin and potential implications of changes in the storm frequency and tracks under a changing climate.

Contents

Declaration of Authorship	xxi
Acknowledgements	xxiii
1 Introduction and Background	1
1.1 Introduction	2
1.2 Objectives and Motivation	4
1.3 Background	4
1.3.1 Circulation	4
1.3.1.1 The West Greenland Current	6
1.3.2 Convection	7
1.3.3 Restratification and the role of eddies	8
1.3.4 Interannual variability of properties in the Labrador Sea	9
1.3.5 The role of freshwater in the Labrador Sea dynamics	10
1.4 Overview of Thesis	11
2 Heat and Freshwater of the Labrador Sea, 2002 – 2011	13
2.1 Introduction	14
2.2 Data and Methods	14
2.2.1 Region definitions	14
2.2.2 Argo floats	15
2.2.3 Air-Sea fluxes	19
2.2.4 Calculation of Lateral fluxes	21
2.2.5 1-D Mixing Model	22
2.3 Basin-averaged properties	22
2.3.1 Temperature	23
2.3.2 Salinity	27
2.3.2.1 Regional properties	31
2.4 Surface fluxes	34
2.4.1 Surface heat fluxes	34
2.4.2 E-P	35
2.5 Lateral fluxes	36
2.5.0.1 Lateral heat fluxes	37
2.5.1 Lateral freshwater fluxes	39
2.6 Surface freshwater changes	41
2.6.1 Freshwater differences in two pentads	41
2.6.2 Surface freshening of the basin	43

2.7	Discussion	44
2.7.1	Seasonal Variability	44
2.7.2	Long-term Changes	45
2.7.3	Lateral Fluxes	47
2.7.4	Comparison to previous freshening periods.	48
2.7.5	Possible sources and mechanisms of freshening	49
2.8	Summary and Conclusions	51
3	Freshwater pathways into the Labrador Sea basin	53
3.1	Introduction	54
3.2	Data and Method	56
3.2.1	Model data	56
3.2.1.1	ORCA-N01 and ORCA-N06	57
3.2.2	ARIANE	59
3.2.3	Experiment Setup	59
3.2.4	Crossing from boundary into basin	59
3.2.5	Regions	61
3.2.6	Origin of water	61
3.2.7	Projection of velocities	61
3.2.8	Linear regression	63
3.2.9	Model validation	64
3.3	Origin of Labrador Sea Basin surface water	70
3.4	Freshwater pathways	74
3.5	Seasonality of freshwater advection	79
3.6	Seasonality of potential forcings: Eddy and Ekman transport	84
3.6.1	Eddies	86
3.6.2	Ekman transport	87
3.6.3	The role of Eddies versus Ekman transport	90
3.7	Interannual Variability of crossings	92
3.8	Interannual forcing	98
3.9	Summary and Discussion	103
3.10	Conclusions	109
4	The impact of atmospheric forcing during active convection	111
4.1	Introduction	112
4.2	Data and Methods	113
4.2.1	CTD Data	113
4.2.2	Identification of Mixed Layers	114
4.2.3	Intrusions	115
4.2.4	Atmospheric Reanalysis Fields	116
4.2.5	Storm Tracking	117
4.2.6	1D-mixing model	118
4.3	Atmospheric conditions of Winter 1996/1997	119
4.3.1	Monthly means	120
4.3.2	Storm Tracks	121
4.4	Impact of Atmospheric forcing on Mixed Layer Variability	126
4.4.1	Observed mixed layers	126

4.4.2	Predicted mixed layer depth	129
4.5	Observed small-scale structure within mixed layers	133
4.6	Relationship of small-scale structure to storms	133
4.7	Summary and Discussion	136
5	Conclusions and outlook	139
5.1	Outlook	142
A	Freshwater pathways in ORCA-N01	145
A.1	Freshwater pathways in ORCA-N01	146
B	Parameters of ORCA-N06	161
B.1	Parameters in ORCA-N06	162
	Bibliography	165

List of Figures

1.1	Figure from Schmidt (2008): Schematic surface currents in the Labrador Sea. Blue are in general cold fresh currents, red warmer saltier ones. The extension of the Irminger Current is mainly beneath the West Greenland and Labrador Current. The width of the currents is not linear correlated to velocities or transports. 1000 m, 2000 m and 3000 m isobath indicated. The location of maximum EKE in the Labrador Sea is marked green. The southern West Greenland Current branch is meandering strongly, indicated by the wiggly line.	5
1.2	The yearly NAO index for 1970 – 2015. The data was downloaded from http://www.cpc.ncep.noaa.gov	10
2.1	The Labrador Sea with the four regions used in this study marked by the red lines and numbers. The solid black lines show the streamlines as determined by Lavender et al. (2000).	15
2.2	Top panel: All temperature profiles measured by Argo floats in the basin (before quality control was performed) are shown in gray, with their mean profile in red. Colored dots mark points that were removed according to the cleaning procedure described in Section 2.2.2 . The dots are color coded according to the month during which they were recorded. Bottom panel: same as above but for salinity	16
2.3	Top panel: The Labrador Sea and the location of the profiles in the basin (red) and outside the basin (blue) between 2002 – 2011. Bottom panel shows the number of profiles in the basin each month (black line) and the mean number per year (red line and dots).	17
2.4	Monthly mean value of turbulent heat fluxes in the Labrador Sea basin obtained from NCEP (black) and ERA-Interim (red) data	20
2.5	Monthly mean evaporation-precipitation in the Labrador Sea basin obtained from ERA-Interim data. Positive values show a gain of freshwater to the region.	21
2.6	Maps of temperature, obtained from the Argo floats, for the different layers (a) surface layer: 0 – 100 m, b) mid-layer: 100 – 800 m, c) deep layer 800 – 2000 m, and d) entire water column 0 – 2000 m.	23
2.7	Same as Figure 2.6 but for salinity	24
2.8	Basin-average temperature for 2002 – 2011, gridded onto a regular grid of 50 m depth and 14 days. The different layers (surface layer (0 – 100 m, mid-layer (100 – 800 m) and deep layer (800 – 2000 m)) are shown in separate panels. Note that the upper layers are stretched compared to the deep layer. The black contour shows the 4°C isotherm.	25
2.9	Basin-average temperature time series for surface (0 – 100 m, top panel), mid-layer (100 – 800 m, middle panel) and deep layer (800 – 2000 m, bottom panel) shown in dark red, dark purple, and dark blue, respectively. The temperature anomalies (monthly mean - annual monthly mean) are shown as the thin light line in each panel. The broken black line shows the linear fit of the anomalies.	26

2.10	Climatology of basin averaged temperature (with the associated standard deviation shown as the broken lines) for the surface layer (0 – 100 m, left panel). The right panel shows the climatologies of the mid-layer (100 – 800 m) in purple and the deep layer (800 – 2000 m) in blue.	27
2.11	Basin-average salinity for 2002 – 2011, gridded onto a regular grid of 50 m depth and 14 days. The different layers (surface layer (0 – 100 m, mid-layer (100 – 800 m) and deep layer (800 – 2000 m)) are shown in separate panels. Note that the upper layers are stretched compared to the deep layer. The black contour shows the 34.65 isohaline.	28
2.12	Same as Figure 2.9 but for salinity	29
2.13	Same as Figure 2.10 but for salinity	29
2.14	Temperatures for the different regions (shown in the bottom middle panel) for 2002 - 2011. The three layers, surface (0 – 100 m), mid-layer (100 – 800 m), and deep layer (800 – 2000 m) are shown in separate panels for each region. Note that the upper layers are stretched compared to the deep layer. The black contour shows the 4°C isotherm.	30
2.15	Temperature climatology of the surface layer (0 – 100 m) in the four regions. The colors correspond to the regions shown in the right panel.	31
2.16	Salinity for the different regions (shown in the bottom middle panel) for 2002 - 2011. The three layers, surface (0 – 100 m), mid-layer (100 – 800 m), and deep layer (800 – 2000 m) are shown in separate panels for each region. Note that the upper layers are stretched compared to the deep layer. The black contour shows the 34.65 isohaline.	32
2.17	Salinity climatology of the surface layer (0 – 100 m) in the four regions. The colors correspond to the regions shown in the right panel.	33
2.18	a) Seasonal surface heat fluxes from ERA-interim over the Labrador Sea basin. b) Annual heat loss calculated by integrating the heat flux from May of the current year to April of the following year. Negative fluxes show a heat loss of the ocean to the atmosphere.	34
2.19	Same as Figure 2.18 but for precipitation minus evaporation obtained from the ERA-interim fields. Negative fluxes show a flux of freshwater to the ocean. . . .	35
2.20	Top Panel: Surface heat fluxes from ERA - Interim (black, using May of each year as initial conditions), vs. observed heat content of the surface layer (blue). Bottom Panel: surface freshwater fluxes from ERA - Interim (black) using May of each year as initial conditions vs. observed salt content of the surface layer . .	36
2.21	Climatology of lateral heat fluxes for the entire water column (0 – 2000 m, red), for all months, and the surface (0 – 100 m, black) and deep layer (100 – 2000 m, gray) during May – November (restratification period).	38
2.22	Interannual changes of heat content due to lateral fluxes. The solid red line shows the total heat change of the 0 – 2000 m layer each year. Black bars show the lateral fluxes of heat in the 0 – 100 m layer during May – November. Gray bars show the same for the 100 – 2000 m layer also during May – November. The dashed red line is the heat change due to lateral fluxes during December – April. Hence, the sum of the grey and black bars and the red dashed line will result in the red solid line. The bottom panel shows the yearly change in heat content due to heat loss to the atmosphere (obtained from ERA-Interim). . . .	38
2.23	Climatology of lateral freshwater fluxes for the entire water column (0 – 2000 m, red) for all months and the surface (0 – 100 m, black) and deep layer (100 – 2000 m, gray) during May – November (restratification period).	40

2.24	Same as Figure 2.21 but for lateral fluxes of freshwater in the basin.	40
2.25	Mean surface (0 – 100 m) salinity for 2002 – 2006 (left) and 2007 – 2011 (right) from Argo floats. The white crosses show the locations at which fewer than five profiles were available.	42
2.26	Same as Figure 2.25 but for the mean temperatures.	42
2.27	The amount of freshwater required to explain the month to month changes in salinity of the surface layer (0 – 100 m). Negative values (red bars) indicate the removal of freshwater and positive values (blue bars) a freshwater increase in the basin. i.e., a decrease in salinities.	43
2.28	Yearly change in surface (0 – 100 m) salinities of the Labrador Sea basin (light red) and the yearly change in surface freshwater (dark red) that is required to explain the observed changes in salinity.	44
2.29	Left: The basin-averaged density profiles of October for each of the years 2002 – 2011. The different years are shown as color. Right: The mixed layers from the PWP mixing model and the heat fluxes used to force the model. Again, colors correspond to the years shown as the colorbar.	46
3.1	Schematic of the proposed eddy pathways into the basin. The base map and EKE (gray shading, $[m^2/s^2]$) is from de Jong et al. (2012) (their Figure 1). The thick red line shows the pathway of Irminger Rings into the basin as proposed by Lilly et al. (2003). The thick blue line shows the pathway of eddies as proposed by Hatun et al. (2007) and Schmidt (2008). The small blue lines show the boundary current eddies that form everywhere along the boundary current (e.g., Chanut and Barnier (2008); Katsman et al. (2004)).	54
3.2	Bathymetry (in color) from ETOPO (left), used in the ORCA0083-N01 simulation (middle) and the ORCA0083-N06 simulation (right).	58
3.3	The difference in topography used in the ORCA-N06 and ORCA-N01 run. Positive values show that topography used in ORCA-N06 is deeper than in the previous run. Negative values show locations where the new topography is shallower.	58
3.4	Mean speed of the top 30 m in the basin by distance from the 2500 m isobath.	60
3.5	Number of particles that cross the 2500 m isobath within a certain time after being released. The red line shows the 7 month threshold that is used in this chapter.	60
3.6	The Labrador Sea and the four regions of the boundary (2500 m isobath). The regions are shown in color. The east is red, northern region is blue, northwest is green and the southwest pink. The black dots in the basin show the release points used in ARIANE.	62
3.7	The five sources of water entering the Labrador Sea: Water can enter through Hudson Strait (green), Baffin Bay (blue), EGC inshore (yellow), EGC offshore (red) and the North Atlantic (filled region). The inset panel shows the mean salinity for 1993 – 2009 along the section shown by the black line crossing the EGC inshore and offshore region. The vertical black line shows the location of the 1000 m isobath and the deviation between the inshore and offshore region of the EGC used in this chapter.	63

3.8	Mean salinity of the top 100 m for the winter period (Dec – May, top row) and summer periods (Jun – Nov, bottom row) of 2002 – 2011. The left panels show the salinity as observed from Argo floats (for more details on how this temperature map was constructed please refer to Chapter 2). The salinities observed in the NEMO ORCA-N01 and ORCA-N06 run are shown in the middle and right panels, respectively.	65
3.9	Same as Figure 3.8 but for the temperature of the top 100 m	66
3.10	Left: the seasonal cycle of salinity of the top 100 m in the basin (region inside the 3000 m isobath, as defined in Chapter 2), observed from the ARGO data (black), ORCA-N01 (red) and ORCA-N06 (blue). Right: the same but for temperature.	67
3.11	The mean surface velocity (top row) and eddy kinetic energy (bottom row) for the period of 2002–2011. The left panels show velocities and eddy kinetic energies derived from the AVISO sea surface height. The middle and right panels show the same for velocities from the two NEMO simulations, ORCA-N01 and ORCA-N06.	68
3.12	The seasonal cycle of eddy kinetic energy of the region shown as the black box in Figure 3.11 , calculated from the AVISO velocities (black), ORCA-N01 (red) and ORCA-N06 (blue).	69
3.13	Mean winter mixed layer depth observed from hydrographic data in 1997 (left panel, for more details see Chapter 4). The mean winter (Dec–Mar) mixed layer depth in the NEMO simulations is shown in the middle (ORCA-N01) and right panel (ORCA-N06).	70
3.14	Percentage of the 198,200 trajectories (that cross into the basin) that pass through each 0.5° longitude x 0.3° latitude grid point. The black contour shows the 2500 m isobath (i.e. the boundary of the basin). The red dots show the release positions of the particles.	72
3.15	Number of crossings origination in each of the origin, East Greenland Current offshore (red). East Greenland Current inshore (yellow), other regions in the North Atlantic (purple), unidentified origins (black), Baffin Bay (blue) and Hudson Strait. The five sources are shown in Figure 3.7	73
3.16	The distribution of particles of different origin in the basin at the time of their release. The colored sections indicate the sources, EGC offshore (red), EGC inshore (yellow), other sources in the North Atlantic (purple), Baffin Bay (blue) and Hudson Strait (green). The circles in the basin show the proportion particles from each source at the time of their release in each part of the basin. Colors refer to the five sources. Black circle fraction show the amount of trajectories for which no origin could be identified (see text for details).	74
3.17	a) The relative number of crossings per 100 km boundary section is indicated by the size of the red circles. b) The mean salinity of the crossings particles is indicated as color. The circles have the same size as in a) and again show the relative number of crossings per section. c) Again the size of the circles remains the same. Color shows the freshwater flux into the basin, where positive (blue) fluxes are freshwater divergence into the basin and red colors (negative values) indicates divergence of salty water, both with respect to the reference salinity of 34.95.	75

- 3.18 Top panel: The number of crossings per 100 km section along the 2500 m isobath (solid line and dots) and the error estimated using a Monte-Carlo method (dashed line). Second panel: The average salinity of the crossings particles at each 100 km section (solid line) and the error (dashed lines). The black horizontal line shows the reference salinity used to calculate the freshwater flux (see text for more details). Third panel: The average speed of the particles at the point of crossing into the basin (solid line) and the error (dashed lines). Bottom panel: The accumulated freshwater flux (solid line) at each section and the associated error (dashed line). Positive fluxes indicate freshwater advection to the basin, negative values salt water divergence into the basin. The vertical lines in all four panels associate with the red dots in the bottom figure (map) to help orient the reader geographically. 76
- 3.19 Same as **Figure 3.17** but for the four main water sources, EGC offshore water (top panels). inshore water (second row of panels), other sources in the North Atlantic, excluding the offshore and inshore water (second last row of panels), and Baffin Bay (bottom panels). 77
- 3.20 Same as **Figure 3.18** but for the three water sources, EGC offshore (red), inshore (yellow) and other sources in the North Atlantic (blue). The top panel shows the number of crossings (10^3), second panel shows the average salinity, the third panel the average speed at the point of crossing, and the bottom panel shows the accumulated freshwater flux due to water from each source. The vertical lines refer to the red dots in the bottom figure of **Figure 3.18**. 78
- 3.21 a) The seasonal cycle of the number of particles crossing the 2500 m isobath (solid line) and the error associated with it, calculated using a Monte Carlo approach (dashed line). b) the seasonal average salinity of the crossing particles (solid line) and the associated error (dashed line). The black horizontal line shows the reference salinity of 34.95 that is used to calculate the freshwater fluxes. c) the average speed with which the particles cross into the basin (solid line) and the associated error (dashed line). d) the accumulated seasonal freshwater flux into the basin (solid line) and the error (dashed line). Positive fluxes show freshwater fluxes into the basin and negative fluxes show fluxes of salty water into the basin. 80
- 3.22 Seasonal cycle of the amount of particles crossing into the basin in the a) north-east and b) southeast, (see **Figure 3.6** for references on the location of the regions). c-d): Seasonal cycle of freshwater fluxes into the basin by the particles crossing in the c) northeast and d) southeast. e-f): Same as a-b) for the speed with which the particles cross. g-h) Same but for the freshwater fluxes. In all panels, the colors show the sources of the water: yellow shows the water originating in the EGC inshore section, red the water in the EGC offshore section, purple the water from other sources in the North Atlantic and black the water with unidentified source. The dashed lines show the associated errors, calculated using a Monte Carlo method. 82
- 3.23 Same as **Figure 3.22** but for the northwest and southwest regions. 83
- 3.24 The three monthly mean of Eddy Kinetic Energy in the Labrador Sea, 1993 – 2009. Top left panel: Winter (Dec – Feb). Top right: Spring (Mar – May). Bottom left: Summer (Jun – Aug). Bottom right (Sep – Nov). 85
- 3.25 Seasonal cycle of EKE (1993 – 2009) in the southeast box (solid red line) with the associated standard deviation (broken line) and in the northeast box (solid blue line) with the associated standard deviation (broken line) See **Figure 3.6** for region definition. 85

3.26	Number of crossings in the southeast (left column) and northeast (right column) of the different origins together with the EKE in the same regions. Top panels: EGC offshore water crossings into the basin in the southeast (left) and northeast (right). Middle panels: same for EGC inshore water. Bottom panels: same for water from other North Atlantic sources.	86
3.27	Wind speed (color: m/s) and wind direction (arrows) in the Labrador Sea using the ERA-interim product. Top left panel: Winter (Dec – Feb). Top right panel: Spring (Mar – May). Bottom left: Summer (Jun–Aug) and bottom right: Fall (Sep – Nov).	88
3.28	Ekman transport [mSv] across the four sections defined in Figure 3.6 . Red curve shows the total Ekman transport across the southeast section, blue the transport across the northeast section, green across the northwest section and pink across the southwest section. Positive values indicate transport into the basin, and negative values transport out of the basin.	88
3.29	Number of crossings in the southeast (left column) and northeast (right column) of the different origins together with the Ekman transport in the same regions. Top panels: EGC offshore water crossings into the basin in the southeast (left) and northeast (right). Middle panels: same for EGC inshore water. Bottom panels: same for water from other North Atlantic sources.	89
3.30	Percentage of trajectories from each source that pass through each 0.5° longitude x 0.3° latitude grid point. The black contour shows the 2500 m isobath. Left column: Trajectories during months of high EKE and Ekman transport (Feb – Mar). Right column: trajectories during months of low EKE and Ekman transport (Jul – Aug). Top row: for water with EGC inshore origin. Middle row: for EGC offshore water. Bottom row: for water with other origins in the North Atlantic.	91
3.31	The relative number of crossings per 50 km boundary section is indicated by the size of the red circles for 1993 – 2012. The color indicates the amount of freshwater brought into the region at each section [m^3/s]	93
3.32	Top: Total number of crossings into the basin per year. Second panel: Average salinity of crossing water. Third Panel: Average speed of the crossing. Bottom: Yearly freshwater flux into the basin. Positive values show freshwater advection to the basin, negative values show advection of salty water. Errors are calculated using a Monte Carlo error calculation.	94
3.33	Top: Number of crossings into the basin per year. Second panel: Average salinity of crossing water. Third Panel: Average speed of the crossing. Bottom: Yearly freshwater flux into the basin. Positive values show freshwater advection to the basin, negative values show advection of salty water. Red curves shows water with EGC offshore origin, yellow water with EGC inshore origin, purple water with origins elsewhere in the North Atlantic and blue water from Baffin Bay. . .	95
3.34	Year-to-year variability of the number of crossings with Baffin Bay origin. . . .	95
3.35	The number of crossings in the a) northeast and b) southeast. The salinities of the advected particles in a) the northeast and b) the southeast. The speed of the crossing particles in c) the northeast and d) the southeast and the associated freshwater fluxes entering the basin in e) the northeast and f) the southeast. The colors refer to the water’s origin: yellow shows the EGC inshore water, red the EGC offshore water and purple the water from other sources in the North Atlantic. Black shows the water of unidentified sources. The dotted lines show the errors estimated using a Monte Carlo approach.	96

3.36	Top: yearly NAO index. Bottom: the yearly number of crossings into the basin	99
3.37	Top row: The EKE [m^2/s^2] for months which had an exceptionally high amount of crossings (left) and months that had exceptionally low numbers of crossings (right). Bottom row: Ekman transport for the same months.	100
3.38	Left: Crossing anomaly in the southeast (three monthly number of crossings with the seasonal cycle removed, black) and the EKE anomaly (red). Right: The same crossing anomaly as on the left figure (in black) but with the Ekman transport anomaly (blue).	100
3.39	Left side: Three-monthly number of crossing anomaly in the southeast and the Ekman transport anomaly in the same region (dots) and the linear fit (red line). Right column: The number of crossings (black line) and the reconstructed number of crossings from Ekman transport (blue) and from EKE (red). The top row shows the crossings of EGC inshore and offshore water, the middle row the crossings of EGC inshore water only and the bottom row the crossings of EGC offshore water. When R values are given, the correlation is significant at 99%	101
3.40	Same as Figure 3.38 but for the northeast	101
3.41	Same as Figure 3.39 but for the northeast	102
3.42	The last reported location of the trajectories that could not be identified to be from one of the water sources	105
4.1	The location of CTD stations. The colored dots show the location of the stations in the boundary (blue), western basin (red) and eastern basin (yellow). Black stations are not included in the study due to being in water shallower than 500 m or having mixed layers shallower than 100 m. Numbers are the station number allocated during the cruise. Note that the middle section in the west was occupied twice and some stations therefore have two station numbers. Grey contours show the isobaths with 500 m spacing. The black contour is the 3000 m isobath.	114
4.2	Two profiles measured by (left) the ICTD and (right) the Mark III CTD 9. Please refer to (Figure 4.1 for the location of Station 15 (left) and Station 71 (right).	115
4.3	Example of a mixed layer depth using station 65. The dashed lines show the two-standard deviation envelope and the red curve shows the lowpass using a 100 m filter width.	116
4.4	The number of temperature (top) and salinity (bottom) intrusions that are smaller than a certain threshold. The black line shows the accuracy of the instrument, the red line the chosen threshold for the definition of an intrusion. Note that for salinity the red and black line are in the same position since the chosen threshold and the definition for intrusions are identical.	117
4.5	An example for the three classes of intrusions. The left panel shows the density of the mixed layer of station 93. The three other panels (temperature, salinity and density) show the region between the two blue lines seen in the left panel. The part of the mixed layer that is filled green shows an intrusion occurring in temperature and salinity. This particular intrusion is not compensated but governed by salinity. The purple area shows a salinity intrusion and the corresponding signature in density. The orange shows a temperature intrusion and the corresponding signature in density.	118

4.6	Monthly mean sea level pressure fields (color: mbar) obtained from ERA-Interim, the 10 m wind fields (vectors: m/s) and the 50 % ice edge (black contour) for December 1996 (top left), January 1997 (top right), February 1997 (bottom left), and March 1997.	119
4.7	Monthly mean turbulent heat flux fields (sum of sensible and latent heat fluxes, color: W/m^2) obtained from ERA-Interim, the 10 m wind fields (vectors: m/s) and the 50 % ice edge (black contour) for December 1996 (top left), January 1997 (top right), February 1997 (bottom left), and March 1997.	120
4.8	Cyclone tracks during December 1996 (top left), January 1997 (top right), February 1997 (bottom left), and March 1997 (bottom right). The tracks are colored by the corresponding sea level pressure (mbar) observed at the center of the system at each position. Black circles show the position at which the storm was first observed, purple circles show the last position of the storm in the domain.	122
4.9	Top panel: turbulent heat flux time series of the Labrador Sea with the 400 W/m^2 threshold shown as a dashed line. Below: the corresponding wind speed timeseries for the Labrador Sea. Bottom panel: mean turbulent heat flux field for times when heat flux in the Labrador Sea exceeded 400 W/m^2 (color: W/m^2). The 10 m wind field is shown as vectors (m/s) and the 50% ice edge is shown as the white contour. The black box shows the region over which the turbulent heat flux and wind speeds were averaged for the top two panels.	124
4.10	Same as Figure 4.9 but for the mean wind speed field (color: m/s) and the wind direction. Mean sea level pressure is shown as black contours and the 50% ice edge as the white contour.	125
4.11	Storm tracks of low pressure systems that caused heat fluxes to exceed 400 W/m^2 in the Labrador Sea (blue). The red fragments correspond to the time of high heat fluxes in the Labrador Sea. Grey tracks are storms during which heat fluxes remained below 400 W/m^2	126
4.12	Mixed layer depth as observed from the CTD data. The black contours show the streamlines.	127
4.13	The mixed layer depth of each region (top panel). Circles and line fragments show the observed mixed layer depths from the CTD profiles. Mixed layers of stations taken further apart than 7 days are not connected by a line. The numbers at the top show the station number. Solid, thin lines show the predicted mixed layer depth as found in the 2-D PWP mixing model. The bottom panel shows the turbulent heat flux. Dots and line fragments show the mean heat flux half a day before the corresponding station was sampled at the location of the station. The thin, solid line shows the forcing used in the model, the mean turbulent heat flux in the Labrador Sea. Yellow shows mixed layer depth and forcing in the eastern basin, red in the western basin and blue in the western boundary.	128
4.14	Left Panel: The density profile of the eastern basin (yellow) and western basin (red) from the October 1996 AR7W data. Top right panel: the mixed layers for the eastern (yellow) and western (red) basin from PWP when forced with constant forcing of 500 W/m^2 . Bottom right panel: the mixed layers for the eastern (yellow) and western (red) basin from PWP when forced with 500 W/m^2 and 600 W/m^2 , respectively.	130

4.15	Top panels a-c): Percentage of intrusions found at each percentage depth of its mixed layer, a) for temperature intrusions, b) for salinity intrusions, and c) for compensated intrusions. Bottom panels d-f): Percentage of intrusions with a certain length (in m), for d) temperature intrusions, e) salinity intrusions, and f) compensated intrusions.	132
4.16	Top panels: a) The turbulent heat flux in the Labrador Sea during the time period of the cruise. Yellow dots show the time of stations measured between storms and red dots the time of stations measured during storms. b) The location of the stations measured between storms (yellow) and during storms (red). Bottom panel c): The number of intrusions per mixed layer for stations measured between (yellow) and during (red) storms, for all intrusions, compensated intrusions, temperature intrusions and salinity intrusions (from left to right). . .	134
4.17	Top panels a-b): Percentage of intrusions found at each percentage depth of its mixed layer, a) for intrusions found in mixed layers measured during storms (red), b) for intrusions found in mixed layers measured between storms (yellow). Bottom panels c-d): Percentage of intrusions with a certain length (in m), for c) intrusions found in mixed layers measured during storms, and d) intrusion found in mixed layers measured between storms.	135
A.1	Number of particles that cross the 2500 m isobath within a certain time after being released. The red line shows the 7 month threshold that is used in this chapter.	153
A.2	Number of trajectories with different criteria	154
A.3	Percentage of the 198,200 trajectories (that cross into the basin) that pass through each 0.5° longitude x 0.3° latitude grid point. The black contour shows the 2500 m isobath (i.e. the boundary of the basin). The red dots show the release positions of the particles.	154
A.4	Number of crossings origination in each of the origin, East Greenland Current offshore (red). East Greenland Current inshore (yellow), other regions in the North Atlantic (purple), unidentified origins (black), Baffin Bay (blue) and Hudson Strait. The five sources are shown in Figure 3.7	155
A.5	Number of crossings origination in each of the origin, East Greenland Current offshore (red). East Greenland Current inshore (yellow), other regions in the North Atlantic (purple), unidentified origins (black), Baffin Bay (blue) and Hudson Strait. The five sources are shown in Figure 3.7	156
A.6	Number of crossings origination in each of the origin, East Greenland Current offshore (red). East Greenland Current inshore (yellow), other regions in the North Atlantic (purple), unidentified origins (black), Baffin Bay (blue) and Hudson Strait. The five sources are shown in Figure 3.7	157
A.7	a) The seasonal cycle of the number of particles crossing the 2500 m isobath (solid line) and the error associated with it, calculated using a Monte Carlo approach (dashed line). b) the seasonal average salinity of the crossing particles (solid line) and the associated error (dashed line). The black horizontal line shows the reference salinity of 34.95 that is used to calculate the freshwater fluxes. c) the average speed with which the particles cross into the basin (solid line) and the associated error (dashed line). d) the accumulated seasonal freshwater flux into the basin (solid line) and the error (dashed line). Positive fluxes show freshwater fluxes into the basin and negative fluxes show fluxes of salty water into the basin.	158

- A.8 The relative number of crossings per 50 km boundary section is indicated by the size of the red circles for 1993 – 2012. The color indicates the amount of freshwater brought into the region at each section [m^3/s] 159


List of Tables

2.1	Freshening periods in the Labrador Sea as described and quantified in the literature.	49
3.1	Number of trajectories with different criteria	71
4.1	Number of intrusions of each class (compensated, temperature, and salinity) found in the 103 mixed layers.	132

Declaration of Authorship

I, Lena M. Schulze , declare that the thesis entitled **Freshwater fluxes and vertical mixing in the Labrador Sea** and the work presented in the thesis are both my own, and have been generated by me as the result of my own original research. I confirm that:

- this work was done wholly or mainly while in candidature for a research degree at this University;
- where any part of this thesis has previously been submitted for a degree or any other qualification at this University or any other institution, this has been clearly stated;
- where I have consulted the published work of others, this is always clearly attributed;
- where I have quoted from the work of others, the source is always given. With the exception of such quotations, this thesis is entirely my own work;
- I have acknowledged all main sources of help;
- where the thesis is based on work done by myself jointly with others, I have made clear exactly what was done by others and what I have contributed myself;

Signed:.....

Date: 03 March 2016.....

Acknowledgements

First and foremost, I would like to thank my supervisors Eleanor Frajka-Williams and Sheldon Bacon, who have supported me patiently throughout the PhD. I am especially grateful to Eleanor who has been endlessly helpful and insightful. I have been very lucky to have had a supervisor so enthusiastic and resourceful. She has been there endless times to listen, discuss or make me think about my science. She is not only a fantastic supervisor but also a role model. I am grateful that I have had the opportunity to work with her.

I am also grateful to Bob Pickart for working with me on Chapter 4 of this Thesis. Bob introduced me to the world of oceanography as an undergraduate and let me discover my love for the sea and observational oceanography by taking me on many many cruises.

Thank you also to Bob Marsh for introducing me to Ariane, and Jeff Blundell and Zoe Jacobs for introducing Ariane to Jasmin, so that I could use the new ORCA-N06 data in Chapter 3.

Rosie, Sarah, Chris and Lucie, thank you for keeping me entertained, well fed and making everything more fun. A special thank you to Rosie for reading through the entire thesis.

My parents I want to thank for their constant support and excitement about my science and life as an oceanographer. Thank you also to my sister Anna for showing me how it is done and sending me many care packages throughout the years.

Last but not least, Mike, thank you for being there and always encouraging and supporting me.

Ava, even though she can't possibly understand how much she has helped, thank you for never leaving my side, always being happy, keeping me sane and for helping me maintain perspective.

Chapter 1

Introduction and Background

1.1 Introduction

Generally speaking the Atlantic meridional overturning circulation (AMOC) consists of two cells, one of the North Atlantic Deep Water and the second of northward flowing dense Antarctic Bottom Water (AABW) that eventually upwells into the lower part of the NADW. The circulation itself consists of four main branches: a surface current that transports relatively warm and light water from low to high latitudes, deep water formation in several locations, where the water becomes dense and sinks a deep current and an upwelling process that connects the two. It spans the entire Atlantic ocean, both hemispheres and the entire ocean depth. The AMOC is a strong driver and regulator on how much heat is transported by the ocean, on distribution of water masses and the storage of chemical, e.g. carbon dioxide. The approximately 1 PW (10^{15} W) (Hall and Bryden; Trenberth and Caron, 2001) of northwards transport of heat contributes to the mild climate in Europe and a change in its strength would manifest itself not only in the climate but also in the sea level in the North Atlantic (Levermann et al., 2005) and the marine ecosystem (Schmittner, 2005).

In the classic view of the AMOC, warm and saline water is transported polewards in the surface layers. In the subpolar regions, namely the Greenland-Iceland Sea and the Labrador Sea, it is cooled by air-sea fluxes and subsequently becomes dense and sinks, resulting in convection. The deep dense water recirculates towards the equator where it upwells or diffuses, closing the circle (Stommel and Arons, 1960a,b; Mauritzen, 1996). However, the question of what mechanism is the main driver of this circulation has long been under investigation. Two different mechanisms have repeatedly been discussed: The traditional thermohaline mixing and wind-driven upwelling. The classic view of the thermohaline driving mechanism was proposed as early as 1916 (Sandstrom). Here mixing transports heat from the surface downwards and across isopycnals (such isopycnal mixing is described in detail by Munk and Wunsch (1998)). This takes mainly place due to waves that dissipate into small-scale motion and cause turbulent mixing allowing light waters to reach the deeper ocean and eventually resulting in a rising at low latitudes. The resulting surface water is advected north and transformed into dense water in the high latitudes. The second idea of wind being the main driver of upwelling was first put forward in 1993. Toggweiler and Samuels (1993) concluded that the actual amount of observed diapycnal mixing is insufficient to sustain the observed overturning circulation. They suggested that most of the upwelling is instead wind-driven and taking place in the Southern Ocean. A third way to look at the mechanisms driving the AMOC is to also consider the amount of deep water formation in the North Atlantic. This process can change the AMOC's spatial pattern and strength drastically and will be discussed in more detail below. Other, more recent studies have called into question some of the details of the AMOC that were previously thought to be facts. For example, Dengler et al. (2004) finds that the southwards flow of dense water in the Deep Western Boundary Current (DWBC) breaks up into eddies around 11°S, while Bower et al. (2009) argues

that the DWBC might not be the dominant pathway of water to flow from subpolar to subtropical regions. Instead they find that most of the southward flow of deep water takes place along interior pathways instead of the Deep Western Boundary Current. Several other studies agree however, that the DWBC exists and transports most of the deep water southward (Pickart (1992); Smethie et al. (2000)). Recently the role of eddies has been investigated closer and it is becoming more and more apparent that eddies not only mix the water but also, in some places, contribute to the main transport (Dengler et al., 2004).

The Labrador Sea is one of the places in the North Atlantic where the formation of deep dense water, in form of convection, takes place. This relatively small ocean is the site of some of the deepest convection in the world's ocean, with mixing as deep as 2000 m (Lazier, 1980). The convection is driven mainly by buoyancy removal through winter atmospheric heat fluxes but also depends on the existing stratification in the region. This will be further discussed below.

Other studies, models as well as studies of past climate have shown that rapid changes in climate (temperature, precipitation patterns etc.) in Europe are usually also associated with changes in the overturning circulation (e.g. Pohlman et al. (2006); Brauer et al. (2008); Jacob et al. (2005)). The role of freshwater in the convection regions first became apparent when Broecker 1991 showed that rapid climate fluctuations during the Earth's last glacial period were due to strong fluctuations in the overturning circulation. This was presumed to be a direct result of the melting of the continental ice sheets and the large increase in freshwater in high latitudes.

As freshwater is the most likely source of buoyancy in the Labrador Sea, it is important to understand freshwater fluxes to regions of convection. Only then can we accurately predict the resulting deep mixing and its impact on the MOC. The 'Great Salinity Anomaly' observed in 1967 – 1977 highlights the impact of freshwater anomalies on the dynamics of the Labrador Sea. During this time, large patches of freshwater propagated through the North Atlantic, causing a salinity decrease of 1 psu in the Labrador Sea (Dickson et al., 1988). This led to a shut down of convection for five years. Deep mixing was only resumed when the effect of significantly cooler surface temperatures, strong atmospheric forcing and advection of salty water into the region allowed the removal of enough buoyancy (Gelderloos et al., 2012).

With its proximity to the Arctic, the Labrador Sea is sensitive to current and future changes in ice melt and increased freshwater supply. The additional freshwater could drastically increase the surface buoyancy in the Labrador Sea and suppress or dampen convection, if it was to reach the region of deep mixing. So far it is not clear if the recent changes in the Arctic have or will impact the dynamics in the Labrador Sea and consequently the overturning circulation and the global ocean dynamics.

1.2 Objectives and Motivation

This thesis is motivated by the need to understand freshwater fluxes in the Labrador Sea. The objectives are:

- to identify whether increased ice melt in recent years has already influenced the properties and stratification of the Labrador Sea.
- to understand pathways and mechanisms through which freshwater is advected into the Labrador Sea basin, i.e., the region of convection.
- to identify the sources of freshwater in the Labrador Sea basin
- to investigate the ocean's response to atmospheric forcing, using a case study.

This work aims to better understand the impact of additional freshwater in the Arctic on the dynamics of the Labrador Sea and to identify the mechanisms that allow freshwater to enter the region of deep convection. Is it, for example, possible that additional freshwater will not impact convection directly because the mechanisms that allow it to enter the basin regulate these fluxes in some way? The knowledge of the amount of freshwater influxes to the region allows us to assess changes and possible trends but an understanding of the mechanisms driving these fluxes would make it possible to better estimate the strength of convection and the subsequent changes in the MOC in the light of recent and future climate trends.

1.3 Background

The Labrador Sea is part of the North Atlantic Subpolar Gyre and its properties are governed by the advection of temperature and salinity from the North Atlantic and the Arctic. Furthermore, it is a place of severe meteorological conditions with winter sea ice, ice export from Greenland's fjords, large air-sea temperature contrast, and frequent winter storms that bring cold and dry Arctic air to the region. The following describes the main characteristics of the Labrador circulation and dynamics.

1.3.1 Circulation

The Labrador Sea basin is surrounded by fast moving, cyclonic boundary currents. In the east of the basin, the West Greenland Current (WGC) flows along the Greenland shelf as a continuation of the East Greenland Current (**Figure 1.1**). In the west the Labrador Current (LC) flows south along the basin. The boundary currents are considered to stay inshore of the 3000 m isobath, with average velocities of 30 cm/s (Cuny and

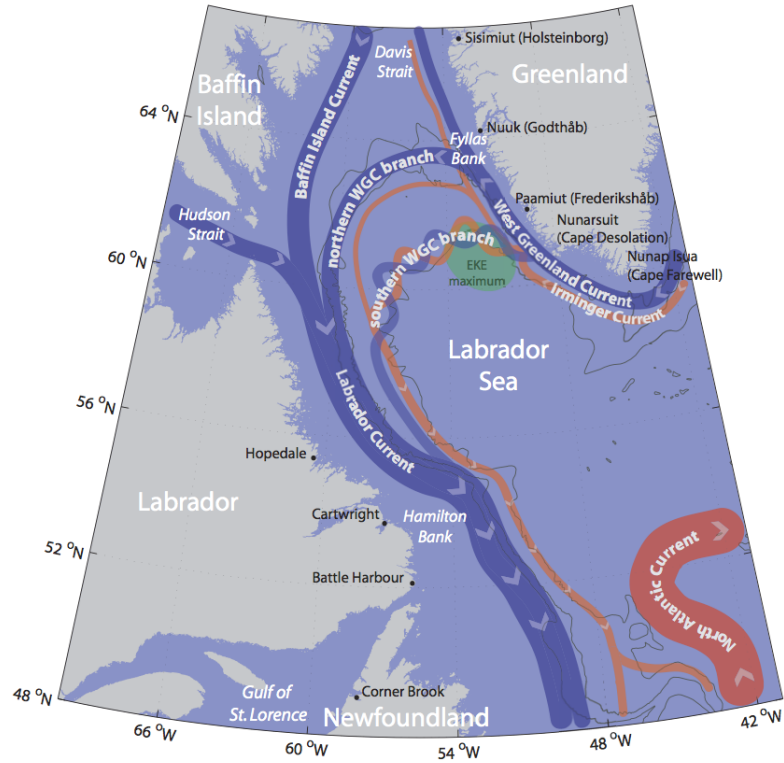


Figure 1.1: Figure from Schmidt (2008): Schematic surface currents in the Labrador Sea. Blue are in general cold fresh currents, red warmer saltier ones. The extension of the Irminger Current is mainly beneath the West Greenland and Labrador Current. The width of the currents is not linear correlated to velocities or transports. 1000 m, 2000 m and 3000 m isobath indicated. The location of maximum EKE in the Labrador Sea is marked green. The southern West Greenland Current branch is meandering strongly, indicated by the wiggly line.

Rhines, 2002). Two slower, less well defined flows connect the West Greenland Current and the Labrador Current from east to west, branching away from the coast where the 3000 m isobath diverges from the shelf. One branch follows the 2500 m isobaths with velocities of about 12 cm/s and the second branch crosses the interior between the 2000 m and 1000 m isobath, reaching speeds of up to 20 cm/s (Cuny and Rhines, 2002).

The shallow part of the boundary currents are, compared to the interior, cool and fresh from the Arctic waters that it carries and driven mainly by the resulting cross-shelf density gradient. In fact, most of the seasonal variation in the current flow is driven by the enhancement of the baroclinic component, due to a stronger Irminger Current core in the winter (Rykova et al., 2014). Changes in the barotropic component are relatively small. The WGC is fastest in the autumn (Rykova et al., 2014) but its mean transport remains around 85 mSv throughout the year (Bacon et al., 2014). A salinity maximum beneath the shallow, fresh WGC is caused by the presence of Irminger Water, referred

to as the Irminger Current. This current transports the warm water around the basin at a depth of 200 – 800 m, cooling and freshening along the way (Yashayaev, 2007). In the west, the LC is fed by the WGC, outflow from Baffin Bay (Curry et al., 2014) and Hudson Strait (Straneo and Saucier, 2008). The main branch of the LC is located over the shelf break, transporting up to 26 Sv of water per year (Fischer et al., 2004). The flow varies seasonally, with minimum flow in the spring and maximum flow in October. Observations from profiling floats found two branches of the LC around 51°N (Fischer and Schott, 2001). The onshore component leaves the region following the topography towards Flemish Cape. Much of the offshore component is deflected north, forming long lasting eddies before re-entering the boundary current and exiting the region.

The circulation of the interior is characterized by relatively slow movement. Lavender et al. (2000) observed anticyclonic circulation of about 5 cm/s at 700 m that extends to the surface (Cuny and Rhines, 2002). The circulation is typically strongest in regions with large wind stress curl (Spall and Pickart, 2003). Due to the different water masses on the shelf and in the basin, a front causes an upwards sloping of isopycnals towards the open ocean. This leads to a weak stratification in the basin, preconditioning the Labrador Sea for convection.

The deep basin is filled with Labrador Sea Water (LSW) formed by deep mixing in winter. It can remain in the basin for several years (Palter et al., 2007; Lavender et al., 2005) before leaving the Labrador Sea via the Deep Western Boundary Current (DWBC). In years with weak convection this layer is isolated, causing LSW from previous years to drain and the layer to become thinner until it is renewed during a year with deep convection (Lazier, 2002; Yashayaev, 2007).

1.3.1.1 The West Greenland Current

Several studies have shown that the West Greenland Current (WGC) is the main source of freshwater and heat for the interior of the Labrador Sea, both fundamental in the dynamics of the region (Straneo, 2006; Schmidt and Send, 2007; Myers, 2005). The WGC is the continuation of the East Greenland Current (EGC) flowing south along the eastern coast of Greenland before rounding Cape Farewell and flowing into the Labrador Sea where it becomes the WGC. When rounding the Cape, the EGC and Irminger Current merge, with the Irminger Water subducting under the low-salinity polar water (Bacon et al., 2002). While the WGC can be described as a jet with a single core located near the shelf break, it should really be divided into two components, a cold and fresh surface component and the warm and salty sub-surface Irminger Current component (Fratantoni and Pickart).

The upper fresh and cold water has undergone strong variability over the last century. Several freshening periods were for example observed: In the 1960's, during the Great Salinity Anomaly, Dickson et al. (1988) found a linear decline in salinity and temperature. Other freshening anomalies were also observed in 1970's and 1990's (Houghton

and Visbeck, 2002).

The Irminger Water also undergoes large interannual variabilities. For example, Yashayaev (2007) noted a large volume of warm and salty water appearing over the continental slope of West Greenland during the 2000's. He (Yashayaev, 2007) and Mortensen and Valdimarsson (1999) agree that this change originated in the Irminger Sea. Such changes have been shown to be connected to the NAO and sub-polar mode water formation in the Irminger Basin (Myers et al., 2007), and the dynamics of the sub-polar gyre circulation (Hatun et al., 2005). Current speeds of the WGC are estimated to be between 20 - 35 cm/s at the shelfbreak (Schmidt and Send, 2007; Fratantoni and Pickart) with occasional velocities offshore exceeding 1 m/s (Bacon et al., 2002). The transport of East Greenland Water was found to be around 3 Sv and 11 Sv for the Irminger Water (Clarke; Bacon et al., 2002; Myers et al., 2009).

Large variability is seen when considering the salinity of the upper layer. It can vary as much as 3 salinity units and also in its extent, some years show significant amounts of freshwater extending off the shelf, while in others there is only a small amount present on the shelf. This also impacts the front between the boundary current and basin, making it quite steep in some years (Myers et al., 2009). Transport has been declining since the peak in the early 1990's. This is consistent with the weakening of the subpolar gyre circulation at the same time observed by Häkkinen and Rhines (2004). It is challenging to conclude anything about the seasonal cycle, since most measurements (e.g. hydrographic sections) are made in the spring and there is usually no year around coverage. However, models suggest that the transport at Cape Farewell and Cape Desolation is largest in winter and early spring (Myers et al., 2009). Freshwater transport increases between Cape Farewell and Cape Desolation. While this increase is rather small it could be explained by the melting of the ice that has often been seen in this area (Myers et al., 2009). This shows that the freshwater from the EGC might not be the only source of freshening to the region. Two studies have shown that freshwater is exchanged with the Labrador Sea basin around Cape Desolation (Schmidt and Send, 2007; Myers et al., 2009). About 60 -80 mSv are exchanged in the summer.

1.3.2 Convection

Several conditions must be met in order for convection to occur, including a cyclonic circulation that results in the outcropping of isopycnals, weakened stratification and strong surface buoyancy loss (Marshall and Schott, 1998). These criteria are met in the Labrador Sea, making it a prime location for deep water formation. The strength of convection is set by surface heat loss by any given winter and preconditioning of the ocean from previous years. Large buoyancy fluxes are frequently observed when winter storms drag cold, dry continental air from Canada over the Labrador Sea. Winter heat loss is on average between 200 – 300 W/m² but can be as high as 1000 W/m² during individual storms (Marshall et al., 1998; Marshall and Schott, 1998; Pickart et al., 2002).

This leads to convection often exceeding 2000 m (Lazier, 2002; Yashayaev and Loder, 2009; Vage et al., 2008). The deepest mixed layers have been found in the western part of the basin (Pickart et al. (2002); Lavender et al. (2002) and **Chapter 4, Figure 4.12**). Despite unfavorable ocean conditions, convection has also been observed in the boundary currents where air-sea fluxes are large due to the position of the ice-edge (Pickart et al., 2002; Moore et al., 2014; Vage et al., 2008).

In general, convection takes place in the winter when air-sea heat loss exceeds the heat flux into the region, resulting in buoyancy loss of the surface layer. The water column becomes unstable and dense water mixes downwards in plumes. Using hydrographic data from 1990 – 1997, Pickart and Spall (2007) describe convection in the Labrador Sea to simply be water mass transformation with very small vertical velocities. Contradicting this, Lavender et al. (2002) find a downward motion of water with upwelling patches between convection plumes by analysing float data for the same time period. Estimates of LSW production rates vary widely between studies. Most studies calculate production rates below 5 Sv, using methods ranging from box models, mass budgets or by estimating mixing from air-sea fluxes (Worthington, 1976; Clarke, 1983, 1992; Speer et al., 1995; Pickart and Spall, 2007). However, several studies have calculated overturning rates exceeding 10 Sv, especially during the period of intense convection in the Labrador Sea in the 1990s (Marsh, 2000; Rhein et al., 2002). Similar calculations have also been attempted to calculate LSW production rates from models. Here values range from 5 Sv to 9 Sv (Böning et al., 1996; Brandt et al., 2007; Mauritzen and Häkkinen, 1999).

Due to its unique characteristics of low potential vorticity and pronounced salinity minimum, LSW can be tracked throughout the Atlantic. It has been found in the North Atlantic, north of 40 °N and as far south as 18°N (Talley and McCartney, 1982). LSW that is formed directly in the boundary is able to enter the DWBC more effectively and faster than LSW formed in the basin (Palter et al., 2007). However, water exchange at depth due to eddy mechanisms and divergence due to the mean flow are other possible ways for LSW to enter the DWBC.

1.3.3 Restratification and the role of eddies

After convection ceases, the basin quickly restratifies due to a combination of eddy stirring in the interior and import of heat and freshwater from the boundary currents. The exact dynamics of each of these mechanisms is unclear but it is thought that the initial restratification takes place due to eddies, formed when the large density gradients between the convective patch and surrounding interior become unstable (Jones and Marshall, 1993). The resulting convective eddies help to remove the initial, strong density gradient. Besides these convective eddies, eddy fluxes from the boundary play a role in the restratification process (Chanut and Barnier, 2008; Katsman et al., 2004). These eddies form due to baroclinic instabilities along the boundary currents. The largest eddies

formed in this way, are the so called Irminger Current eddies (or Irminger Rings) that form in the northeast of the Labrador Sea, close to the west coast of Greenland. Here, altimetry data and surface drifters have shown enhanced variability of the WGC, and hence enhanced Eddy Kinetic Energy (EKE) (e.g., Cuny and Rhines (2002); Lilly et al. (2003); Prater (2002)). This region of high EKE is caused by the local bathymetry (Eden and Böning, 2002; Bracco and Pedlosky, 2003). At roughly 61°N and 52°W the topography undergoes a sharp change and the shelf becomes wider. The adjustment of the boundary current to this change results in instabilities with the strongest variabilities just downstream. The EKE has a pronounced seasonal cycle, with maximum levels in the spring and a slow southward propagation in the summer (Brandt et al., 2004). The Irminger Current Eddies formed in this region consist of a warm and saline body of Irminger Current water but can have pronounced freshwater caps in the spring (de Jong et al., 2012) and thus helps to carry heat and freshwater to the basin (Lilly et al., 2003; Katsman et al., 2004; Straneo, 2006). They range in size from 15 to 55 km and are thought to balance most of the seasonal heat loss in the basin (Lilly et al., 2003; Straneo, 2006). However, the seasonal increase in heat and freshwater observed in the Labrador Sea basin after convection ceases cannot be completely explained, even when including boundary current eddies. This will be discussed further in **Chapter 3**.

1.3.4 Interannual variability of properties in the Labrador Sea

To first order, deep convection is dependent on late summer stratification (i.e. preconditioning) and atmospheric forcing, where the latter is highly correlated to the North Atlantic Oscillation (NAO). The NAO is the dominant mode of atmospheric variability in the North Atlantic and accounts for more than one third of the total variance in the winter sea level pressure (Hurrell, 1995). The strength of this mode, given by the NAO index, is generally defined by the sea level pressure difference between Iceland and the Azores. A positive NAO index is associated with a shift of storm tracks that causes intense low pressure systems to pass the Labrador Sea. These storms draw cold and dry air from Canada over the relatively warm surface water of the ocean, enhancing the air-sea buoyancy fluxes and favoring convection (Pickart et al., 2002).

Over the last two decades (1990 – 2015) the NAO changed from a mainly positive state to more negative NAO index (**Figure 1.2**). In fact, the early part of the 1990's characterized by very intense mixing in the Labrador Sea (Yashayaev, 2007; Pickart et al., 2002) coinciding with a strongly positive NAO index. A general warming and increase in salinity was observed (Hatun et al., 2007; Sarafanov et al., 2010; Yashayaev, 2007) together with a weakening of the circulation in the subpolar gyre (Häkkinen and Rhines, 2004; Belkin et al., 1998). The decline in circulation strength was linked to changes in the wind stress curl due to the high NAO. The mixing weakened after the winter of 1994/95 (Yashayaev, 2007), coinciding with a change to more negative NAO

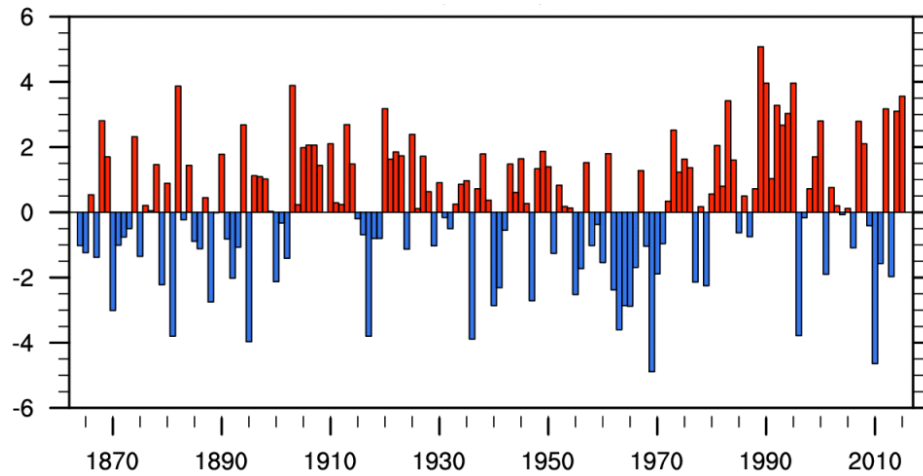


Figure 1.2: The yearly NAO index for 1870 – 2015. The data was downloaded from <http://www.cpc.ncep.noaa.gov>.

index. However, the absence of convection deeper than 1400 m after 1995 cannot be explained by the NAO alone (Lazier, 2002; Stramma et al., 2004). Instead, properties and convection often vary on decadal timescales that are not directly associated to the NAO (Avsic et al., 2006; Dickson et al., 1988). For example, Deser and Blackmon (1993) found a 10 – 15 year fluctuation of a dipole in sea surface temperature anomalies between the subpolar and subtropical region that is closely linked to the decadal variation in sea ice in the Labrador Sea. Furthermore, and of more immediate importance to convection, are several periods of freshening over the last decades, e.g., in 1967 – 1977 (known as the ‘Great Salinity Anomaly’) (Dickson et al., 1988) and 1990 – 1994 (Häkkinen, 2002). Both periods were characterized by extremely low salinities in the surface layers and the former resulted in a shutdown of convection for several years (Dickson et al., 1988; Häkkinen, 2002). The changes in water properties independent from the NAO and the impact of preconditioning on convection results in a nonlinear relationship between the NAO and strength of the mixing.

1.3.5 The role of freshwater in the Labrador Sea dynamics

On a seasonal cycle, two freshwater pulses are observed in the Labrador Sea basin. A first pulse in April, and a second, stronger pulse in the fall (Schmidt and Send, 2007). Lateral fluxes from the boundary current are the source of these pulses, while air-sea freshwater fluxes and ice melt can be ruled out (Schmidt and Send, 2007). In particular, precipitation minus evaporation adds water to the basin evenly throughout the year. Local ice melt on the other hand, occurs more rapidly, but the central Labrador Sea stays free of sea ice and most of the melt occurs and stays inshore of the boundary currents (e.g. Mysak et al. (1990); Wang et al. (1994)). Furthermore, the timing of the

sea ice melt, and the observed freshening pulses do not coincide it can therefore be ruled out as the source of the freshening (Schmidt and Send, 2007). Historically, the Labrador Current was considered as the main source of the freshwater brought to the basin via lateral fluxes (e.g., Lazier (1973)) but more recent studies have shown that the West Greenland Current provides most of the freshwater advected to the basin (e.g., Cuny and Rhines (2002); Schmidt and Send (2007)).

In high latitudes, where salinity has a much stronger impact on the density of the ocean than temperature, freshwater has the potential to impact ocean dynamics significantly. Hence, an increase in freshwater in the Labrador Sea would introduce large amounts of buoyancy to the ocean. This, in turn, would impact the formation of LSW by capping the basin and making it harder for air-sea fluxes to remove the surface buoyancy. An example of this is the ‘Great Salinity Anomaly’, which is thought to have occurred due to abnormal export of freshwater through Fram Strait (Dickson et al., 1988). This also highlights the connection between freshwater export from the Arctic via the East Greenland Current and the surface salinities and convection in the Labrador Sea (Aagaard and Carmack, 1989; Dickson et al., 1996).

When using coarse models and adding additional freshwater to the Arctic, most models show an almost uniform spread of this freshwater throughout the entire North Atlantic region, including the Labrador Sea (e.g., Weaver et al. (1994)). Such an increase in freshwater in the Labrador Sea leads to a modification of LSW production and an abrupt decrease of the MOC transport (Manabe and Stouffer, 1995; Jahn and Holland, 2013). However, more recent, finer resolution models have shown that the impact of freshwater input on the Labrador Sea remains unclear. An increase of freshwater (by 60%) would have little effect on the Labrador Sea basin, if entering the region through David Strait. Instead it would be flushed out of the region by the boundary currents (Myers, 2005) and it is still unclear what impact additional freshwater in the Arctic will have on the dynamics in the Labrador Sea.

In recent years, the MOC has been closely monitored by the RAPID-MOCHA array at 26°N. Data from this array has shown a decline in the strength of the overturning circulation (Smeed et al., 2013). Robson et al. (2014) suggest that this trend is not a short-term fluctuation but part of a longer term trend. In fact, they argue that the large decrease in Labrador Sea Water density found in observational data could lead to a MOC reduction of about 5 – 6 Sv. This again highlights the importance of understanding the dynamics in the Labrador Sea, since changes here, especially changes in freshwater fluxes, can have impacts on a global scale.

1.4 Overview of Thesis

This thesis is structured in the following way:

Chapter 2 uses Argo data to examine the relationship between heat and freshwater in the Labrador Sea and lateral fluxes to the basin on a seasonal and interannual time scale and what changes these dynamics might have undergone. Furthermore, the freshwater content of the Labrador Sea is investigated in light of the recent increase in sea ice melt in Arctic.

Chapter 3 aims to understand the pathways of freshwater into the Labrador Sea basin. Using an ocean model and a Lagrangian approach, the main pathways of freshwater to the basin are described on a seasonal and interannual timescale. Here, the use of the ocean model enables the development of a coherent picture of the connection between the boundary region and basin which is not possible from observations only. The role of Ekman transport in advecting water to the basin is investigated.

In Chapter 4 I look at the impact of large scale forcing on mixing in the Labrador Sea. Storm tracks are analysed and their relationship to mixing is described. Additionally, the impact on the mixed layers themselves and the resulting variability in their structure is investigated.

The last chapter, Chapter 5, provides a summary and discussion of the major findings of this thesis with suggested wider implications and potential avenues for future work.

Chapter 2

Heat and Freshwater of the Labrador Sea, 2002 – 2011

2.1 Introduction

The aim of this chapter is to describe and understand changes in the heat and freshwater budget of the Labrador Sea over the last decade. Lateral fluxes of heat and freshwater drive the restratification of the basin and result in an increase of freshwater that is observed every year in the spring and summer (Straneo, 2006; Yashayaev, 2007). Much of what regulates the fluxes is unknown, despite their importance. This Chapter will follow the approach of Straneo (2006) in investigating the lateral fluxes (this is further explained in **Section 2.2.4**). Using profiling floats (for 1996 – 2000) and mooring data (1964 – 1974), she found that lateral fluxes occur at a rapid rate during the first months following convection when restratifying the basin. They slow but persist throughout the entire year reflecting a continuous exchange between boundary and basin. Lateral exchange was also observed in the years of the ‘Great Salinity Anomaly’ when convection was shut down. This suggests that the lateral fluxes are correlated to the mean horizontal density gradient rather than the convective process itself. In the vertical, lateral fluxes advect cold and freshwater to the surface layer, overlaying warm, salty Irminger Water. Straneo (2006) found that about 0.5 m of freshwater is brought to the basin by lateral fluxes. Only a fraction of this is mixed downward by convection and the subsurface divergence is not large enough to balance the annual gain such that some of the freshwater must be removed by mixing with surrounding saltier waters. Her findings on the seasonal cycle of lateral fluxes during convection and restratification are robust, but large uncertainties remain on the interannual variability of these fluxes.

Here, I want to revisit these lateral fluxes and analyse them for the more recent period of 2002 – 2011 with the goal to see if the previous results are robust across different time periods or if the characteristics of the lateral fluxes have change and affected convection. Another open question is whether the two freshwater pulses observed by Schmidt and Send (2007) are a robust signal. Straneo (2006), for example, sees only one freshening even in her data set. The reason for this is unclear.

Secondly, over the last years multiple studies have reported a large increase in Arctic Ice melt and Greenland runoff (Bamber et al., 2012; Markus et al., 2009) and here I aim to understand if this increase in freshwater has already impacted convection in the Labrador Sea, or will do in the future.

2.2 Data and Methods

2.2.1 Region definitions

To separate processes in the deep basin from those taking place within the boundary currents I concentrate on the Labrador Sea basin. The basin is defined as the region offshore of the 3000 m isobath and the boundary currents and the line connecting the

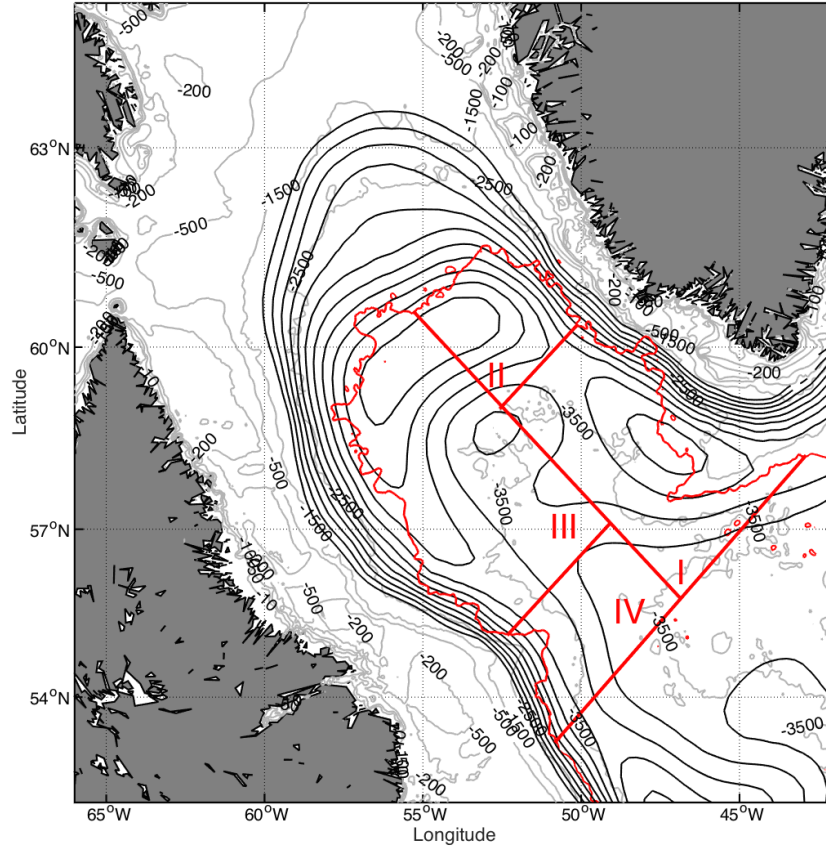


Figure 2.1: The Labrador Sea with the four regions used in this study marked by the red lines and numbers. The solid black lines show the streamlines as determined by Lavender et al. (2000).

southwest and southeast corner of the Labrador Sea (**Figure 2.1**). To help gain insight into regional differences, the basin is further divided into four regions that reflect the pattern and location of high heat fluxes, deep convection, eddy kinetic energy and streamlines (**Figure 2.1**). The eddy kinetic energy (EKE) field close to Cape Desolation defines the location of Box II (Eden and Böning, 2002). This region also has the weakest convection observed in the basin (**Chapter 4**). The highest heat fluxes and most vigorous convection takes place in the western part of the basin. This defines the location of Box III. Only occasional convection is observed in Box I and IV, which are located at the entrance and exit (southeast and southwest) of the Labrador Sea basin.

2.2.2 Argo floats

The Argo float program, launched in 2000, was initiated to measure temperature and salinity of the world's ocean and relate these measurements to global and regional signals

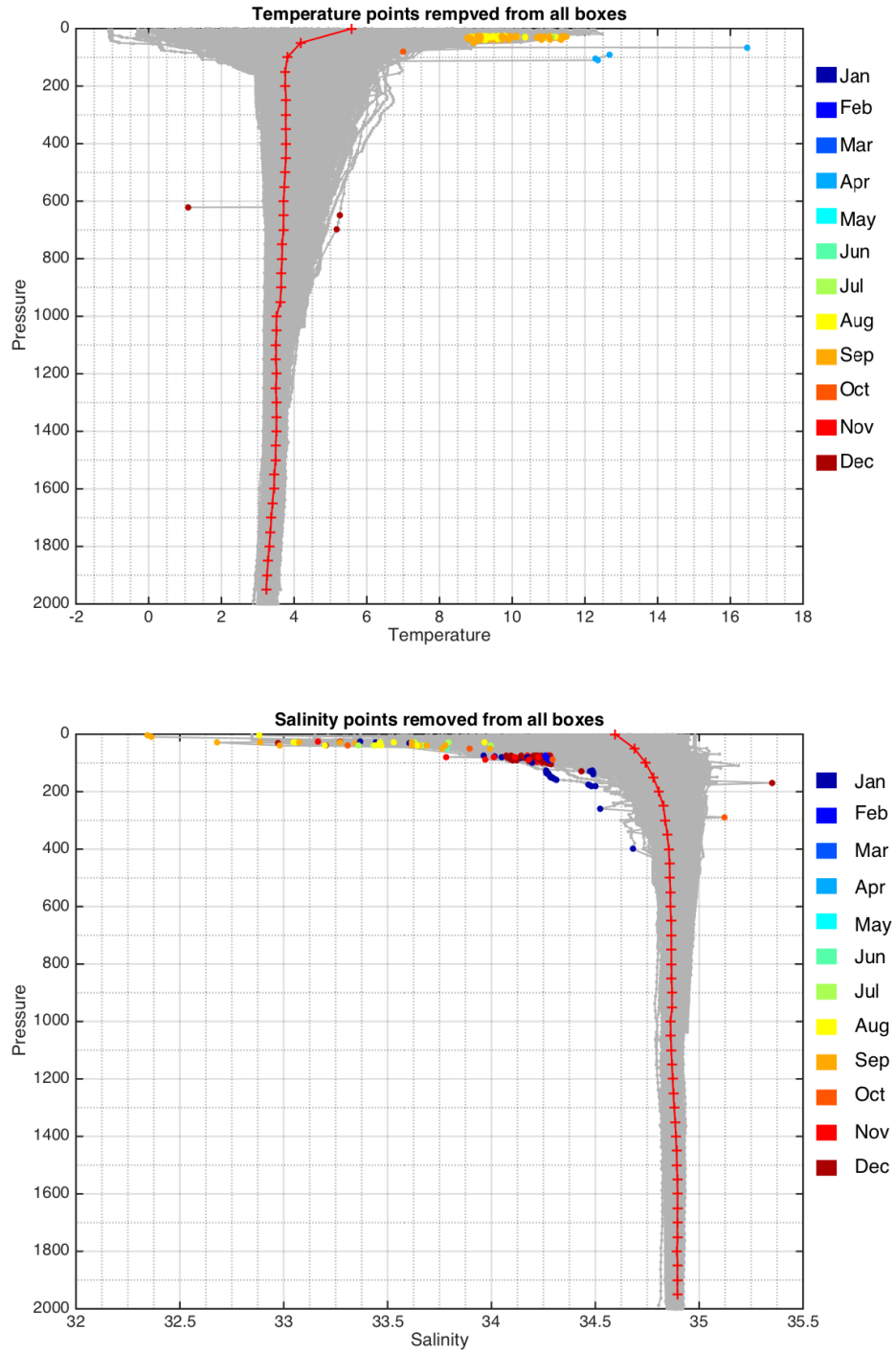


Figure 2.2: Top panel: All temperature profiles measured by Argo floats in the basin (before quality control was performed) are shown in gray, with their mean profile in red. Colored dots mark points that were removed according to the cleaning procedure described in **Section 2.2.2**. The dots are color coded according to the month during which they were recorded. Bottom panel: same as above but for salinity

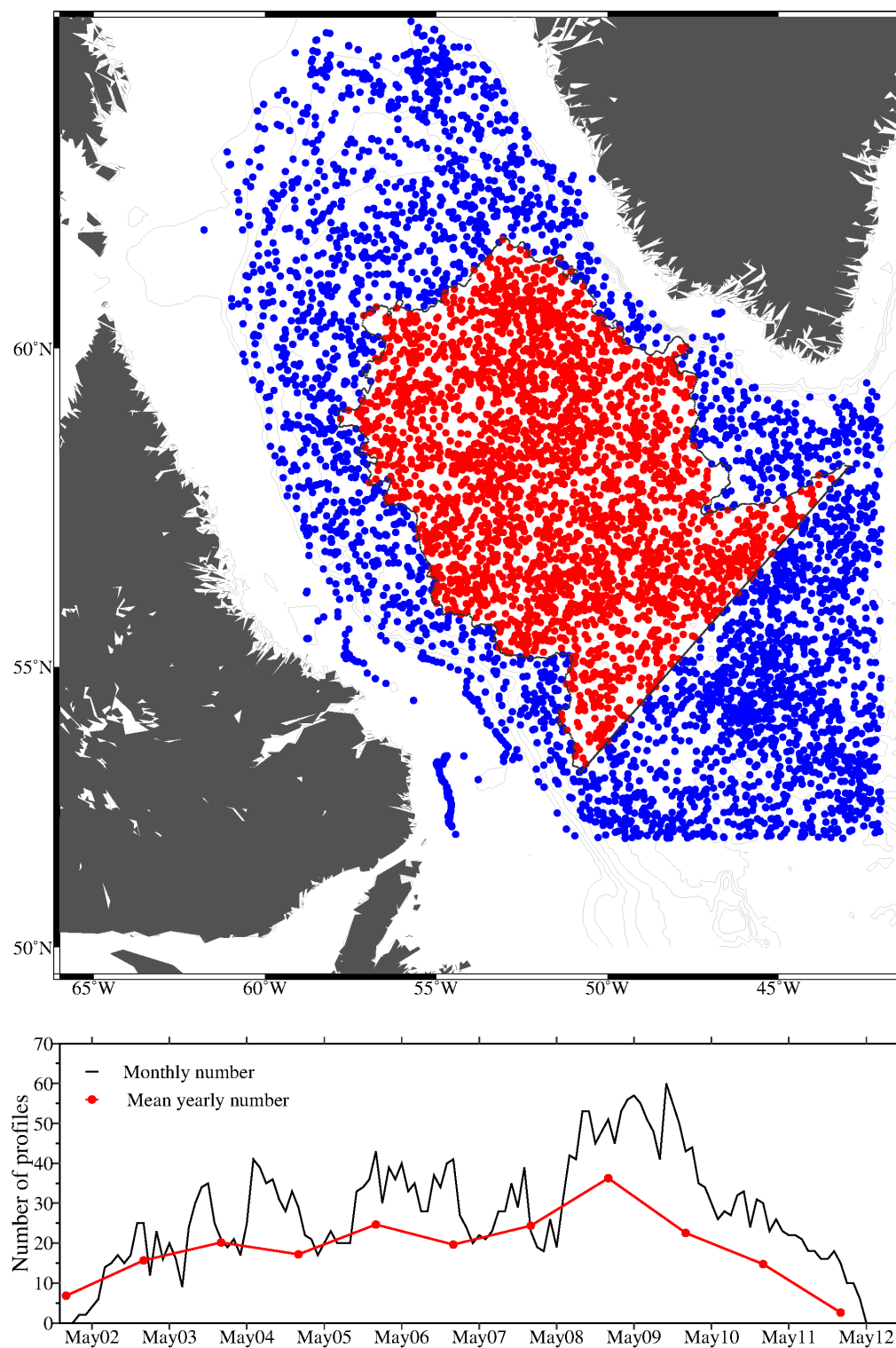


Figure 2.3: Top panel: The Labrador Sea and the location of the profiles in the basin (red) and outside the basin (blue) between 2002 – 2011. Bottom panel shows the number of profiles in the basin each month (black line) and the mean number per year (red line and dots).

of climate change. These data were collected and made freely available by the International Argo Program and the national programs that contribute to it (<http://www.argo.ucsd.edu>, <http://argo.jcommops.org>). The Argo Program is part of the Global Ocean Observing System. The program is ongoing with a deployment rate of around 800 floats per year. All Argo float data used in this work are part of the global array of approximately 3606 free-drifting floats (as of 20 Oct 2013), resulting in more than 10,000 profiles of salinity and temperature per month (about one profile every 10 days per float). Data is transmitted to data centers across the globe where the first stage of quality control takes place. This is done mainly automatically, allowing users to access data within 24 hours of recording. The procedure is described by Gaillard et al. (2009) and the Argo quality control manual is available at <http://argodatamgt.org/Data-Mgt-Team/News/Argo-quality-control-manual-version-2.8-release>. The procedure tests parameters such as identification, date, location, and position, speed, global range of pressure, temperature, salinity, oxygen, spikes, density inversion and sensor drifts. A non-mandatory visual inspection is performed by some data-centers.

After this, profiles undergo a second stage of processing and are made available as the ‘delayed-mode’. Here, each profile is examined for errors such as spikes, jumps and sensor drifts etc. by relating the profile to nearby floats or historical data. Each data point is then assigned a quality flag 1 – 4 (from ‘good’ to ‘bad’). Data with quality flag 1 are assumed to be ‘good’ while data with flag 2 might have some uncertainties. If data has a quality flag of 3 the observation is thought to be bad but might be recoverable if further extensive quality control is applied. A flag of 4 shows data that is bad and irrecoverable. For the study period of 2002 – 2011, 3217 vertical profiles of temperature and 3319 salinity profiles were downloaded from <http://odc.noaa.gov/argo/accessData.html>. Only delayed-mode profiles and data points with quality flag 1 or 2 have been considered for this study. Measurement uncertainties are expected to be less than 0.005°C for temperature and 0.01 for salinity.

In this study, I concentrate on profiles taken within the basin. All together, 2692 temperature and 2783 salinity profiles were measured here (red dots in **Figure 2.3**). It is important to note, that the number of profiles in the basin varies from year to year (**Figure 2.3**, bottom panel). As 2002 was one of the early years in the Argo era, few floats found their way into the Labrador Sea. Fewer profiles are also available in 2011, since this data set was downloaded in 2012 and delayed-mode data takes up to one year to be released to the science community. While there are months with more than 40 or 50 profiles in the basin, others only have 10 or 20 (e.g., June and July 2003 and April and May 2008). This variability in data availability is not of immediate concern, but has to be kept in mind when interpreting the data.

A third stage of quality control is provided for data used in this study, to assure that no further errors, such as additional spikes or salinity drift, are present. Several studies apply a similar personal quality control (e.g., Levitus et al. (2000); Roemmich and Gilson (2009); Willis et al. (2004); Ivchenko et al. (2012)). These studies eliminate

entire profiles if parts of the profile deviates more than 2 – 6 standard deviations from the monthly climatology. Here I chose a slightly different approach and eliminate single points if they:

- are out of range (temperatures $>23.0^{\circ}\text{C}$ and $<-2.5^{\circ}\text{C}$, and salinity >35.7 and <27)
- are separated by more than 800 m from the point above and/or below within the same profile (e.g., deepest point more than 800 m away from second deepest point).

This procedure removes 3178 out of 639,963 (0.005%) and 93 out of 637,363 (0.0001%) temperature and salinity points, respectively. Additionally, each profile is compared to the mean profile for 2002 – 2011. Data points are eliminated if they are outside seven standard deviations of the reference profile. Seven standard deviations were chosen as a criteria to avoid an unwanted biased removal of points in the part of the water column that undergoes large seasonal changes. An additional 149 temperature and 196 salinity points were removed following this comparison. Together, about 0.0052% of temperature and 0.0005% salinity points are removed. While this is a very small fraction of points, the process is necessary for certain profiles with spikes or offsets in salinity (**Figure 2.2**).

2.2.3 Air-Sea fluxes

Air-sea fluxes are assessed using daily reanalysis fields. Several products are currently available, such as ERA-Interim (European Center for Medium Range Weather Forecasting), MERRA (Modern Era Retrospective-analysis for Research and Application), OA Fluxes (Ocean-Air Fluxes from Woods Hole Oceanography Institution), NOCS fluxes (from the National Oceanography Center Southampton), ASR (Arctic system reanalysis), and NCEP/NARR (North American Regional Reanalysis), NCEP/DOE (also known as NCEP reanalysis II). Most of these products are not suitable for the purpose of this study since certain variables were not available (e.g., MERRA - no radiation fields) or the products did not cover the entire time period of this study (e.g., NOCS and ASR), etc.

The NCEP data were obtained directly from the NOAA website (www.esrl.noaa.gov) and ERA-Interim data from <http://data-portal.ecmwf.int>. Both products were downloaded as daily fields for the region between 65°W – 42°W and 53°N – 70°N . and gridded onto a 0.3° longitude by 0.2° latitude grid.

I compare the turbulent heat flux of the two products. The reanalysis flux fields depend strongly on the numerical models used to calculate them and a comparison to observational data shows that ERA-Interim turbulent heat fluxes agree reasonably well (overestimating the observations by 13% and 10% for sensible and latent heat, respectively). The NCEP reanalysis however, drastically overestimates the turbulent

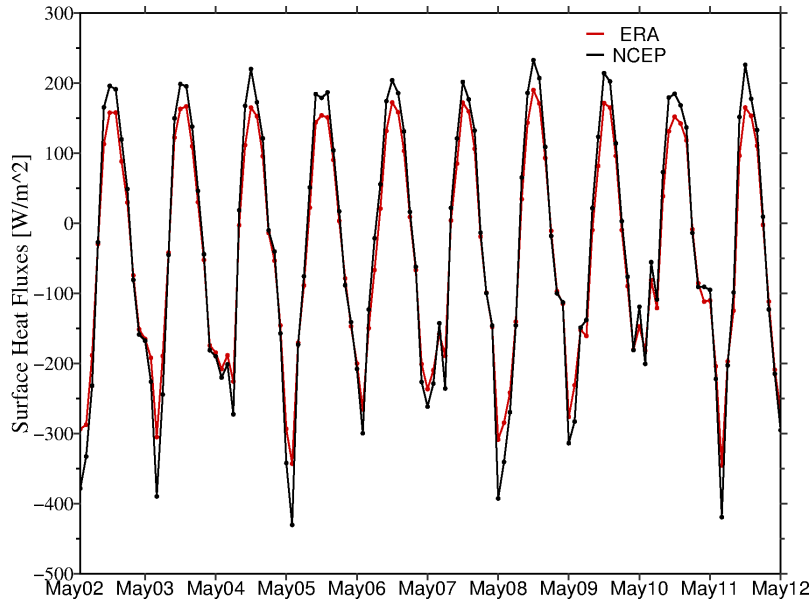


Figure 2.4: Monthly mean value of turbulent heat fluxes in the Labrador Sea basin obtained from NCEP (black) and ERA-Interim (red) data

heat flux by 51% and 27% for sensible and latent heat (Moore and Renfrew, 2002; Renfrew et al., 2002). These shortcomings are especially pronounced during high wind events that are combined with large air-sea temperature differences, as is the case in the Labrador Sea in the winter. Both products reproduce the cooling in winter and warming in summer (**Figure 2.4**). The ocean loses heat for at least half the year, but the NCEP reanalysis estimates 14% more cooling compared to the ERA-Interim product. Summer heating is 21% larger in the NCEP reanalysis.

For this study the ERA-interim product will be used since it has been shown to more accurately represent the surface flux conditions in the Labrador Sea ((Moore and Renfrew, 2002). Furthermore, it has been noted by Latarius and Quadfasel (2010) that, for the Greenland Sea, the NCEP/NCAR data shows a large discrepancy to other data sets. More details about the NCEP-NCAR project and ERA-Interim can be found in (Dee et al., 2011).

Large uncertainties remain in the estimates of evaporation (E) and precipitation (P), due to scarce measurements in the region. For example in the Labrador Sea, estimates of precipitation range from 0.8 m/yr (Ikeda (1987), obtained from measurements of the surrounding land) to 1.26 m/yr (Sathiyamoorthy and Moore (2002), from measurements at OWS Bravo). Using the ERA-Interim product results in a slightly higher estimate of 1.45 m freshwater gain per year through precipitation. Climatologies show that as much as 0.1 mm/hr of freshwater is added to the Labrador Sea in the winter while freshwater fluxes in the summer decrease to around 0.02 mm/hr (da Silva et al., 1994). The seasonal cycle found in the ERA-Interim data is similar to these findings and will be discussed further in **Section 2.4.2**.

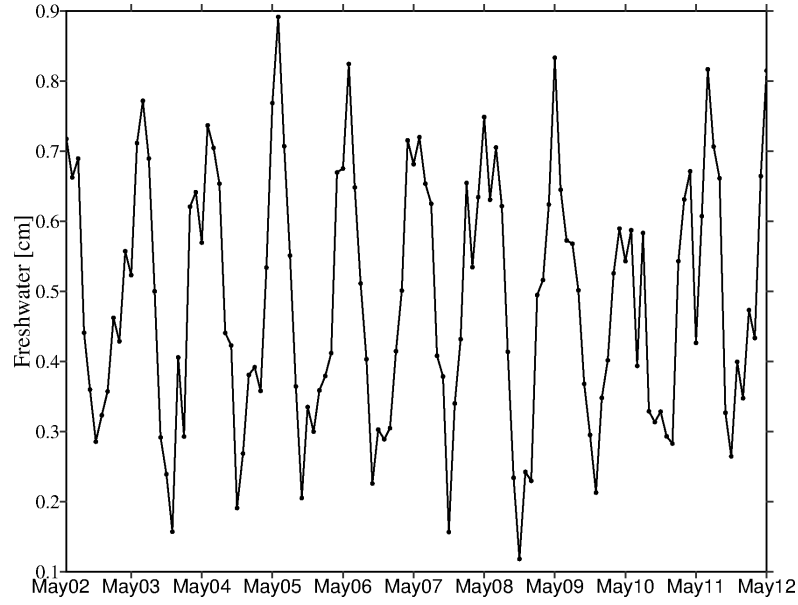


Figure 2.5: Monthly mean evaporation-precipitation in the Labrador Sea basin obtained from ERA-Interim data. Positive values show a gain of freshwater to the region.

2.2.4 Calculation of Lateral fluxes

Changes in temperature and salinity of the basin due to the atmospheric fluxes are separated from changes due to lateral fluxes of heat and freshwater from the surrounding ocean following Straneo (2006)’s approach. Hence, I compare the expected changes in heat content (due to the surface fluxes) to the observed changes in heat content (from Argo floats). May of each year, when convection has ceased and the surface layer starts to warm, is taken as the initial condition. Hence, every year comprises of May – December of the current year and January – April of the following year.

The observed heat content is calculated from the temperature measured in the upper 100 m of the basin by Argo floats. For every month the floats are binned into boxes of 0.9° longitude and 0.55° latitude, before averaging them to calculate the monthly heat content. The same is repeated for salinity and the freshwater content of the basin. The implied heat content is calculated by assuming that all changes are due to surface fluxes alone. Hence, I integrate the heat fluxes due to atmospheric forcing throughout the year and add the initial heat content (from May).

For salinity, the E-P freshwater flux (in meters) is converted to salinity using

$$FW = \frac{S_{ref} - S}{S_{ref}} \quad (2.1)$$

the reference salinity is taken to be 34.7 for the upper 100 m. This is the average salinity of this layer over the timeperiod studied here. Again, the salinities of May are used as

the initial conditions. Observed changes are then compared to the implied ones (**Figure 2.20**).

2.2.5 1-D Mixing Model

To better understand the oceans response to changes in salinity in the surface layer during the convective season, a one-dimensional mixed layer model (Prince et al. (1986), hereafter PWP) was employed. To implement the model, heat fluxes, freshwater and momentum (wind stress) from ERA-Interim were imposed at the surface for each time step. Note that the results vary only slightly when wind stress is set to zero, and the main findings would not change if this was done. Mixing in the model is carried out until three different stability criteria are satisfied. These criteria are based on the vertical density gradient (static stability), the Richardson number (mixing layer stability) and the gradient Richardson number (shear flow stability), where the latter two reflect the wind stress mixing processes. Hence, both Richardson processes would be inactive without wind forcing. In particular, the mixing in the model is carried out as followed: if, after the surface forcing is applied, static instability is present near the ocean surface, it is relieved according to this procedure: If water in layer 2 is less dense, it is mixed with layer 1. If water in layer 3 is less dense than the mixed water above, it is again completely mixed. This is repeated until the profile is once again stable. The model then performs additional mixing according to a bulk Richardson number criterion. Finally, the depth of the mixed layer is identified as the depth of the first interface below the surface where the density jump exceeds a prescribed value.

2.3 Basin-averaged properties

The surface layer of the Labrador Sea basin is, compared to the adjacent shelf region, warm and salty with the warmest waters found in the south and saltiest water in the southeast and northwest (**Figure 2.6 a** and **Figure 2.7 a**). Temperature differences between the boundary current and basin are as large as 4°C and salinities are about 0.4 higher in the basin. Two regions of high salinities are identified, one in the northeast, likely caused by the retroflexion of the salty Irminger Current (Holliday et al., 2007), and a second in the northwestern part of the basin, in the region of the strongest convection. Here freshwater is mixed downwards in the winter, causing an increase in salinities at the surface. The mid-layer (100 - 800 m) has more evenly distributed temperature and salinity characteristics (**Figure 2.6 b** and **2.7 b**). Both, temperature and salinity are highest in the east with a minimum in the southwest. This results in the largest temperature gradients in the southwest where surface temperatures are highest overlaying the coldest mid-layer temperatures. Salinities and temperatures in the deep layer are even more uniform throughout the region, with an average basin temperature

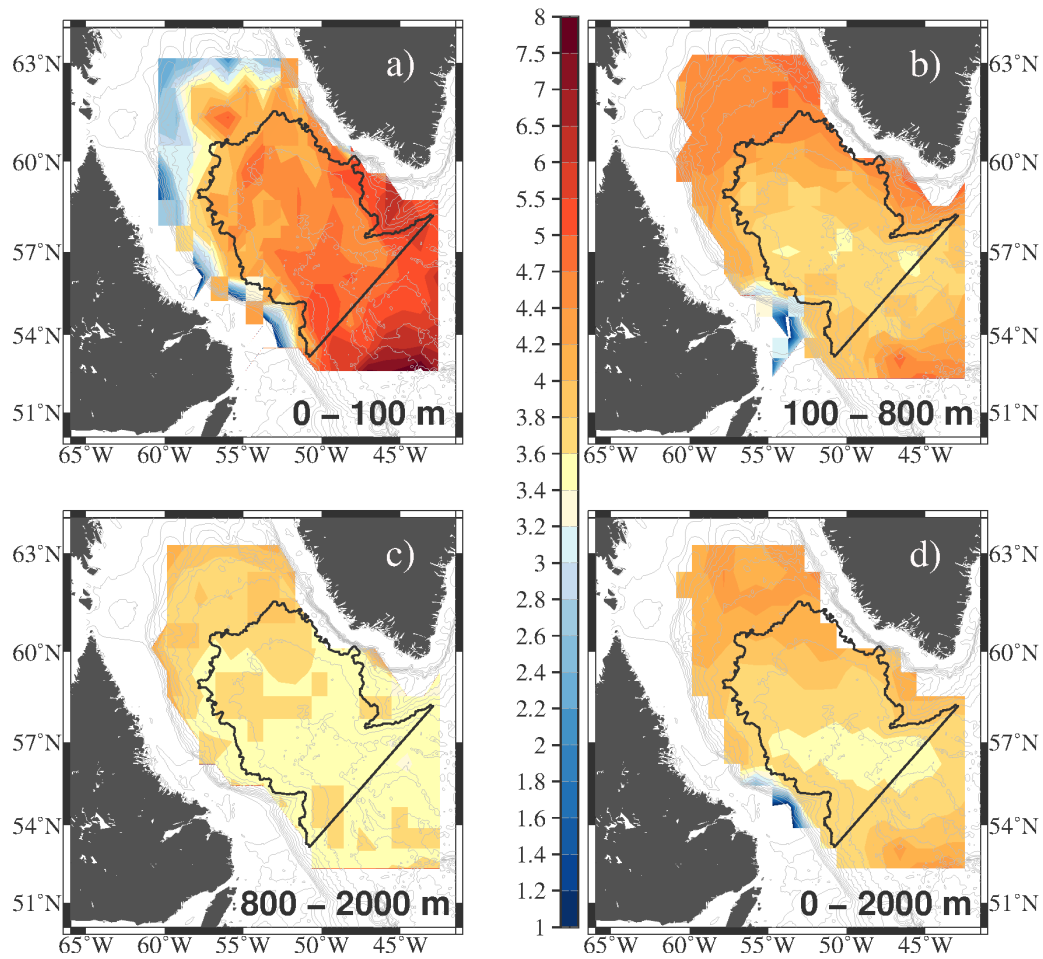


Figure 2.6: Maps of temperature, obtained from the Argo floats, for the different layers (a) surface layer: 0 – 100 m, b) mid-layer: 100 – 800 m, c) deep layer 800 – 2000 m, and d) entire water column 0 – 2000 m.

of 3.5°C and 34.85 psu salinity (**Figure 2.6c** and **Figure 2.7c**). Overall, for the entire 0 – 2000 m layer, the surface layer of the basin is saltier and warmer than the adjacent region, while the opposite is true for mid- and deep layer. This is due to the presence of the deep Labrador Sea Water (LSW) in the basin, formed by downward mixing of cold and fresh surface water in the winter.

2.3.1 Temperature

Changes in temperature and salinity over time can be visualized by plotting the basin-averaged properties of the Labrador Sea as a function of depth and time (**Figure 2.8**). This is accomplished by binning the Argo profiles into boxes of 0.9° longitude and 0.55° latitude before calculating the monthly mean of the entire basin. Temperature and salinity are then interpolated onto a regular grid of 14 days and 50 m depth intervals

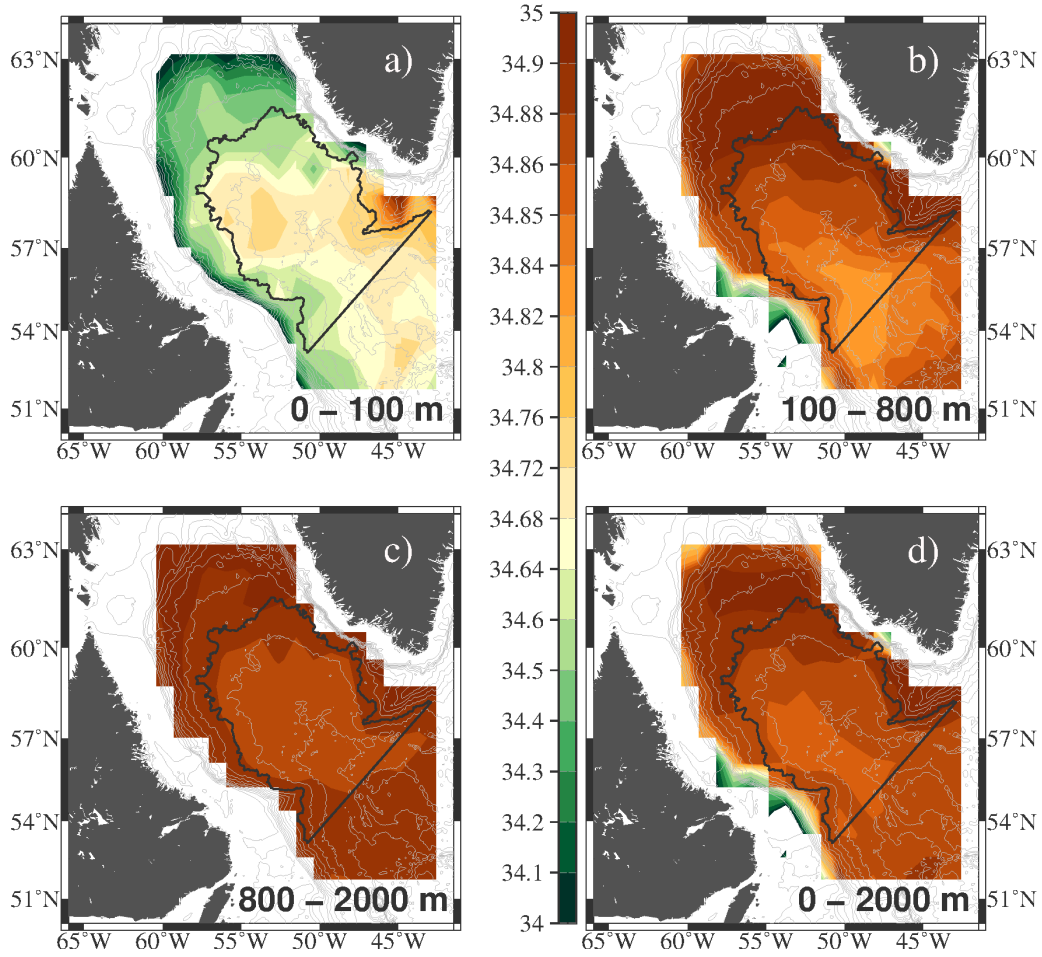


Figure 2.7: Same as **Figure 2.6** but for salinity

using a Laplacian-spline interpolation previously used in several other publications (e.g. Spall et al. (2008); Nikolopoulos et al. (2009); Schulze and Pickart (2012)).

The surface (0 – 100 m) temperature of the basin is strongly dominated by a seasonal cycle (**Figure 2.8** and **Figure 2.9 a**), resembling the heat changes due to solar radiation seen in **Figure 2.18**. Maximum temperatures in the summer (August – September) can reach up to 12°C. After the peak heating, cold winter winds and heat loss to the atmosphere cause temperatures to decrease rapidly in the upper layer, reaching temperatures as low as -1°C. The buoyancy loss due to winter cooling causes the mixing of fresh and cool surface water downwards, often deepening the mixed layers to 1000 m or more (e.g., in winter 05/06 and 07/08). While the interannual variability of heating/cooling is strong, the temperature anomaly of the surface shows no longterm trend (**Figure 2.9 a**). The mean annual decrease of about 1° C in temperature between 2006 and 2009 is balanced by warmer temperatures in 2010 and 2011 and the trend of the linear fit shown is not significant. The decrease in temperature is mainly due to the anomalously cold temperatures in winter 07/08 and 08/09, where mean surface

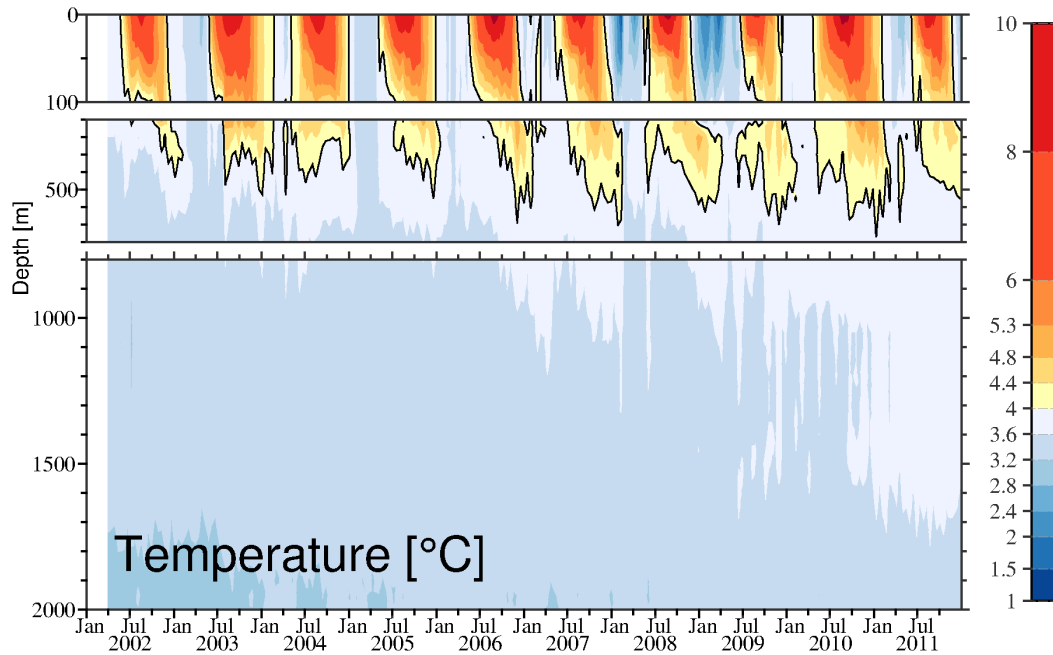


Figure 2.8: Basin-average temperature for 2002 – 2011, gridded onto a regular grid of 50 m depth and 14 days. The different layers (surface layer (0 – 100 m, mid-layer (100 – 800 m) and deep layer (800 – 2000 m)) are shown in separate panels. Note that the upper layers are stretched compared to the deep layer. The black contour shows the 4°C isotherm.

temperatures fell below 3°C. Temperatures of the corresponding summers (2008 and 2009) are also colder than temperatures of other years making them the two coldest summers of the decade. Temperatures in 2003 and 2010 on the other hand are the two warmest years of the study period and the abnormally warm water in 2010 helps offset the cooling of the two previous years. Seasonal heating and cooling usually penetrates the mid-layer (100 – 800 m). Here lateral fluxes play a much more important role than air-sea interaction, resulting in a weakening and distortion of the seasonal cycle (**Figure 2.9 b**). The summer-time depth of the 4°C isotherm increases throughout the decade, reaching depths of around 600 m in 2002 – 2006 but penetrating the water column as deep as 1000 m in the later years (**Figure 2.8**). This coincides with a warming of 0.4°C over the last 10 years (**Figure 2.9 b**). This trend is significant within 90% confidence levels. Strong interannual changes in heat content are confined to the deep ocean (800 – 2000 m). Here temperatures increased by approximately 0.5°C between 2002 and 2011 (3.3°C to an average of 3.9°C). The trend has a statistical significance of 95% and is only briefly interrupted by a period of cooling in winter 07/08, when deep convection mixed cool surface waters to depth of up to 2000 m.

Seasonally, temperatures of the surface layer range from $3.3 \pm 0.7^\circ\text{C}$ in February to $6.4 \pm 0.6^\circ\text{C}$ in September (where standard deviations are calculated on the monthly

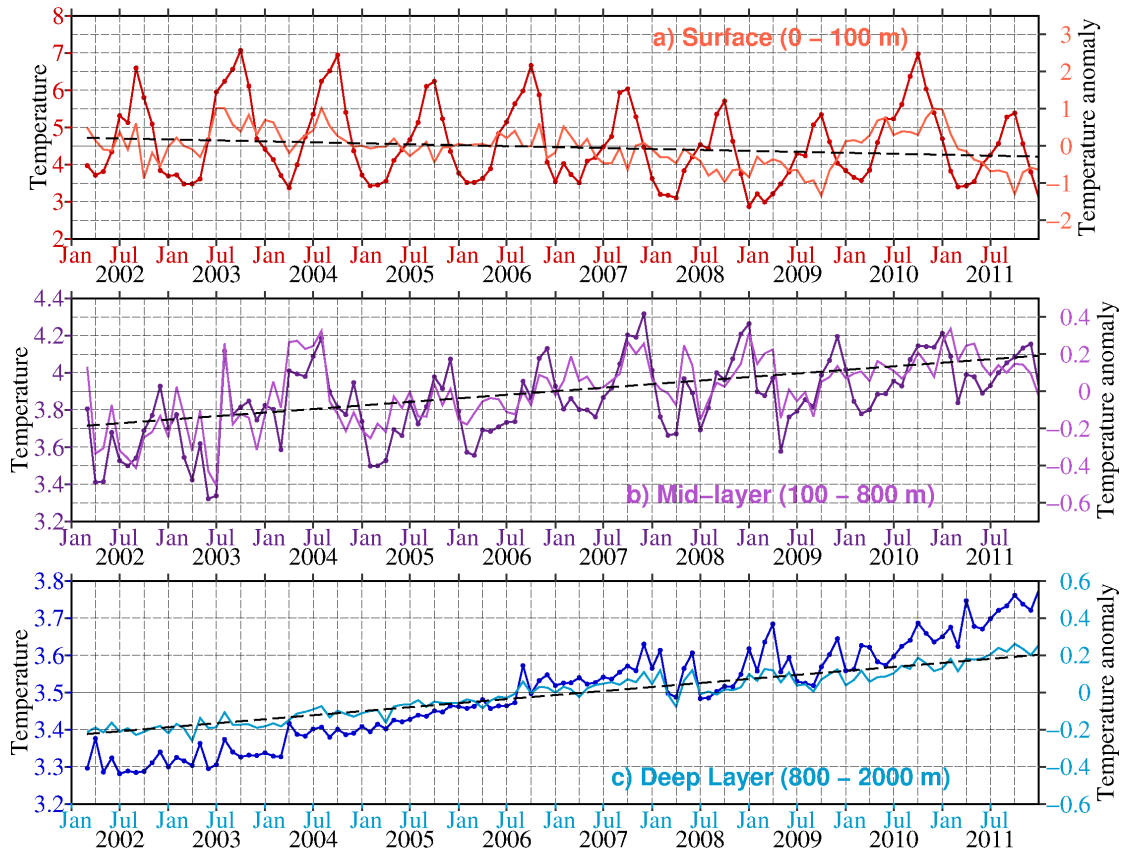


Figure 2.9: Basin-average temperature time series for surface (0 – 100 m, top panel), mid-layer (100 – 800 m, middle panel) and deep layer (800 – 2000 m, bottom panel) shown in dark red, dark purple, and dark blue, respectively. The temperature anomalies (monthly mean - annual monthly mean) are shown as the thin light line in each panel. The broken black line shows the linear fit of the anomalies.

values). The most intense warming coincides with the maximum sea-air heat flux in June – August (**Figure 2.10**). The seasonal cycle of the 100 – 800 m layer is weaker with a temperature range of $0.5 \pm 0.2^\circ\text{C}$. The peak heating/cooling lags those at the surface by about one month and minimum temperatures of $3.7 \pm 0.2^\circ\text{C}$ occur in March. After this, the water warms throughout the rest of the year, until reaching its maximum temperatures of up to $4.2 \pm 0.2^\circ\text{C}$ in December. The onset of warming in April corresponds to an increase in salinity (**Figure 2.13**) and is associated with the beginning of the restratification period and hence the isolation of the mid-layer from the cold surface waters. With the beginning of convection in winter, the warming of the mid-layer ceases (November and December) and temperatures start to fall as cold and fresh water is mixed down from the surface. Temperatures in the deep layer vary little and remain around $3.5 \pm 0.2^\circ\text{C}$ year around.

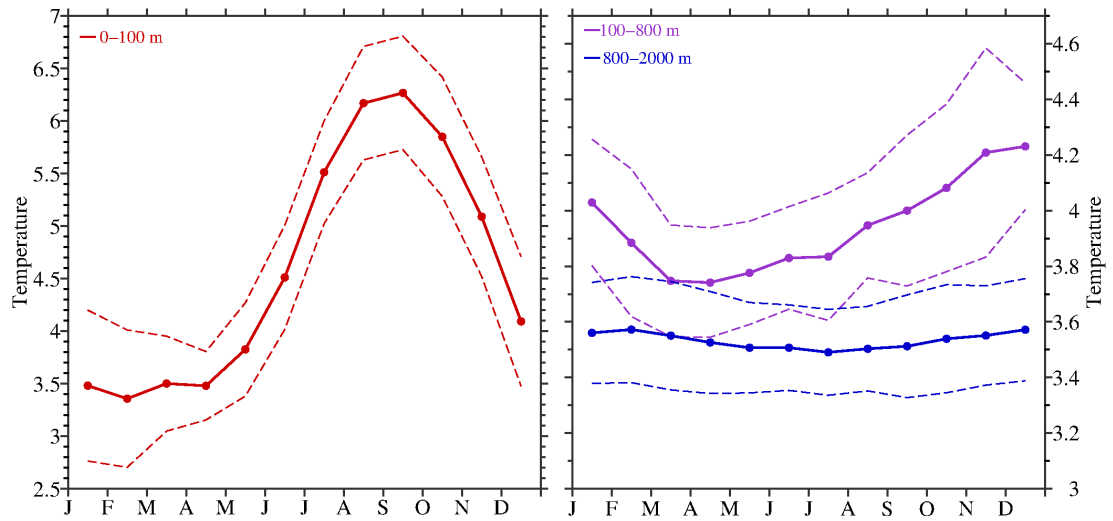


Figure 2.10: Climatology of basin averaged temperature (with the associated standard deviation shown as the broken lines) for the surface layer (0 – 100 m, left panel). The right panel shows the climatologies of the mid-layer (100 – 800 m) in purple and the deep layer (800 – 2000 m) in blue.

2.3.2 Salinity

The surface layer of the basin is characterized by a freshening period in summer/fall (**Figure 2.11** and **Figure 2.12**). Seasonal changes in salinity are much more variable than seen for temperature. A fresh layer forms between March and late winter and can reach depth of more than 100 m. The freshening becomes more dominant in the later half of the decade as seen by the depths of the 34.65 isohaline. It is located on average at 50 m but deepens throughout the decade until exceeding 100 m during the later five years. Furthermore, the freshening periods become longer. In particular, salinities below 34.5 are observed for less than one month in the first three winters but last up to five or six months in the later years. This results in a slight overall freshening of the surface layer causing a decrease of mean salinities from 34.7 to 34.6 over the 10 years analysed here (**Figure 2.12 a**). Thietrend is, however, statistically not significant and mainly driven by a large freshening starting in summer 2007. This long lasting and strong surface freshening continued through to December 2008 (**Figure 2.11** and **Figure 2.12 a**). During these 18 months, basin-averaged salinities decreased from 34.8 to 34.4. The trend is only briefly interrupted in February 2008 when deep convection mixed saline sub-surface water into the surface layer. By the beginning of 2010 salinities had mostly recovered. Interestingly, the trend in freshening is not felt by the layer below (100 – 800 m). In fact, here salinities increase over the same period, reaching maximum salinities of 34.9 at the end of 2009, making it the saltiest winter of the decade. The trend towards saltier waters during the 2002 – 2011 period in this layer is significant within 95% confidence levels. The deep ocean (800 – 2000 m) shows no seasonality. There is, similar to the mid-layer, an increase in salinity throughout the decade (also

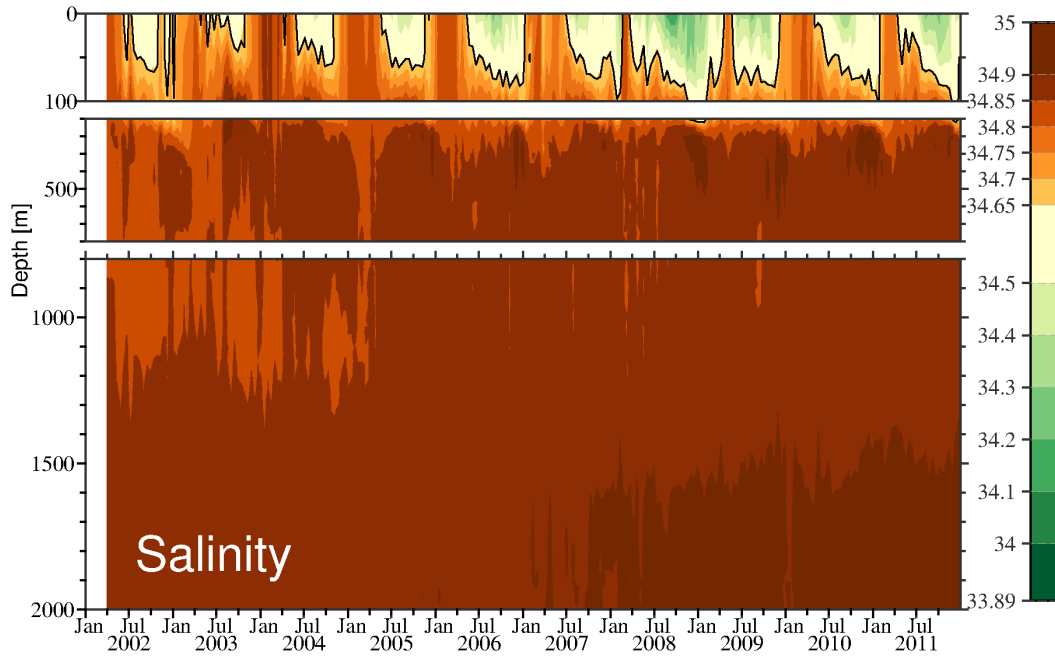
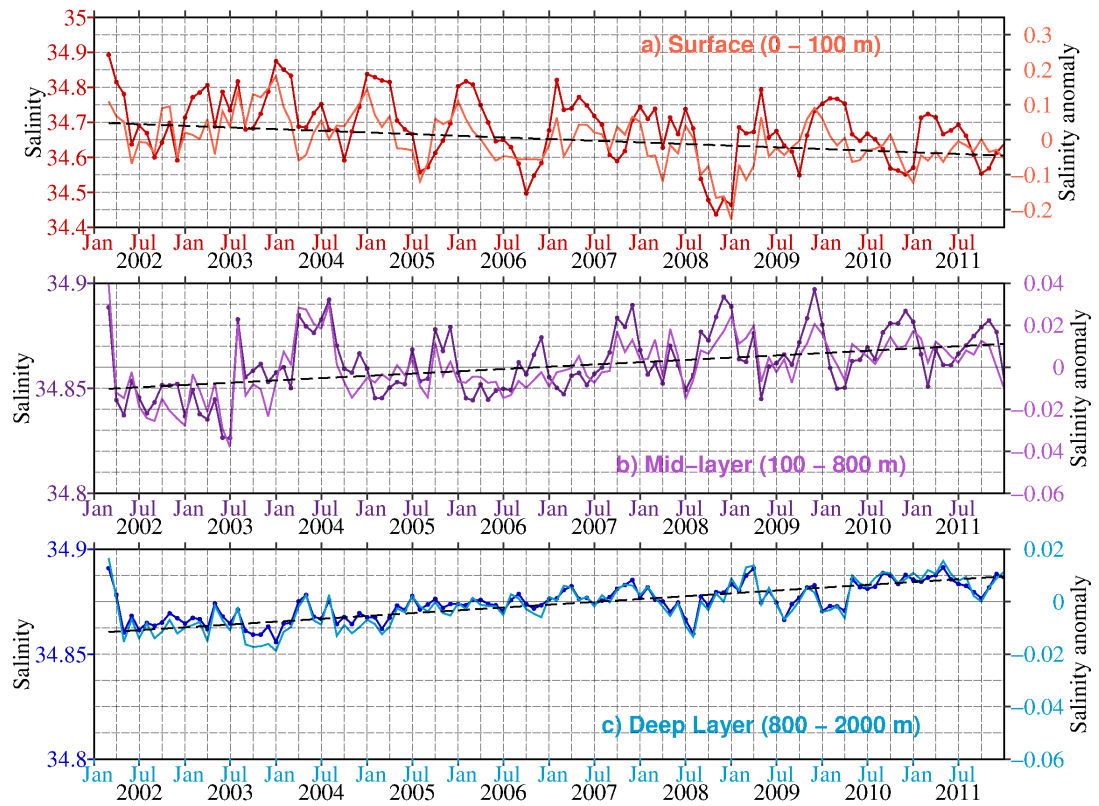
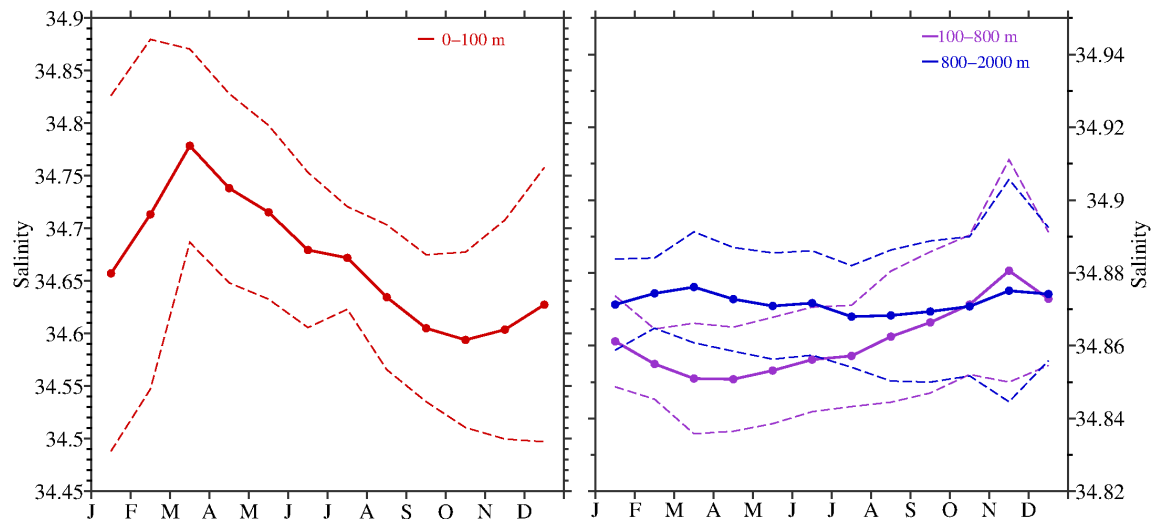


Figure 2.11: Basin-average salinity for 2002 – 2011, gridded onto a regular grid of 50 m depth and 14 days. The different layers (surface layer (0 – 100 m, mid-layer (100 – 800 m) and deep layer (800 – 2000 m)) are shown in separate panels. Note that the upper layers are stretched compared to the deep layer. The black contour shows the 34.65 isohaline.

within 95% confidence levels). Average salinities increased by as much as 0.1 (**Figure 2.12 c**). The deep convection in 07/08 is seen again as a reversal of the trend in the deep layer between January 2008 and July 2008. A similar warming trend has previously been observed by Yashayaev (2007) and will not be discussed further in this thesis.

In the surface layer seasonal salinities range from 34.59 ± 0.02 in October to 34.79 ± 0.015 in March (**Figure 2.12**). The seasonality in salinity of the mid-layer is relatively pronounced compared to the very weak seasonal changes in temperature seen above. The lowest salinities coincide with the lowest temperatures, and hence occur in March. At the same time peak salinities are reached in the 0 – 100 m layer. Peak salinities in the mid-layer (34.88) are reached at the end of the restratification period in November. The seasonal anti-correlation of the two layers can mostly be explained by convective mixing of fresh surface water to deeper layers. During restratification in the summer months, interaction between the two layers ceases and freshwater is advected into the surface layer from the surrounding ocean. This results in the decrease of surface salinities and increase in the deep layer, that is now isolated from the fresh surface waters. Salinities of the deep layer remain around 34.87 ± 0.015 throughout the year.

Figure 2.12: Same as **Figure 2.9** but for salinityFigure 2.13: Same as **Figure 2.10** but for salinity

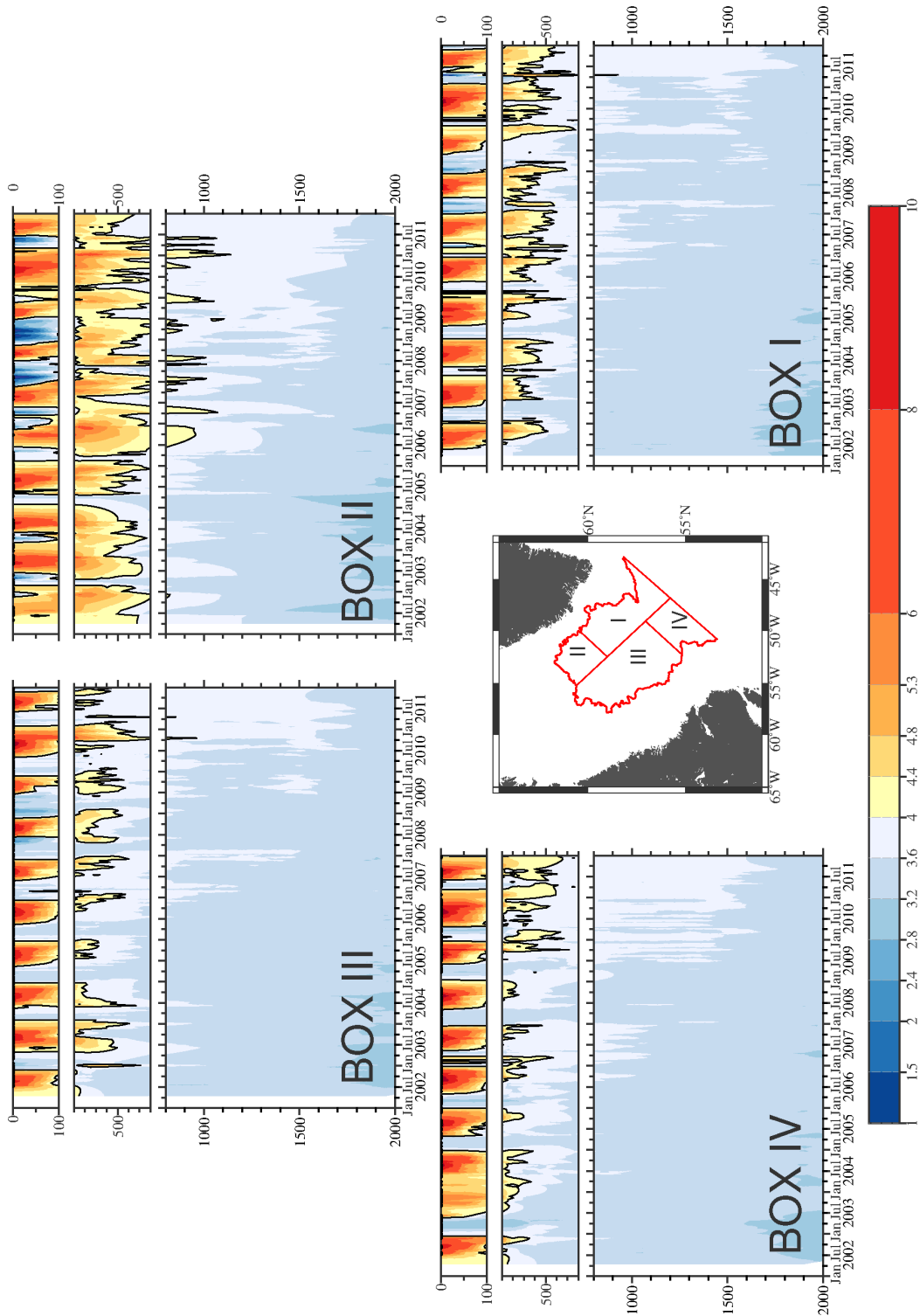


Figure 2.14: Temperatures for the different regions (shown in the bottom middle panel) for 2002 - 2011. The three layers, surface (0 – 100 m), mid-layer (100 – 800 m), and deep layer (800 – 2000 m) are shown in separate panels for each region. Note that the upper layers are stretched compared to the deep layer. The black contour shows the 4°C isotherm.

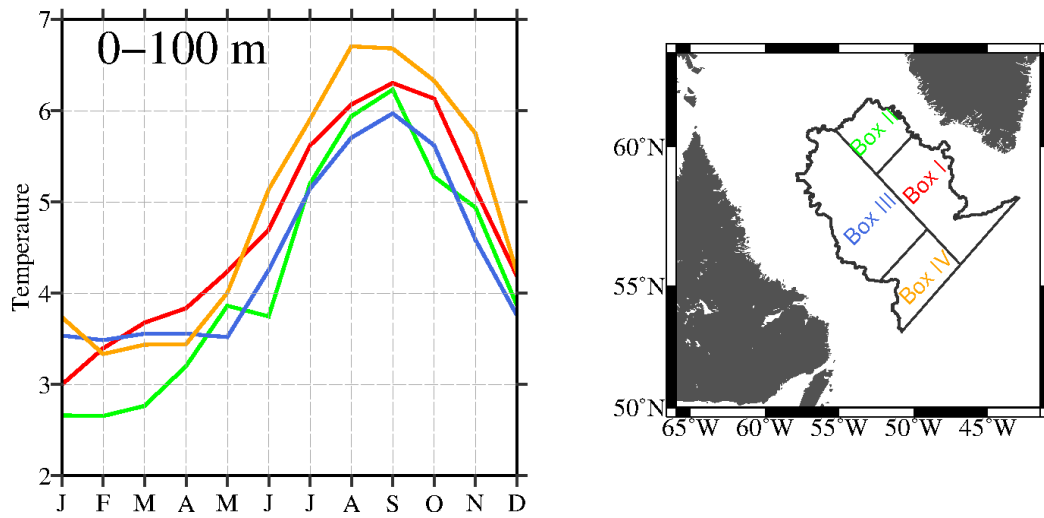


Figure 2.15: Temperature climatology of the surface layer (0 – 100 m) in the four regions. The colors correspond to the regions shown in the right panel.

2.3.2.1 Regional properties

To better understand the spatial distribution and local differences in the observed water properties, I show the basin-averaged temperatures and salinities of the four regions introduced in **Section 2.2.1**. Regional differences might occur due to different processes in the basin. In particular, Box II is chosen to represent the area of high EKE and it is thought that eddies enter the basin through this region. Box III on the other hand, is a region of weak recirculation and deep convection.

Throughout the basin, the surface layer is characterized by a strong seasonal temperature cycle (**Figure 2.14** and **Figure 2.15**). The strength and timing is comparable for all regions since the surface variability is mainly forced by atmospheric fluxes, which are similar for the entire Labrador Sea. However, in Box II the seasonal cycle is distorted and cold periods shorter compared to the other regions. The seasonal warming, represented by the 4° C isotherm, penetrates the mid-layer much stronger than in the rest of the basin, leaving the upper 800 m of this region warmer with an average of $4.3 \pm 0.1^\circ\text{C}$ compared to $3.9 \pm 0.15^\circ\text{C}$. The mid-layer in particular is much warmer here than anywhere else in the basin. The 4°C isotherm reaches depths of up to 1000 m while it is constrained to the upper 200 – 600 m elsewhere. The deepening of this isotherm seen in **Figure 2.8** is most prominent here. It is not present in Box I and III but can be seen in Box IV although it is less pronounced. Hence, the warming of the 100 – 800 m layer throughout the decade is mainly seen in Box II and IV. The anomalous cooling of winter 07/08 and 08/09 is also most prominent in Box II with only weak presence in the neighboring Boxes I and III.

Cold water clearly separates the warming periods in the northwest region (Box III), while exceptions can be seen in the other regions, e.g., no cold water in Box IV in winter

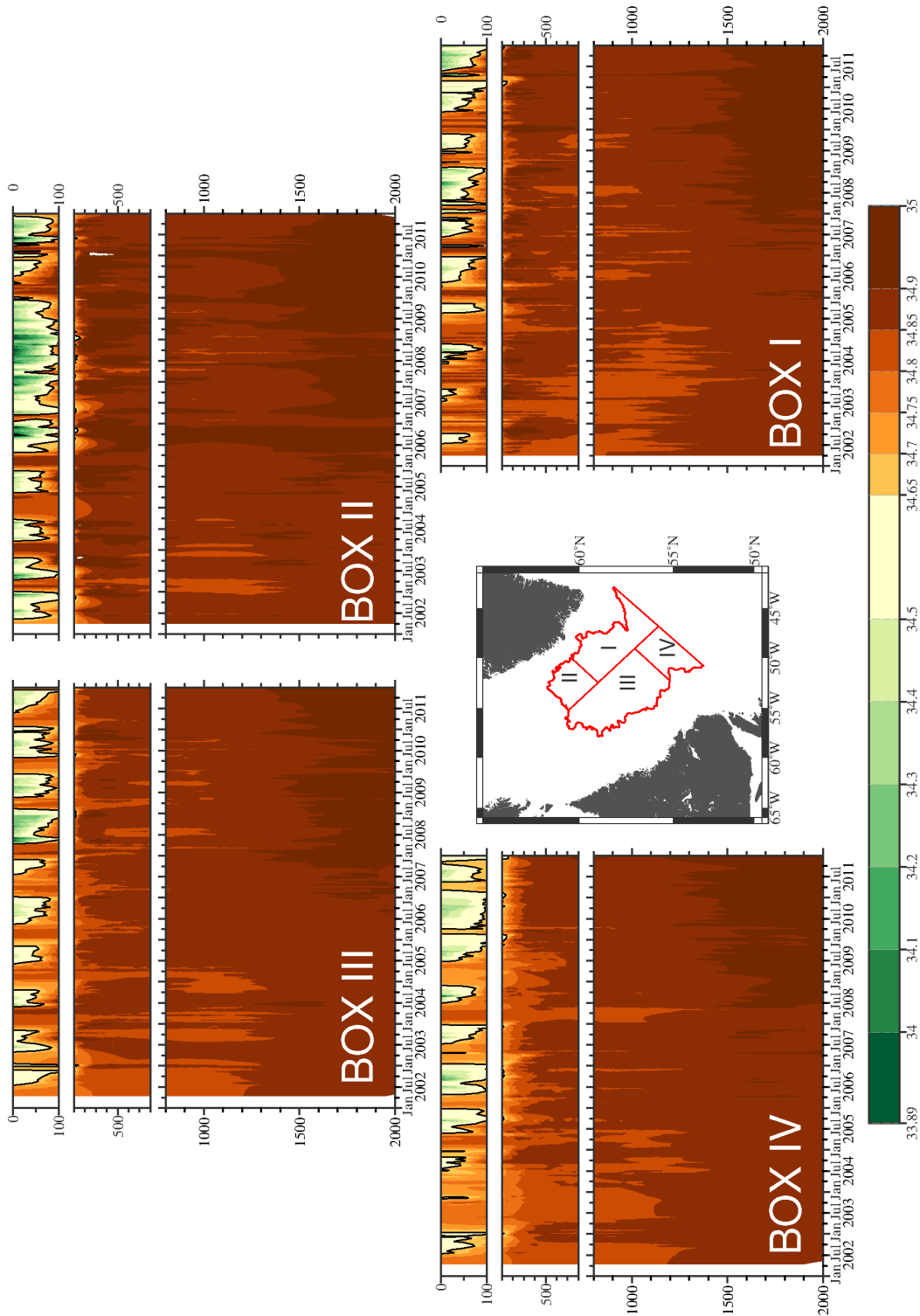


Figure 2.16: Salinity for the different regions (shown in the bottom middle panel) for 2002 - 2011. The three layers, surface (0 – 100 m), mid-layer (100 – 800 m), and deep layer (800 – 2000 m) are shown in separate panels for each region. Note that the upper layers are stretched compared to the deep layer. The black contour shows the 34.65 isohaline.

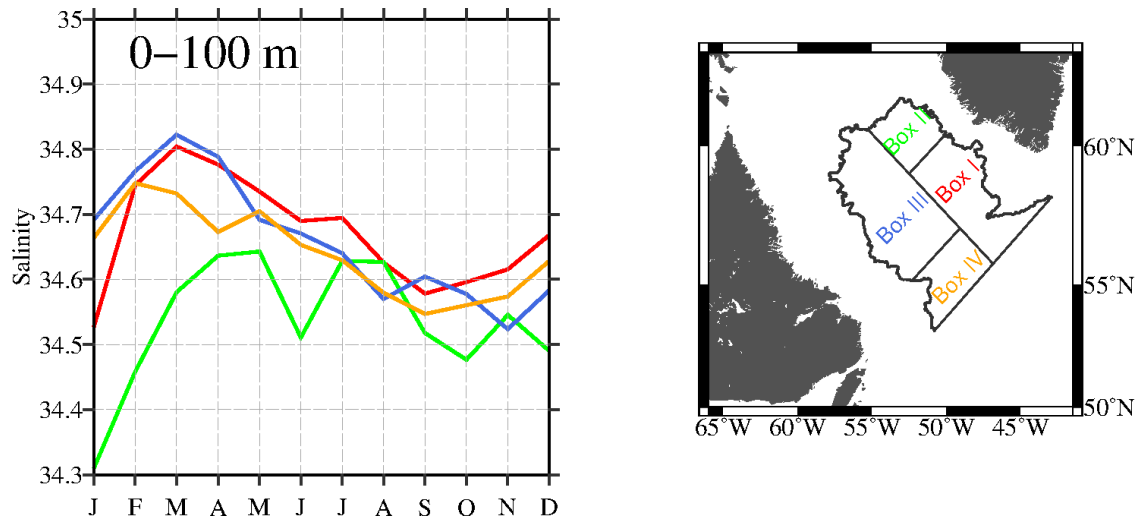


Figure 2.17: Salinity climatology of the surface layer (0 – 100 m) in the four regions. The colors correspond to the regions shown in the right panel.

03/04 or weak and short presence of cold water in 06/07 in Box I. Maximum temperatures occur at the same time in all regions (August – September) but are up to 0.5 – 0.8°C higher in Box IV, while they are lowest in Box III (**Figure 2.15**). The seasonal cycle in Box II is slightly distorted, as in some years the warming is reversed sooner than in the other regions and cold water enters the region sooner after the convection period. It is likely that this is due to advection of cold water through eddies that bring fresh and cold water into the region (de Jong et al., 2012; Hatun et al., 2007).

Convection, seen in **Figure 2.8** as uniform cold water extending to depth from the surface is seen only in Box III and IV. This is no surprise since these are the regions in which convection is known to be strongest (**Chapter 4**). The warming of the deep layer is clearly visible in all regions, showing that the mechanism responsible has the same affect on the entire basin.

The seasonal freshening described above, occurs in all four regions (**Figure 2.16**). However, the timing and strength varies from location to location. The strong freshwater anomaly identified earlier is present in the upper layer of Box II in 2007 – 2009, coinciding with the cooling described above. Here salinities of the surface layer remain below 34.5 for 18 months. In contrast to temperature, only a hint of anomalous freshwater is seen in Box I and none at all in Box III. With the exception of Box II, freshening periods are shorter and weaker in the first years of the decade. In particular in Box I, III and IV salinities drop (in the early years of the decade) to around 34.3 in late summer and the 34.65 isohaline is present between 1 month and 5 months each year, reaching depths of 80 m. In the second part of the decade the same isohaline is often present for more than 8 months, penetrating as deep as 200 m. Furthermore, salinities now often drop to 34 or below. Coinciding with this freshening, salinity in the mid-layer and deep layer increase in all regions, but particularly in Box II.

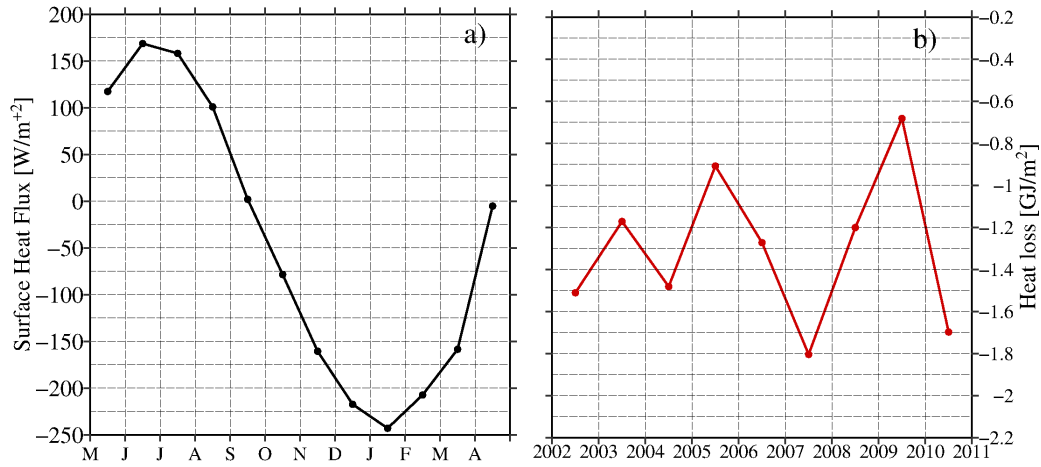


Figure 2.18: a) Seasonal surface heat fluxes from ERA-interim over the Labrador Sea basin. b) Annual heat loss calculated by integrating the heat flux from May of the current year to April of the following year. Negative fluxes show a heat loss of the ocean to the atmosphere.

Freshwater starts to arrive in the basin at the beginning of the summer and lasts until the beginning of the convection period in October/November (**Figure 2.17**). Box II is an exception. Here freshwater arrives in two pulses, one in May – June and the second in August – September. Furthermore, Box II surface layer is generally up to 0.4 fresher, while its mid-layer is saltier by up to 0.1 compared to the other regions.

2.4 Surface fluxes

2.4.1 Surface heat fluxes

Annually averaged surface heat fluxes for the Labrador Sea region have previously been estimated to be around 28 W/m^2 (Smith and Dobson (1984) from OWS Bravo and Renfrew et al. (2002) from the corrected NCEP-NCAR fields). Here we use the ERA-interim reanalysis fields with a mean annual heat loss of 43 W/m^2 .

The amplitude of the seasonal warming/cooling is 300 W/m^2 (**Figure 2.18 a**), which agrees with amplitudes of the NCEP-NCAR fields (200 W/m^2 , Straneo (2006)). In Straneo (2006)'s study, as well as here, the seasonal amplitude is much greater than the interannual variability of the 2002 – 2011 heat flux time series (not shown). The largest heat fluxes to the ocean are found in June and July with values of around 150 W/m^2 . Maximum heat loss takes place in January, with average values of -250 W/m^2 . However, heat fluxes can be as high as -1000 W/m^2 during storms.

The annual heat loss is calculated by integrating the monthly heat flux from May of the current year to April of the following year. In other words, the heat loss of e.g.,

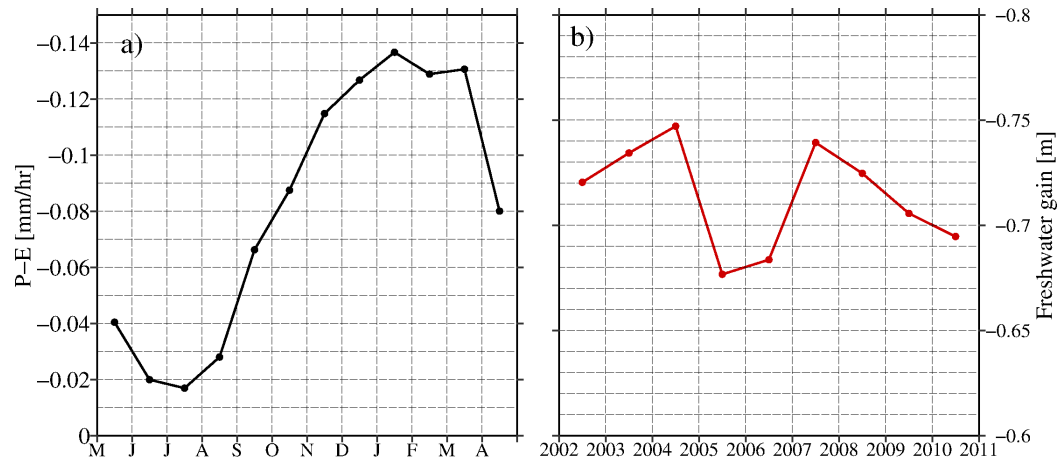


Figure 2.19: Same as **Figure 2.18** but for precipitation minus evaporation obtained from the ERA-interim fields. Negative fluxes show a flux of freshwater to the ocean.

2002/03 is calculated from the monthly heat fluxes of May - Dec 2002 and Jan - April 2003. For all years, surface fluxes cause an overall heat loss in the Labrador Sea basin (**Figure 2.18 b**). This heat loss varies by up to 1 GJ/m² between years, especially in the second half of the decade. The largest heat loss is found in 2007/08, coinciding with the deep convection observed during that winter (Vage et al., 2008). Heat loss was at a minimum in 2009.

2.4.2 E-P

Direct measurements of evaporation (E) and precipitation (P) are scarce in the Labrador Sea and E-P estimates typically have large uncertainties. However, different dataset (e.g., NCEP and ERA) all agree that precipitation exceeds evaporation throughout the year in the Labrador Sea. From ERA-Interim the annual mean freshwater loss through evaporation is 0.48 m, while freshwater gain from precipitation is about 1.45 m. This results in a yearly gain of freshwater of 0.97 m (**Figure 2.19 a**). The variability of annual freshwater input between 2002 – 2012 varies little with a minimum in 2005/06 of 0.67 m and a maximum in 2004/05 with 0.75 m. A total of 65 cm (about 0.1 mm/hr) of the yearly freshwater gain is added to the basin by the atmosphere in winter (November – March). This is in agreement with the climatology of da Silva et al. (1994).

It is interesting to note that the timing of the peak freshening due to E-P and the timing of the freshest waters in the surface layer of the basin do not agree (January from E-P and October with freshest water in the surface layer). The timing of peak heating and peak surface temperatures, on the other hand, fall together much closer (July vs. August).

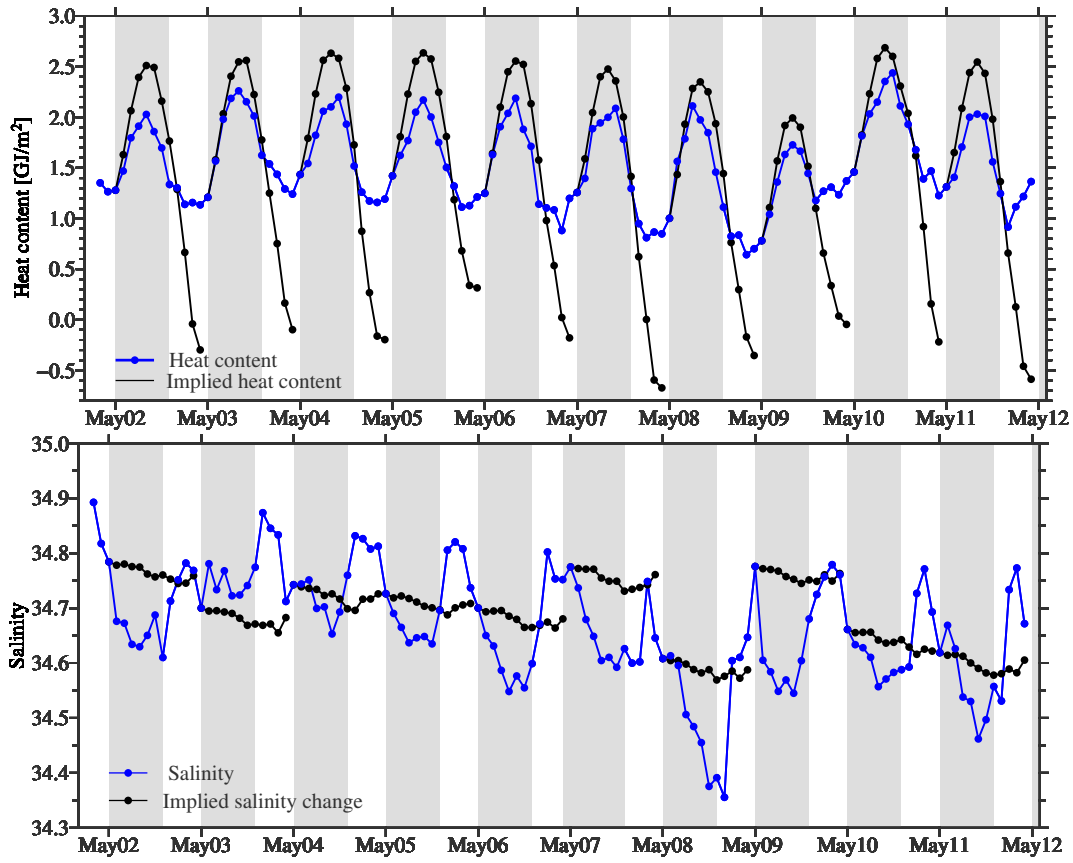


Figure 2.20: Top Panel: Surface heat fluxes from ERA - Interim (black, using May of each year as initial conditions), vs. observed heat content of the surface layer (blue). Bottom Panel: surface freshwater fluxes from ERA - Interim (black) using May of each year as initial conditions vs. observed salt content of the surface layer

2.5 Lateral fluxes

To understand the influence of lateral fluxes on the heat and freshwater budget of the basin I calculate the lateral heat and freshwater fluxes as described in **Section 2.2.4**. The observed changes in heat and freshwater in the 0 – 100 m layer are then compared to the changes in the implied content. The observed and implied heat and freshwater content are shown in **Figure 2.20**. In other words, if all changes in heat/freshwater content would be due to atmospheric forcing alone, the implied and observed changes would be identical. This means, referring to **Figure 2.20**, that the blue line showing the observed heat/salinity would be identical to the black line showing the change in heat/salinity due to atmospheric forcing. The difference between the two, as seen in **Figure 2.20** is due to changes in heat and salinity due to lateral fluxes.

While the change in heat content closely resembles the heating and cooling expected from surface fluxes, differences arise especially in the summer and winter months when the heating/cooling expected from surface fluxes is larger than actually observed. In

particular, the implied warming in summer is about 14% larger than the observed change. The expected cooling in winter is about 21% larger. The discrepancy in winter can be explained by convection causing the cold surface water to mix down into deeper layers. Simultaneously, warmer water from below is mixed upwards, warming the surface. In summer, lateral fluxes must prevent the surface from warming as much as expected from surface fluxes alone. Hence, the residual between the implied and observed changes in heat content must be due to lateral fluxes. This means that, if the assumption that vertical exchange is small is true, lateral heat fluxes must be warming the surface layer in the winter while cooling it in the summer. The residual between the observed and expected heat changes can therefore be taken to be due to lateral fluxes.

The large uncertainties in the precipitation and evaporation products automatically imply large uncertainties in the lateral freshwater fluxes. It is generally believed that 0.5 m/yr of freshwater is required to balance the change in salinity at OWS Bravo (Lazier, 1980). This means that E-P alone could account for the seasonally observed salinity changes, though it is believed that lateral fluxes play a much more important role (Lazier, 1980, 2002; Khatiwala and Visbeck, 2002; Straneo, 2006). In fact, salinity changes in the surface layer seem to be independent from the E-P freshwater input. The freshwater input from the atmosphere occurs gradually throughout the year and does not match the rapid seasonal freshening. This suggests that lateral fluxes of freshwater play a much more dominant role in the freshening of the basin than the exchange with the atmosphere. Again, we consider the residual between the observed and implied salinity to be due to lateral fluxes.

2.5.0.1 Lateral heat fluxes

As described above, the residual of observed heat fluxes and implied heat fluxes are taken to be the lateral fluxes in and out of the basin. Positive lateral fluxes indicate heat converging in the basin (hence an increase of heat) while negative fluxes show a cooling of the region. Considering the lateral fluxes for different layers is not trivial since separating them is only possible during restratification, when any mixing between surface and deep layer is expected to be minimal. After the onset of restratification in April and before the start of convection, i.e., for May – November, lateral fluxes are separated into a surface (0 – 100 m) and a deep layer (100 – 2000 m). During these months the sum of lateral heat fluxes in the two layers will add up to the heat flux of the 0 – 2000 m layer. Between December – April only the 0 – 2000 m layer is considered and it is not possible to determine in which layer lateral fluxes warm/cool the basin.

Lateral heat fluxes of the 0 – 2000 m layer warm the basin for 9 months out of the year. The heat arrives in two peaks, one at the beginning of convection in December (90 W/m²) and a second at the end of convection in March (80 W/m²) (**Figure 2.21**). In the months following convection (June – August) the lateral fluxes cool the region, importing relatively cold water from the boundary regions into the basin (with a maximum of up

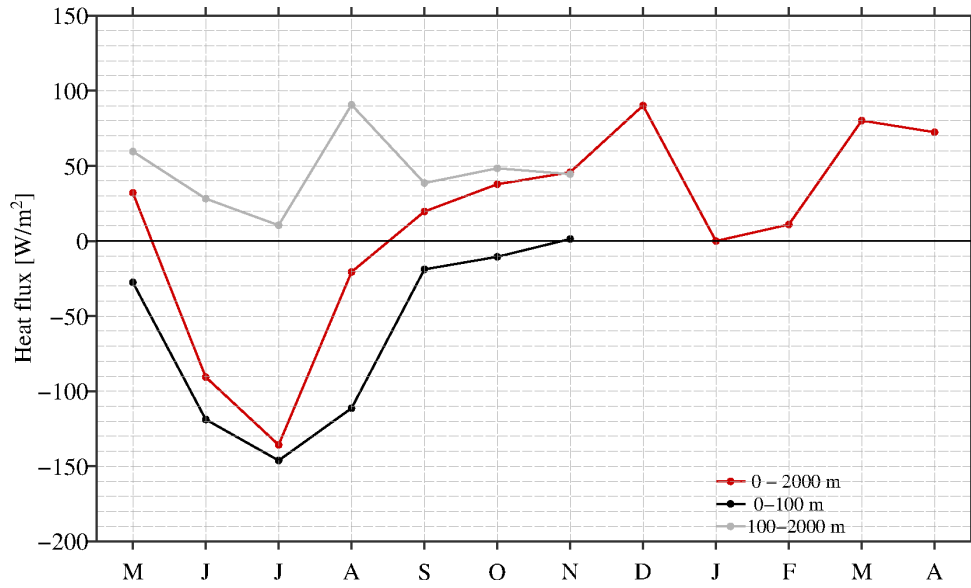


Figure 2.21: Climatology of lateral heat fluxes for the entire water column (0 – 2000 m, red), for all months, and the surface (0 – 100 m, black) and deep layer (100 – 2000 m, gray) during May – November (restratification period).

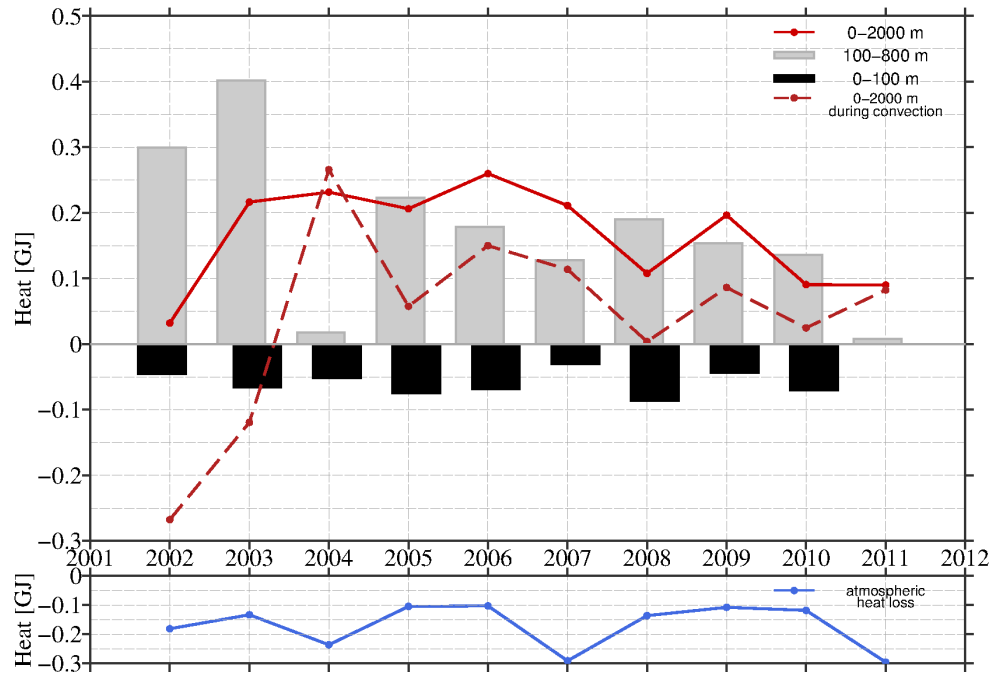


Figure 2.22: Interannual changes of heat content due to lateral fluxes. The solid red line shows the total heat change of the 0 – 2000 m layer each year. Black bars show the lateral fluxes of heat in the 0 – 100 m layer during May – November. Gray bars show the same for the 100 – 2000 m layer also during May – November. The dashed red line is the heat change due to lateral fluxes during December – April. Hence, the sum of the grey and black bars and the red dashed line will result in the red solid line. The bottom panel shows the yearly change in heat content due to heat loss to the atmosphere (obtained from ERA-Interim).

to 135 W/m^2) and keeping the basin cooler than expected from atmospheric forcing alone. The deep layer (100 – 2000 m) continuously warms the basin with a mean of 46 W/m^2 and peak heat convergence in August.

Interannual changes of heat gain and loss due to lateral fluxes are shown in **Figure 2.22**. Again, the 0 – 2000 m layer is split into a surface and deep layer during the restratification period, while annual heat gain is calculated only for the 0 – 2000 m layer. The fraction of heat that cannot be explained by lateral heat fluxes during restratification is also calculated and shown as the dashed red line in **Figure 2.22**. In other words, this is the fraction of heat changes in the basin that is not explained by the lateral fluxes of the surface and deep layer in May – November but needs to be supplied/removed from the basin in December – April.

In general, lateral fluxes of the deep layer (100 – 2000 m) act to warm the basin, while surface heat fluxes cool the region. When considering only the 0 – 2000 m layer over the entire year, lateral fluxes consistently warm the region. In fact, 75 % of the heat converges in the 100 – 2000 m basin during restratification. The first two years of the decade, 2002 and 2003, stand out with large amount of heating due to lateral fluxes during restratification and a cooling of the 0 – 2000 m layer during the convection period (December – April). During all other years additional heat was gained in December – April. It is not clear at what depth this heat was gained, however. Since the surface is closely linked to the atmosphere, which cools the water at the surface at this time of year, it is likely that this additional heat converged in the mid-layer.

The year to year variability of heat gain in the basin does not correlate to the loss of heat through surface fluxes (**Figure 2.22**, bottom panel). However, there might be an indication that lateral fluxes at depth decrease when heat loss to the atmosphere is high, e.g., the three years with the highest atmospheric heat fluxes (2004, 2007 and 2011) also have the lowest heat convergence due to lateral fluxes.

2.5.1 Lateral freshwater fluxes

The calculation is repeated for freshwater fluxes. That is, the observed and expected salinities are converted to freshwater using **Equation 2.1**. The residual of the two is taken to be the freshwater advected in/out of the basin by lateral fluxes. The fluxes are expressed as freshwater thickness (per m^2). Positive fluxes show freshwater that is added to the basin, negative fluxes show a loss of freshwater, with respect to the reference salinity of 34.7.

Throughout the entire water column (0 – 2000 m) the freshwater gain and loss due to lateral fluxes over a typical year balance each other. The mean freshwater loss is less than 1 cm throughout the year, (**Figure 2.23**). All of the 0.6 m of freshwater gain in this layer converge between May and October, with a peak of 0.19 m in September. After this peak, between October and February, the basin rapidly loses freshwater. This loss coincides with the convection period, when fresh surface waters are mixed downward into

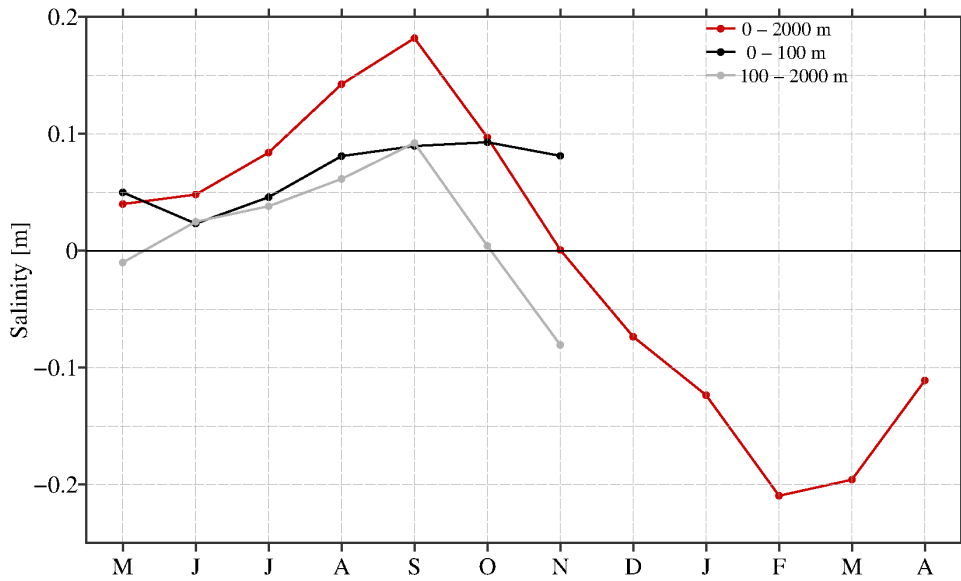


Figure 2.23: Climatology of lateral freshwater fluxes for the entire water column (0 – 2000 m, red) for all months and the surface (0 – 100 m, black) and deep layer (100 – 2000 m, gray) during May – November (restratification period).

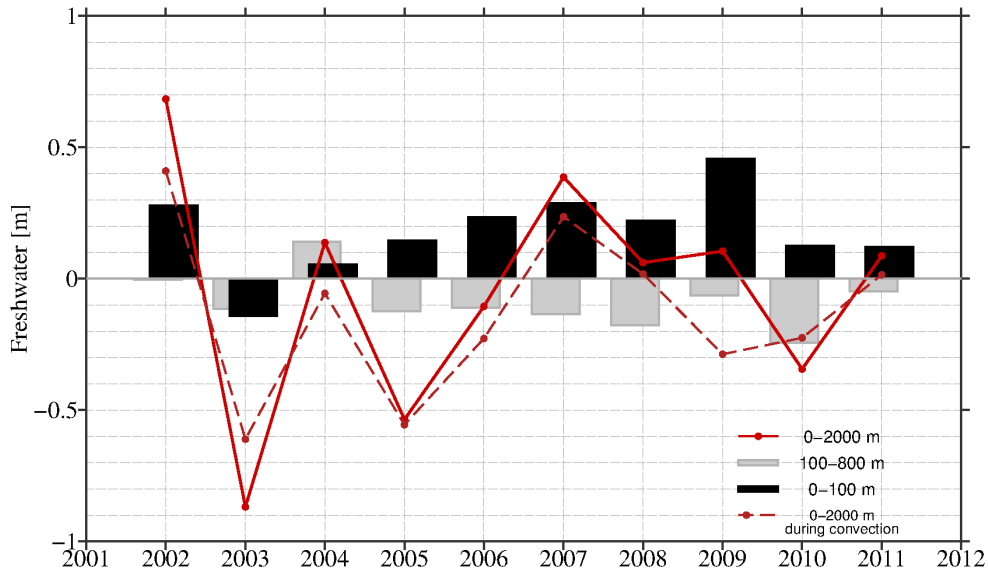


Figure 2.24: Same as **Figure 2.21** but for lateral fluxes of freshwater in the basin.

the deep basin. During restratification, lateral fluxes in the surface layer continuously freshen the basin. Interestingly, freshwater fluxes in the deep layer also mainly contribute to the overall freshening during that period.

The year to year variability of lateral freshwater fluxes in and out of the basin is large when considering the 0 – 2000 m layer, with changes as large as 1.6 m (70 cm in 2002 and -90 cm m in 2003) (**Figure 2.24**). In six out of ten years, 2002, 2004, 2007 –

2009, and 2011, the basin gains freshwater (between 10 cm – 70 cm), while freshwater is lost during the other four years (-40 cm to -90 cm). Overall, this results in a loss of freshwater in the 0 – 2000 m layer of -40 cm between 2002 – 2011. Between May to December the 0 – 100 m layer continuously gains freshwater (with the exception of 2003), with an increase in freshwater fluxes starting between 2003 – 2009. After this, in 2010 and 2011, lateral freshwater fluxes decrease again. This is consistent with the trend of salinities in the 0 – 100 m layer described in **Section 2.3.2**. Lateral fluxes supplied as much as 0.45 m of freshwater in 2009, at the end of the large freshwater anomaly seen in **Figure 2.11** and **Figure 2.12**, making it the year with the largest lateral freshwater fluxes. The 100 – 2000 m layer on the other hand loses freshwater throughout the decade (with the exception of 2004). Again, 2009 is an anomalous year in that we see the smallest amount of freshwater divergence due to lateral fluxes in this layer.

The amount of freshwater change during convection (broken red line) is closely correlated to the total freshwater change during restratification. In other words, most changes in freshwater due to lateral fluxes occur during restratification, so that only a small amount is added/removed during the convection period. Again, 2009 is an exception. Seven of the ten years have an overall freshwater loss during convection. For the other three years, freshwater was added by lateral fluxes during the convection period.

2.6 Surface freshwater changes

Here I investigate the increase in freshwater during the last half of the decade in the upper 0 – 100 m shown in **Section 2.3.2**. Changes in salinity from lateral fluxes and E-P are shown, hence the overall freshening of the surface layer. In other words, no distinction has to be made between the convection and restratification period since the total change in salinity is investigated. This allows us to split the water column into a surface layer (0 – 100 m) throughout the entire year.

2.6.1 Freshwater differences in two pentads

The mean salinities of the basin for 2002 – 2006 and 2007 – 2011 are calculated first, as described above for **Figure 2.8** and **Figure 2.11**. For both periods the southeast corner of the basin is the saltiest part of the region, with salinities of up to 34.9 (**Figure 2.25**). Salinities in the basin range between 34.5 to 34.8 in 2002 – 2006 and 34.3 to 34.7 in 2007 – 2011. The freshening takes place predominantly in the north and east, while the salinities in the west remain relatively constant. The region outside the basin is also much fresher in the latter time period, with salinities as low as 33.7. During the early time period, a patch of salty water in the north (at 58°W and 62°N) shows one branch

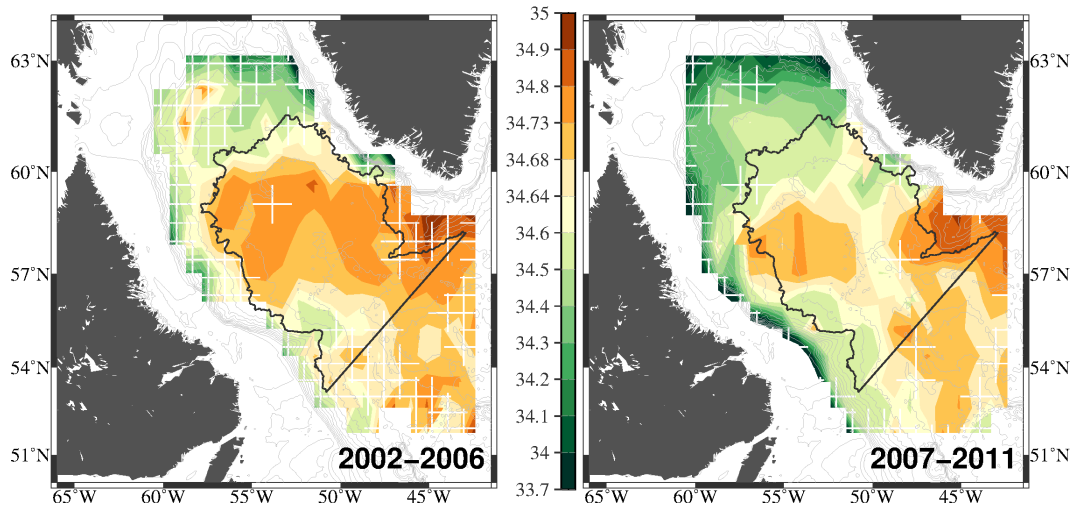


Figure 2.25: Mean surface (0 – 100 m) salinity for 2002 – 2006 (left) and 2007 – 2011 (right) from Argo floats. The white crosses show the locations at which fewer than five profiles were available.

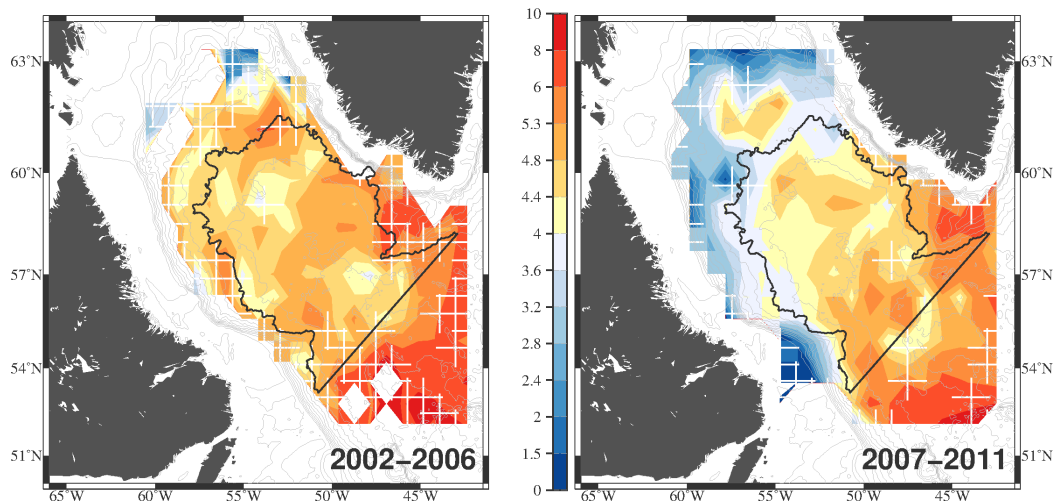


Figure 2.26: Same as **Figure 2.25** but for the mean temperatures.

of the West Greenland current crossing the basin to connect with the Labrador Current (see **Introduction** for a schematic). Though the data coverage is sparse, salinity has also decreased in the regions adjacent to the basin, with the most pronounced freshening located in the north and along the boundary in the east. The region of deep convection remains as salty as in the earlier years but shrinks in size.

The spatial pattern of temperature indicates a strong cooling along the north boundary (**Figure 2.26**). Different from the freshening pattern, temperatures also decrease in the northwest and the region of convection but the overall change in the basin is weaker than seen for salinity. It therefore seems that the fresher water in the north reaches the basin, while the colder water leaves the region to the south, via the boundary currents,

without entering the basin.

2.6.2 Surface freshening of the basin

The surface freshening of the basin is shown as the amount of freshwater needed to explain changes of observed salinity, with respect to the reference salinity of 34.7 (using Equation 2.1).

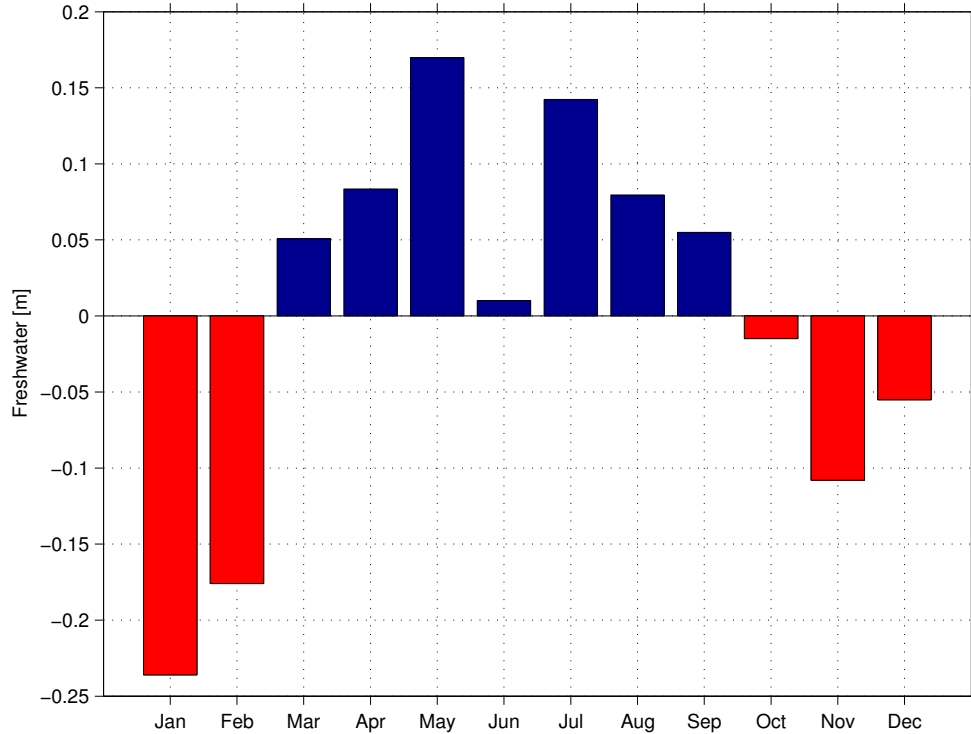


Figure 2.27: The amount of freshwater required to explain the month to month changes in salinity of the surface layer (0 – 100 m). Negative values (red bars) indicate the removal of freshwater and positive values (blue bars) a freshwater increase in the basin. i.e., a decrease in salinities.

The mean annual freshwater gain of the 0 – 100 m layer is 56 cm (**Figure 2.27**). Note that this is the overall freshening due to lateral fluxes and E-P, other than in the above section where only lateral fluxes were considered. Freshwater reaches the interior in two peaks, lasting three months (March – May and July – September), each importing around 27 cm of freshwater. The removal of freshwater, balancing the freshwater import, is strongest in January and February. Hence, the freshwater that accumulated during the summer and fall is primarily fluxed out of the region during the early convection period. The removal of freshwater in these two months alone accounts for 90% of the overall freshwater loss.

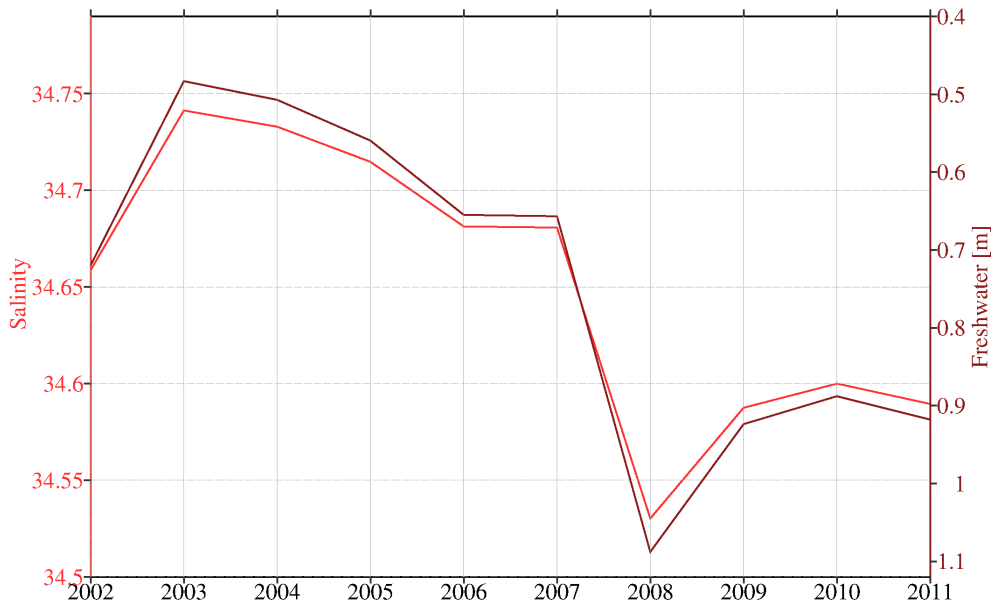


Figure 2.28: Yearly change in surface (0 – 100 m) salinities of the Labrador Sea basin (light red) and the yearly change in surface freshwater (dark red) that is required to explain the observed changes in salinity.

The basin-averaged salinity of the top 100 m changes from 34.71 in 2003 – 2007 to 34.57 in 2008 – 2011 (**Figure 2.28**). How much freshwater would be required to explain the observed change? To answer this, the freshwater content of each year is calculated. The result is expressed as freshwater thickness (per square meter). On average, an additional 39 cm of freshwater was present in the basin in the latter part of the decade (59 cm vs. 98 cm). Out of all years, the largest freshwater gain was in 2008 (gain of 45 cm of freshwater out of the total of 1.1 m), reflecting the onset of the abnormal freshening of the surface layer in 2007. Between 2002 and 2003 almost 20 cm of freshwater were removed making 2003 the saltiest year of the decade. In 2009, salinities increased slightly (freshwater content decreases) but remain low (high for freshwater) through 2011. The 39 cm of additional freshwater in the second part of the decade are equivalent to a freshwater gain of about 0.1 m/yr.

2.7 Discussion

2.7.1 Seasonal Variability

The Labrador Sea experiences large seasonal cycles in temperature and salinity. Temperature is mainly governed by the heat input and loss from the atmosphere. However, during the summer and winter, lateral fluxes become important. They keep the Labrador Sea warmer (in the winter) and cooler (in the summer) than expected from atmospheric

forcing alone. On the other hand, changes in salinity are governed by lateral fluxes year around. While the atmosphere adds freshwater gradually throughout the year, freshening in the basin occurs rapidly in the spring and summer, leaving the basin at its freshest before the onset of convection. The freshwater arrives in two peaks, as also seen by Schmidt and Send (2007). These peaks are discussed in more detail in the next chapter. However, it is worth to briefly discussing their origin here as well. In his PhD thesis, Schmidt (2008) shows that the seasonality of salinity varies widely depending on what part of the Labrador Sea is considered. For example, seasonality close to or in the boundary currents are very different from those observed in the basin itself and the two freshening peaks are only clearly observed in the basin itself. Schmidt and Send (2007) match the first pulse in April – May to exchange with the Labrador Current and the second stronger pulse to freshwater from the West Greenland current. Here, as the two pulses are strongest in Box II, it is likely that both pulses of freshening originates from the West Greenland Current rather than the Labrador Current. Furthermore, the stronger warming and larger changes in salinity in this region seem to imply that the strong EKE observed here is responsible for these strong changes in temperature and salinity. It seems that freshwater at the surface and salty, warm water in the mid-layer readily enter the basin, which is a characteristic of Irminger Rings formed along the West Greenland Current (de Jong et al., 2012). The abnormal freshening and cooling in 2007 – 2009 is also strongest in this region and leaves the impression that this water entered the basin from the northeast, hence the West Greenland Current, via eddies. Studies agree that eddies play a major role in the advection of water to the basin, but have failed to show that all of the seasonal freshening can be explained by them. The major pathways and importance of different forcing mechanisms in the advection of water to the basin will be discussed further in **Chapter 3**.

2.7.2 Long-term Changes

Has the decrease of salinities in the surface layer and the increase in salinity in the subsurface layer impacted the potential of forming Labrador Sea Water? To recap, the salinity difference between the surface and mid-layer increased from an average of 0.22 in the first five years to 0.37 in the second half of the decade. This could have an impact on the potential for deep convection. For example, if a large amount of fresh buoyant water was added to the surface of the basin, the resulting freshwater cap could suppress mixing and alter the formation of deep water, as seen during the ‘Great Salinity Anomaly’ (Dickson et al., 1988). On the other hand, an increase in stratification could also suppress convection due to an increase in the resistance to mixing. In other words, a larger amount of surface fluxes would be needed to remove the stratification and initiate mixing.

I use the PWP 1-D mixing model to briefly investigate the impact of the increase in stratification seen here. The basin-averaged profile of October is used as initial conditions

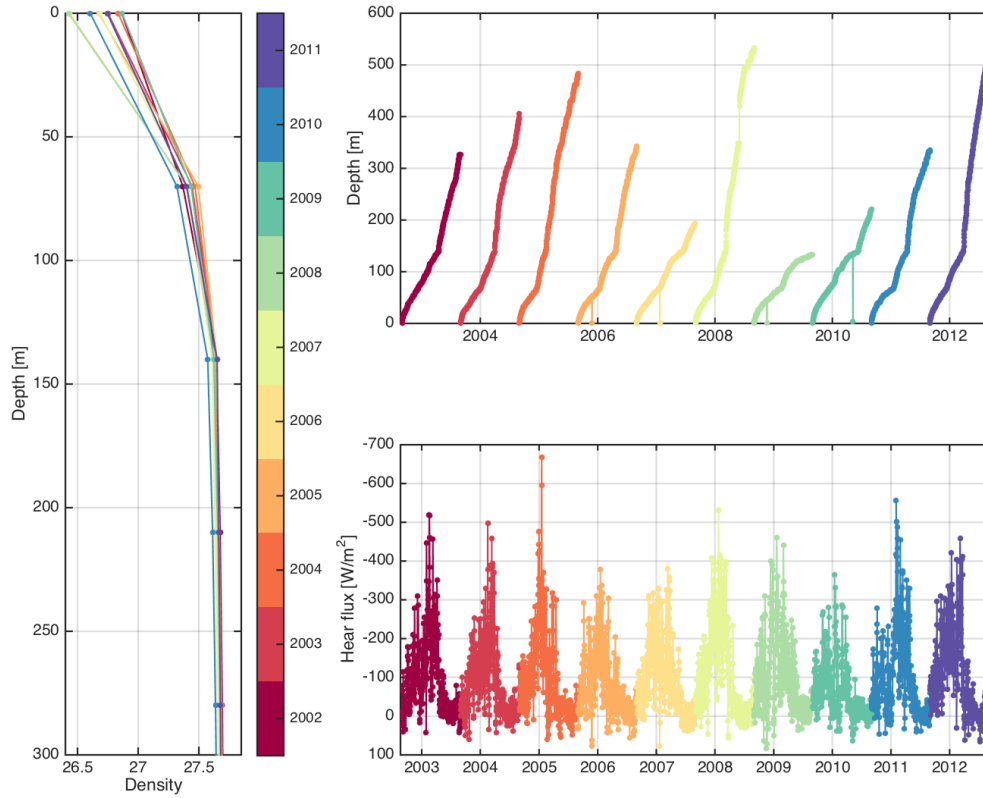


Figure 2.29: Left: The basin-averaged density profiles of October for each of the years 2002 – 2011. The different years are shown as color. Right: The mixed layers from the PWP mixing model and the heat fluxes used to force the model. Again, colors correspond to the years shown as the colorbar.

for each year between 2002 to 2011. All profiles are shown in **Figure 2.29** (left panel). As expected, the upper layer in October 2008 is the freshest out of all years, while the earlier years are much saltier by comparison. The model is then forced with ERA-Interim heat fluxes averaged over the Labrador Sea basin (**Figure 2.29** right bottom panel). The wind forcing, evaporation and precipitation are not considered here, since they do not change the overall depth of the mixed layer (not shown). The resulting mixed layers are shown in **Figure 2.29** (top right panel).

The deepest mixed layers for the period of 2002 – 2011 are found in 07/08. This is consistent with observations (Vage et al., 2008; Yashayaev and Loder, 2009). The observed mixed layers exceeded 2000 m while the 1-D model shows mixed layers to be only 550 m deep. The discrepancy is due to initial conditions averaged over the entire basin instead of concentrating on the western side of the basin where convection is known to be strongest. After onset of the strong surface freshening in 2008, mixing, according to the model, is suppressed for 08/09 and 09/10 even though the forcing is

similar to previous years that had deeper mixed layers. However, after the 09/10 winter the convection becomes stronger again. In fact, the winter of 2011/12 has the second deepest mixing of the decade. The model results show that the freshening of the surface and the increase of salt in the subsurface have suppressed mixing for at least two years. The following warm and high salinity years however, resulted in the return of deep mixing. With this there is potential of a Labrador Sea Water class that is denser than in previous years as, once mixing is restored, saltier water will be mixed down to great depths. However, it is important to note that the PWP mixing model is only a very simple tool to investigate convection in the Labrador Sea. In fact, observations have shown that not only did winter 07/08 have extremely deep mixed layers but that mixing in 08/09 was also surprisingly deep, mainly due to preconditioning. It is likely that the strong freshening of the eastern basin biases the initial conditions used in the model, resulting in much shallower mixed layers than actually observed.

2.7.3 Lateral Fluxes

In general, lateral heat fluxes warm the surface of the basin in the winter due to convection warming the surface layer by mixing of subsurface water upwards. During restratification the properties of the basin are mainly altered due to lateral fluxes from the surrounding ocean, i.e., buoyant water converges in the surface and dense LSW is removed deeper down. Lateral heat fluxes in the surface occur rapidly right after convection but continue at a slower rate throughout the year. The second, slower phase of exchange is likely a background exchange with the boundary and is consistent with the observations of continuous restratification in the absence of convection. This indicates that restratification is not an immediate result of the convection itself but associated with the mean horizontal density gradient between the interior and boundary currents. This is also supported by lateral fluxes observed during the Great Salinity Anomaly, where freshwater slowly accumulated in the surface layer, reducing freshwater and heat exchange with the boundary leaving the surface layer anomalously cold and fresh (Straneo, 2006).

While the seasonality can be explained mainly by the convective activity in the basin, the interannual variability is more puzzling. Straneo (2006), using a simple model that parameterizes the exchange between the interior and boundary, found that the restratification rate varies with the square of the lateral density gradient. In other words, the rate depends on the amount of LSW that is present in the basin. Years with large LSW volume will restratify at a faster rate than years with only small volume of LSW. This relationship explains some of the features observed here well. For example, some of the highest lateral heat and freshwater fluxes were observed during 2008 and 2009 after the winter of deep convection that formed large amounts of LSW. However, large heat fluxes were also observed in 2002 and 2003 when no deep convection was reported. Several studies have shown that 2003 was characterized by large lateral heat fluxes that

led to a rapid warming of the central Labrador Sea which, in turn, affected the amount and properties of LSW formed (Avsic et al., 2006; Bersch, 2002; Brandt et al., 2004). There is evidence that these changes are associated with an increase in the number of eddies reaching the interior of the Labrador Sea (Lilly et al., 2003). A remaining issue is how representative this and previous datasets are for the processes happening in the Labrador Sea. For example, Straneo (2006) finds roughly the same amount of seasonal surface freshening as found here (0.6 m) but concluded that the convergence of salt in the subsurface layer could not balance this completely. Here, the seasonal increase and removal of freshwater due to lateral fluxes are balanced.

2.7.4 Comparison to previous freshening periods.

Two freshening pulses, as seen in (**Section 2.6.2**), were also found in years of the ‘Great Salinity Anomaly’ by Straneo (2006) and for 1996 – 2001, from OWS Bravo (Schmidt and Send, 2007). In the latter study the authors note a first, weaker peak of about 20 cm in April – May and a second, stronger peak of about 50 cm in July – September. By matching the salinity seasonality of the boundary current to the freshening in the basin the authors conclude that the peaks are attributed to the Labrador and West Greenland Current, respectively. However, no measurements exist to directly show this. The timing of the pulses observed here matches the timing of the previously observed peaks well. However, I observe 30% less freshening than Schmidt and Send (2007). This is likely due to the different depth of the chosen layer. While the previous study uses 150 m, here only the top 100 m are considered. The yearly freshwater input of 56 cm, however, agrees well with Lazier (2002) study.

Freshening periods in the Labrador Sea have previously been observed in e.g., the 1970s and 1990s (e.g., Häkkinen (2002); Houghton and Visbeck (2002)). Is the gain of freshwater observed here comparable to these freshening periods?

Estimates of freshwater gain in the Labrador Sea during the ‘Great Salinity Anomaly’ and a second freshening period in the 1990’s vary depending on publication (**Table 2.1**). Published salinity measurements are taken from different layers (also listed in the table). The freshwater gain is calculated by using these salinity values and **Equation 1**. In particular, I calculate the amount of freshwater at the beginning of the time period and compare it to the amount of freshwater at the end of the freshening.

To compare the freshening observed here, the calculation above in **Figure 2.6.2** is repeated, by using basin averaged salinities of the different layers listed in the literature (**Table 2.1**). In 1968 – 1971, (Lazier, 1980) describe a reduction of near-surface salinities by 0.2, similar to the decrease in salinity observed here. Furthermore, the freshwater gain for 2008 – 2011 compared to 2003 – 2007 over the upper 5 m is 0.01 m/yr, comparable to the freshening observed by Häkkinen (2002). For the 0 – 250 m layer, the freshening is smaller than previously observed for the GSA (0.15 m/yr observed here vs.

Table 2.1: Freshening periods in the Labrador Sea as described and quantified in the literature.

Publication	Years	Region	Depth [m]	Freshening [m/yr]	Notes
Häkkinen (2002)	1990 – 2000	45 – 55°N and 50 – 40°W	0 – 5 m	0.012 m/yr	Fig. 2c
Lazier (1995)	1967 – 1972	OWS Bravo at	0 – 250 m	0.41 m/yr	Fig. 7
Lazier (1980)	1967 – 1972	OWS Bravo at	0 – 1500 m	0.23 m/yr	Fig. 5
Yashayaev (2007)	1971 – 1977	AR7W line	150 – 3250 m	0.51 m/yr	Fig. 2
Yashayaev (2007)	1990 – 1994	AR7W line	150 – 2000 m	0.4 m/yr	Fig. 2

0.4 m/yr during the GSA). The surface layer as well as the deeper layer freshened during the GSA, while here the 0 – 1500 m layer neither gains nor loses freshwater between the two halves of the decade. In fact, the deeper 150 – 3250 m layer becomes saltier (0.13 m/yr less freshwater), capturing the increase in salinity also seen in **Figure 2.11**. A similar increase of salt was also observed by Lazier (1980) below 400 m. However, the average salinities of this layer still showed a net freshening due to freshwater input to a thicker layer at the surface. It is worth noting that **Figure 2** in Yashayaev (2007) shows a large long-term freshening of 6 m over a 25 year period, during which the GSA and freshening in the 90's are comparably small. However, as for the GSA, the freshening of the 90's also resulted in an overall freshening of the deep layer as well as freshening at the surface (Yashayaev, 2007; Häkkinen, 2002). This indicates that the surface freshening observed here is comparable to the one seen during the GSA but with a weaker vertical extent due to an increase of salt below 100 m.

2.7.5 Possible sources and mechanisms of freshening

What are the likely sources of additional freshwater seen in the Labrador Sea?

Greenland runoff is likely to become more important to the Labrador Sea as its rate increases. Over the period of 1995 – 2010 freshwater anomalies of Greenland, including runoff and ice discharge, exceeded $3200 \pm 358 \text{ km}^3$, or about $213 \text{ km}^3/\text{yr}$ (Bamber et al., 2012). From this, $109 \text{ km}^3/\text{yr}$ was discharged from regions close to the Labrador Sea, while an additional $46 \text{ km}^3/\text{yr}$ was added further north, to Baffin Bay, hence 155 km^2 of freshwater are added from Greenland in the proximity of the Labrador Sea each year. If all of this freshwater was to reach the Labrador Sea basin the observed freshening could be explained fully (0.36 m over an area of about 3.62 km^2 is equivalent to 130 km^3). While it is unlikely that all additional freshwater enters the basin, increased transport of the East Greenland Current (Daniault et al., 2012) would support more freshwater fluxes from the East Greenland coast to the LS region. However, the exact amount of freshwater entering the basin from the boundary currents has to be determined.

For the GSA of the 1970s, freshwater anomalies linked to a low NAO and originating from Baffin Bay were identified to be the primary source of freshening (Houghton

and Visbeck, 2002). Interestingly, the NAO index was low between 2000 – 2006 but turned positive during the period of increased freshwater content in 2008 – 2011. On average, 93 mSv of liquid freshwater and 10 mSv of solid freshwater are transported south through Davis Strait each year (Curry et al., 2014). While the freshwater fluxes show large interannual variability, no clear trend was observed over the period of 2004 – 2010. In fact, less Arctic water but more warmer and more saline North Atlantic water entered Baffin Bay during this period. But even a 4% increase of the 103 mSv outflow from Baffin Bay (which is equivalent to 8.9 m of freshwater if all of it were to reach the basin) would be enough to account for the 0.36 m of freshwater increase in 2008 – 2011. However, models show that freshwater added at Davis Strait exits the LS via the boundary currents without reaching the basin (Myers, 2005).

The outflow of liquid freshwater from Hudson Bay was measured to be 78 – 88 mSv in 2004 – 2005 (Straneo and Saucier, 2008) (including recirculated water from Baffin Bay). While an increase in freshwater flux here is possible, **Figure 2.25**, shows only a slight freshening in the west, downstream of Hudson bay outflow. This indicates that freshwater fluxes from there are most likely confined to the shelf, exiting the region to the south without impacting the freshwater budget of the LS. This is also confirmed by Schmidt and Send (2007), who determine that freshwater from the Labrador Shelf is unimportant to the seasonal freshening of the Labrador Sea basin.

A freshening of the LS basin could be caused by several processes, including changes in vertical mixing, flow pattern or Ekman transport, and increased eddy activity. Surface freshwater fluxes (evaporation minus precipitation) and solid freshwater inputs from the Arctic or Greenland contribute to the freshwater budget of the basin. However, the ERA-interim E-P product indicates that the change in surface fluxes were negligible between the two time periods, changing from 1.79 to 1.81 m. Furthermore, the yearly freshwater contribution from surface fluxes shows no correlation with the yearly change in freshwater content (not shown). Solid freshwater transport into the Labrador Sea has not been estimated, but Schmidt and Send (2007) point out that the timing of the freshwater increase in the basin makes local ice melt unlikely as a source of freshwater.

Eddies, background circulation or surface Ekman transport may contribute to bringing freshwater from the boundary currents to the central basin. Point vortex eddies, shedding from the West Greenland Current, can be capped by freshwater in the spring (de Jong et al., 2012). Based on a single spring eddy observation, Hatun et al. (2007) suggests that 25 of these eddies would be required to fully explain the seasonal freshening in the basin. Large interannual variability in the location and strength of the eddy kinetic energy (EKE) (Brandt et al., 2004) make it difficult to understand the relationship between eddy activity and freshwater fluxes and the exact number of these eddies entering the basin remains unknown.

Another possible cause for increased freshwater in the basin is a change in lateral fluxes from the background geostrophic flow. This flow can be estimated using surface

velocities from altimetry. Between the two time periods, the net inwards transport derived from these velocities is similar, with a slight increase in the WGC in the latter period (see **Chapter 3**). With the observed velocity increase for 2008 – 2011, mean salinities of 32.4 would be needed to cause an accumulation of 0.36 m of freshwater by geostrophic transport alone. This is much fresher than even the lowest salinities observed around the basin.

Surface Ekman transport, by the typically northerly winds (Moore and Renfrew, 2005), can also carry freshwater from the Greenland shelf to the Labrador Sea basin. Localized wind effects caused by the steep topography of Greenland intensify these winds and could increase the amount of freshwater reaching the basin. However, no present studies exist to estimate the role of winds in freshwater transport in the Labrador Sea.

Lastly, a decrease in convection could result in a freshening of the basin, since deep mixing increases the salinity of the surface layer. Peak basin-averaged mixed layer depths were between 170 – 642 m (370 m on average) for 2003 – 2007 and 145 – 630 m (350 m on average) for 2008 – 2011 (estimated from the Argo profiles). We would also expect the mid-layer (100 – 800 m) to show an opposite trend to the surface layer (freshwater is no longer mixed down, leaving the mid-layer saltier). While the mid-layer is in fact losing freshwater, it does not correlate to the increase of freshwater at the surface (**Figure 2.11**) and suggests that vertical mixing can be neglected as the main cause of the observed freshening.

2.8 Summary and Conclusions

We analysed 10 years of Argo data to describe recent changes in heat and freshwater of the Labrador Sea and to describe the role of lateral fluxes. Additionally we evaluate the impact of increased Arctic ice melt on the Labrador Sea and the convection observed there.

- There is no longterm trend in surface temperature but salinities have decreased significantly. Additionally, the deeper layers have warmed and increased in salinity throughout the last decade. This is due to lateral freshwater fluxes, which have increased steadily between 2003 and 2009.
- Seasonally, freshwater arrives in the basin in two peaks, as also shown by Schmidt and Send (2007). Relative magnitudes differ, and the first pulse observed here is of similar magnitude to the second pulse, where as in Schmidt and Send (2007), the first pulse was much smaller than the fall pulse. This can partly be attributed to the fact that the surface layers were defined differently between the studies. It is also possible that the increase of lateral freshwater fluxes impacted the strength of the two freshening events, thus strengthening the earlier pulse. The fact that Straneo (2006) did not see two pulses during the years of the ‘Great Salinity

Anomaly' gives rise to the assumption that the pulses are tied to stronger lateral fluxes and hence convection. In other words, they might only be present when lateral fluxes are strong due to the presence of convection, which was not the case in the 'Great Salinity Anomaly' years.

- The freshwater gain of 40 cm in the surface layer of the Labrador Sea is comparable to other large freshening periods only in the surface layer. The horizontal structure however, differs in that the freshening is confined to the surface instead of affecting the entire water column. A 1-D mixing model showed that the increase in freshwater had the potential to suppress convection for 1-2 years. After this, convection resumed and was predicted to be as strong as in previous years.
- Evaporation minus precipitation and changes in vertical mixing can be ruled out as the source of the additional freshwater in the basin. Instead, it is likely that an increase in freshwater in the EGC is the source. It is further possible that the mechanisms that allow the advection of water from the boundary currents to the basin changed and aided the increase in fresh lateral fluxes. This is further addressed in the next Chapter.

Chapter 3

Freshwater pathways into the Labrador Sea basin

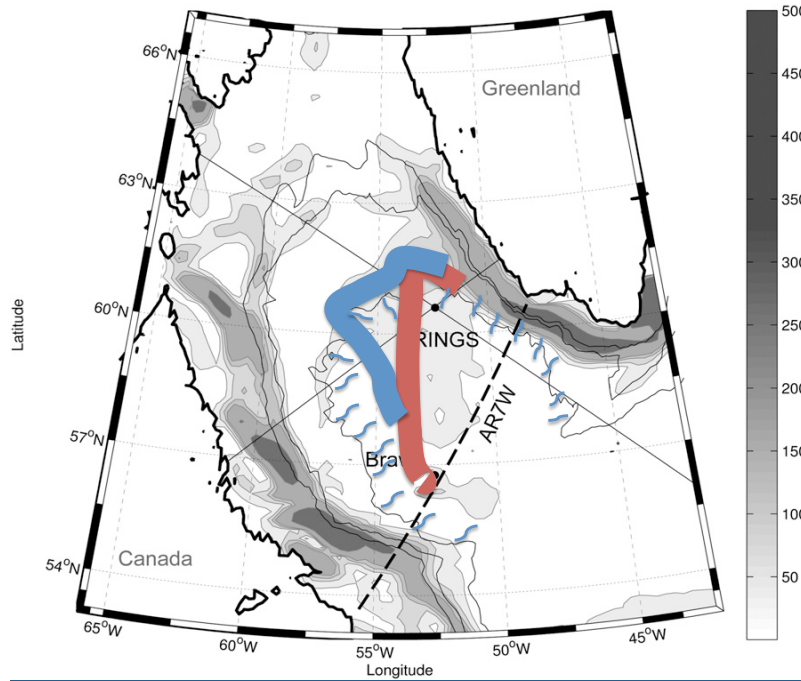


Figure 3.1: Schematic of the proposed eddy pathways into the basin. The base map and EKE (gray shading, m^2/s^2) is from de Jong et al. (2012) (their Figure 1). The thick red line shows the pathway of Irminger Rings into the basin as proposed by Lilly et al. (2003). The thick blue line shows the pathway of eddies as proposed by Hatun et al. (2007) and Schmidt (2008). The small blue lines show the boundary current eddies that form everywhere along the boundary current (e.g., Chanut and Barnier (2008); Katsman et al. (2004)).

3.1 Introduction

Following the winter months, convection in the Labrador Sea basin ceases and the basin starts to restratify due to the advection of heat and freshwater. This seasonal cycle has been observed and described in many studies, including the previous Chapter. During an average year the freshwater is added to the basin in two separate freshening events; a smaller spring pulse and a larger, fall peak that originates in the West Greenland Current (WGC) (Schmidt and Send, 2007). The origin of the first peak is unclear but the Labrador Current has been suggested as a possible source (Schmidt and Send, 2007). Other sources could be precipitation and evaporation, sea ice melt or freshwater outflow and runoff from the Arctic via Baffin Bay or Hudson Strait. In **Chapter 2** I have shown that evaporation minus precipitation cannot be the source of the seasonal freshening signal due to its timing. On the other hand, the timing of the maximum sea ice extent matches well with the observed freshwater pulse making it a possible source of the freshwater together with the WGC, outflow from Baffin Bay and Hudson Strait, and inflow from the North Atlantic. Of these sources, the WGC, Baffin Bay and Hudson Strait are the most likely for supplying freshwater, and it is thought that the WGC is

the main source overall (e.g., Cuny and Rhines (2002); Schmidt and Send (2007); Lilly et al. (2003)). In the past, studies have concentrated on eddies as the main mechanism by which heat and freshwater is imported into the basin. Studies often focus on the Irminger Rings that shed off the boundary current near to the northeast corner of the basin and carry warm and buoyant Irminger Current water. Observations of these eddies has been accomplished in the past, using satellite altimetry (e.g., Lilly et al. (2003)). A spatial distribution map of the observed eddies shows their highest frequency in the northeast corner of the basin, extending diagonally across to the southwestern corner (their Figure 36 and **Figure 3.1**). In total, between 1994 and 1999, 33 eddies were detected (between 15 – 30 km in size). Other observational studies see the main path of eddies in a different region, further downstream, in the northwest corner of the basin (Schmidt, 2008; Hatun et al., 2007) (**Figure 3.1**). This pathway would allow the eddies to reach the region of deep convection much quicker and would lead to a more effective and faster restratification. A second class of eddies, boundary current eddies, also plays a role in the restratification process of the basin (Chanut and Barnier, 2008). These eddies form along the boundary current due to baroclinic instabilities.

Model studies have shown that restratification would not take place as quickly as observed without the presence of these two classes of eddies (Katsman et al., 2004). Irminger rings alone could explain the annual heat loss to the atmosphere by 55% – 92%, if 30 eddies with an average radius of 30 km, were shed each year. Another study, also using 30 km as their average eddy size, comes to a similar conclusion. It suggests that about 25 eddies would be needed to explain not only the heat, but also the annual freshwater input of 60 cm (Hatun et al., 2007). However, both of these studies assume a large number of large eddies. Lilly et al. (2003), on the other hand, concluded that the 33 eddies, with an average size of 20 km, observed over a 5 year study period would only account for 28% – 55% of the heat and freshwater needed to explain the seasonal cycle. Even when including boundary current eddies, 30% of the observed heat increase due to advection remains unaccounted for. Hence, an unresolved discrepancy exists between the advection due to eddies and the required heat and freshwater fluxes needed to balance the annual heat and freshwater gain of the basin. This leaves up to 60 % of the seasonal freshening unexplained (Straneo, 2006).

Here, I propose that other mechanisms, such as Ekman transport, are important in the advection of water from the boundary to the basin. This has not been investigated previously in models or observations, even though Ekman transport is known to be one of the most important processes in transporting water off the shelf in e.g., the Beaufort Sea (Schulze and Pickart, 2012) and around Scotland (FastNet, see <http://www.sams.ac.uk/fastnet/front-page-items/fastnet-full-science-case>).

The knowledge of the freshwater sources to the basin would allow some predictability of the Labrador Sea stratification before the onset of convection and hence the subsequent convection activity. Additionally, identifying pathways of freshwater into the basin and the mechanisms advecting this water will allow a better understanding of

possible changes to the boundary-basin exchange and to the production of LSW that feeds the MOC.

This Chapter aims to tackle these three questions. Firstly, what are the main pathways of water from the boundary currents to the basin? Secondly, what is the origin of this water, especially the freshwater, that reaches the basin? This is investigated on both, interannual and seasonal timescales. Lastly, what mechanisms are important in transporting the water to the basin? In particular, are eddies the most important mechanism or do we need to additionally consider other dynamics, such as Ekman transport?

3.2 Data and Method

3.2.1 Model data

To understand the exchange between the boundary and basin of the Labrador Sea, a high-resolution, eddy-resolving model simulation is needed. Here I use global ocean circulation model output from NEMO (Nucleus for European Model of the Ocean). The model was built to study the ocean and its interactions with other components of the earth climate system for a large range of time and space scales. To accomplish this, NEMO couples the ocean dynamics and thermodynamics (using OPA9, described in Madec (2008) with other ocean related engines, such as LIM2 (for sea-ice dynamics, Fichefet and Maqueda (1997)) and TOP for biogeochemistry. The horizontal resolution of the model is $1/12^\circ$ (4322×3059 grid points) but varies with location due to the tri-pole grid (one pole in Canada, one in Russia and one at the South Pole). The $1/12^\circ$ is referenced to the latitude of the equator where it is coarsest with a resolution of 27.75 km. The resolution increases to about 14 km at 60°N and 6 km at 26°N . In the Labrador Sea the resolution is 4 – 5 km. This means that NEMO resolves mesoscale eddies in the Labrador Sea but smaller eddies still have to be parameterized.

The bottom topography is derived from the 1-minute resolution ETOPO bathymetry field of the National Geophysical Data Center (available at <http://www.ngdc.noaa.gov/mgg/global/global.html>) and is merged with satellite-based bathymetry. To interpolate this onto the model grid, all ETOPO2 grid points falling into an ORCA grid box are taken and their median is calculated. This method smooths the topography, especially in regions with very steep topography. The model has 75 vertical levels that are finer near the surface (about 1 m) and reach 250 m at the bottom.

The atmospheric forcing used in the NEMO simulation was developed by the DRAKKAR consortium (<http://www.drakkar-ocean.eu/>). It has a horizontal resolution of 1.125° and uses precipitation, downward shortwave and longwave radiation from the CORE forcing data set (Large and Yeager, 2004). Wind, air humidity and air temperature are taken from the ERA-40 and ECMWF reanalysis fields. The turbulent

heat fluxes are calculated using the bulk formulae from Large and Yeager (2004). Surface momentum in the model is applied directly as a wind stress vector using daily mean wind stress.

There are no heat or salt fluxes across solid boundaries but momentum fluxes (e.g. friction) are parameterized. Surface boundary layer and interior vertical mixing are also parameterized according to a turbulent closure model adapted by Blanke and Deleclue (1993).

To avoid large drifts in salinity and an excessive spin-down of the overturning circulation, the sea surface salinity is restored with -33.33 mm/day over the open ocean. A list of parameters (including the eddy viscosity and eddy diffusivity) used in creating the ORCA-N06 data is shown in the **AppendixB**. The namelist for ORCA-N01 is shown in **AppendixA**.

3.2.1.1 ORCA-N01 and ORCA-N06

Two $1/12^\circ$ NEMO runs are available; ORCA0083-N01 and the newer ORCA0083-N06. Here, I will refer to them as ORCA-N01 and ORCA-N06, respectively. Between the ORCA-N01 and ORCA-N06 runs three main changes were made in the subpolar North Atlantic:

- wind forcing
- topography, especially along the west Greenland coast.
- partial non-slip condition for the same region

The DRAKKAR wind forcing used for the ORCA-N01 simulation is combined of two different forcings, DFS4 (for 1978 – 2005) and DFS5 (2006 – 2010). Both data sets extract wind, humidity and air temperature from ERA-40 for the time period of 1958 – 2001, and from ECMWF for 2002 – 2010. Winds in the DFS4 data set are rescaled so that their climatologies match those of the NASA Quick Scatterometer (QuikSCAT) winds. The ERA-interim data used for atmospheric variables after 2001 underwent large improvements in the atmospheric model itself but also in the data assimilation system. Discrepancies between ERA-40 and ERA-interim are likely and will hence impact the ORCA-N01 model simulation.

The newer NEMO simulation, ORCA-N06, uses DFS5 only, which was build to take advantage of the ERA-interim reanalysis fields, used for the period of 1979 – 2012. To construct a consistent data set for the entire period of 1958 – 2012 the atmospheric forcing had to be extended backwards. However, this is not of relevance here as this Thesis will only consider data from 1993 – 2012. More details about the construction of DFS5 can be found at <http://www.drakkar-ocean.eu/forcing-the-ocean/the-making-of-the-drakkar-forcing-set-dfs5>.

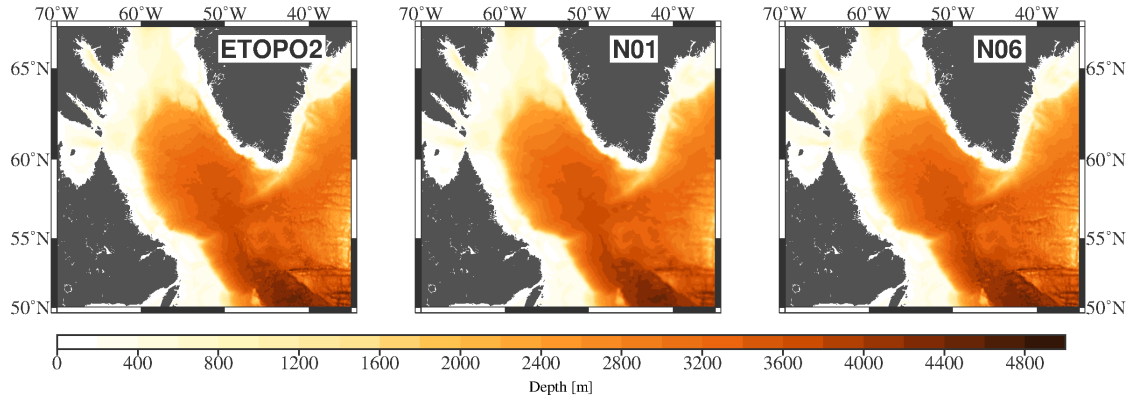


Figure 3.2: Bathymetry (in color) from ETOPO (left), used in the ORCA0083-N01 simulation (middle) and the ORCA0083-N06 simulation (right).

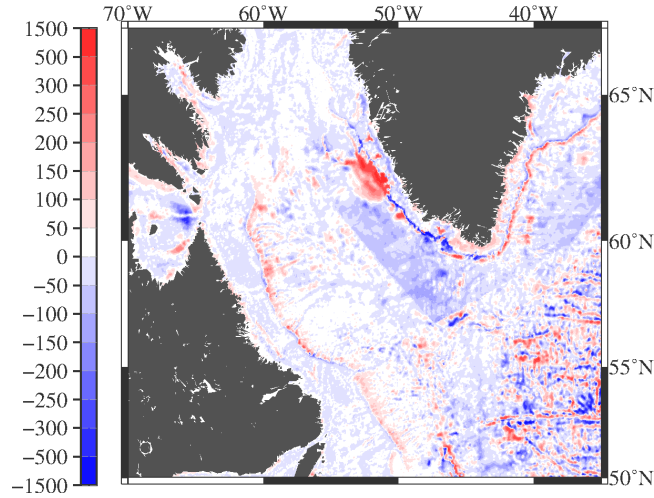


Figure 3.3: The difference in topography used in the ORCA-N06 and ORCA-N01 run. Positive values show that topography used in ORCA-N06 is deeper than in the previous run. Negative values show locations where the new topography is shallower.

The topography of ETOPO, ORCA-N06, and ORCA-N01 is shown in **Figure 3.2**. Changes in the topography were designed mainly to accomplish more energetic boundary currents in the Labrador Sea, which in turn will result in an increased amount of eddy fluxes. Previously used bathymetry was relatively smooth in much of the Labrador Sea and the roughness of the bathymetry in ORCA-N06 was increased in large areas, sometimes changing as much as several hundred meters (**Figure 3.3**). Several of these changes stand out, in particular on the eastern side of the basin. Here the topography is, in general, around 100 m shallower than in ORCA-N01. The steep continental slope along the west coast of Greenland was made even steeper by decreasing the bathymetry by up to 300 m. In contrast, in the northeast corner of the basin the bottom depth was increased by as much as 500 m. On the western side of the basin the continental slope was also made steeper by increasing the bottom depth by around 100 m.

Together with these changes in topography, a partial no-slip condition (hence, an increase in friction at the boundaries) was implemented in the Labrador Sea. This is used as an artificial way to destabilize the current and promote the formation of eddies. The changes resulted in differences in the salinity and temperature fields, as well as in velocities and EKE. This is discussed further in **Section 3.2.9**.

3.2.2 ARIANE

ARIANE is an off-line Lagrangian tool available at <http://www.univ-brest.fr/lpo/ariane> and described in detail by Blanke and Raynaud (1997). ARIANE's particles use the prescribed velocity fields of the model (here NEMO). With these velocities, trajectories of the particles are computed for each grid cell. The location, depth, and properties are recorded at each time step and trajectories can be traced forward or backwards. This method allows the calculation of thousands to millions of trajectories over very long period. Since particles are only advected by the modeled velocities, turbulent diffusion processes are not specifically calculated along their trajectories.

3.2.3 Experiment Setup

This chapter aims to understand the exchange of water between the boundary currents and basin and how this water is advected to the basin. To be able to discuss these questions, over the period of 1993 – 2012, every 10 days particles are released in the basin. The release takes place at three different depths, 0 m, 15 m, and 30 m and they are tracked backwards for one year. The 264 release positions are shown in **Figure 3.6**. Each year 28,512 particles are released, resulting in a total of 570,240 particles released over the 20 year period (1993 – 2012).

3.2.4 Crossing from boundary into basin

Trajectories are tracked backwards from their release point to find where and when they cross the boundary of the basin, hence the 2500 m isobath. In other words, a particle is considered to have entered the basin as soon as it crosses the 2500 m isobath from shallow into deeper water, within the top 30 m of the water column. However, particles do not always leave the boundary current right away. This is especially true along the eastern side of the basin where the boundary current is often centered on the 2500 m isobath. Here particles can cross the 2500 m isobath but remain in the boundary current, and hence, not enter the basin right away. A second criterion is therefore implemented, to determine when and where particles leave the boundary current and become part of the basin. This criterion is based on the velocities of the basin versus those in the boundary currents. Average speed exceed 0.25 m/s within 20 km of the 2500 m isobath

but they decrease rapidly to 0.15 m/s when moving further away from the boundary (**Figure 3.4**). Only at a distance of 50 km or further are speeds relatively constant at around 0.1 m/s. Hence, a particle is considered to have left the boundary current and fully entered the basin if it is at least 50 km away from the 2500 m isobath.

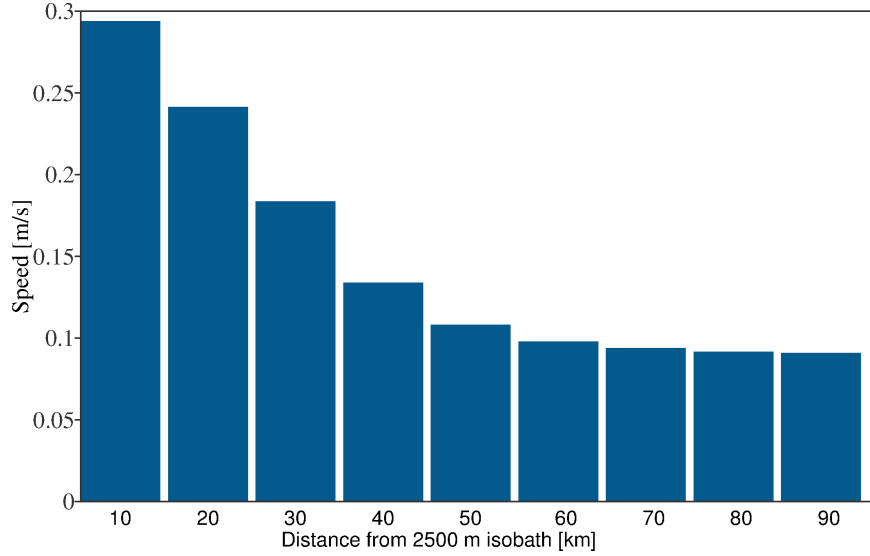


Figure 3.4: Mean speed of the top 30 m in the basin by distance from the 2500 m isobath.

Most particles enter the basin within two months before arriving at their release points (**Figure 3.5**). In fact, more than 50% of trajectories that cross the 2500 m do so within the first three months after being released, and 90% after 7 months. Here, I

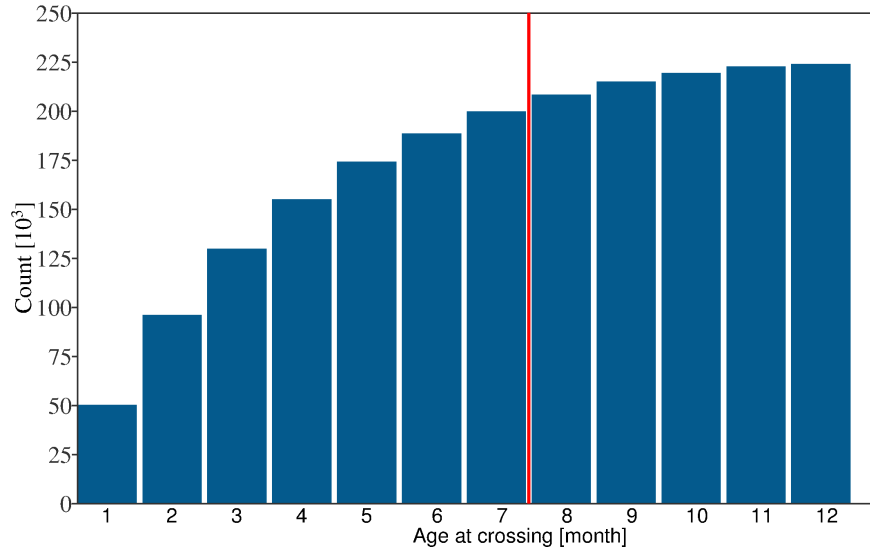


Figure 3.5: Number of particles that cross the 2500 m isobath within a certain time after being released. The red line shows the 7 month threshold that is used in this chapter.

use 7 months as a threshold and will consider only trajectories that cross within that 7 month time period. This results in 198,200 crossing particles instead of 224,075.

Note that even though the particles were tracked backwards in time, all analysis in this chapter will consider the trajectories forward in time. For example, instead of referring to the crossings of trajectories between boundary and basin as when and where they ‘left’ the basin (backward in time) this will be referred to as where and when they ‘entered’ (forward in time).

3.2.5 Regions

The Labrador Sea boundary and basin are defined by location of the boundary currents (**Figure 3.11**). The boundary current is located outside the 2500 m isobath. For this reason, the boundary of the basin will be defined by this isobath in this chapter. The boundary itself is split into four regions: East, north, northwest and southwest (**Figure 3.6**).

3.2.6 Origin of water

Five sources of water entering the Labrador Sea are identified; Hudson Strait, Baffin Bay, East Greenland Current inshore (EGC inshore), East Greenland Current offshore (EGC offshore), and water from other sources in the North Atlantic (also referred to as North Atlantic water), (**Figure 3.7 a**). The East Greenland Current (and then continuing as the West Greenland Current once in the Labrador Sea) is split into an inshore and offshore portion, due to the strong gradient of salinity (**Figure 3.7 b**).

When identifying the origin of trajectories, particles are considered to be from Hudson Strait if they, at any point along their trajectory, cross west of 65°W and 64°N. Similarly, every particle that crossed north of the Baffin Bay line at 65°N is considered to have its origin there. For the EGC inshore and offshore origins, every trajectory that crossed through the respective box is considered to have their origin in the EGC. All other particles must have their origin elsewhere and are called North Atlantic particles.

Solid freshwater, hence ice melt, is another possible freshwater origin. Unfortunately, the model does not include sea ice and its contribution can not be quantified.

3.2.7 Projection of velocities

The velocity of NEMO is given in two components u , the zonal flow and v the meridional flow. This allows us to quantify the magnitude of the flow:

$$U = (u_{nemo}^2 + v_{nemo}^2)^{1/2} \quad (3.1)$$

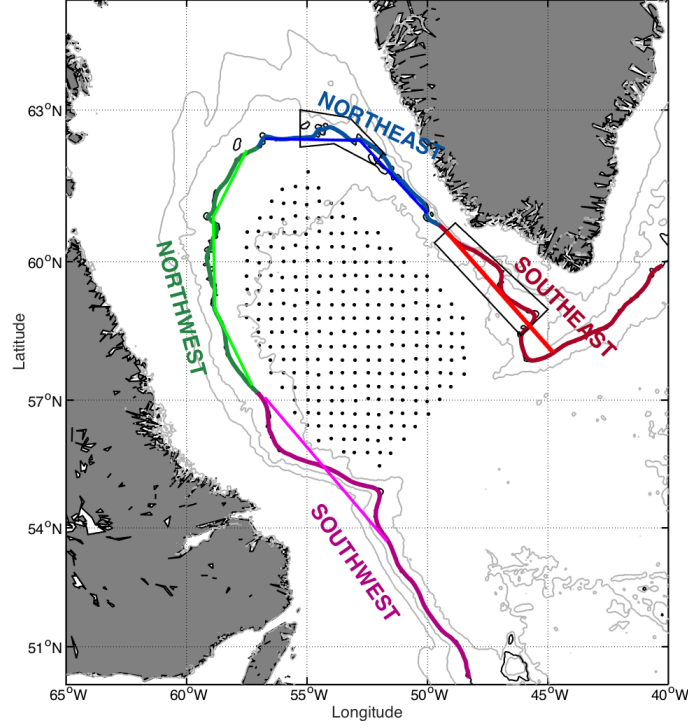


Figure 3.6: The Labrador Sea and the four regions of the boundary (2500 m isobath). The regions are shown in color. The east is red, northern region is blue, northwest is green and the southwest pink. The black dots in the basin show the release points used in ARIANE.

and the angle of the flow

$$\alpha = \tan^{-1} \frac{u_{nemo}}{v_{nemo}} \quad (3.2)$$

where u and v are the zonal and meridional components of the velocities, respectively. Here, to calculate e.g., freshwater fluxes into the basin we need to know the component of this velocity in the direction perpendicular to a section (or in the case of calculating Ekman transport, we need to know the component of wind parallel to a section). Projecting the velocities onto the section will accomplish this. In other words, we move into a new system of coordinates, where one axis is oriented to be ‘along’ the section (parallel) and the other ‘across’ (perpendicular). For each particle the velocity is calculated across a 6 km long section on the 2500 m isobath, in the location where it enters the basin. For the Ekman transport the sections shown in **Figure 3.6** are used.

We assume that the angle of the section, in a North-East system is β . Knowing α and β we can obtain the angle needed for the velocity component to be perpendicular

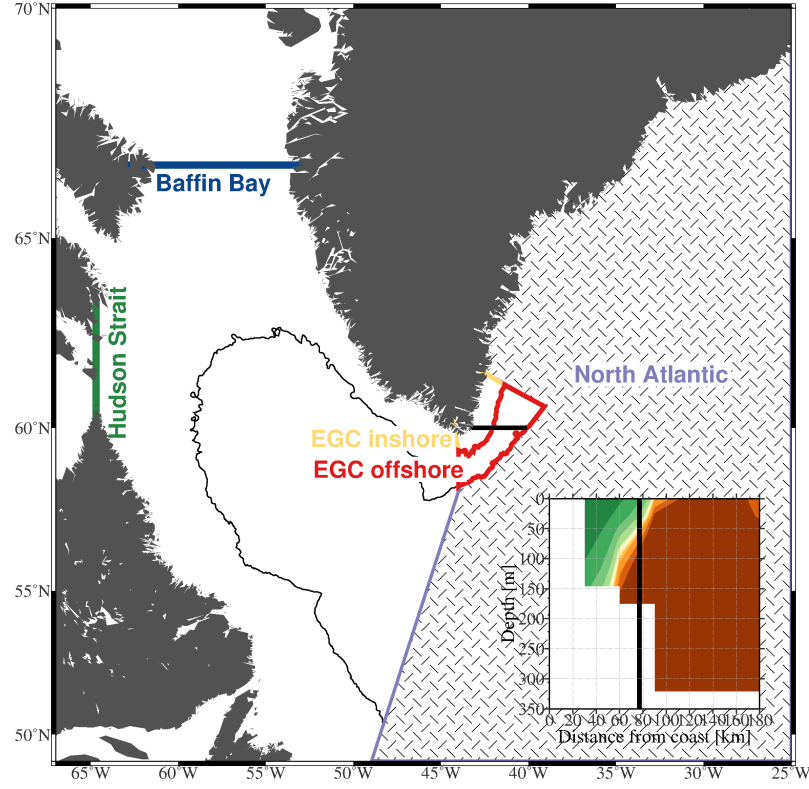


Figure 3.7: The five sources of water entering the Labrador Sea: Water can enter through Hudson Strait (green), Baffin Bay (blue), EGC inshore (yellow), EGC offshore (red) and the North Atlantic (filled region). The inset panel shows the mean salinity for 1993 – 2009 along the section shown by the black line crossing the EGC inshore and offshore region. The vertical black line shows the location of the 1000 m isobath and the division between the inshore and offshore region of the EGC used in this chapter.

to the section: $\gamma = \alpha - \beta$ and so

$$V_{across} = |U| \sin \gamma \quad (3.3)$$

$$V_{along} = |U| \cos \gamma \quad (3.4)$$

In the following this is used to calculate the freshwater fluxes of each particles crossing into the basin (using the associated ‘across’ velocities from NEMO) and also to calculate the Ekman transport into the basin (using the ‘along’ wind velocities from ERA-Interim).

3.2.8 Linear regression

Linear regressions are calculated by using the Pearson method of calculating correlation coefficients. Number of freedoms of the data are determined through the integral time scales of decorrelation (see for example Emery and Thomson (1997)). Significance is reported at 95% significance levels.

3.2.9 Model validation

While NEMO models the general ocean circulation and thermodynamics of the ocean well, here we compare the model mean fields and variability to observations specifically for the Labrador Sea. Overall, the Labrador Sea basin is saltier in the model than from Argo float observations (**Figure 3.8**). This is especially true in the northern part of the basin where salinities are on average 0.25 fresher in the winter and 0.15 in the summer months. The largest difference between the salinities of the two NEMO runs appears to be in the southern part of the Labrador Sea, which is up to 0.30 fresher in ORCA-N06 compared to ORCA-N01. In fact, the south (south of 57°N) is the region with the freshest waters in the NEMO-N06 data, while the freshest and coldest region in the ARGO data is the north. Some of the fresher water extending into the northern part of the basin can also be seen in the ORCA-N06 run, but not in ORCA-N01. The salinity distributions of the summer months are similar to those observed in the winter months. In all three data sets the basin is now fresher.

Temperatures of ORCA-N06 are up to 3°C warmer along the boundary of the basin compared to ORCA-N01 and ARGO (**Figure 3.9**). The coldest region is located in the western part of the basin. In the winter months, the temperatures of the ARGO floats and NEMO simulations agree much more closely than the salinities. However, ORCA-N06 is almost 2°C warmer than ORCA-N01 (but only 0.8 °C warmer than the ARGO data). The differences in temperatures and salinities of ARGO floats and NEMO simulations can be due to several factors. For example, uneven Argo float profile distribution may result in biases in Argo-based estimates. The cold and freshwater seen in the northern part of the basin in the ARGO data but not in the NEMO data could be due to an underestimation of advection in the NEMO simulations. This advection due to eddies typically brings in fresh and cold water from the boundary to the basin. To further investigate which of the simulations best represents the conditions of the Labrador Sea, I investigate the seasonality of temperature and salinity in the basin, hence calculating both by averaging over the entire basin (as defined in **Chapter 2**).

While the NEMO simulations appear biased towards colder and fresher water in the Labrador Sea basin, the seasonal cycles are in phase (**Figure 3.10**). Salinity (temperature) peak in the spring (fall). A slight difference in timing is observed for the salinities where the maximum of the NEMO data occurs one month later than in the ARGO data. However, the amplitudes for both, salinity and temperature, is similar in all three cases.

To compare velocities between NEMO and the real Labrador Sea, I use the AVISO gridded altimetry product. Some of the limitations of the AVISO product include limited resolution (due to the wide spacing between altimetry ground tracks, roughly 200 km at mid-latitudes and decreasing with increasing latitudes), inaccurate measurements near the coastlines and several smoothing methods applied before the data is made available.

The surface velocity and eddy kinetic energy of the NEMO simulations is compared

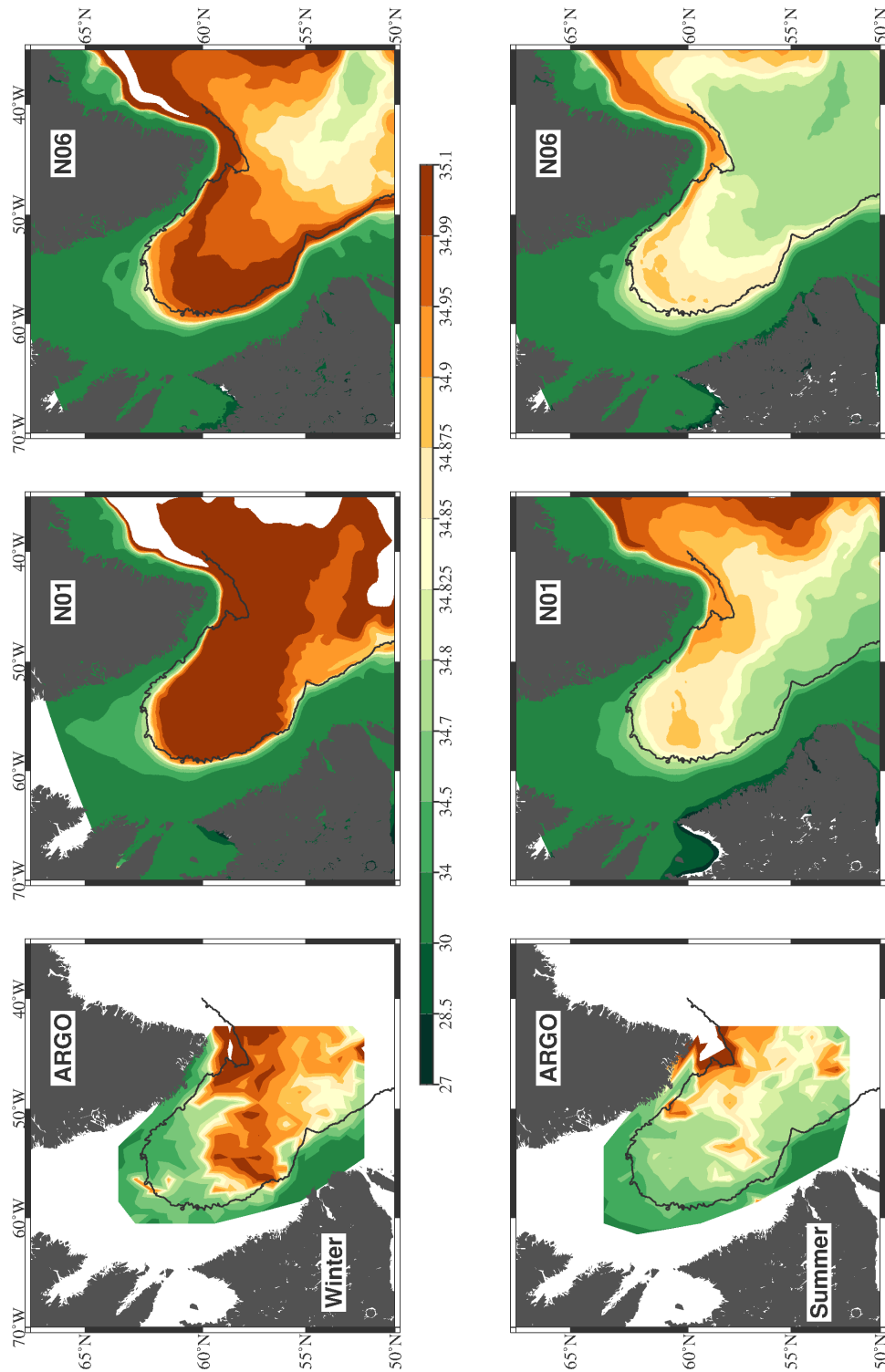


Figure 3.8: Mean salinity of the top 100 m for the winter period (Dec – May, top row) and summer periods (Jun – Nov, bottom row) of 2002 – 2011. The left panels show the salinity as observed from Argo floats (for more details on how this temperature map was constructed please refer to **Chapter 2**). The salinities observed in the NEMO ORCA-N01 and ORCA-N06 run are shown in the middle and right panels, respectively.

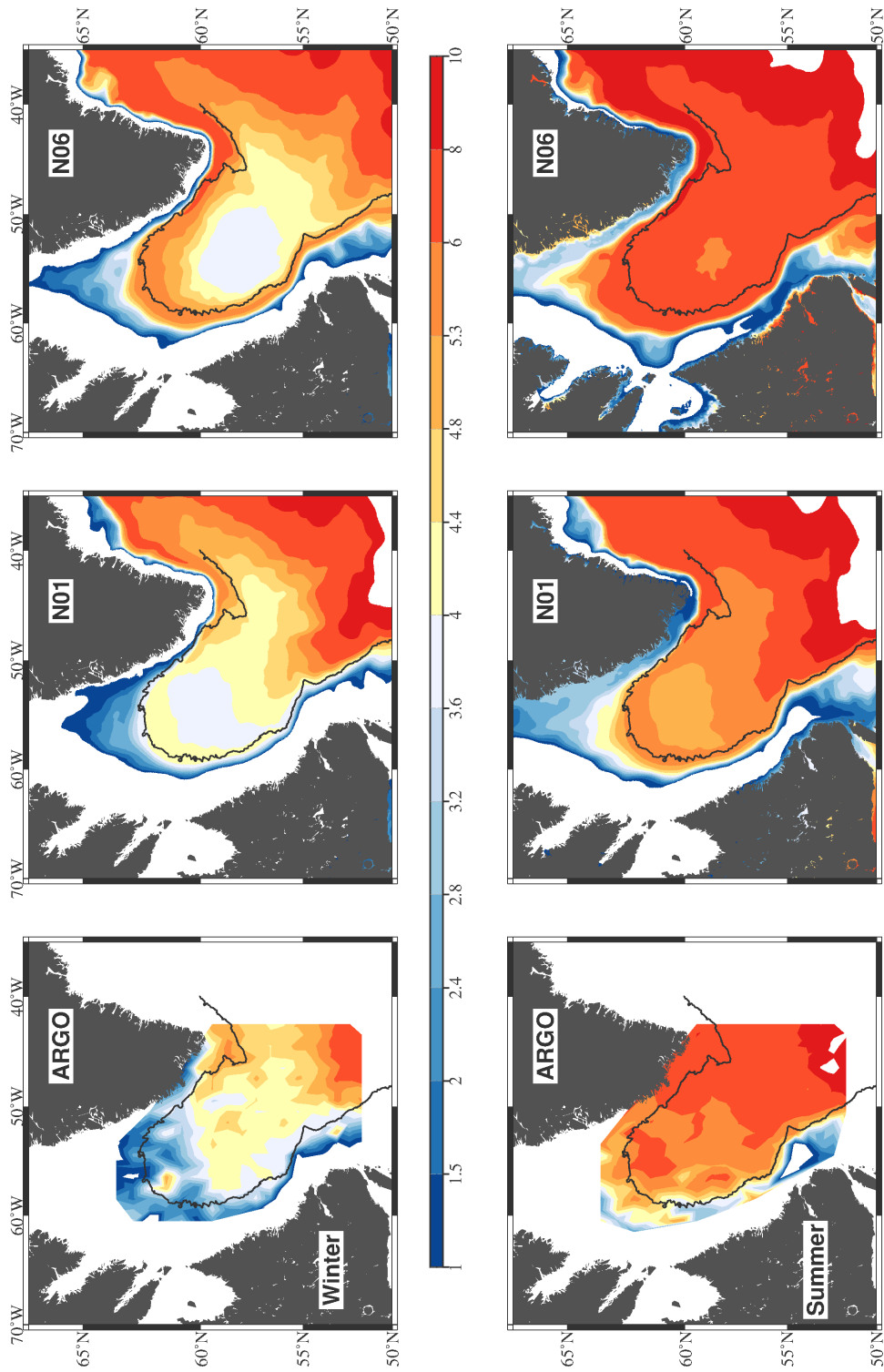


Figure 3.9: Same as **Figure 3.8** but for the temperature of the top 100 m

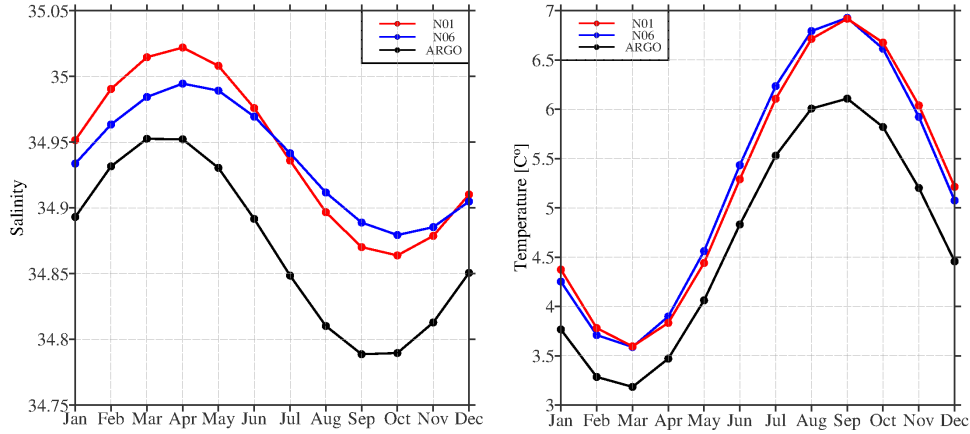


Figure 3.10: Left: the seasonal cycle of salinity of the top 100 m in the basin (region inside the 3000 m isobath, as defined in **Chapter 2**), observed from the ARGO data (black), ORCA-N01 (red) and ORCA-N06 (blue). Right: the same but for temperature.

to data from AVISO (**Figure 3.11**). In all three cases the location of the West Greenland and Labrador Current is comparable. However, the currents are much weaker in the AVISO data than seen in the NEMO simulations. This is especially true for the northern branches of the boundary current, crossing the Labrador Sea from east to west. These branches of the current are not visible in the AVISO data but shown with speeds of up to 40 cm/s in the NEMO velocities. In the AVISO data, a recirculation cell in the northeastern part of the basin is present that was also identified by Lavender et al. (2000). The recirculation is not present in the ORCA-N01 run but is very pronounced in the ORCA-N06 run. Another difference between the two NEMO runs is the circulation in the southwest of the basin, where a circulation cell extends into the basin along the 2500 m isobath in the ORCA-N01 data. This is not the case in the AVISO nor the N06 data.

As for the velocity, the EKE calculated from AVISO is much lower than seen in either of the NEMO runs. In particular, the EKE remains below $50 \text{ m}^2/\text{s}^2$ everywhere outside the basin with the exception of the northeast corner. The region of high EKE in the northeast extends well into the basin with maximum values of up to $150 \text{ m}^2/\text{s}^2$. The EKE calculated from ORCA-N01 and N06 is higher throughout the entire region, especially in ORCA-N06. However, the region of known enhanced EKE in the northeast is not present in the ORCA-N01 data. Instead, high EKE is observed outside the 2500 m isobath at the location of the boundary currents (but not extending into the basin). This issue is partly solved in the N06 run. Higher EKE is now found everywhere in the northeastern region of the basin. This EKE is higher than observed from the AVISO data reaching up to $250 \text{ m}^2/\text{s}^2$. Furthermore, outside the basin a patch of extremely high EKE (with values of up to $450 \text{ m}^2/\text{s}^2$) is observed. Again, in the ORCA-N01 data, the recirculation in the southwest of the basin is seen as a patch of high EKE. This is not the case in ORCA-N06 or AVISO.

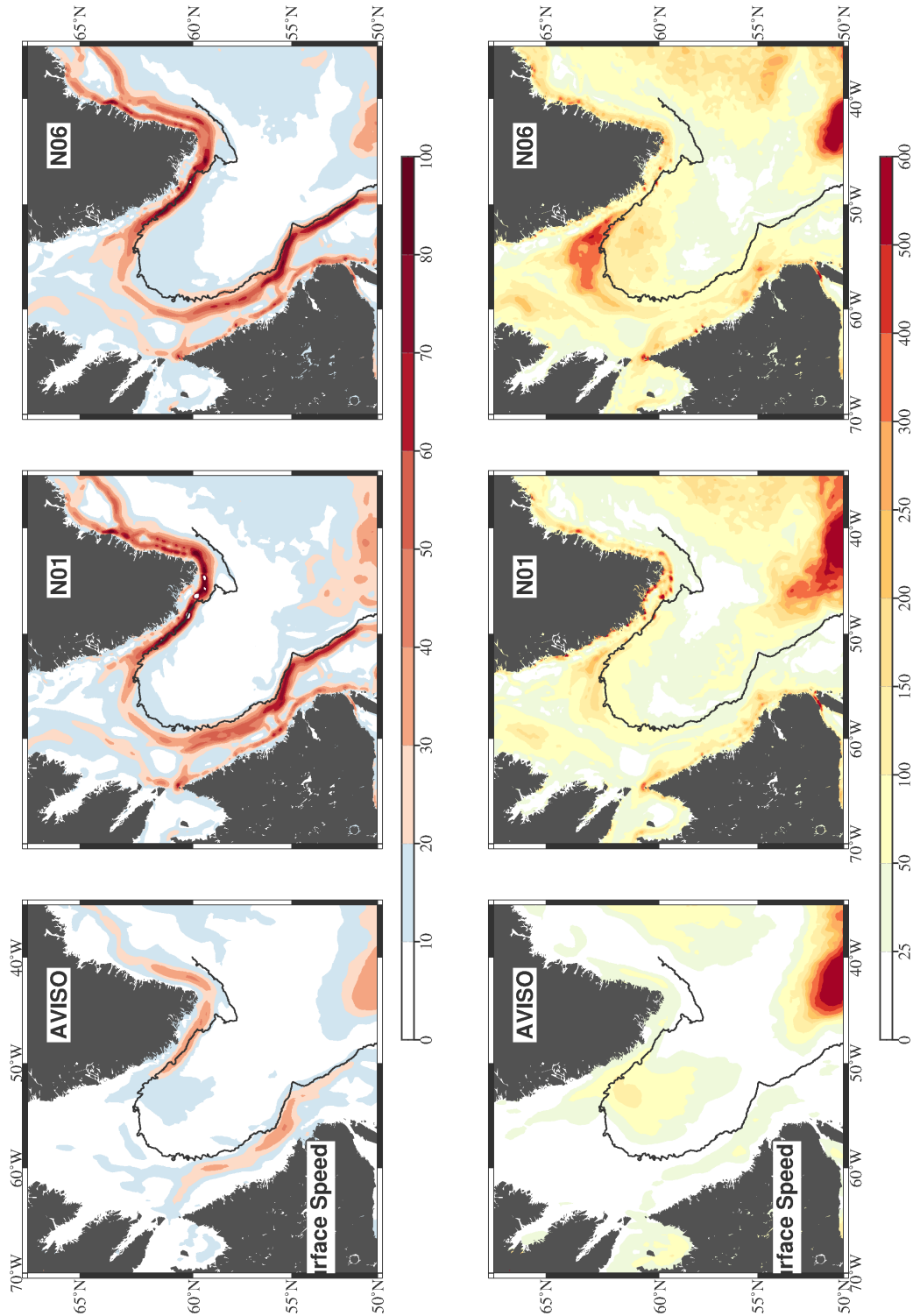


Figure 3.11: The mean surface velocity (top row) and eddy kinetic energy (bottom row) for the period of 2002–2011. The left panels show velocities and eddy kinetic energies derived from the AVISO sea surface height. The middle and right panels show the same for velocities from the two NEMO simulations, ORCA-N01 and ORCA-N06.

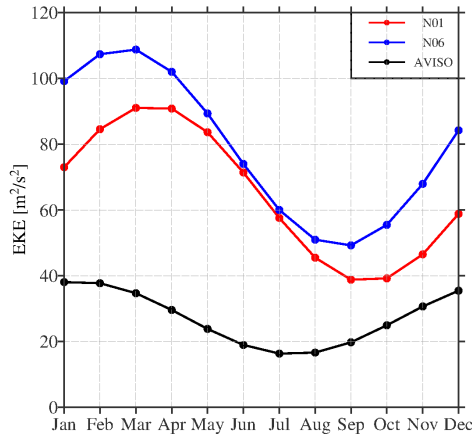


Figure 3.12: The seasonal cycle of eddy kinetic energy of the region shown as the black box in **Figure 3.11**, calculated from the AVISO velocities (black), ORCA-N01 (red) and ORCA-N06 (blue).

While the differences between the AVISO and NEMO data seem severe, they can partly be explained by issues that arise with the construction of the AVISO data. In particular, the resolution of this data set is $1/4^\circ$, three times lower than the NEMO resolution. In the Labrador Sea this translates to a difference of 8 km between AVISO ($1/4^\circ$) and NEMO ($1/12^\circ$). Hence, small features can not be resolved by the present configuration of altimeters. In a bespoke gridding of the altimetry track data, Brandt et al. (2004) find higher EKE outside the 2500 m isobath than is shown by the AVISO product. This suggests that additional smoothing has been applied in constructing of the gridded AVISO product, though their gridding method is not published. Interestingly, the EKE field in Brandt et al. (2004) shows a region of very high EKE outside the 2500 m isobath, with magnitudes agreeing with the ones observed in ORCA-N06. Enhanced EKE located close to the coast is also not expected to be visible in the gridded AVISO data due to its problems of detecting features close to land.

The seasonal cycle of EKE is calculated in the northeastern box (see **Figure 3.6**). As described above, the magnitude of the EKE does not agree between the three data sets. The EKE is much higher in the N06 run than for both the other data sets. However, the minimum and maximum of EKE coincide between this run and the AVISO data with the maximum EKE in the winter and a minimum during the summer months. For ORCA-N01 the maximum and minimum occur about one month after the maximum and minimum in N06, in April and September (N01) respectively.

Finally, I compare the mixed layer depth of the model to those observed (see **Chapter 4** for a description of the observational data). Observations have shown that the deepest mixed layers are usually found in the western part of the basin, exceeding 1000 m in many years (Lazier, 2002; Pickart et al., 2002). Due to the stable boundary currents and the resulting underestimation of eddies in the ORCA-N01 run, mixed layers are on average too deep. Furthermore, the deepest mixed layers are located in the northern

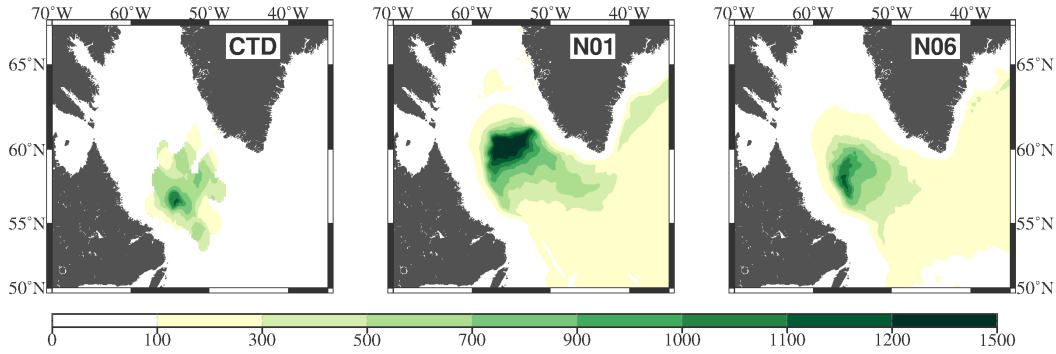


Figure 3.13: Mean winter mixed layer depth observed from hydrographic data in 1997 (left panel, for more details see **Chapter 4**). The mean winter (Dec–Mar) mixed layer depth in the NEMO simulations is shown in the middle (ORCA-N01) and right panel (ORCA-N06).

part of the basin instead of the western part. In the newer ORCA-N06, mixed layers are appropriately shallower (with an average depth of 1000 m). Furthermore, they are located in the western part of the basin.

The depth of the mixed layers and the location of the deepest mixed layers (**Figure 3.13**) as well as the amount of advection to the basin are crucial in driving the advection of freshwater and heat, as well as setting the preconditioning for deep convection. In the ORCA-N01, where the region of high eddy kinetic energy in the northeast is missing, the boundary currents are too stable and do not allow enough eddies to form and hence, enough advection to take place. The exchange with the basin is suppressed. This is especially clear when looking at the mixed layer depth of this run, which are too deep and in the wrong location due to the lack of restratification in this region. The following analysis is therefore done with the ORCA-N06 simulation that is more realistic in terms of mixed layers depths and boundary current instabilities. Furthermore, as seen later, winds play a large role in the advection of water as well as boundary current instabilities. A change in atmospheric forcing as done for ORCA-N01 would introduce large uncertainties within the analysis and the year to year variability of fluxes. See **Appendix A** for additional figures using ORCA-N01.

3.3 Origin of Labrador Sea Basin surface water

Of the 570,240 particles that were released in the basin between 1993 and 2012, 198,200 (34.7 %) crossed into the basin in the top 30 m, within 7 months of reaching their release points (following the criteria described in **Section 3.2.4**). The majority of these particles (>85%) did not leave the surface layer, while a small fraction sank below 30 m at some point along their trajectory. However, even the ones that sank crossed and arrived at their release points in the top 30 m of the water column. An additional 25,875 particles crossed the boundary of the basin in the top 30 m after 7 months. Hence a

Table 3.1: Number of trajectories with different criteria

	Count	% of total
Total	570,240	
Crossings <30 m	224,075	39%
Crossing with in 7 mth	198,200	
• Stay <30 m	169,294	
• Leave top 30 m	28,906	
Crossing later	25,875	4.5%
• Stay <30 m	22,103	
• Leave in top 30 m	3772	
Crossings >30 m	1620	<1%
Enter in south	329,768	57.8 %
• Stay <30 m	62,460	
• Leave top 30 m	267,307	
Stay in basin	14,777	2.6%
• Stay <30 m	1354	
• Leave top 30 m	13,423	

total of 224,075 trajectories, 39% of all released particles, crossed into the basin. A small amount (1620) of the remaining 346,165 particles entered the basin below 30 m. The largest number (329,768) however, entered the basin from the south, within the 2500 m isobath. Of these particles, 267,307 entered below 30 m but arrived at their release point in the surface layer, hence were mixed upwards. A further 2.6 % (14,777) of particles remained in the basin throughout their one-year lifetime but mostly originated from deeper in the water column. Please refer to **Table 3.1** for further information and exact number (and percentages) of particles in each category.

The following analysis concentrates on the 198,200 particles that crossed into the basin in the top 30 m and within 7 months of their release. Hence, ‘trajectories’ or ‘particles’ in the following analysis refer to those 198,200 trajectories. The focus here is on the pathways of freshwater into the basin and the forcing that regulates this advection. In order to close a budget of freshwater in the basin all trajectories would have to be taken into account, plus the vertical mixing and advection out of the basin that was not captured by the set up of this experiment. This needs to be kept in mind when interpreting the results below.

Of the 198,200 trajectories entering the basin, 30% pass through the south-east of the basin (**Figure 3.14**). Around 15% continue into the north-eastern part of the basin where they are concentrated away from the 2500 m isobath. The probability of trajectories passing close to the 2500 m isobath in the north is less than 1%. This gives us a first indication to where water enters the basin; to reach the northern basin without passing across the northern boundary, they must have been advected across the eastern boundary. Only about 6% of trajectories stay close to the western boundary before diffusing into the central region of the basin.

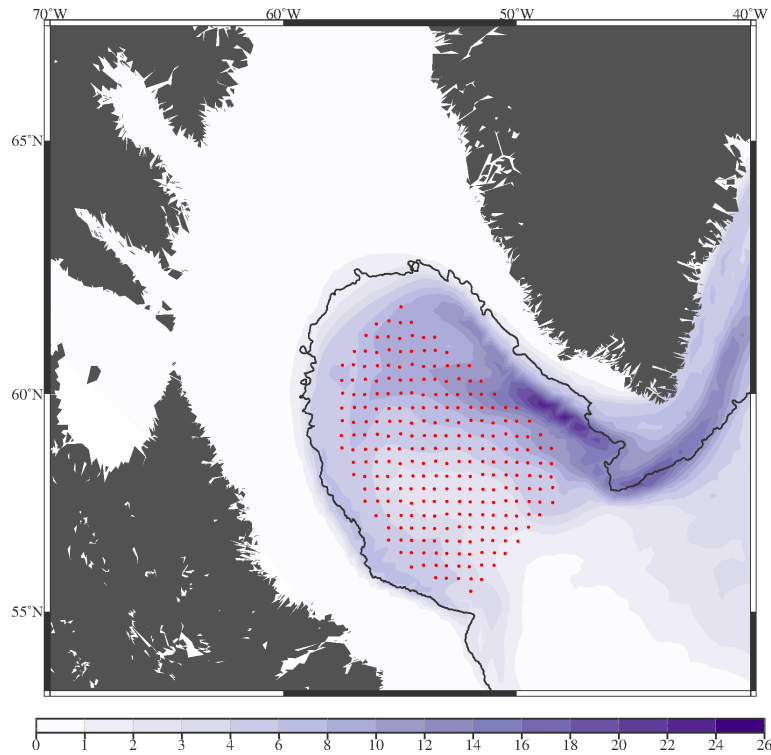


Figure 3.14: Percentage of the 198,200 trajectories (that cross into the basin) that pass through each 0.5° longitude \times 0.3° latitude grid point. The black contour shows the 2500 m isobath (i.e. the boundary of the basin). The red dots show the release positions of the particles.

The majority of the trajectories originated from the East Greenland. Upon reaching Cape Farewell, the main pathway of trajectories is centered on the 2500 m isobath but the water does not immediately enter the basin. As seen in **Figure 3.11**, the boundary current, flowing north, is centered on the 2500 m isobath along the entire east side of the basin and hence, water crossing the 2500 m isobath in the south-eastern corner of the basin does not necessarily leave the boundary current immediately. This is one of the reasons why a second criteria was introduced in **Section 3.2.4**. This allows us to determine where the particles leave the boundary current completely to become part of the basin.

Of the particles entering the basin, about 78% (158,317) originated in either the inshore or offshore part of the East Greenland Current (**Figure 3.15**, see **Section 3.2.6** for the definition of the different water sources). Of these, 88,385 came from the offshore part and the other 69,932 from the inshore region of the current. A further 13% (27,627) of the particles originated in other regions of the North Atlantic, hence were not part of the East Greenland current before rounding Cape Farewell but got entrained into the West Greenland current at or west of it. Only 159 particles (<1%) came from Baffin Bay and five particles of the 198,200 particles originated in Hudson Bay. Due to the

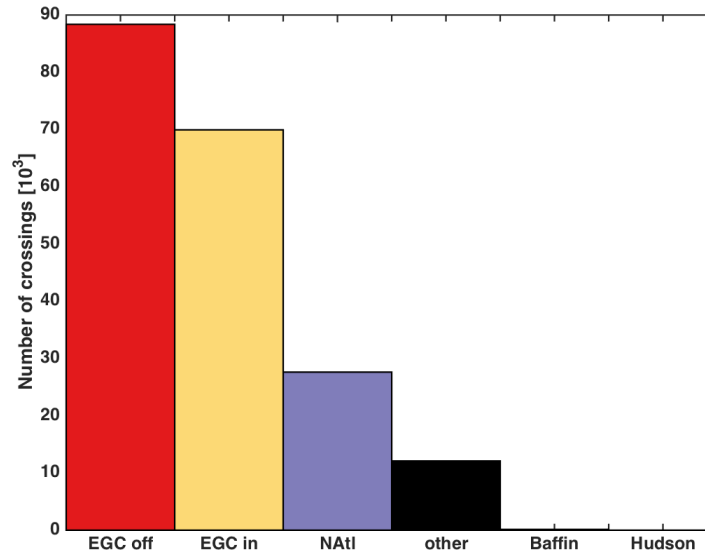


Figure 3.15: Number of crossings origination in each of the origin, East Greenland Current offshore (red). East Greenland Current inshore (yellow), other regions in the North Atlantic (purple), unidentified origins (black), Baffin Bay (blue) and Hudson Strait. The five sources are shown in **Figure 3.7**

one-year runtime of ARIANE, 6% (12,095) of particles could not be traced back to their origin and were still in the Labrador Sea at the end of their lifetime. However, most of them were found in the West Greenland Current, Baffin Bay and Hudson Bay can be ruled out as their origin. Furthermore, the offshore EGC source would remain the dominant source of water entering the Labrador Sea basin, even if all of the remaining, unidentified particles had originated in the inshore part of the EGC or in other regions of the North Atlantic.

Most water in the southeast and along the eastern boundary of the basin is of EGC offshore origin (**Figure 3.16**). Here, more than 50% of the water that was advected to the basin is of EGC offshore origin. In the southeast, the other 50% is made up, almost equally, of inshore and North Atlantic water, but the inshore water becomes more dominant when moving north along the boundary. Only very few trajectories here could not be traced back to their origin and remain of unidentified origin. No water from either Baffin Bay or Hudson Strait is found here. In the northeast, the same amount of inshore and offshore water reaches the basin, but much less of the North Atlantic water. Moving north to south along the western side of the basin, the amount of EGC offshore water decreases and the inshore water becomes more dominant until in the southwestern corner of the basin only one quarter of water is from the offshore source and about one half from the inshore source. This is also the region where most of the unidentified particles are found. Due to the small number of Baffin Bay and Hudson

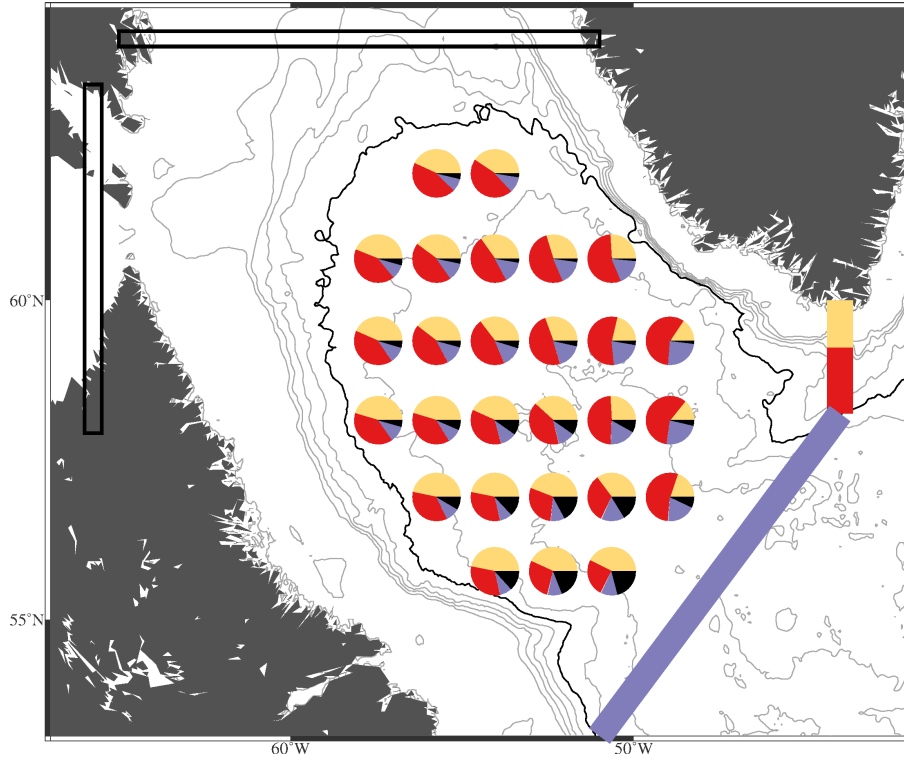


Figure 3.16: The distribution of particles of different origin in the basin at the time of their release. The colored sections indicate the sources, EGC offshore (red), EGC inshore (yellow), other sources in the North Atlantic (purple), Baffin Bay (blue) and Hudson Strait (green). The circles in the basin show the proportion particles from each source at the time of their release in each part of the basin. Colors refer to the five sources. Black circle fraction show the amount of trajectories for which no origin could be identified (see text for details).

Straight particles it is hard to see their presence in the basin even though they are shown grouped together in white. They are exclusively present in the southwest corner and south central basin. Due to the extremely low number of crossings, the analysis below will concentrate on the three main water sources: EGC inshore, EGC offshore and other North Atlantic water.

3.4 Freshwater pathways

Not only are most of the crossings in the southeast, but the freshest waters are also found in the east. We investigate the detailed pattern of the region of crossings, their origin and salinity in the following section. To assess the influence of crossings on freshwater content of the basin we plot the number of crossings per 100 km section of the boundary (**Figure 3.17**). The salinity of each particle at the time of its crossing and its associated freshwater flux are also shown. To calculate a proxy for freshwater flux in the top 30 m

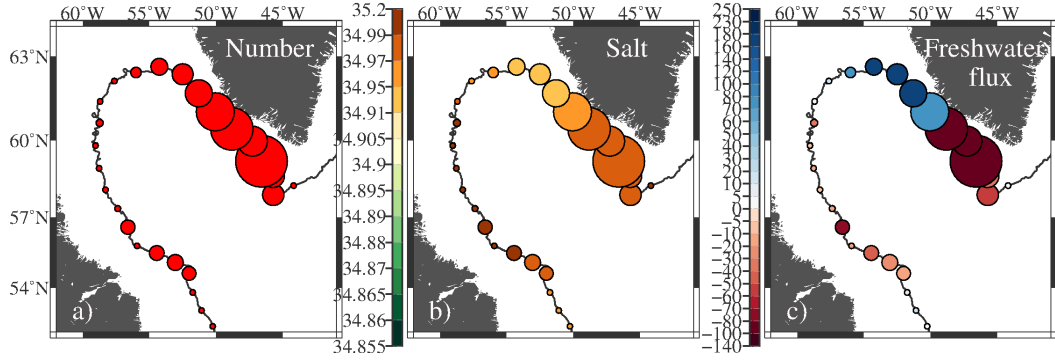


Figure 3.17: a) The relative number of crossings per 100 km boundary section is indicated by the size of the red circles. b) The mean salinity of the crossings particles is indicated as color. The circles have the same size as in a) and again show the relative number of crossings per section. c) Again the size of the circles remains the same. Color shows the freshwater flux into the basin, where positive (blue) fluxes are freshwater divergence into the basin and red colors (negative values) indicates divergence of salty water, both with respect to the reference salinity of 34.95.

we use:

$$FWF = \sum_{n=1}^N dz \times dx \times v \times F \quad (3.5)$$

where FWF is the freshwater flux and v is the speed of the particle at the time of crossing. dz is the depth that each particle represents, here 15 m due to the set up of the experiment (particles were released 15 m apart). dx is the horizontal length of 6 km, which is the size of the model resolution at this latitude. Also,

$$F = \frac{S_{ref} - S}{S_{ref}} \quad (3.6)$$

and $S_{ref} = 34.95$ (the mean salinity of the basin for 1993 – 2012). In other words, the freshwater flux with respect to a reference salinity is found for each crossing individually, before added per section along the boundary (or per month/year later in the analysis). Due to a large decrease in salinity of the basin after 2009 the following analysis will concentrate on the years 1993 – 2009 since a large change in salinity could also mean a change in forcing, and pathways. Here the goal is to find typical pathways and relationships with forcing and so 2010 – 2012 is not included into the analysis.

Water enters the basin mainly via the east, with some elevated numbers of crossings in the southwest, south of 57°N (**Figure 3.17** and **Figure 3.18**). Along the eastern side the crossings are, on average, 0.7 psu saltier in the south than the north (34.97 versus 34.93 respectively). In fact, the freshest water is advected across the northeast sections II and III and also in the southwest at section VI. The saltiest water enters the basin in the southeast (Section I) and northwest (Section IV) with salinities of up to 35 psu.

On average, freshwater is brought into the basin via the northeast (**Figure 3.17c**),

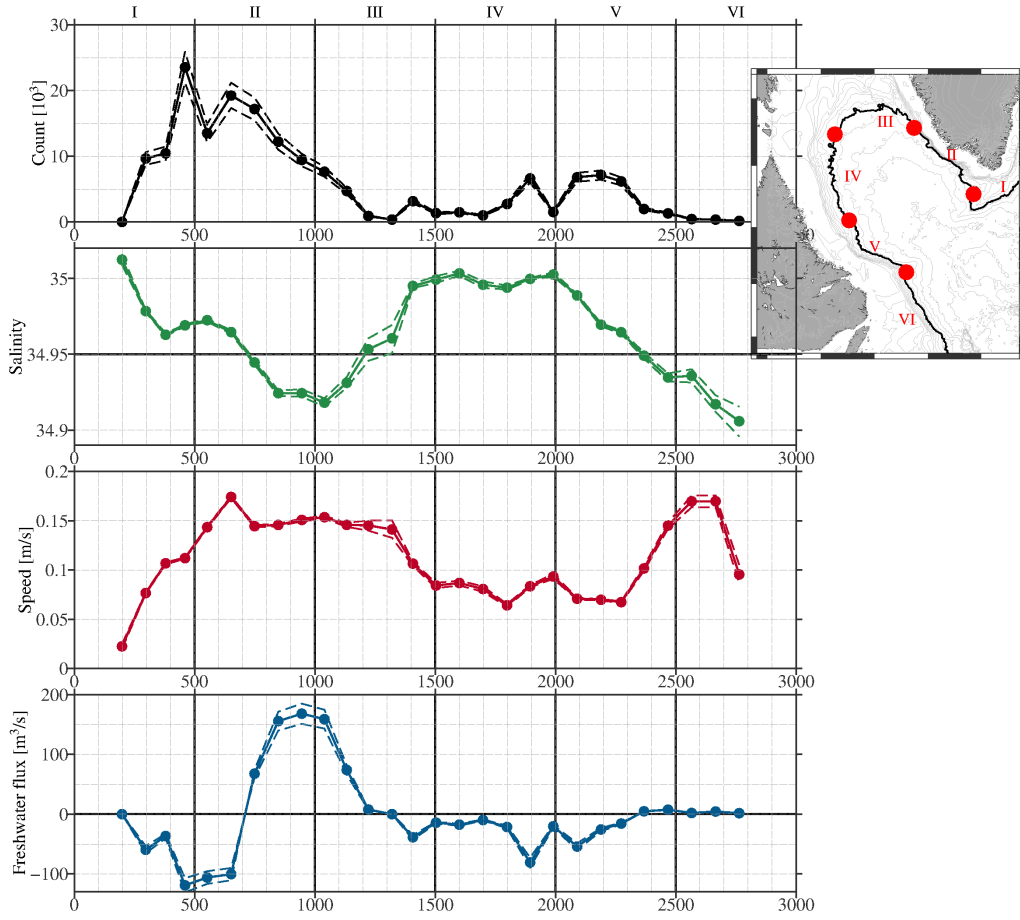


Figure 3.18: Top panel: The number of crossings per 100 km section along the 2500 m isobath (solid line and dots) and the error estimated using a Monte-Carlo method (dashed line). Second panel: The average salinity of the crossings particles at each 100 km section (solid line) and the error (dashed lines). The black horizontal line shows the reference salinity used to calculate the freshwater flux (see text for more details). Third panel: The average speed of the particles at the point of crossing into the basin (solid line) and the error (dashed lines). Bottom panel: The accumulated freshwater flux (solid line) at each section and the associated error (dashed line). Positive fluxes indicate freshwater advection to the basin, negative values salt water divergence into the basin. The vertical lines in all four panels associate with the red dots in the bottom figure (map) to help orient the reader geographically.

while advection in the southeast and west adds salt to the basin. The input of salt in the southeast is due to the large number of crossings with relatively high salinities, while the salt fluxes in the west are dominated by high salinities rather than the number of crossings (**Figure 3.18**). The freshwater input, on the other hand, is due to a combination of low salinities, relatively high numbers of crossings and fast crossing speeds (**Figure 3.18**). Over the 17 years studied here, advection added a total of 0.42 ± 0.04 mSv of salty water via the southeast and 0.3 ± 0.03 mSv via the west, hence 0.72 ± 0.07 mSv in total. The total freshening due to advection is 0.86 ± 0.06 mSv

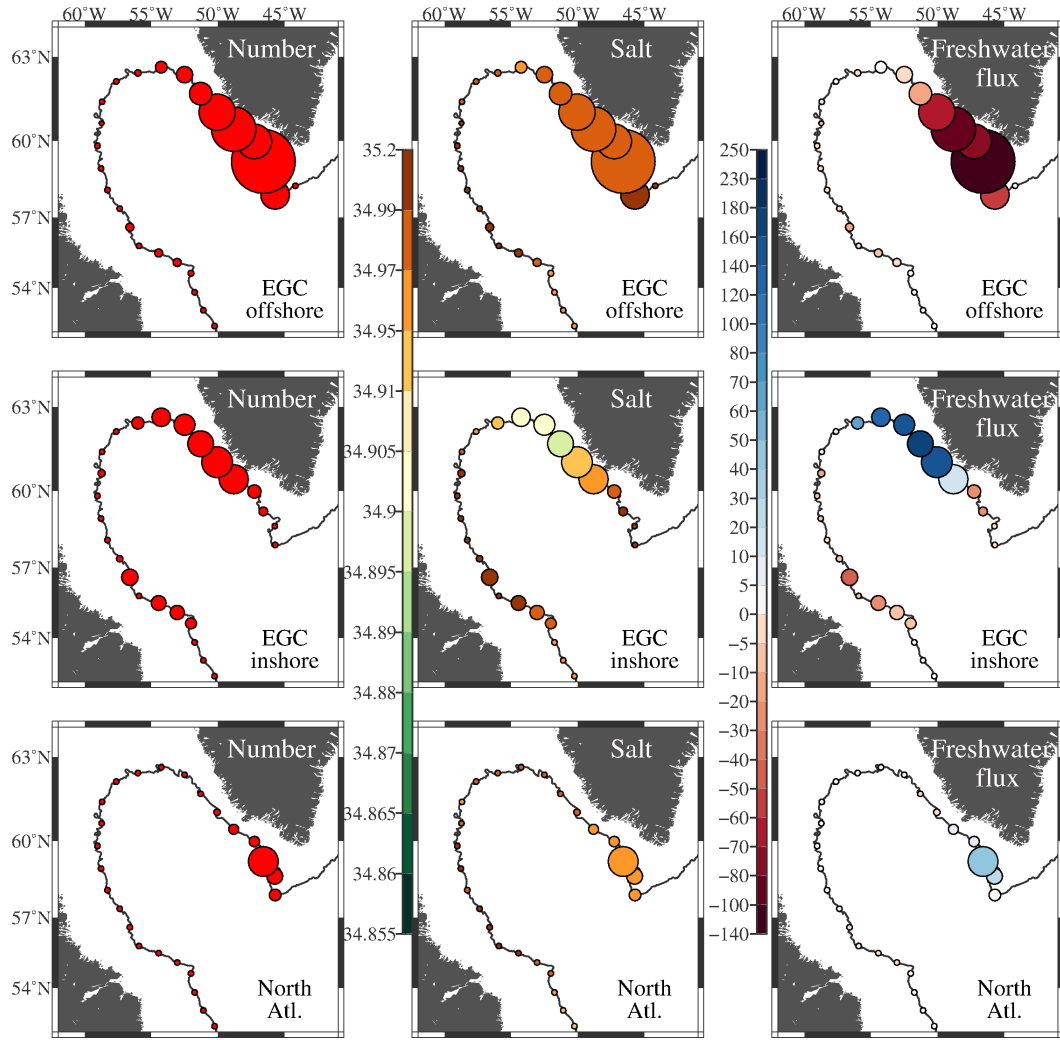


Figure 3.19: Same as **Figure 3.17** but for the four main water sources, EGC offshore water (top panels), inshore water (second row of panels), other sources in the North Atlantic, excluding the offshore and inshore water (second last row of panels), and Baffin Bay (bottom panels).

and balances the input of salty water to the surface layer to 0.14 ± 0.01 mSv. This is equivalent to a freshening of 36 ± 3 cm over the time period of 1993 – 2009.

Water from the offshore EGC enters the basin a short distance downstream from Cape Farewell, along the east side of the basin (**Figure 3.19** top row). The main pathway of EGC inshore water into the basin is via the northeast with a slightly elevated amount of water crossings in the southwest (**Figure 3.19** second row). In fact, more of this water enters here than in the proximity to Cape Farewell. There is significantly less water entering the basin from other regions in the North Atlantic (**Figure 3.19**). Similarly to the EGC offshore water, it is advected into the basin via the southeast but in much smaller quantities.

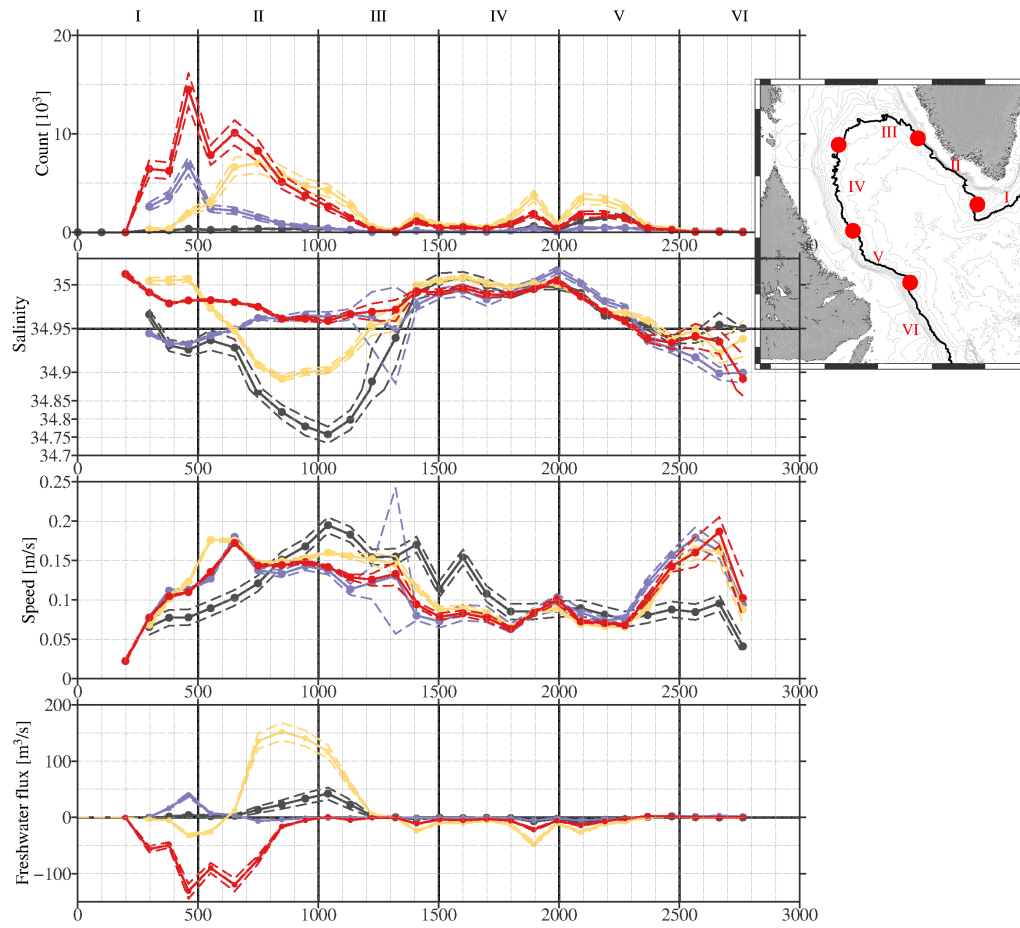


Figure 3.20: Same as **Figure 3.18** but for the three water sources, EGC offshore (red), inshore (yellow) and other sources in the North Atlantic (blue). The top panel shows the number of crossings (10^3), second panel shows the average salinity, the third panel the average speed at the point of crossing, and the bottom panel shows the accumulated freshwater flux due to water from each source. The vertical lines refer to the red dots in the bottom figure of **Figure 3.18**.

On average, the EGC offshore water enters the basin with salinities of up to 35 in the southeast and between 34.97 and 34.99 in the northeast and along the rest of the boundary (**Figure 3.20**). The inshore water on the other hand, brings much fresher water to the basin. In the northeast, salinities are, on average, as low as 34.89. Inshore water is advected along the western side of the basin inshore water, with salinities comparable to those of the offshore water, is advected. In the southeast, the water from other sources in the North Atlantic is 0.04 psu fresher than the EGC inshore and offshore water. It is noteworthy that the freshest water that enters the basin is of unidentified source. This water is as fresh as 34.75 when entering the basin in the north, but the number of crossings is small. It is also interesting that the crossings have a similar salinity pattern to the EGC inshore water.

Overall, the EGC offshore water causes large salinity fluxes to the basin due to its high salinity and the large amount of particles being advected in the southeast (**Figure 3.20**, bottom panel). This results in a freshwater flux of -0.54 ± 0.05 mSv at sections I and II. (Note that negative freshwater fluxes indicate a flux of salty water to the basin). The low salinities of EGC inshore water enters the basin in the northeast, resulting in large freshwater fluxes in this location. Even though there are fewer crossings here than in the south by Cape Farewell, the very fresh water causes freshwater fluxes that balance the flux of salty water in the southeast due to the offshore water. About 0.68 ± 0.06 mSv of freshwater is brought to the basin by the EGC inshore water along sections II and III. In the southeast, next to the salty offshore water, a small amount of freshwater is added by water from other North Atlantic sources (0.07 ± 0.006 mSv). Baffin Bay, due to very few crossings (154 over the 20 years) resulted in freshwater fluxes between -0.0001 mSv and 0.0001 mSv and is not shown for most of the analysis from here on. Despite the small number of crossings, the water of unidentified origin added a surprisingly large amount of freshwater via the same region compared to the EGC inshore water. This freshwater flux is due to the extremely low salinity of this water and adds up to 0.15 ± 0.05 mSv.

The speeds with which the particles enter the basin are almost identical between the different water sources. Hence, they are governed by the location along the boundary rather than the water source itself. They can therefore not explain the differences in freshwater fluxes. Instead, this difference must be due to the volume flux (number of crossings) and salinities of the source waters. It is also interesting to note that the salinities only differ significantly for crossings along the eastern and northern side of the basin. Once reaching the west, the amount of water entering the basin and its salinity is comparable for the EGC inshore, offshore and North Atlantic water, as well as the water from unidentified sources.

3.5 Seasonality of freshwater advection

The number of particles crossing into the basin is largest in the spring (**Figure 3.21a**) and salinities of the water advected to the basin remain high until rapidly freshening in July. However, particles crossing in March and April have lower salinities than the months immediately before and after (**Figure 3.21b**). Hence, there are two times of the year when fresher water enters the basin, first in March – April and then in August – October. The salinities in the spring are, on average, saltier than the reference salinity of 34.95, yet overall the advected water results in freshwater fluxes of around 0.06 ± 0.04 mSv (**Figure 3.21d**). This is because 75% of crossings have salinities above 34.95, averaging about 35 (not shown). However, the 25% that are fresher than 34.95 (average 34.78) are more than three times fresher and are the reason for the overall freshening during these two months. Fewest crossings take place in the summer, with

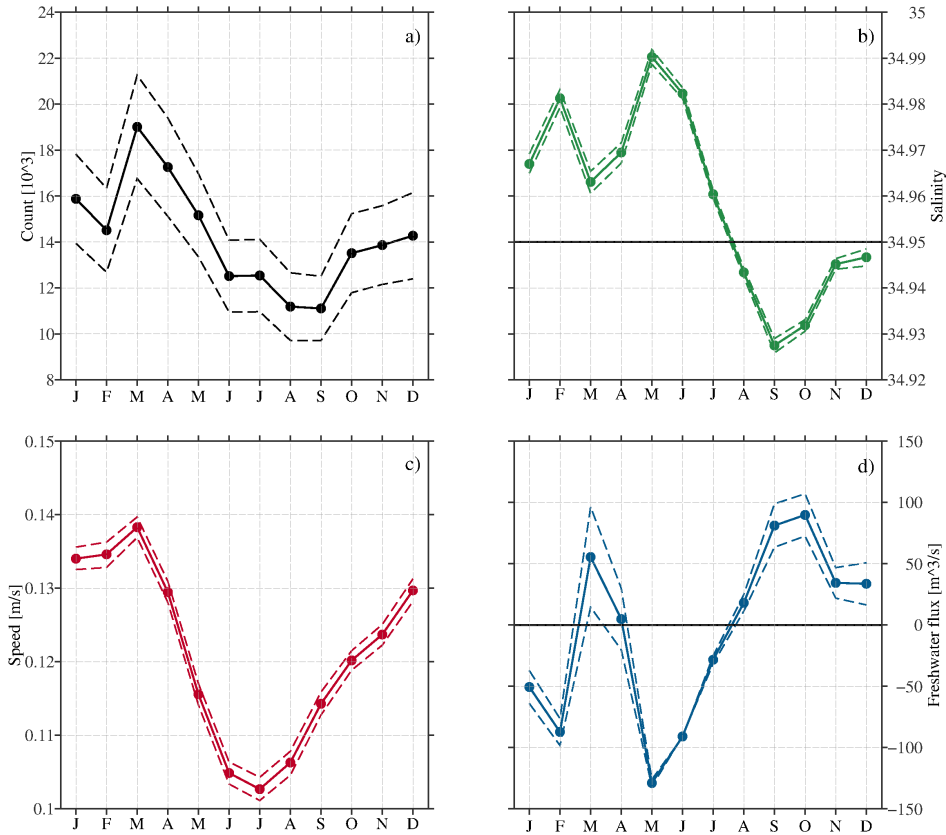


Figure 3.21: a) The seasonal cycle of the number of particles crossing the 2500 m isobath (solid line) and the error associated with it, calculated using a Monte Carlo approach (dashed line). b) the seasonal average salinity of the crossing particles (solid line) and the associated error (dashed line). The black horizontal line shows the reference salinity of 34.95 that is used to calculate the freshwater fluxes. c) the average speed with which the particles cross into the basin (solid line) and the associated error (dashed line). d) the accumulated seasonal freshwater flux into the basin (solid line) and the error (dashed line). Positive fluxes show freshwater fluxes into the basin and negative fluxes show fluxes of salty water into the basin.

a minimum in August and September. During these months some of the freshest water of the entire year is advected to the basin, averaging around 34.93. This results in a large peak of freshening in September and October bringing in around 0.2 ± 0.08 mSv. Additionally, the water crossing into the basin in the spring was, on average, 0.04 m/s faster than the water entering the basin in the summer and fall and the fastest during the year, contributing to the resulting freshening peak. Between these peak, salty water is brought to the basin in January – February and May – July, even though the number of crossings are relatively low during these months. Salinities, however, are high, causing the input of salt.

We see two peaks of freshening in the Labrador Sea. A first, smaller peak in March – April and a second, stronger pulse in September - October. While the first is due to a large number of fast crossings of which some are extremely fresh, the second is due

to less water crossing into the basin more slowly but with significantly lower salinities. Over the entire year an average of 0.07 ± 0.04 mSv of salt is added to the top 30 m of the Labrador Sea basin. This is equivalent to a yearly loss of 3 ± 2 m of freshwater due to advection.

Investigating the seasonal cycle of the different water sources separately can help us to gain a better understanding of where the two pulses of freshwater to the basin originate. The crossing particles are split into origin and the region in which they cross (Southeast, Northeast, Northwest and Southwest, see **Figure 3.6**). I start the analysis with the water entering the basin along the eastern side.

Water from the EGC inshore source is advected to the basin mainly in the spring. In both the south and northeast, the largest amount of inshore water arrives in the basin in March (about 2860 in the southeast and 3960 in the northeast), (**Figure 3.22a**). Only about 50 (in the southeast) and 379 (in the northeast) crossings are observed in the summer. The water entering in the southeast is, on average, saltier than the reference salinity, resulting in no significant freshwater fluxes to the basin (**Figure 3.22c and g**). In the northeast on the other hand, the water is generally fresher than 34.95, adding freshwater to the basin in two distinct peaks, one in March – April, and a second in September. The spring freshening is the larger of the two and starts in December but is at a maximum in March – April, with an overall flux of 0.54 ± 0.01 mSv. The second pulse is much weaker with only 0.05 ± 0.003 mSv. Even though the salinities are comparable for both of these time periods the first pulse is stronger due to about twice the amount of water entering the basin in March – April compared to September. Only during one month (June) does the advection of EGC inshore water result in a negative freshwater flux to the basin (increase of salt of about -0.015 mSv).

In the southeast the advection of EGC offshore water exceeds that of the inshore water throughout the year even though their seasonal cycle of advection is similar. One exception is the smaller peak of offshore water crossings in October. In the northeast, on the other hand, the seasonal cycles of the offshore water advection is weaker with a peak in the summer/fall. In both regions this water brings salty water to the basin. In the southeast, it enters the basin with mean salinities exceeding 35 during the first five months of the year. This results in an influx of -0.46 ± 0.01 mSv of salty water between January – June, with a peak in March – April. This partially reduces the large freshening peak in the northeast due to the EGC inshore water. At the time of the second peak in volume flux in October, salinities have decreased to around 34.49. This advects as much fresh water as the EGC inshore water in the northeast over the same time interval.

Water from the other North Atlantic sources also adds to the freshening peak in the fall. Its largest advection rates occur in the summer, opposite to the EGC inshore and offshore water in the southeast. Its salinity is similar to that of the offshore water and also results in advection of freshwater to the basin in this region during September and October. Again, this freshening is of the same magnitude as due to EGC offshore

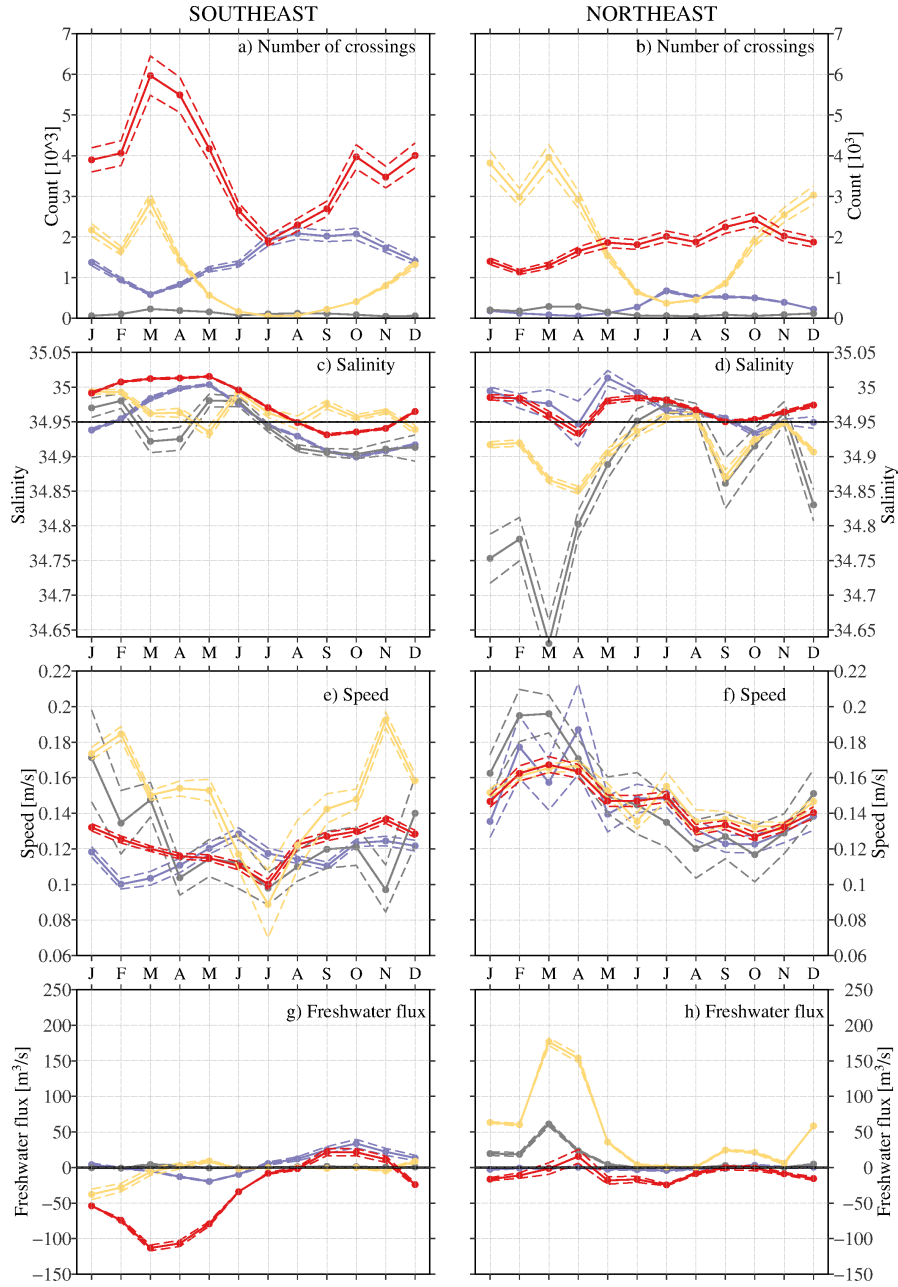


Figure 3.22: Seasonal cycle of the amount of particles crossing into the basin in the a) northeast and b) southeast, (see **Figure 3.6** for references on the location of the regions). c–d): Seasonal cycle of freshwater fluxes into the basin by the particles crossing in the c) northeast and d) southeast. e–f): Same as a–b) for the speed with which the particles cross. g–h) Same but for the freshwater fluxes. In all panels, the colors show the sources of the water: yellow shows the water originating in the EGC inshore section, red the water in the EGC offshore section, purple the water from other sources in the North Atlantic and black the water with unidentified source. The dashed lines show the associated errors, calculated using a Monte Carlo method.

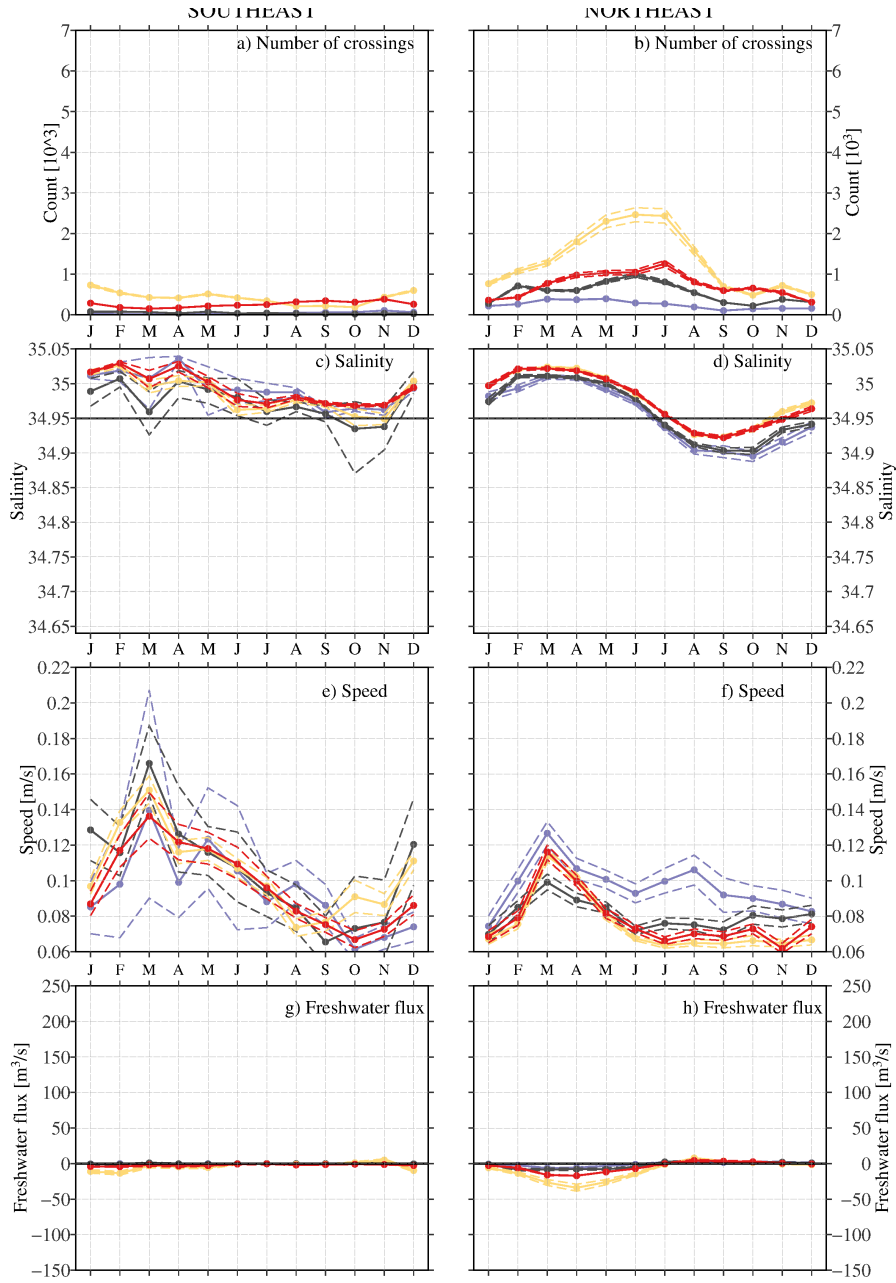


Figure 3.23: Same as **Figure 3.22** but for the northwest and southwest regions.

water in the same region and the pulse of freshwater entering the basin in the northeast due to the EGC inshore water. Together they cause the second, large pulse of freshwater seen in **Figure 3.21**.

An additional fraction of freshwater is advected by the water of unidentified source. Even though the amount that enters the basin is very small compared to the other sources, it is much fresher, especially in the northeast. In March particularly, this water enters the basin with salinities as low as 34.7 causing a large amount of freshwater

advection to the basin in the spring. For the remainder of the year, the salinities of this water are similar to the salinities of the EGC inshore water but, due to the low number of crossings in the fall, this water does not add to the second, fall pulse of freshwater in the basin.

The first, weaker freshening pulse in the basin is therefore the result of strong freshwater influx from EGC inshore water that is balanced by the advection of salty EGC offshore water. The stronger fall peak, on the other hand, is due to a combination of water from inshore, offshore and North Atlantic sources that enter the basin in the southeast (offshore and North Atlantic water) and in the northeast (EGC inshore water).

Water entering the basin along the western side of the basin does not play a role in the advection of water to the Labrador Sea basin (**Figure 3.23**). For all sources (EGC inshore, EGC offshore, North Atlantic and unidentified) the freshwater fluxes are smaller than 0.003 mSv, even though up to 2500 crossings of EGC inshore water are counted in the southwest. However, all of them are relatively salty. In fact, the salinities of all water entering the basin in the southwest are similar to each other.

In summary, freshwater enters the basin in two peak, in March – April and September – October (roughly the same timing as the observed freshening in the basin). The first, weaker pulse can be attributed to water with EGC inshore origin and enters the basin via the northeast. The large amount of freshwater entering the basin during this freshening pulse is partially balanced by salty water brought to the basin in the southeast, due to EGC offshore water. The second peak of freshwater is, overall, larger and due to freshwater fluxes both in the northeast and southeast. All three major water sources (EGC inshore, EGC offshore and other sources in the North Atlantic) contribute to this peak but only the EGC offshore and North Atlantic freshwater enter the basin in the southeast, while the fresher EGC inshore water enters the basin in the northeast.

3.6 Seasonality of potential forcings: Eddy and Ekman transport

Water is advected to the basin in high rates during restratification in the spring. The peak of crossings in March – April found here is consistent with the idea that water from the boundary currents is the main source of restratification. It is, however, not clear what mechanisms force and regulate the influx of water. Eddy fluxes are thought to play a leading role in the advection but other forcing mechanisms, such as winds, might also be important. Here I investigate this further for the advection along the eastern side of the basin, which is the dominant region for the exchange of water.

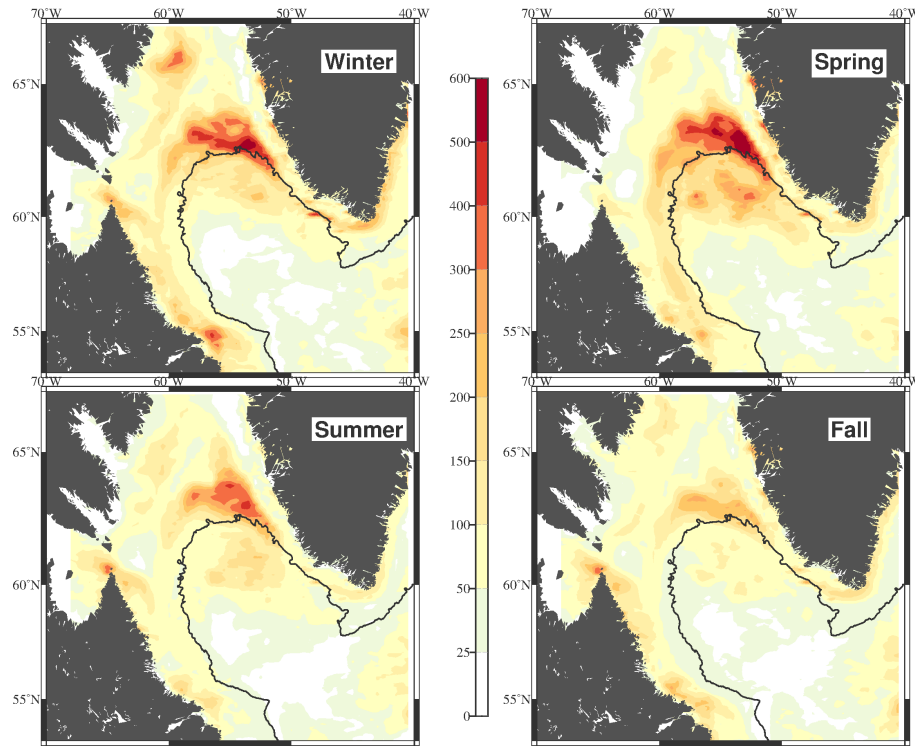


Figure 3.24: The three monthly mean of Eddy Kinetic Energy in the Labrador Sea, 1993 – 2009. Top left panel: Winter (Dec – Feb). Top right: Spring (Mar – May). Bottom left: Summer (Jun – Aug). Bottom right (Sep – Nov).

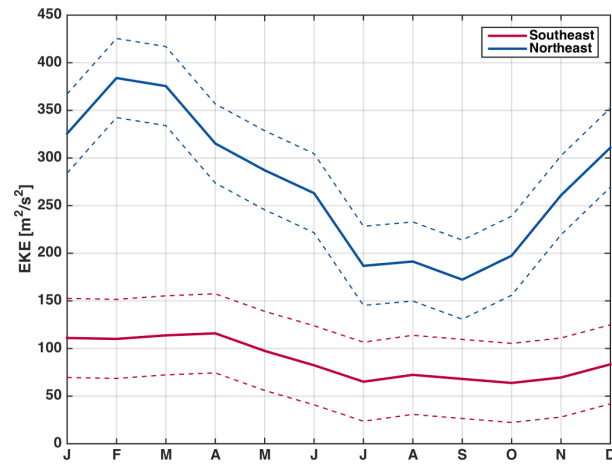


Figure 3.25: Seasonal cycle of EKE (1993 – 2009) in the southeast box (solid red line) with the associated standard deviation (broken line) and in the northeast box (solid blue line) with the associated standard deviation (broken line) See **Figure 3.6** for region definition.

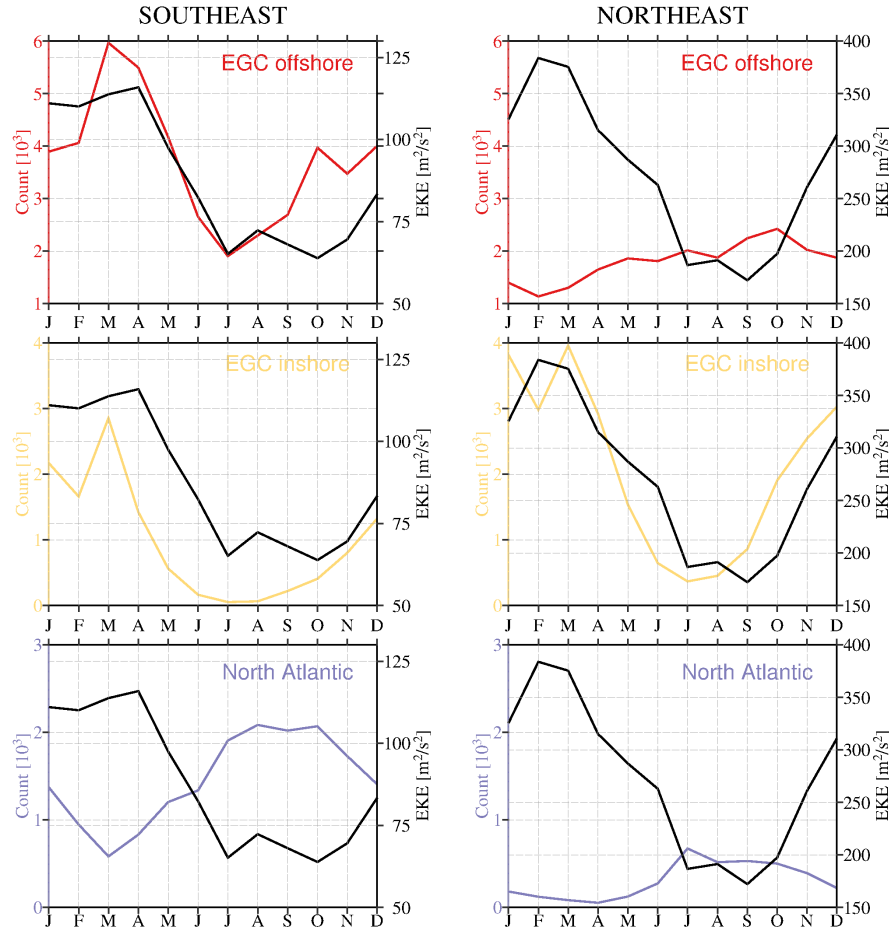


Figure 3.26: Number of crossings in the southeast (left column) and northeast (right column) of the different origins together with the EKE in the same regions. Top panels: EGC offshore water crossings into the basin in the southeast (left) and northeast (right). Middle panels: same for EGC inshore water. Bottom panels: same for water from other North Atlantic sources.

3.6.1 Eddies

In the northeast the EKE is highest in the Spring and weaker (by around $400 \text{ m}^2/\text{s}^2$) in the fall (**Figure 3.24**). In the spring, the high EKE extends into the northeastern corner of the basin, highlighting the region of high advection seen in **Figure 3.14**. In the southeast the seasonal variability is not as strong and the EKE is only slightly lower in the summer and fall. When calculating the seasonal cycles for the two regions it is almost non-existent in the south (**Figure 3.25**, see **Figure 3.6** for the exact locations over which the EKE is averaged for the northeast and southeast). The EKE in the summer and fall differ by only $50 \pm 80 \text{ m}^2/\text{s}^2$ and are thus not distinguishable from each other. In the northeast on the other hand, the seasonal cycle is strong and the EKE is $200 \pm 100 \text{ m}^2/\text{s}^2$ stronger in February – March than in September.

When comparing the seasonal cycle of EKE to the seasonal cycle of crossings (of the different water sources), the peak of EKE in the southeast coincides roughly with a large number of EGC inshore and offshore crossings (**Figure 3.26**, left column). In both cases however, the peak of crossings occurs one month before the peak of EKE. A second peak of advection of offshore water in October – November does not coincide with a second, weak peak of EKE in August. The decrease of the offshore water advection in the southeast from April to July on the other hand, matches the decrease in EKE over the same time period. The decrease of inshore water advection however, precedes the decrease in EKE by one month. The seasonality of advection of North Atlantic water is anticorrelated to the EKE’s seasonal cycle. Note that the errors for the seasonality of EKE are large and that these results should therefore be treated with caution.

In the northeast, where the seasonal cycle of EKE is strong with smaller errors, the highest rate of inshore water enters the basin roughly at the same time as the peak in EKE occurs (**Figure 3.26**, right column). This coincides with a minimum in offshore water advection, which instead peaks when the EKE is lowest. Both the maximum and minimum of EGC inshore water advection occur one month after/before the maximum/minimum of EKE respectively. Again, the water from other sources in the North Atlantic enters the basin out of phase with the EKE, hence peaks in the fall when the EKE is lowest.

3.6.2 Ekman transport

In order to understand the impact of eddies we first consider another potential forcing mechanism, wind, and the Ekman transport that results from it. Ekman transport as a mechanism in forcing advection from the boundary to the basin has not been discussed in the literature so far. Instead, authors usually focus on the role of winds in causing air-sea heat fluxes and in forcing convection. The strongest winds observed in the Labrador Sea are northwesterly winter winds. Wind speeds vary locally between 12.5 m/s in the southeast by Cape Farewell and 10 m/s in the northwest corner of the Labrador Sea (**Figure 3.27**). Winds are weakest in the summer months. To estimate the amount of Ekman transport into the basin, I project the wind onto the four sections along the boundary (southeast, northeast, northwest and southwest section, as defined in **Figure 3.6**). The monthly Ekman transport across these sections is calculated using:

$$V_{ek} = \frac{\tau^x}{f\rho} \quad (3.7)$$

$$U_{ek} = \frac{\tau^y}{f\rho} \quad (3.8)$$

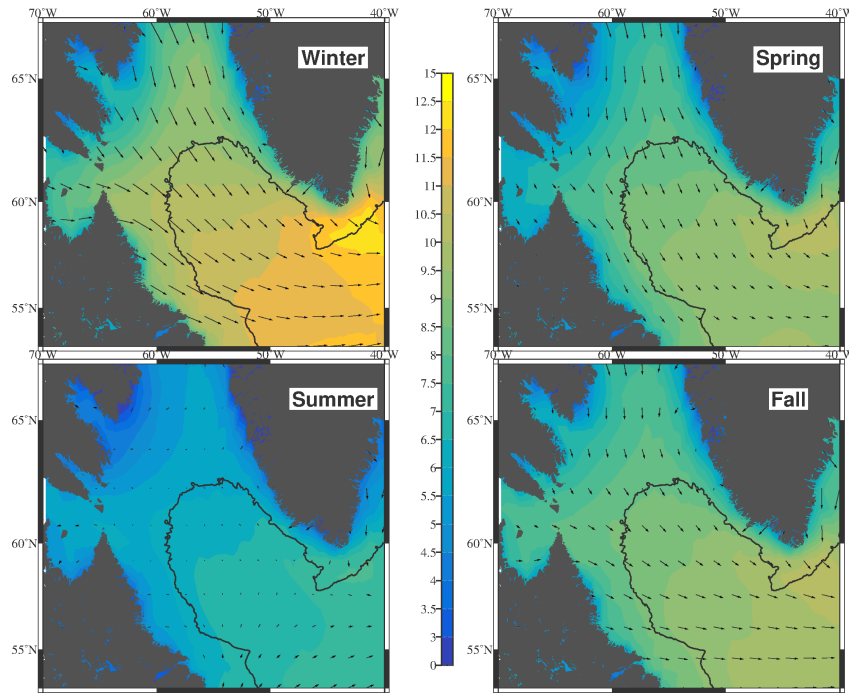


Figure 3.27: Wind speed (color: m/s) and wind direction (arrows) in the Labrador Sea using the ERA-interim product. Top left panel: Winter (Dec – Feb). Top right panel: Spring (Mar – May). Bottom left: Summer (Jun–Aug) and bottom right: Fall (Sep – Nov).

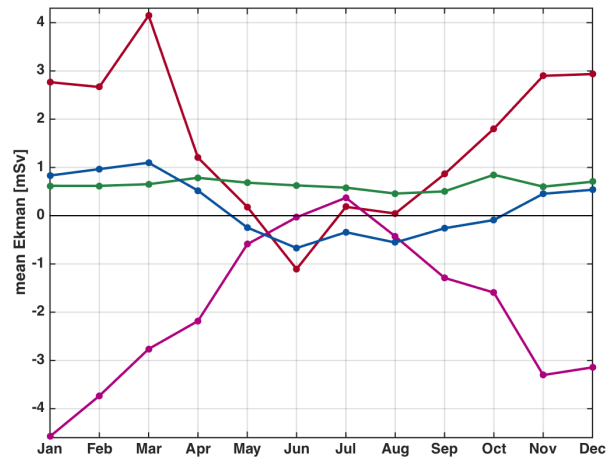


Figure 3.28: Ekman transport [mSv] across the four sections defined in **Figure 3.6**. Red curve shows the total Ekman transport across the southeast section, blue the transport across the northeast section, green across the northwest section and pink across the southwest section. Positive values indicate transport into the basin, and negative values transport out of the basin.

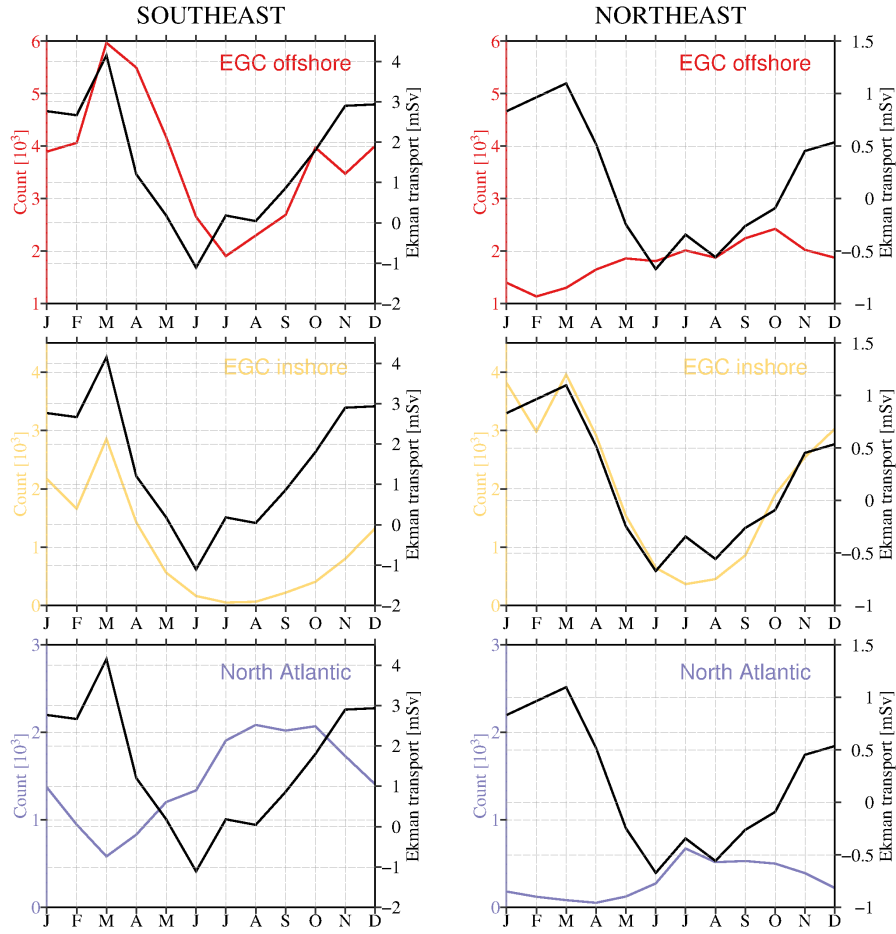


Figure 3.29: Number of crossings in the southeast (left column) and northeast (right column) of the different origins together with the Ekman transport in the same regions. Top panels: EGC offshore water crossings into the basin in the southeast (left) and northeast (right). Middle panels: same for EGC inshore water. Bottom panels: same for water from other North Atlantic sources.

where τ is the wind stress, f the Coriolis force, and ρ the air density at sea level. U_{ek} and V_{ek} are the along and cross section Ekman transport, hence we are here interested in V_{ek} as the ‘across’ section transport.

In the winter, winds are generally strongest in the southeast. At the same time they are oriented almost parallel to the 2500 m isobath resulting in the highest amount of Ekman transport here (**Figure 3.28**). In this part of the Labrador Sea, Ekman transport pushes water into the basin for all but one month (June). A similar seasonal cycle is found for Ekman transport across the northeastern sections, of about half the magnitude. Additionally, Ekman transport is negative throughout the summer and most of the fall. Water is only transported into the basin in November – April. Other than in the east, the northwest has no significant seasonal cycle and Ekman transport remains low but positive throughout the year. In the southwest, the seasonal cycle of Ekman

transport is opposite to that of the east, with transport out of the basin for all months but one (July). Again, I concentrate on the transport along the east side of the basin, where the majority of the exchange and freshwater fluxes take place.

In the southeast, the peak of EGC offshore and inshore advection coincides with the peak of Ekman transport in March (**Figure 3.29**). In fact, the number of crossings in January – March of both water sources closely mirror changes in transport of water due to Ekman transport. However, the decrease of Ekman transport in the beginning of the summer, precedes the decrease of inshore and offshore water advection by one month. Also, the increase of advection in the fall does not correlate well with the increase in Ekman transport seen here. No correlation is found between the crossings of water from other North Atlantic sources and Ekman transport.

The seasonal cycle of Ekman transport in the northeast is very similar to the one in the southeast. Here the EGC inshore water advection correlates closely to the Ekman transport, especially in the spring and fall. The offshore water on the other hand does not show any correlation with the Ekman transport. Water from the North Atlantic is, again, not well correlated overall. However, in the summer, when the Ekman transport out of the basin decreases in July, the advection of this water source increases rapidly, maybe indicating some relationship to the transport due to wind.

3.6.3 The role of Eddies versus Ekman transport

In the northeast, the EGC inshore water enters the basin at its highest rate when the EGC offshore water crossings are at its lowest. This raises the question, what allows the inshore water to leave the shelf, cross the boundary current and enter into the basin while the EGC offshore water advection is reduced? I compute trajectory density maps for those trajectories that entered the basin during the months of high EKE and Ekman transport (February – March) and for months of low EKE and Ekman transport (July – August), (**Figure 3.30**).

During the months of February – March, inshore water enters the basin mainly in the northeast spreading into northeastern basin. Only a small percentage reaches the western side of the basin. At the same time, offshore water enters in the southeast and remains in the southeastern part of the basin. Only <2% of trajectories pass through the north or west. During the months of July – August the picture changes and the inshore water now stays much closer to the 2500 m isobath, travelling further along it while crossing through the northeast and western side of the basin. There is only minimal spreading of this water into the basin. The offshore water on the other hand spreads further north than before. Hence, it seems that high advection of offshore water in the southeast allows the inshore water to spread further away from the coast and closer to the basin, resulting in more advection of this water in the northeast. When offshore water advection is higher in the northeast, the inshore water is ‘blocked’ from entering

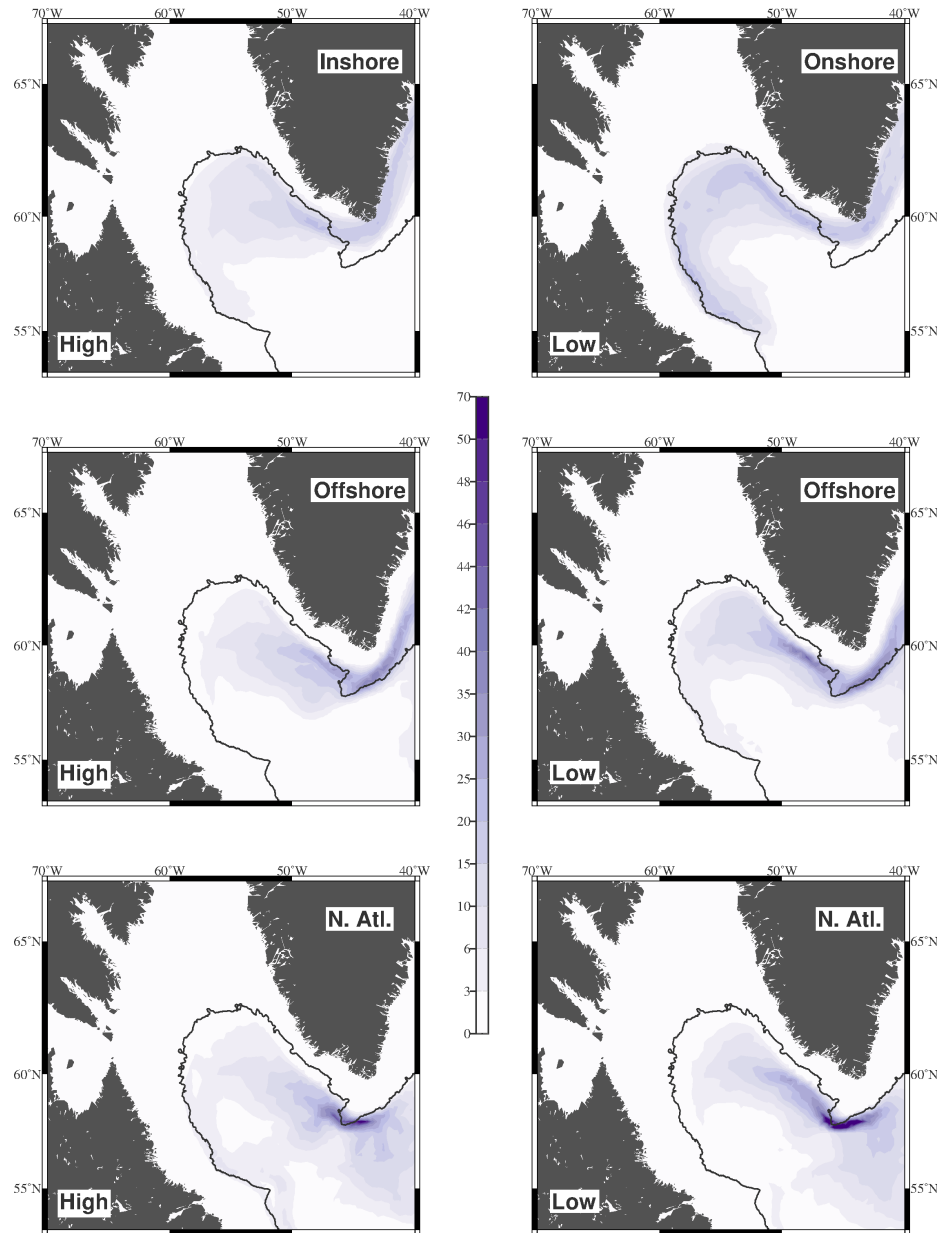


Figure 3.30: Percentage of trajectories from each source that pass through each 0.5° longitude \times 0.3° latitude grid point. The black contour shows the 2500 m isobath. Left column: Trajectories during months of high EKE and Ekman transport (Feb – Mar). Right column: trajectories during months of low EKE and Ekman transport (Jul – Aug). Top row: for water with EGC inshore origin. Middle row: for EGC offshore water. Bottom row: for water with other origins in the North Atlantic.

the basin. It is, unfortunately, not clear which mechanism, EKE or Ekman transport, plays a more important role in setting this pattern of advection. Analysing interannual variability will be necessary to further assess this.

The other North Atlantic water crosses predominantly when the crossing activity of the offshore water is low in the southeast. This could be explained by considering the stability of the boundary current and hence the EKE in this region; when the boundary current is calm and laminar (during low EKE), the water of the North Atlantic is able to merge with the boundary current at Cape Farewell. More North Atlantic water is available in the boundary currents and hence more crossings into the basin are observed.

3.7 Interannual Variability of crossings

The number of crossings and the amount of freshwater brought to the basin, as well as the pathways of freshwater, vary on interannual timescales (**Figure 3.31**). In 11 out of the 20 years, more freshwater entered the basin in the northeast than in the southeast (e.g., 1993, 1995, and 2009), hence following the average pathways seen above. During the other 9 years, freshwater entered either only in the southeast (e.g., 1996 and 2006) or both in the southeast and northeast (e.g., 1998 and 2004). There are also years when, on average, no freshwater was brought to the region (e.g., 2001 and 2002). Furthermore, some years (especially 2005 and 2006) have a surprisingly large amount of water entering in the southwest. This sometimes results in a freshwater flux (e.g., 2006) and for other years in salty water entering the basin (e.g., 2005 and 2000). The large decrease in salinity after 2009 can be seen here in the advected surface water, especially in 2011. However, the salinity decrease is not further discussed in this thesis and as for the seasonal cycle, I will only consider the years 1993 – 2009.

Between 1993 and 2009 the number of particles entering the basin varied between 6450 ± 1650 and 12500 ± 3000 , with an average of 9800 ± 2450 (where the uncertainties were calculated using a Monte Carlo error calculation), (**Figure 3.32**). Salinities of the advected water were relatively constant around 34.96 with the exception of 1995 when water advected to the basin had an average of 34.9. During this year, freshwater entered the basin along the entire eastern boundary, with the strongest fluxes in the northeast (up to 0.1 mSv at individual sections). Crossing speeds of the waters decreased from 0.13 m/s in the early 1990's to 0.1 m/s in 2009. Overall, the flux of freshwater to the basin varies greatly from year to year; some years, such as 2002 – 2003, lose as much as 0.1 ± 0.02 mSv of freshwater, while in 1995, 0.3 ± 0.1 mSv of freshwater were added to the basin. Only during 7 individual years did advection from the boundary currents freshen the basin. However, note that this freshwater flux is calculated with respect to the reference salinity of 34.95 and should be considered as relative freshwater fluxes instead of absolute freshening. So to rephrase, relatively fresh water was advected to the basin in the early 1990's. In the late 1990's and early 2000's the advected water

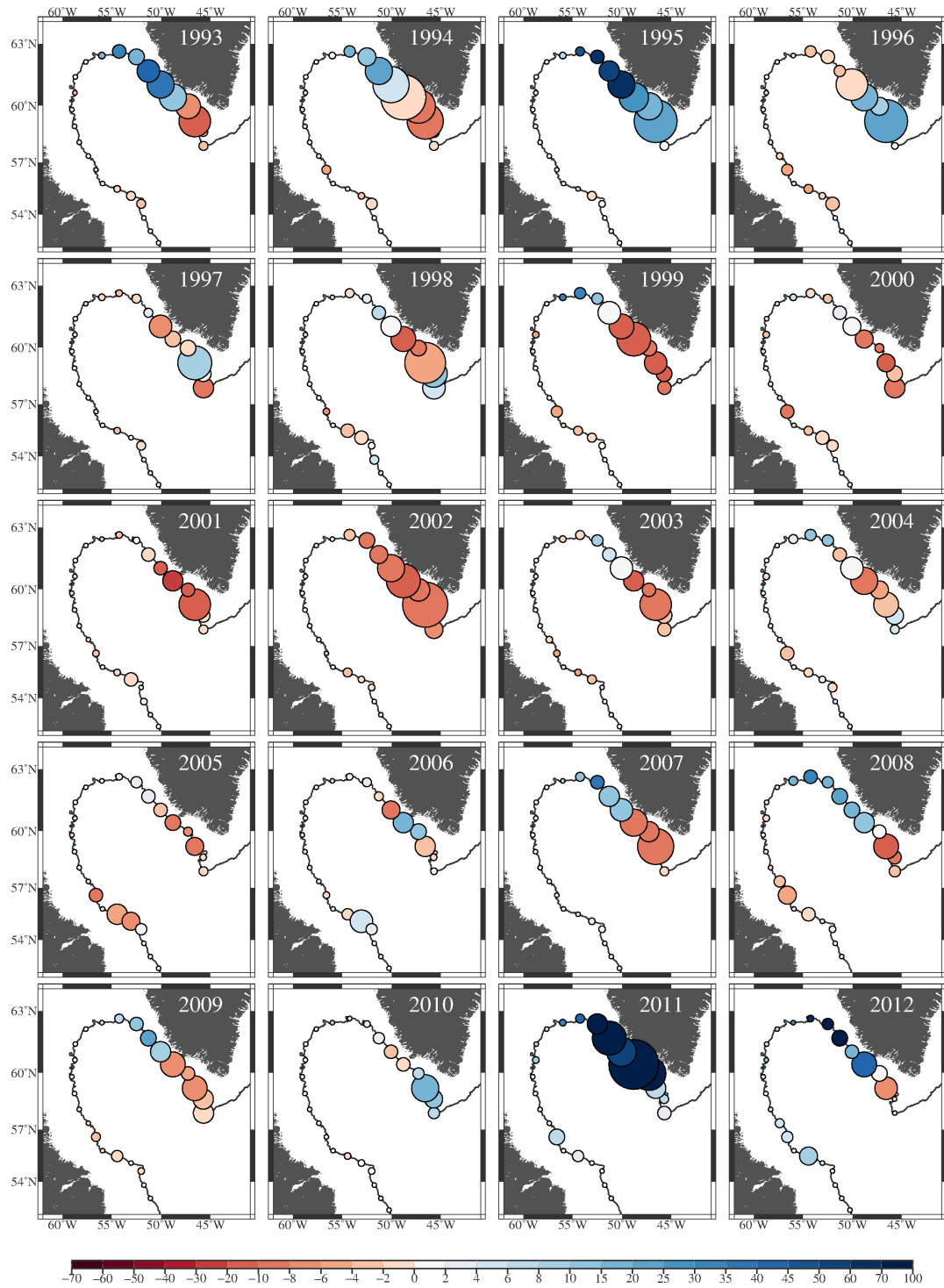


Figure 3.31: The relative number of crossings per 50 km boundary section is indicated by the size of the red circles for 1993 – 2012. The color indicates the amount of freshwater brought into the region at each section [m^3/s]

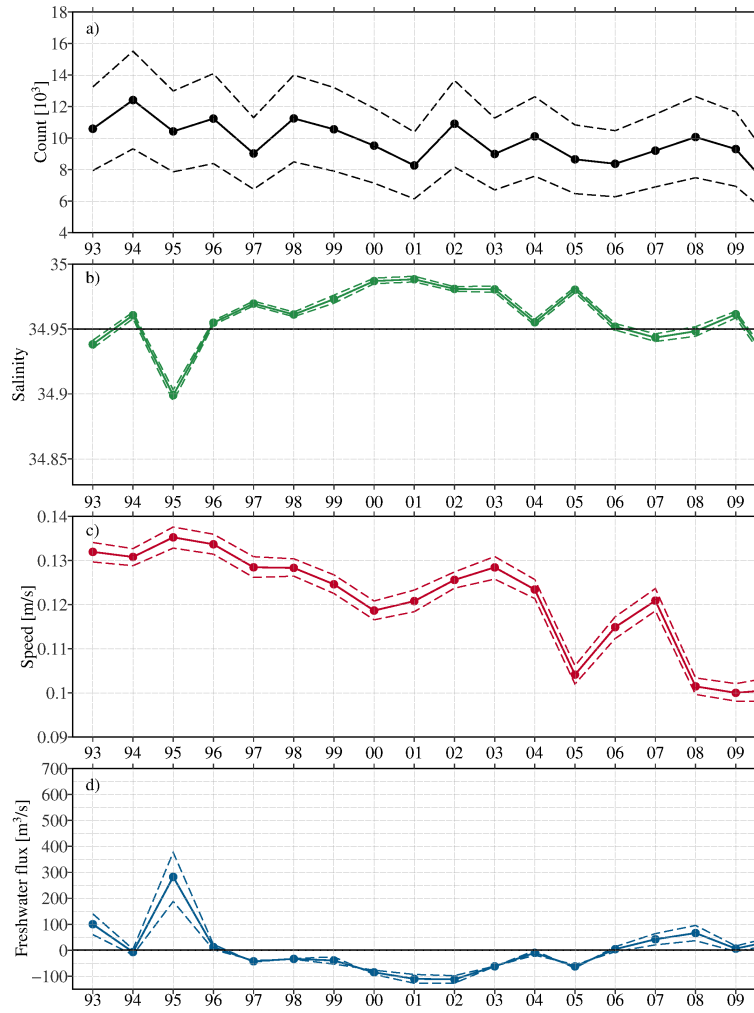


Figure 3.32: Top: Total number of crossings into the basin per year. Second panel: Average salinity of crossing water. Third Panel: Average speed of the crossing. Bottom: Yearly freshwater flux into the basin. Positive values show freshwater advection to the basin, negative values show advection of salty water. Errors are calculated using a Monte Carlo error calculation.

was comparably salty but became fresh again towards the end of the record. Since the number of crossings at the end of the record is comparable to the number in the early 1990's and speeds decreased, the increase in freshwater flux must be due to a decrease in salinities. In fact, the variability of the freshwater fluxes closely mirrors the variability of the salinity (**Figure 3.32**).

The year to year variability of advection is smallest for water from the EGC offshore source. Between 3500 ± 530 and 5700 ± 700 particles of this water, with a mean of 4380 ± 640 , entered the basin between 1993 and 2009 (**Figure 3.33**). The EGC inshore source has larger variability and crossings range between 1725 ± 280 and 5250 ± 760 with a mean of 3350 ± 500 . Only during one year (2008) is there significantly more EGC

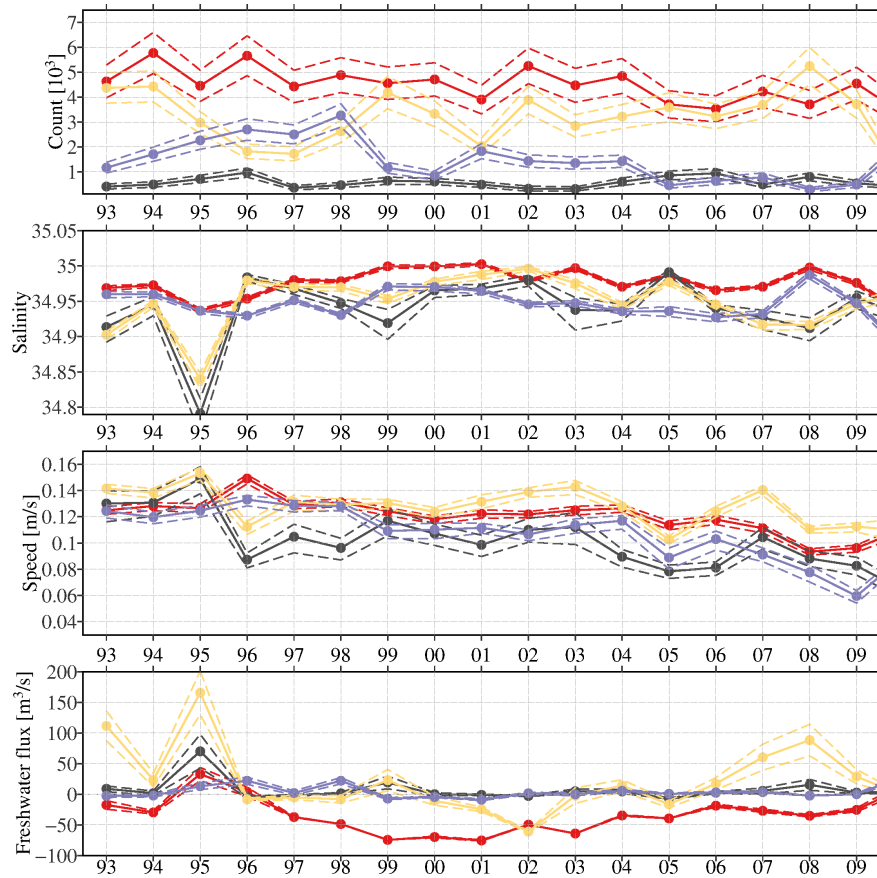


Figure 3.33: Top: Number of crossings into the basin per year. Second panel: Average salinity of crossing water. Third Panel: Average speed of the crossing. Bottom: Yearly freshwater flux into the basin. Positive values show freshwater advection to the basin, negative values show advection of salty water. Red curves shows water with EGC offshore origin, yellow water with EGC inshore origin, purple water with origins elsewhere in the North Atlantic and blue water from Baffin Bay.

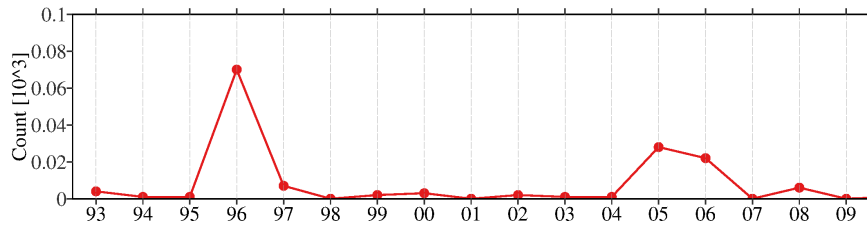


Figure 3.34: Year-to-year variability of the number of crossings with Baffin Bay origin.

inshore water than offshore water entering the basin. The North Atlantic is consistently the least dominant source of water to enter the basin. Three years, 1996 – 1998, are an exception, with North Atlantic water advection exceeding the amount of EGC inshore water that enters the basin. Interestingly, the EGC inshore flux to the basin is lowest during the early 1990's when the freshest water was advected to the basin. In the later 2000's, during the second period of freshwater, the inshore water advection is conversely

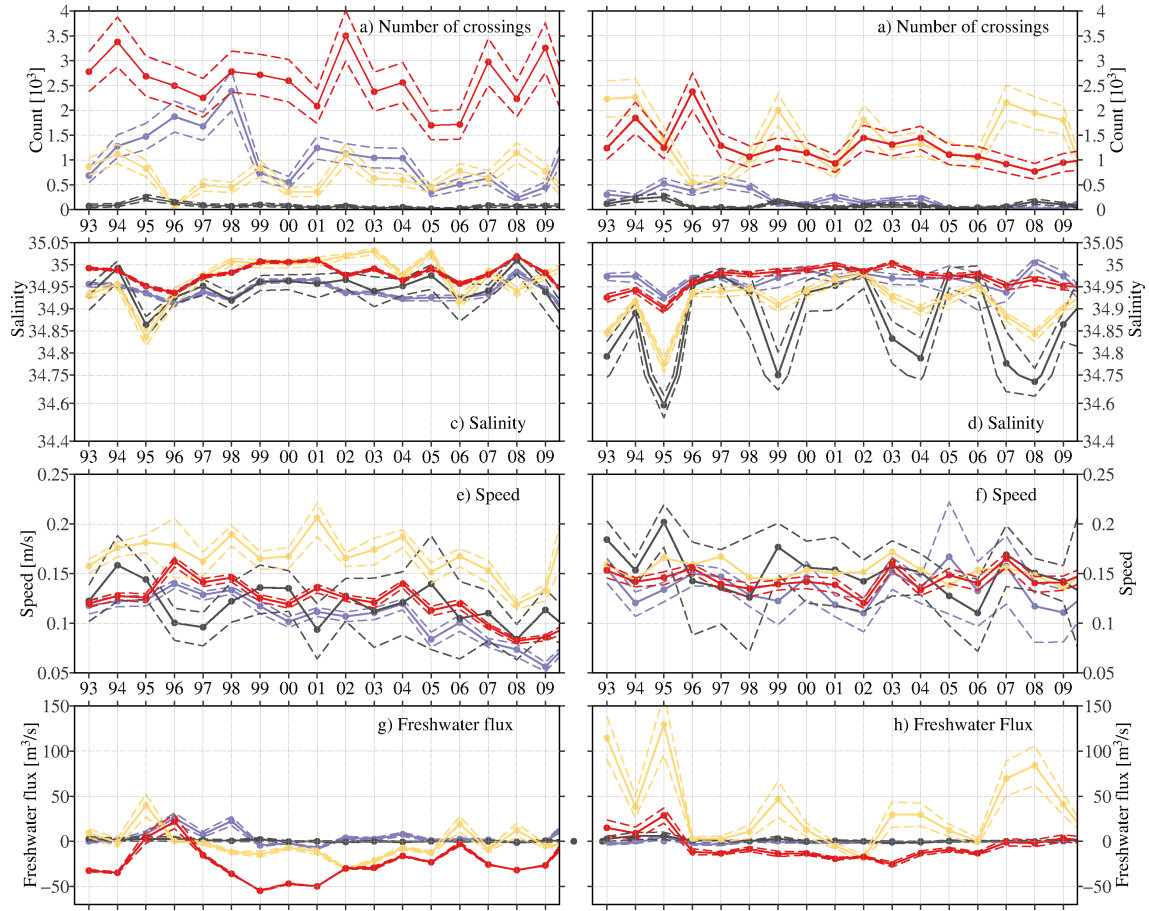


Figure 3.35: The number of crossings in the a) northeast and b) southeast. The salinities of the advected particles in a) the northeast and b) the southeast. The speed of the crossing particles in e) the northeast and f) the southeast and the associated freshwater fluxes entering the basin in g) the northeast and h) the southeast. The colors refer to the water's origin: yellow shows the EGC inshore water, red the EGC offshore water and purple the water from other sources in the North Atlantic. Black shows the water of unidentified sources. The dotted lines show the errors estimated using a Monte Carlo approach.

at its highest. The amount of water entering the basin from the North Atlantic on the other hand, decreases over the length of the 17 years and remains low (below 1000 crossings) for the last 5 years.

The peak of freshwater influx into the basin in the early 1990's is seen only in the EGC inshore water and the water with unidentified source. Both carried especially fresh water in 1993 – 1995 and added a total of 0.3 ± 0.1 mSv of freshwater. After this period, in 1996 – 1998, the water from other sources in the North Atlantic is the only source through which freshwater reaches the basin. There is very little freshwater entering the basin between then and 2006. In fact, between 1996 – 2006 the advection of the EGC inshore, EGC offshore and North Atlantic water results in a flux of salty water to the basin that adds up to -0.48 ± 0.18 mSv. Only the North Atlantic water advects a

small amount of freshwater (0.04 ± 0.009 mSv) to the basin over this time period. The offshore water continuously adds salty water to the basin, with the exception of 1995. In 2007, the EGC inshore water freshens again and a larger amount of this fresher water is advected to the basin. This results in another freshening period during which 0.2 ± 0.07 mSv of freshwater are added to the basin.

Even though the EGC inshore and offshore water and the water from the North Atlantic are the dominant sources of advection to the basin, it is worth noting the interannual variability of the Baffin Bay sourced water (**Figure 3.34**). In 13 out of the 17 years a small amount of Baffin Bay water entered the basin. However, only in 1996, 2005 and 2006 did more than 10 trajectories cross into the basin. In 1996, 70 trajectories with origins in Baffin Bay were found in the basin, and in 2005 and 2006, 28 and 22 trajectories were found respectively. Surprisingly, this water was not as fresh as perhaps suspected due to its origin and entered the basin mainly with salinities exceeding 34.95 (the reference salinity), (not shown).

As before for the seasonality, I investigate the contributions of each water source in advecting water across the eastern side of the basin. In the southeast, the EGC offshore water is the dominant source of advection over the 17 year time period (**Figure 3.35**, left column). In the second half of the record, more than twice as much offshore water than inshore or North Atlantic water reaches the basin. In the first 6 years however, the water from other sources in the North Atlantic plays a large role but its advection decreases rapidly after 1999 and remains below 1500 until 2009. EGC inshore water never exceeds 1300 crossings per year in the southeast, but no trend is found for this and the offshore water. The salinities of the advected water has little variation and is similar to the salinity seen in **Figure 3.33**. Again, the salinity of the water with unidentified sources resembles the EGC inshore water, but only during the first 5 years. After this it starts mirroring the North Atlantic and EGC offshore water salinities. The drop in salinity in 1995 is seen in the southeast but only in the EGC inshore water and the water from unidentified sources. The freshening of these waters results in freshwater fluxes of 0.04 ± 0.02 in 1995. In the following year, both the EGC offshore and North Atlantic water advect freshwater into the basin in the southeast. The second large freshwater pulse in 2007–2009 is not seen in the southwest and was advected solely via the northeast. It is also noteworthy that the inshore water entered the basin with the highest velocities, and that there was a decrease in the speed of the entering water in all three sources over the 17 years.

In the northeast, both the EGC inshore and offshore water are the dominant water sources entering the basin (**Figure 3.35**, right column). With the exception of a few years, both advect about the same amount of water into the basin. The advection rate does not show any trends here. The input of North Atlantic water advection on the other hand, decreased in 1999 and remained low until 2009. The salinity of the advected water has little variation for the offshore and North Atlantic water but shows a oscillation-like

variability for the EGC inshore water and the water with unidentified sources. Every four years the salinity of this water decreases rapidly from an average of 34.93 to about 34.75. The freshening peaks do not correspond to peaks in the number of crossings but result in distinct freshening pulses. The largest of them are in 1993 and 1995 with fluxes of up to 0.16 ± 0.04 mSv. The second largest is seen in the late 2000's with freshening of up to 0.09 ± 0.04 mSv. These are the two periods of freshening also observed in **Figure 3.32**. The two other freshening pulses in 1999 and 2003-2004 did not lead to an overall advection of freshwater due to a simultaneous advection of salty water in the southeast. The offshore water entering the basin in the northeast adds salt to the region continuously throughout the 17 years, with the exception of the early 1990's.

To recap, between 1993 and 2009 the amount of water entering the basin (measured by the number of crossings) has remained relatively constant overall, with a slight decrease of North Atlantic water advection. Two periods, the early 1990's and the later 2000's, were characterized by large amounts of freshwater advection due to very fresh EGC inshore water entering the basin in the northeast. The period 1999 to 2003 also had fresh inshore water advected to the basin, but salty water in the southeast countered this and overall no freshening was observed for these periods. The freshening periods do not coincide with peaks in the number of crossings and are merely due to the abnormally fresh inshore water.

3.8 Interannual forcing

Convection in the Labrador Sea is closely linked to the NAO, or, more precisely, to the changes in storms and the resulting air-sea fluxes due to them (see **Introduction**). Furthermore, Straneo (2006) found that advection from the boundary currents is the main source of restratification after the convection season. The relationship between the NAO index and the convection is not simply linear but, in general, a high NAO index should result in more intense mixing and stronger restratification and hence import a larger amount of water from the boundary after the winter. The number of crossings (hence the amount of advection) and the mean yearly NAO index are in fact weakly correlated ($R=0.66$ with 95% significance), (**Figure 3.36**). There are, however, years when the NAO and number of crossings agreed much better than during others, e.g., in 1993 – 1995, 2004 – 2007 and 2010 – 2012. The weak relationship highlights that advection depends not only on the strength of convection but also on other factors. It is likely that a closer relationship can be found when instead investigating the relationship of the advection to local forcing mechanisms such as EKE and Ekman transport.

For a spatial view of the different conditions during high and low crossing years maps of the mean EKE and Ekman transport are calculated (**Figure 3.37**). In particular, maps of EKE and Ekman transport for months that had crossing numbers higher/lower

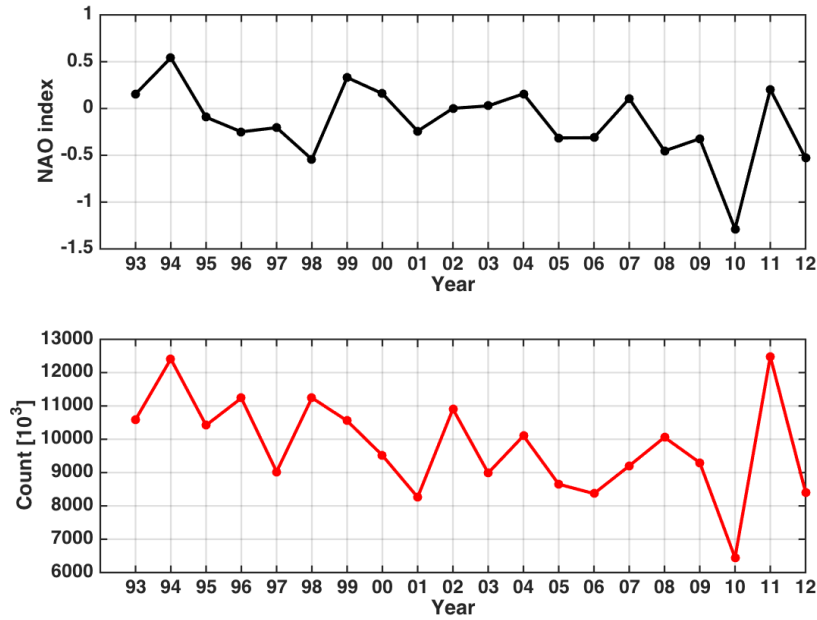


Figure 3.36: Top: yearly NAO index. Bottom: the yearly number of crossings into the basin

a two standard deviation envelope. During months with strong advection the EKE in the region of large variability in the northeast was on average $100 \text{ m}^2/\text{s}^2$ lower than during months with low advection. However, a larger region of increased EKE is found inside the northeastern part of the 2500 m isobath when advection is high. The higher EKE here reaches slightly further to the east with a tongue extending to the southeast corner of the basin. At the same time the Ekman transport into the basin is much stronger. In particular, winds cause strong Ekman transport along the entire eastern side of the basin. During times of low advection on the other hand, Ekman transport into the basin is only strong across the northern boundary. Along the east the winds cause very weak import of water, and the direction of the transport changes towards the southeast. Here, Ekman transport pushes water out of the basin, hence it is opposite to the Ekman transport during months with high advection. In other words, when advection to the basin is high, the EKE in the northeast is weaker and the Ekman transport across the eastern side of the basin is much stronger compared to times with low advection.

How important is Ekman transport to the advection? While the analysis of the seasonal cycle could not entirely answer this question, the interannual variability of the crossings, EKE and Ekman might allow us to draw further conclusions. To compare anomalous variability, timeseries of three-monthly EKE, Ekman transport and number of crossings in the southeast and northeast are constructed. For each, the mean seasonal cycle for 1993 – 2009 is removed and the resulting anomalies in EKE and Ekman

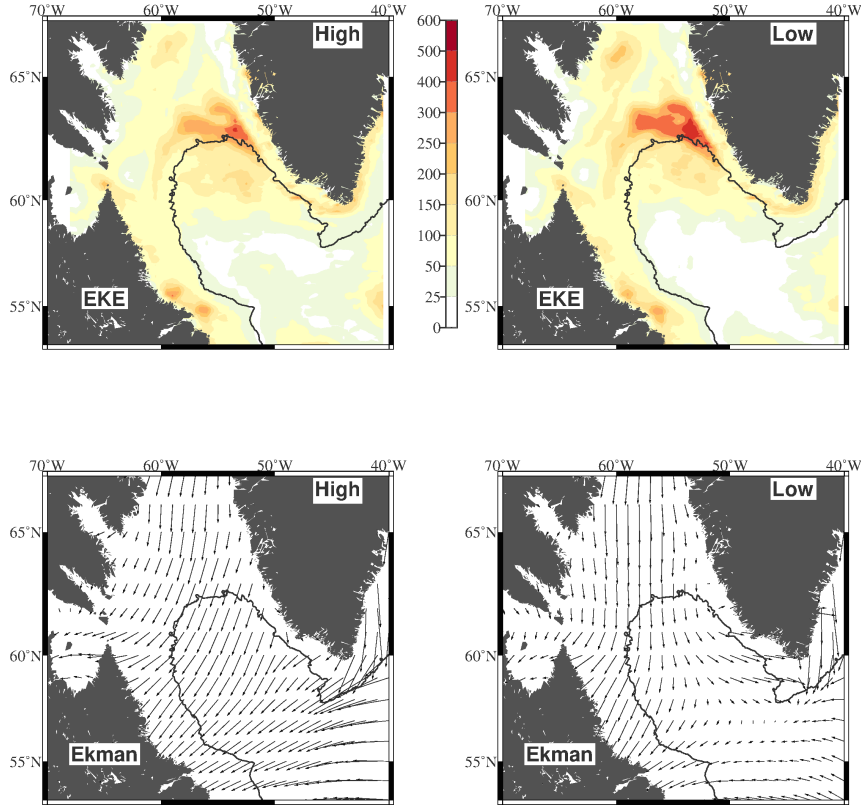


Figure 3.37: Top row: The EKE [m^2/s^2] for months which had an exceptionally high amount of crossings (left) and months that had exceptionally low numbers of crossings (right). Bottom row: Ekman transport for the same months.

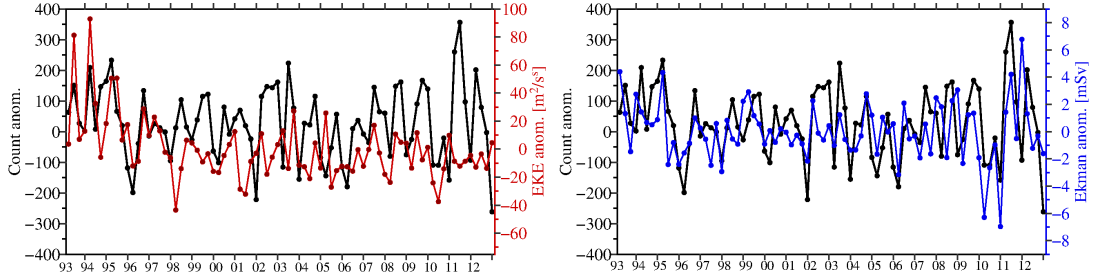


Figure 3.38: Left: Crossing anomaly in the southeast (three monthly number of crossings with the seasonal cycle removed, black) and the EKE anomaly (red). Right: The same crossing anomaly as on the left figure (in black) but with the Ekman transport anomaly (blue).

transport are compared to anomalies of the number of crossings (**Figure 3.38**).

In general, the crossing anomalies in the southeast are not significantly correlated with the EKE anomalies, but have a low (but significant at 99 %) correlation with the Ekman transport anomalies (correlation coefficient of 0.44), (**Figure ??** and **Figure 3.41**). However, when looking at only the first 5 years, the correlation between the number of crossings and EKE becomes significant and the correlation coefficient increases

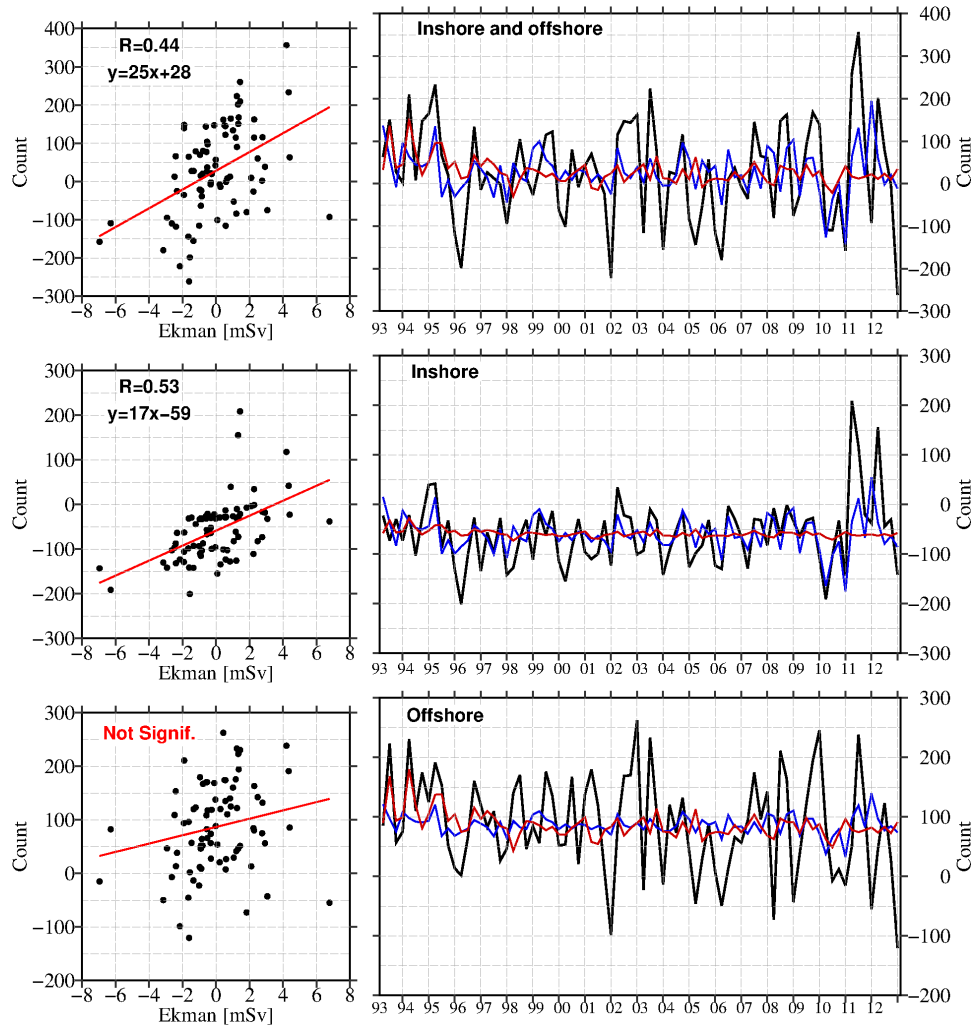


Figure 3.39: Left side: Three-monthly number of crossing anomaly in the southeast and the Ekman transport anomaly in the same region (dots) and the linear fit (red line). Right column: The number of crossings (black line) and the reconstructed number of crossings from Ekman transport (blue) and from EKE (red). The top row shows the crossings of EGC inshore and offshore water, the middle row the crossings of EGC inshore water only and the bottom row the crossings of EGC offshore water. When R values are given, the correlation is significant at 99%

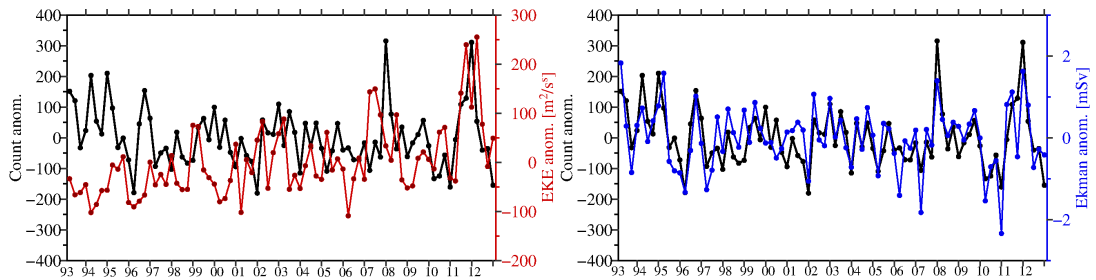


Figure 3.40: Same as **Figure 3.38** but for the northeast

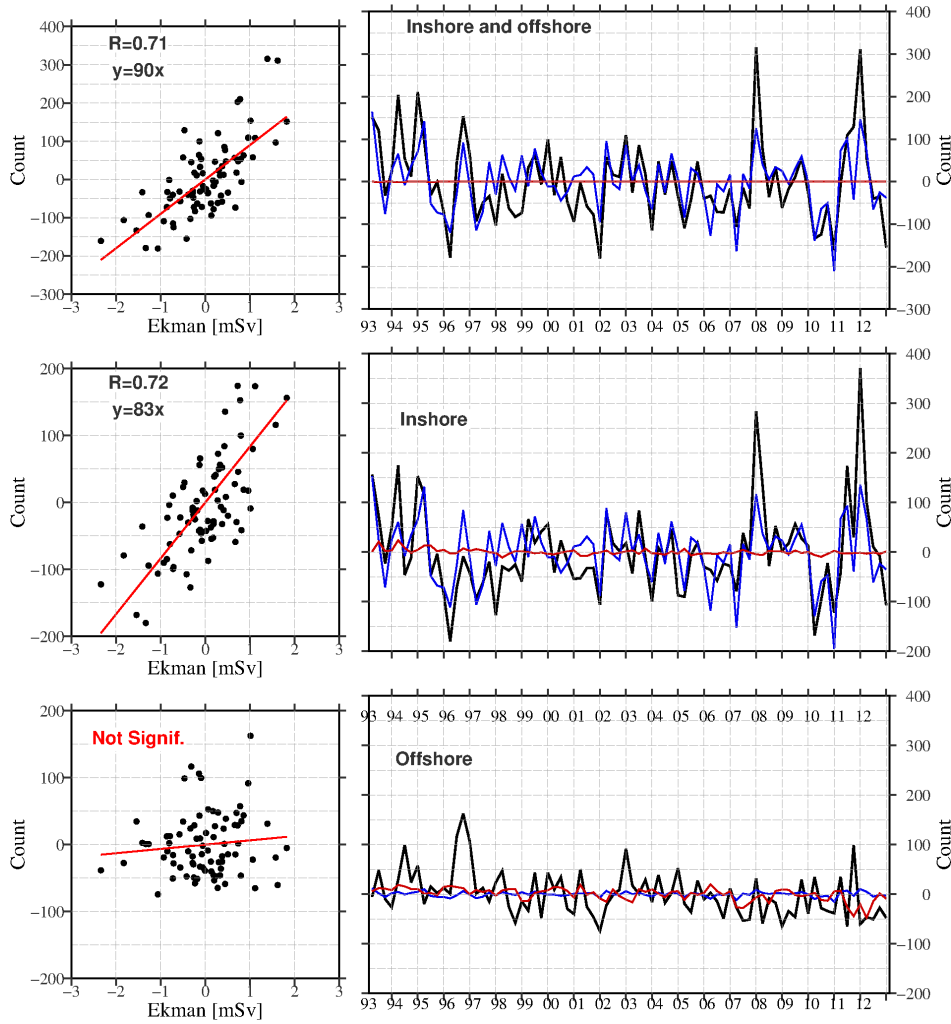


Figure 3.41: Same as **Figure 3.39** but for the northeast

to $R = 0.65$ (from here on, significance refers to a 95 % significance level calculated). For the rest of the time period the correlation remains low. When correlating the Ekman transport and EKE to the crossings of EGC inshore and offshore water separately instead of the combined crossings, the relationships change. Neither the advection of the inshore water nor the offshore water is correlated to the EKE. Additionally, the offshore water advection shows no correlation to the Ekman transport. Only the inshore water is significantly correlated to the transport due to wind ($R=0.53$), (**Figure 3.39**). This indicates that, in the southeast, processes other than eddies and Ekman are important in advecting water to the basin, especially for the offshore water.

When looking at the northeast, there is, again, no significant correlation between the number of crossings and the EKE (**Figure 3.40**). Instead, the variability of Ekman transport explains most of the variability in advection here (**Figure 3.41** top row). When considering the two EGC water masses separately, we see that Ekman transport

is only significantly impacting the advection of water the inshore water but not the offshore water. The correlation to the inshore water advection is robust with a coefficient of 0.72. In fact, about 80% of the variability in EGC inshore advection can be explained by the Ekman transport alone. For the advection of offshore water the EKE plays a slightly larger role than the Ekman transport, but neither are significantly correlated to the advection.

3.9 Summary and Discussion

In this Chapter the ocean model NEMO and the Lagrangian particle tracking tool ARIANE were used to assess the major pathways of freshwater into the basin and to understand the role of eddies and Ekman transport in the advection of water from the boundary to the basin.

Each year, 75% of the advection in the top 30 m takes place along the eastern side of the basin, with more water entering across the southeastern boundary compared to the northeastern boundary. This is consistent with previous studies showing that eddies, shed from the WGC, bring water to the basin along the eastern side, especially after convection. A spatial distribution map made by Lilly et al. (2003) shows the highest frequency of eddies to be in the northeast corner of the basin, extending diagonally across to the southwestern corner and along the eastern side of the basin (their Figure 36). The idea that eddies might form in the region of high EKE but travel with the boundary currents and enter the basin further west (Hatun et al., 2007) is not supported by the spatial pattern of advection found by Lilly et al. (2003) and here in this Chapter. Furthermore, a larger amount of water enters the basin outside the region of the highest EKE, in the southeast. This indicates that other mechanisms also play a role in advecting water into the basin.

The highest rate of advection is found in the spring after convection ceases but fluxes into the basin continue throughout the entire year at a lower rate. This is consistent with the findings in Straneo (2006) and **Chapter 2**, that show that lateral fluxes occur at the highest rates in the first months following convection but persist throughout the year and hence, ensure a continuous exchange between the boundary and basin.

Seasonally, freshwater is advected to the basin in pulses, a first pulse in the spring and a second in the fall. This was also observed by Schmidt and Send (2007), Straneo (2006) and in **Chapter 2**. Schmidt and Send (2007) found a first smaller pulse in April to May and a second larger pulse in July to September. Here, I do not compare the magnitude of freshening to their study for two reasons; the different method applied in their study and the saltier model ocean. In particular, in Schmidt and Send (2007) a month-to-month change in freshwater of the top 150 m is calculated by using the previous months as a reference salinity. In this chapter on the other hand, freshwater fluxes are calculated for the top 30 m only, using a constant reference salinity. However, the results

are consistent in the timing of the freshening pulses and in their relative magnitude, with the second pulse about three times stronger than the first pulse. When analysing the origin of the freshening pulses, Schmidt and Send (2007) could not conclude on the source of the first freshening pulse. Based on particles in the NEMO model, freshwater originating in the inshore region of the boundary current is responsible for the first (March – April) freshening pulse in the Labrador Sea. At the same time, large amounts of salty offshore water enters the basin in the southeast. In fact, the first pulse of freshwater is much stronger than the second pulse, but is counteracted by the advection of salty offshore water and thus results in a weaker freshening of the basin overall.

The second pulse of freshwater was attributed to the West Greenland Current by Schmidt and Send (2007). This is confirmed here but, more specifically, the freshening is due to a combination of weak advection of fresh inshore water in the northeast and stronger advection of offshore water entering in the southeast. The offshore water is not as fresh but due to its higher advection rates results in a overall freshening of the same magnitude as the freshening due to the inshore water. Additionally, water from other sources in the North Atlantic also adds to the freshening of the basin via the same pathway. Hence, the first freshening pulse is due to the fresh inshore water and the high quantity of this water that reaches the basin. This is counteracted by the large amount of high salinity offshore water entering the basin at the same time in the south. The freshening in the fall is, overall, stronger because all three sources, EGC inshore, offshore and the North Atlantic water, advect roughly the same amount of freshwater to the basin. However, while the EGC inshore water still enters the basin in the northeast, the offshore and North Atlantic water is advected in the southeast. Advection along the western side of the basin does not significantly contribute to the overall fluxes to the basin.

The water of unidentified origin also plays a role in freshening the basin. While the amount of this water entering the basin is small, its salinities are very low, 0.2 psu fresher than the water originating in the inshore part of the EGC. Most of its final positions in ARIANE are located in the WGC, close to Cape Farewell (**Figure 3.42**). A large portion is also located very close to the coast, suggesting that they might have their origins in the Greenland coastal regions. Interestingly, due to their very low salinities, they contribute 30% of the spring freshening. This implies two things; firstly that the fresh coastal water can have a significant impact on the freshwater budget of the Labrador Sea and secondly, that a decrease in salinities can have larger impacts on the basin than an increase in volume flux of water with constant salinities. For example, 1000 particles entering the basin with salinities of 34.94 and a speed of 0.14 m/s would result in a freshwater flux of 0.036 mSv. Twice as much freshwater (0.072 mSv) would be added to the basin if all 1000 particles had a salinity of 34.93, hence a 0.01 psu reduction. However, twice as many (2000) particles with higher salinities of 34.94 would have to enter the basin to accomplish the same 0.072 mSv of freshening. The difference in salinities between the offshore water and coastal water can be up to 0.5.

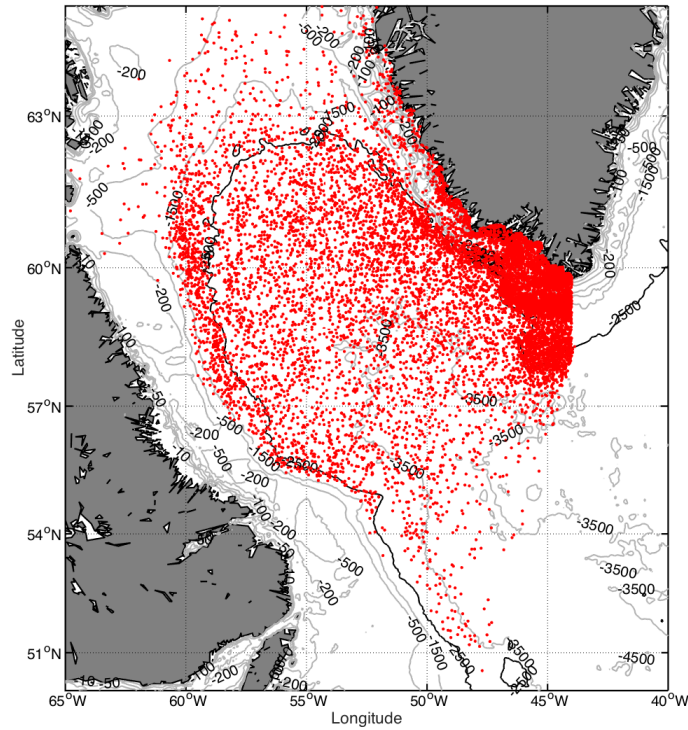


Figure 3.42: The last reported location of the trajectories that could not be identified to be from one of the water sources

This shows that freshwater from the Arctic and from Greenland plays a key role in the freshwater input to the Labrador Sea basin and in modulating convection. In fact, there seems to be a direct connection from the fresh coastal water to the region of deep convection. An increase of freshwater content in these coastal regions, due to e.g., increase in runoff from Greenland, could therefore have a direct impact on the overturning circulation. As mentioned in **Chapter 2**, runoff from Greenland has already increased significantly over the last 20 years (Bamber et al., 2012). While freshening of the Canadian Archipelago and Baffin Bay, does not directly impact the basin, the above analysis shows that an increased runoff from Greenland has that potential. With a rising climate, these rates of freshwater input to the coastal ocean are likely to keep rising and impact the Labrador Sea by increasing its freshwater content. With that it will either dampen convection due to increased stratification or change the properties of the LSW. Both will, in turn, weaken the MOC.

Two time periods between 1993 – 2009 stand out with a large increase in freshwater, 1993–1995 and 2007–2008. During the first time period, the EGC offshore and North

Atlantic water import a small amount of freshwater to the basin whilst the main freshening is a result of the large import due to the inshore water. No increase in advection of the inshore water was found and we can conclude that a decrease of the near-shore water must have been the cause of the overall freshening. Also, 1995 is the only year during which the EGC offshore water resulted in a positive instead of a negative freshwater flux due to a weak freshening.

A decrease in salinities in the Labrador Sea region was also found by Häkkinen (2002) for the late 1990's. However, the observations were focused on the southwest corner of the Labrador Sea instead of the WGC or EGC. The author finds the largest salinity changes in the coastal waters and, at the same time, a lack of the high salinity North Atlantic water. A model, forced with NCEP/NCAR Reanalysis data, showed that the freshening was associated with current anomalies that transported a larger number of icebergs south. The freshening observed in NEMO occurred at about the same time but was not as long lasting. Because we see the freshening in the EGC and WGC it is likely that it was caused by other or additional processes than the freshening observed by Häkkinen (2002), for example a shorter but intense southward transport of fresh Arctic water via the EGC or increased runoff from Greenland. The freshwater input to the basin due to water from sources in the North Atlantic in 1996 – 1998 could, on the other hand, be due to the reduced presence of North Atlantic Current water seen by Häkkinen (2002). At the same time as the freshening, a weakening of the subpolar gyre was observed, that was due to weak buoyancy forcing and a decaying density gradient between the interior and boundary of the gyre (Häkkinen and Rhines, 2004). Such a weakening of the density gradient could lead to decreased lateral fluxes to the basin, as seen for the advection of WGC inshore water. However, as the number of offshore water particles entering the basin remained constant, it is not clear from the data presented here that such reduced rates of lateral fluxes took place overall. Additionally, the velocities of the crossing water remain relatively constant for the 1990's with the exception of a decrease in EGC inshore advection speed in 1995.

In 1997 and 2003, several studies found an abrupt interior warming, hence an increase in density gradient between the boundary and basin (Avsic et al., 2006; Lazier, 2002) and enhanced EKE (Brandt et al., 2004). This coincided with a larger number of Irminger rings with warmer and saltier cores, documented by Lilly et al. (2003) and Brandt et al. (2004). The increase in lateral fluxes in these years (Lilly et al., 2003; Rykova et al., 2014), is not seen here in the NEMO and ARIANE data (neither is the increase in EKE for these years). This might be due to the EKE strength and location in the model that does not completely agree with observations. Furthermore, an increased density gradient between the boundary and basin might be present in the model, but mesoscale turbulences associated with eddies are only solved in the model if the resolution is sufficient. The increase in lateral fluxes might have been due to an increase of eddy fluxes of sub-gridscale size eddies that were not resolved in the model.

The second freshening period found in 2007–2008 coincides with the observed decrease in salinities described in **Chapter 2**. Here we see that the freshening was due to a decrease of the EGC inshore salinities that occurred at the same time as an increase of advection of this water. Hence, other than the 1993 – 1995 freshening, the fresh inshore water, fed by Arctic outflow and runoff from Greenland is solely responsible for the latter freshening of the basin. This suggests that a freshening in the basin can occur even when the offshore, core boundary current does not freshen significantly, as long as the salinities of the inshore, shelf waters decrease sufficiently. Hence, salinity anomalies in the Labrador Sea, such as the Great Salinity anomaly, could manifest themselves more clearly in the shelf waters. Furthermore, increased runoff and ice melt along the coast of Greenland has the potential to directly impact the dynamics of the Labrador Sea, by entering the basin from the inshore region of the EGC and WGC via the northeast of the basin. A hosing scenario, hence a drastic increase in freshwater, capping the region of convection and preventing deep convection, is therefore not an unlikely scenario. However, the mechanisms that drive the advection of this inshore water have to be further assessed.

It is important to remember that the results presented above are entirely from model output. While NEMO represents the large scale circulation and overall heat and freshwater transport well, there are still issues with smaller scale processes and the representation of e.g. vertical mixing and eddies. This is an issue especially in the Labrador Sea, where such processes dominate the dynamics. By changing the bottom topography and adding partial slip-conditions to the regions some of the issues were partly fixed. However, the question remains what else might be poorly represented and how a higher resolution model with better eddy representation and vertical mixing might change the results seen here. Another problem is the salinity drift that is especially pronounced in the Labrador Sea (??). Such salinity drift can lead to water mass properties and LSW formation with unrealistic characteristics. Surprisingly such salinity drifts are also present when running models for North Atlantic configurations only and when adding sea ice to the model (?). It is thought that the excess salt has its source in the North Atlantic Current and the eastern part of the sub-polar gyre (?). For example, increasing salinities of the Irminger Water resulted in strong drifts in the Labrador Sea (?).

Such limitations have to be kept in mind when using model data. However, in this study only relative transport was calculated and not a total freshwater flux to the basin which would be bias because of the saltier model water. Since the drift is reversed by the same amount of freshwater flux each year, the pathways of freshwater and the flux seasonality will still be valid. When looking at interannual variability, only variability larger than the 33.3 mm/day should be taken into account. The large increase in freshwater flux to the basin in 2011 exceeds that value. Additionally, a similar freshening has also been seen in observational data in the EGC (not shown). Again, to avoid problems with model drift and model uncertainties, the analysis concentrates on relative values, hence times when crossing activity is anomalously high/low compared to the overall mean.

Furthermore, the relationship of the crossing to the winds would not be influenced by salinity drift. However, eddies are most likely under-represented in this model and it is not possible to say with any certainty what the relative role of winds is compared to eddies. For this higher resolution altimetry or model output that better represents the eddies is needed. The issues in modeling the convection becomes important when calculating the total flux of freshwater and heat to the basin (hence the restratification) and comparing it to observations. An overestimation of the convection would lead to more restratification and convection in the wrong part of the basin would lead to fluxes from a totally different region (see Appendix A). It is therefore crucial to test the presented freshwater pathways in the ocean and to assure that convection is well represented in the model.

The role of eddies in restratifying the basin has been discussed in many previous studies. However, it has so far not been possible to completely explain the heat and freshwater increase in the basin after convection by only eddy fluxes, hence Irminger Rings and boundary current eddies. Here I considered winds as a possible second mechanism in forcing advection. The correlation between the number of particles entering the basin from the boundary and the Ekman transport is remarkably high, especially in the northeast of the Labrador Sea but only for the advection of the water originating in the inshore EGC. It is possible that the heat and freshwater that enters the basin seasonally has been underestimated by observations because Ekman transport has not been taken into account in the past. However, here we see that the Ekman transport in fact does play a very important role for the advection of the fresh inshore water, the water that subsequently will have the largest impact on the freshwater budget of the Labrador Sea.

This leads me to the following hypothesis: In general, water is transported from the shelf to the basin by Ekman transport. Just west of Cape Farwell is the region with the largest amount of water entering the basin. The advection of the offshore water into the basin is not correlated to the Ekman transport such that other processes, not discussed in this thesis, are more dominant in advecting the offshore water. With the offshore water being closest to the basin, this water dominated the advection here whilst effectively blocking the inshore water from crossing into the basin. The inshore water is pushed off the shelf to the basin by Ekman transport. Moving along the boundary towards the northeast, more and more offshore water enters the basin, still dominated by processes other than Ekman transport and the inshore water is able to spread further away from the coast and closer towards the basin until Ekman transport becomes the dominant mechanism, advecting the fresh inshore water into the basin directly (resulting in a high correlation). Hence the Ekman transport directly impacts the advection of the fresh inshore water that subsequently has the largest impact on the freshwater budget of the Labrador Sea.

Of course, the results presented above were found in a model and need to be confirmed with either higher resolution/better parameterisation or observations. Observations particularly will play an important role because no direct observations of Ekman transport in relation to advection have been made in the past. The higher model EKE outside the 2500 m isobath and the lower EKE inside the northeastern basin are also a concern. A more realistic EKE could mean that more advection would be due to eddies, hence increasing the importance of eddies compared to Ekman transport. Furthermore, observations should also confirm that Baffin Bay and Hudson Strait do not play a role in the advection of water to the basin. If this is not supported by observations, this could drastically change our presented view of the freshwater pathways to the basin. However, the fact that EKE is low along the western side of the basin, and Ekman transport is low or negative here (out of the basin), means that large fluxes into the basin are unlikely. Furthermore, a study using drifters has shown that about 1/3 of the West Greenland Current drifters, but none of the Labrador Current drifters entered the Labrador Sea basin (Cuny and Rhines, 2002) and it is widely believed that the WGC must be the source of the freshwater fluxes to the Labrador Sea.

Lastly, the large freshwater increase in 2011 was not investigated in this thesis. However, it is interesting to note that it was due not only to a large decrease in the inshore water but also to a very large number of inshore water crossings in 2011 (not shown). Hence, both a change in salinity and a change in lateral fluxes seem to have played a role in this freshening.

3.10 Conclusions

Two important results emerge from this study. Firstly, for the first time, we see not only the two freshening pulses occurring in an average year, but also their origin. The inshore water is the main source of the freshwater in the basin, seasonally as well as interannually. This means that changes in the Arctic freshwater budget and increased runoff will impact the Labrador Sea and the convection directly. In light of the changing climate this could mean a significant reduction in the formation of LSW and a potential slowdown of the MOC. Additionally, we have seen that a temporary change in the location or strength in North Atlantic Circulation, impacting the import of salt to the region, can also result in a change of the freshwater budget of the basin (like in 1993-1995). Not only could a decrease in the salinity mean an increase of freshwater to the basin but may seasonally result in larger freshwater pulses. This would leave the basin highly stratified at the beginning of the convection period, potentially weakening convection.

Secondly, at least in the model environment, Ekman transport plays a major role in the advection of water to the basin, while the connection to eddies is less apparent. This result requires further testing, especially with field observations, but would explain

why, so far, none of the existing studies that consider only eddies could explain all of the observed heat and freshwater fluxes to the basin.

Chapter 4

The impact of atmospheric forcing during active convection

4.1 Introduction

Historically it has been thought that the production of LSW is, to first order, dictated by the strength of the North Atlantic Oscillation (NAO). A high NAO index reflects a strengthening of the westerly winds, with a greater number of low pressure systems and a shift of storm tracks to a more northeasterly orientation (Dickson et al., 1996). These conditions would favor convection in the Labrador Sea; more cold air from continental Canada would be drawn over the warmer surface waters of the Labrador Sea and subsequently cause increased air-sea buoyancy fluxes. However, as detailed in **Chapter 1**, it is important to note that the relationship between NAO and convection is not simply linear as there are other factors at play. For example, the strength of the air-sea fluxes in the Labrador Sea varies with the changing location of the northern center of the NAO (Moore et al., 2013), as well as the detailed spatial distribution of the pack-ice (Moore et al., 2014). Oceanic preconditioning also complicates the relationship between the NAO index and the Labrador Sea convection. If there are multiple years of weak overturning, a buoyancy cap can develop over the surface of the sea, making it harder for atmospheric forcing to remove this barrier and initiate convection, even under strong cooling (for example, during the ‘Great Salinity Anomaly’, see **Introduction** for details). Conversely, successive winters of rigorous convection will result in a weakly stratified water column that is favorable for convection, even under mild forcing. This was the case during the winter of 1997/96 where convection reached 1500 m despite moderate surface forcing (Pickart et al., 2002).

Despite its importance, many aspects of LSW formation remain only partially understood, including the exact relationship between the hydrographic characteristics of the convected water column, the atmospheric forcing and the preconditioning of the basin. This is partly because of the inherent difficulties in obtaining direct measurements of this process, but also because the overturning is spatially and temporally very variable. In some years, little to no deep convection occurs, while in other years mixed layers can exceed 2000 m (Rhines and Lazier, 1995). Furthermore, the impact of increasing storm magnitudes and frequency under changing climate on the formation of deep water is not entirely answered. While it is clear that stronger storms can increase the air-sea fluxes and hence the resulting convection, it is not clear how a shift in storm tracks might impact the latter.

This chapter will investigate the relationship between atmospheric forcing and the structure of the mixed-layers during wintertime convection in the Labrador Sea. This includes small scale variability that is often observed during the convection process, but seldom described. I use shipboard data from the Labrador Sea Deep Convection Experiment (Marshall et al., 1998) that took place during the winter of 1996/97. This winter was characterized by a moderate value of the NAO index and can be seen as a transition year, although the month of February 1997 had the second largest heat loss of all Februaries over the previous 20 years (Pickart et al., 2002).

I begin with a description of the atmospheric forcing during that winter, including the character of the storms and the resulting buoyancy fluxes. This is followed by a description of the bulk mixed-layer properties and their relationship to the forcing. Finally, I characterize the small scale structure of the mixed layers and investigate links between them and the basin-scale hydrography, as well as air-sea fluxes.

4.2 Data and Methods

4.2.1 CTD Data

The primary oceanographic data used in this study were collected during a hydrographic cruise in the Labrador Sea from 2 February – 20 March 1997. The environmental conditions during the cruise, as described by Pickart et al. (2002), were favorable for overturning, with frequent storms resulting in strong winds and cold air temperatures. The mean wind speed during the 6-week period was 12 m/s out of the west-northwest with mean air temperatures of -8°C . During the cruise, multiple transects comprised of 127 conductivity-temperature-depth (CTD) stations were occupied (**Figure 4.1**, the middle section in the western part of the basin was occupied twice, separated by 10 days). A detailed description of the instrument performance, sensor calibration and accuracies, and data processing procedures are found in Zimmermann et al. (2000). During the course of the cruise, three different CTDs were used. One of them was designated exclusively for towed sampling whose data are not included in this study. Here we use data from a NBIS Mark III CTD 9 and ICTD. A comparison cast of the two instruments showed very similar structure in the water column (**Figure 4.2**). Overall the temperature and salinity accuracy was determined to be 0.001°C and 0.0025, respectively. Downcast profiles were produced for each station with 2-db averaged bins.

In this Chapter I am also interested in the small-scale hydrographic structure and temperature-salinity (T-S) intrusions within the mixed-layers. Therefore, all spikes in the CTD profiles have been removed. A spike was defined as a jump in temperature/salinity that returned to its original value (within the accuracy of the sensor) at the following depth-bin. Such spikes were removed from the mixed layers, replaced by interpolated estimates, and the density values re-calculated. In total, 1024 spikes in temperature and 659 spikes in salinity were removed following this procedure. This is equivalent to 4.7% / 3% of temperature/salinity points of the mixed layers. No geographical region or depth range contained more or fewer spikes, which is consistent with the notion that they were the result of instrument noise.

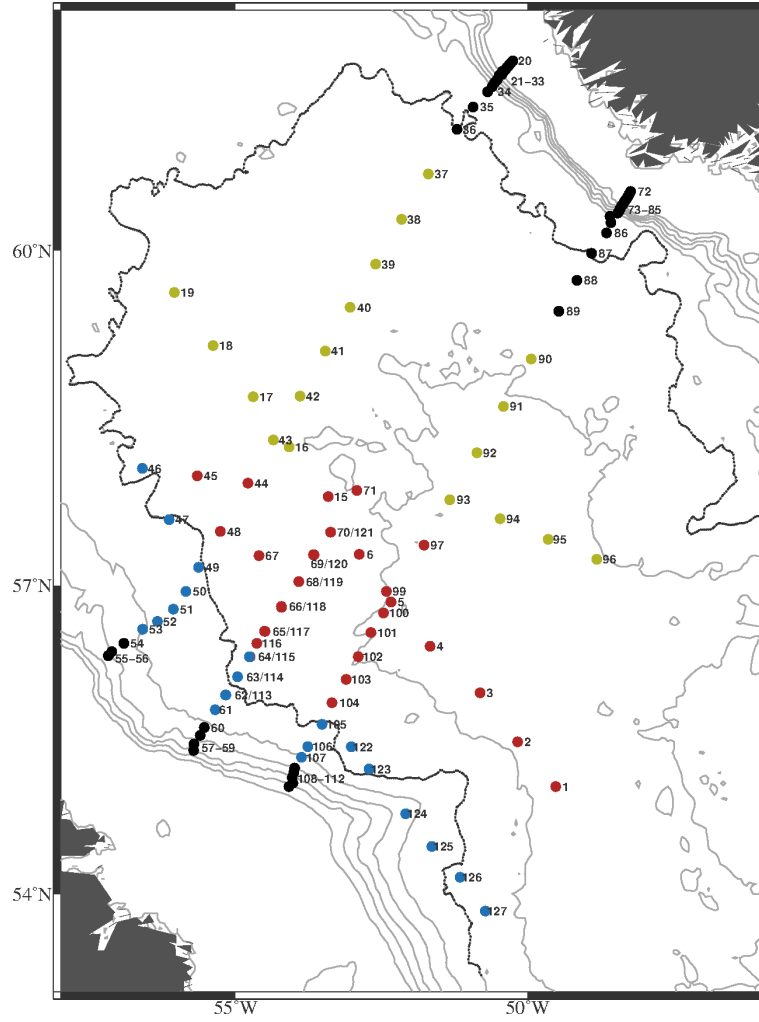


Figure 4.1: The location of CTD stations. The colored dots show the location of the stations in the boundary (blue), western basin (red) and eastern basin (yellow). Black stations are not included in the study due to being in water shallower than 500 m or having mixed layers shallower than 100 m. Numbers are the station number allocated during the cruise. Note that the middle section in the west was occupied twice and some stations therefore have two station numbers. Grey contours show the isobaths with 500 m spacing. The black contour is the 3000 m isobath.

4.2.2 Identification of Mixed Layers

For each profile, the depth of the mixed layer is identified following the method described by Pickart et al. (2002) (see their Figure 11). In summary, the mixed layer depth was first estimated visually, and the standard deviation in density was computed over this depth range. The depth at which the profile permanently passed out of the two-standard deviation envelope was then taken as the mixed layer depth (**Figure 4.3**). In all but a few cases this technique returned unambiguous results. For the remaining profiles the procedure was applied to the individual traces of temperature and salinity, which

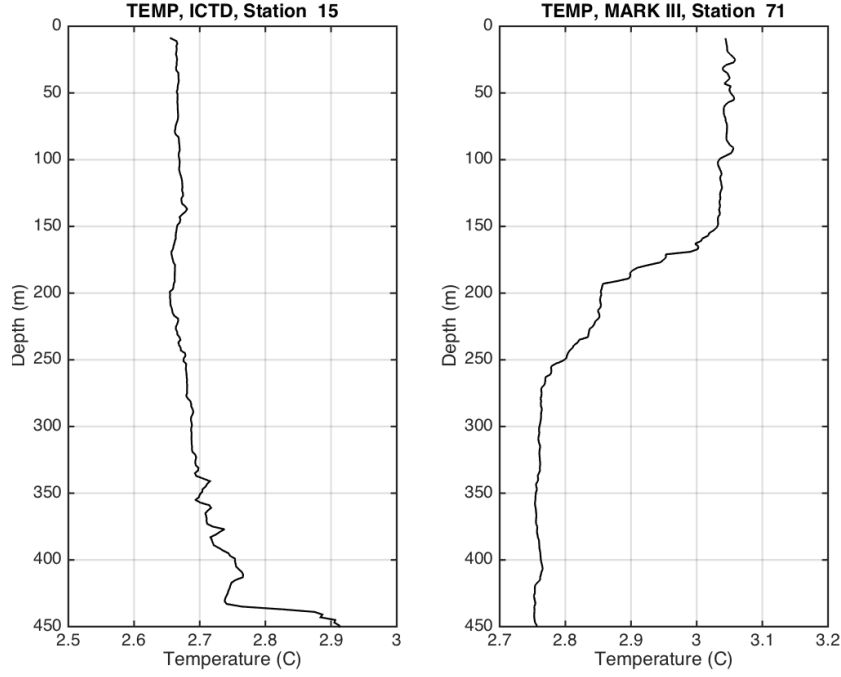


Figure 4.2: Two profiles measured by (left) the ICTD and (right) the Mark III CTD 9. Please refer to **(Figure 4.1)** for the location of Station 15 (left) and Station 71 (right).

cleared up any uncertainty. In this study only mixed layers exceeding 100 m from CTD stations occupied in water depths deeper than 500 m are considered (see colored stations in **Figure 4.1**). Of the 127 stations, 75 fulfilled these criteria. Notably, all of the mixed layers were stably (though weakly) stratified. As discussed in Pickart et al. (2002), some profiles showed multiple mixed layers, which means that in total 103 separate mixed layers are considered. (This study does not investigate whether these stacked mixed layers arose due to separate mixing events, small-scale lateral variability, or slantwise convection).

4.2.3 Intrusions

To isolate intrusions in the mixed layers, the de-spiked temperature and salinity profiles are low-passed using a filter width of 100 m (the results are not sensitive to the precise choice of filter width) and the original profile is subtracted from the low-passed profile. Only intrusions exceeding 0.01°C and /or 0.0025 in salinity were considered (**Figure 4.4**). Intrusions are classified as temperature (salinity) intrusions when the temperature (salinity) criterion alone was met. For cases when temperature and salinity intrusions coincided with each other, the changes in density due to each variable alone are estimated using:

$$\Delta\rho_s = (t, s + s_{anom}, p) - \rho(t, s, p) \quad (4.1)$$

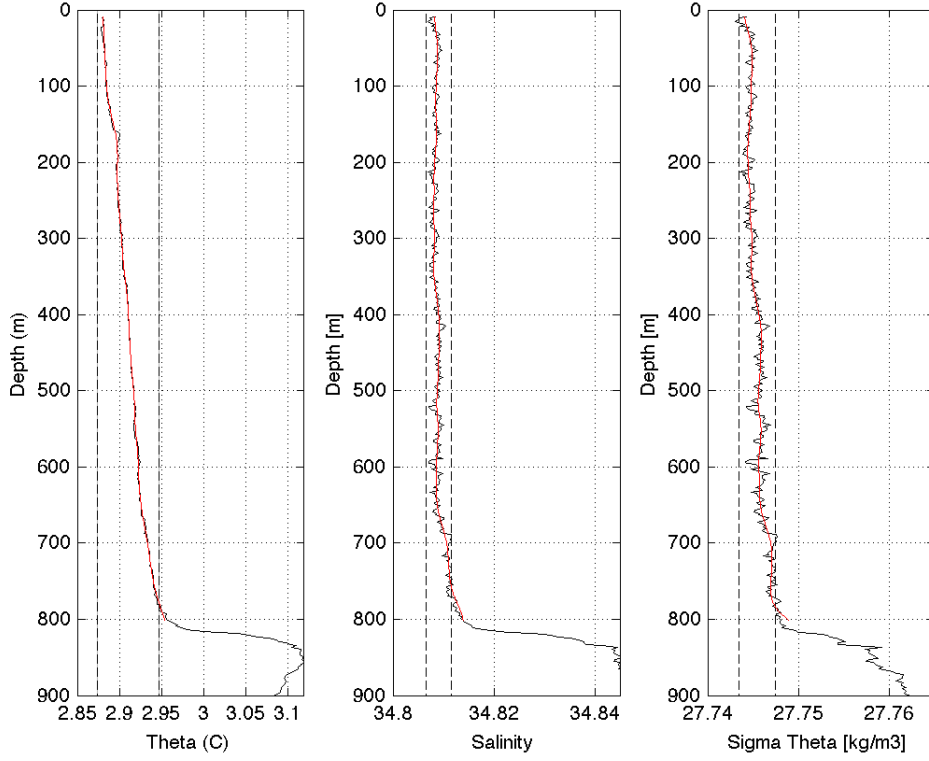


Figure 4.3: Example of a mixed layer depth using station 65. The dashed lines show the two-standard deviation envelope and the red curve shows the lowpass using a 100 m filter width.

and

$$\Delta\rho_t = \rho(t + t_{anom}, s, p) - \rho(t, s, p) \quad (4.2)$$

where t and s are the mean of the low-passed temperature and salinity over the depth of the intrusion and t_{anom} and s_{anom} are the mean of the temperature and salinity anomaly over the same depth. An intrusion was considered to be compensated in density when the measured $\Delta\rho$ over the depth range of the feature was less than both $|\Delta\rho_s|$ and $|\Delta\rho_t|$. Otherwise the intrusion was classified as a temperature intrusion when $|\Delta\rho_t| > |\Delta\rho_s|$, and as a salinity intrusion when the opposite was true (**Figure 4.5**).

4.2.4 Atmospheric Reanalysis Fields

To characterize the atmospheric conditions during the winter of 96/97 I have used the ERA-Interim reanalysis fields. These are produced by the European Center for Medium range Weather Forecasting and are described in detail by Dee et al. (2011) and **Chapter 2**. The data was extracted from the global analysis from 0600 UTC 1 Dec 1996 to 1800 UTC 31 Mar 1997 on a fixed grid with a 0.25° resolution and 6 hourly time intervals. Reanalysis flux fields depend strongly on the numerical models used to calculate them

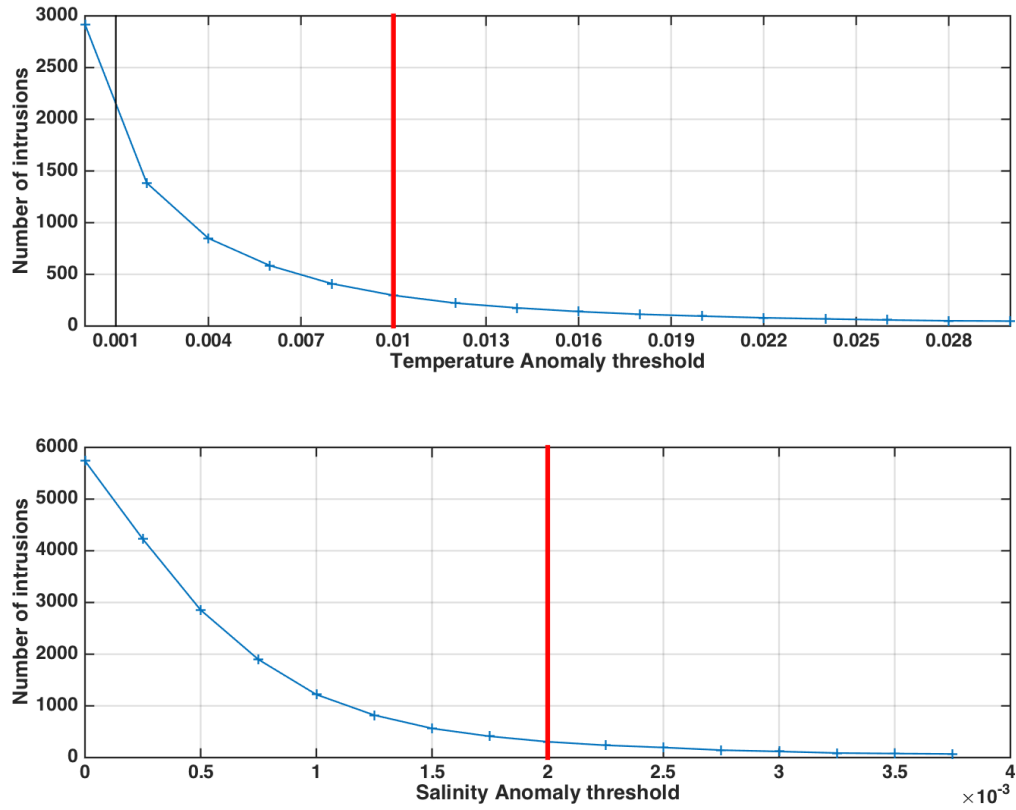


Figure 4.4: The number of temperature (top) and salinity (bottom) intrusions that are smaller than a certain threshold. The black line shows the accuracy of the instrument, the red line the chosen threshold for the definition of an intrusion. Note that for salinity the red and black line are in the same position since the chosen threshold and the definition for intrusions are identical.

but ERA-Interim heat fluxes have been shown to compare well to observed fluxes (Renfrew et al., 2002). However, during high wind events errors can become significant due to the treatment of the ice-edge and surface heat flux algorithm that are not adequate for areas with large air-sea temperature differences (Renfrew et al., 2002). This should be kept in mind when considering the results below.

4.2.5 Storm Tracking

Although automatic storm tracking methods have been used in previous studies (e.g., Serreze et al. (1997); Zhang et al. (2004)), in this study the method of Pickart et al. (2009) is followed and the task is performed manually using the ERA-Interim analysis fields. The domain for tracking the low pressure systems is extended from 120°W to 0°W and 20°N to 80°N. At each 6-hour interval the coordinates and the central sea level pressure of the low were documented from its first appearance in the region to the

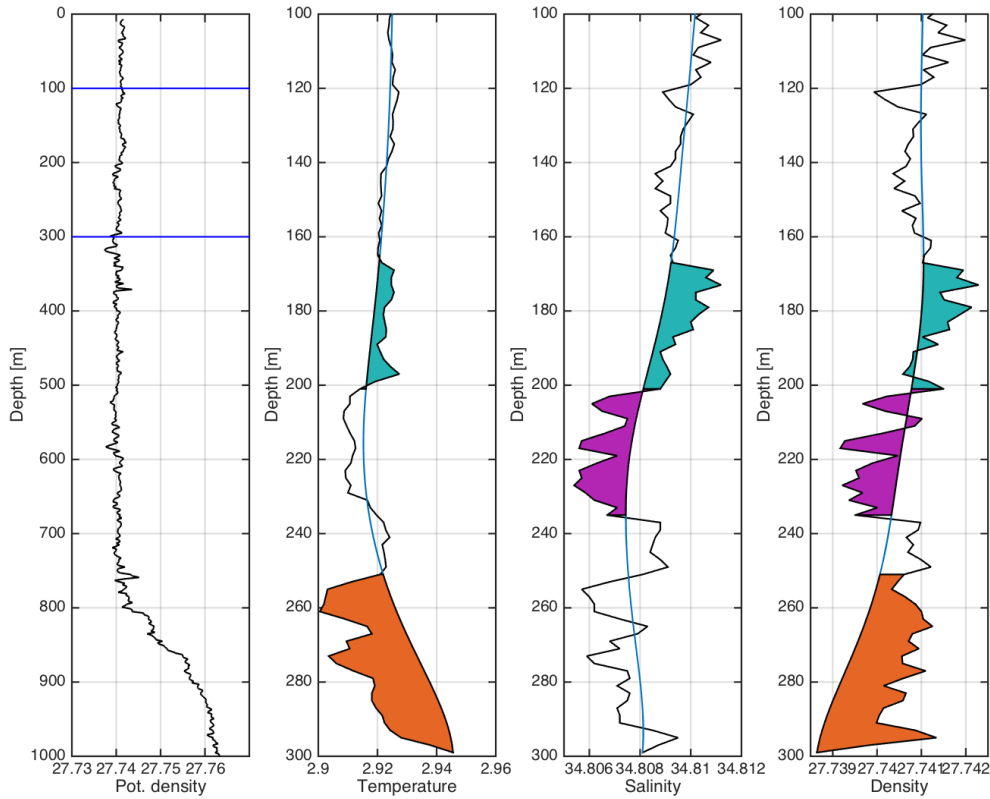


Figure 4.5: An example for the three classes of intrusions. The left panel shows the density of the mixed layer of station 93. The three other panels (temperature, salinity and density) show the region between the two blue lines seen in the left panel. The part of the mixed layer that is filled green shows an intrusion occurring in temperature and salinity. This particular intrusion is not compensated but governed by salinity. The purple area shows a salinity intrusion and the corresponding signature in density. The orange shows a temperature intrusion and the corresponding signature in density.

time that the storm either exited the domain or dissipated. Multiple storms were often present in the study region, which led to merging events, or a single storm would divide into two distinct systems. The main advantage of manually tracking storms is that such events can be detected and are less likely to be misrepresented.

4.2.6 1D-mixing model

The 1-D mixing model previously introduced in **Chapter 2, Section 2.2.5** is used again here. This time, the model is forced with heat fluxes from ERA-Interim that are representative of the three Labrador Sea regions shown in **Figure 4.1** (in the three colors).

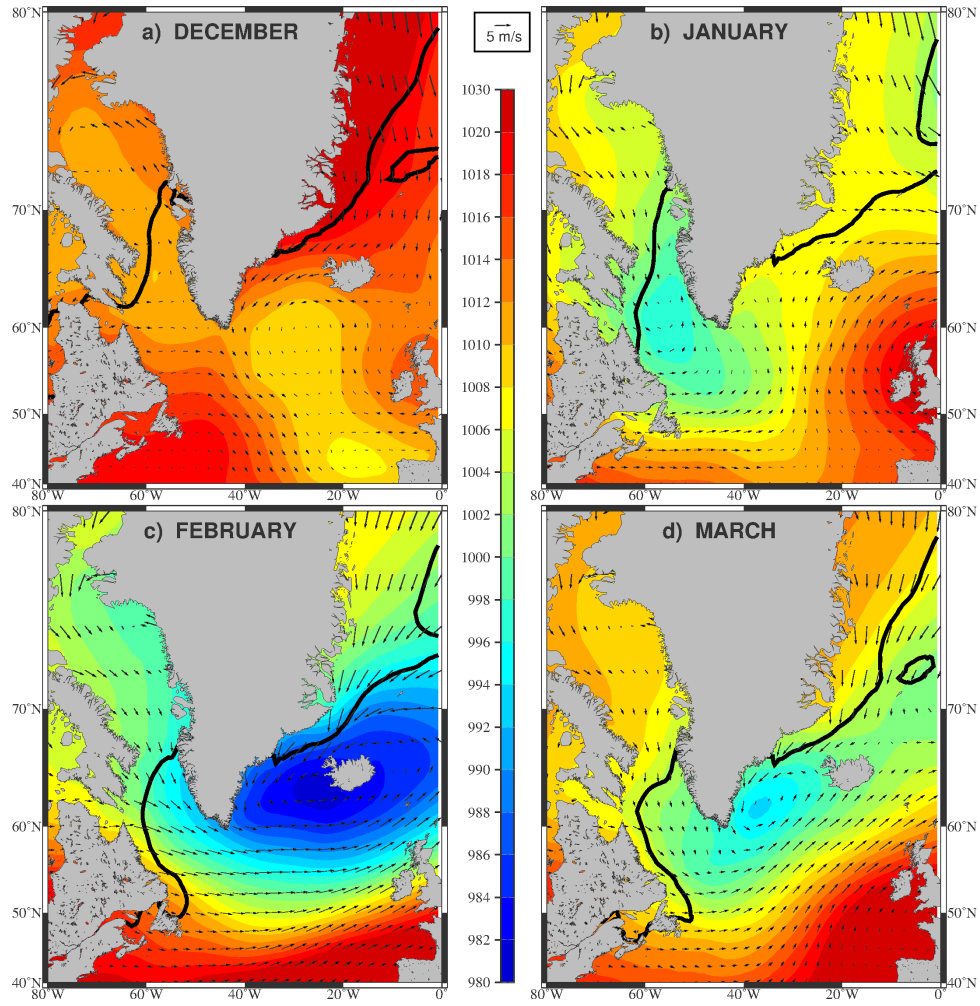


Figure 4.6: Monthly mean sea level pressure fields (color: mbar) obtained from ERA-Interim, the 10 m wind fields (vectors: m/s) and the 50 % ice edge (black contour) for December 1996 (top left), January 1997 (top right), February 1997 (bottom left), and March 1997.

4.3 Atmospheric conditions of Winter 1996/1997

During winter, the most prominent atmospheric feature in the North Atlantic is the Icelandic Low, centered southeast of Greenland (Moore et al., 2014). The cyclonic circulation associated with the Icelandic Low tends to advect cold air over the Labrador Sea and results in a net transfer of heat from the ocean to the atmosphere. This is the primary driver of the convection that forms LSW. The long-term averaged turbulent heat flux in the basin during winter (Dec - Jan) is 980 W/m^2 . Typically the heat flux increased by 17% in midwinter (Jan - Feb) compared to early winter (Nov - Dec), although the spatial flux pattern remains similar (Moore et al., 2014).

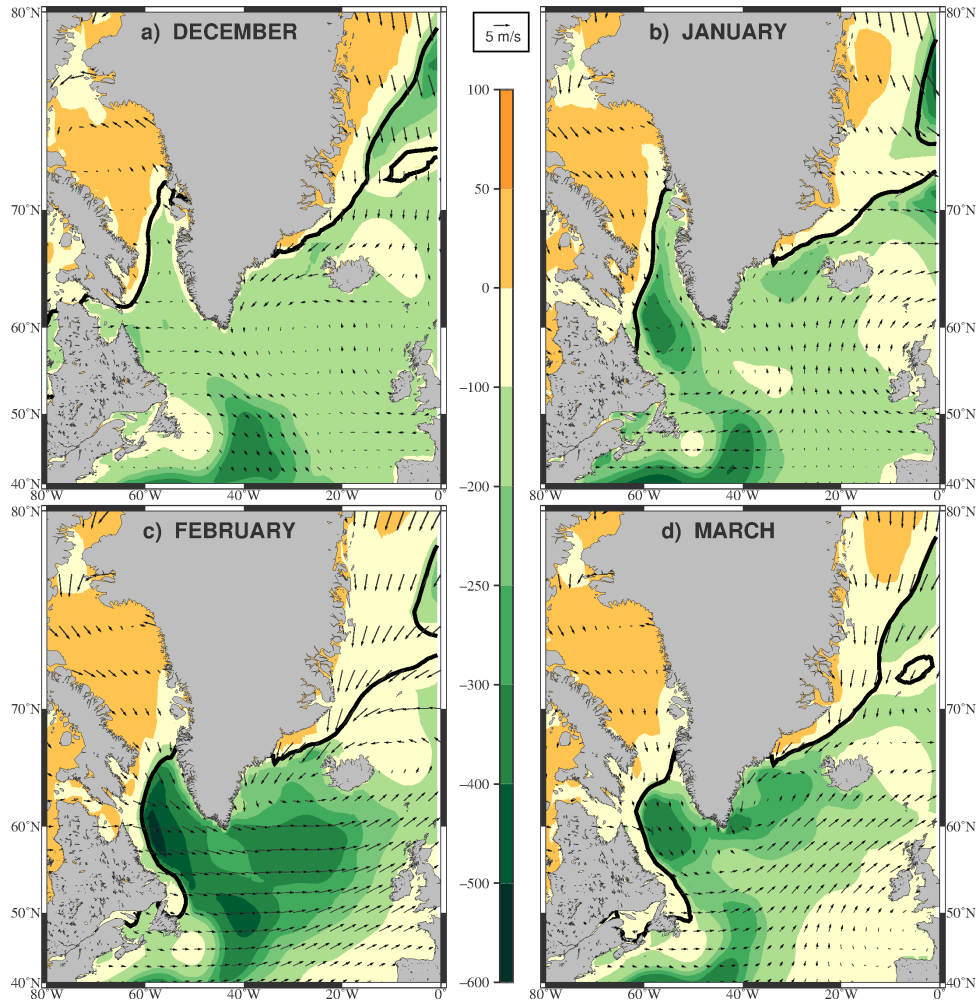


Figure 4.7: Monthly mean turbulent heat flux fields (sum of sensible and latent heat fluxes, color: W/m^2) obtained from ERA-Interim, the 10 m wind fields (vectors: m/s) and the 50 % ice edge (black contour) for December 1996 (top left), January 1997 (top right), February 1997 (bottom left), and March 1997.

4.3.1 Monthly means

The month of December 1996 was exceptionally calm with no signature of the Icelandic Low (**Figure 4.6a**). The sea level pressure (SLP) of the entire North Atlantic domain remained above 1006 mb and high pressure prevailed over the Nordic Seas. The average wind speed in the Labrador Sea was only 2.3 m/s compared to the climatological average of 8 m/s (Moore et al., 2014). The predominant wind direction was westerly, and heat fluxes barely exceeded 200 W/m^2 (**Figure 4.7a**). While January 1997 was colder and stormier, the conditions were also atypical compared to the long-term average (Moore et al., 2014). The Icelandic Low is still not present; instead, the Labrador Sea was characterized by relatively low SLP (as deep as 996 mbar). This was associated with northerly winds off the ice edge (**Figure 4.6**) which led to enhanced heat fluxes over

the western part of the basin (exceeding 300 W/m^2 , **Figure 4.7b**). However, the winds remain anomalously weak, with an average speed of only 2.2 m/s . The situation changes drastically in February 1997. A deep Icelandic Low developed (minimum SLP of 980 mb , **Figure 4.6c**) with strong northwesterly winds advecting cold air off the continent and ice edge over the Labrador Sea (with the average wind speed of 8.6 m/s). This resulted in strong turbulent heat fluxes that exceeded 600 W/m^2 along the western margin of the basin (**Figure 4.7c**). In March the low was still in its typical position but had filled considerably (minimum SLP of 992 mb , **Figure 4.6d**). Winds remain from the northwest, but weakened (average wind speed of 3.5 m/s). As such, the average heat flux was lower, comparable to that in January, although, the eastern part of the basin experienced stronger heat flux than in January (**Figure 4.7b**).

4.3.2 Storm Tracks

What caused the pronounced change in winds and heat flux over the Labrador Sea in winter 1996/97? To shed light on this question, I analysed the storm tracks over the broad region of the North Atlantic, using the method described in **Section 4.2.5**. In all, 85 storms were identified and tracked between December 1996 and March 1997 (**Figure 4.8**). Most storms were first detected over the North American continent or in the Gulf Stream region. However, some were also formed near the southeast tip of Greenland. These usually split from a cyclone already in the area, hence they are considered secondary storms. In general, there is a deepening of the low pressure systems as they traverse from southwest to northeast along the North Atlantic storm track. As noted above, December 1996 was an exceptionally calm month. Remarkably, none of the cyclones crossed into the Irminger Sea where storms typically deepen (**Figure 4.8a**), although some small storms still formed in this region. Overall, the 26 storms in December were weak. Interestingly, there tended to be a bimodal pattern to their paths: a number of storms traversed the North Atlantic from west to east, generally south of 60°N , while others veered northwards and crossed the Labrador Sea. This was due to a blocking high pressure system over the UK during Dec – Jan. The former pattern resulted in the region of low SLP south of the Irminger Sea (**Figure 4.6a**). The latter pathway contributed to the weak winds and low heat fluxes in the Labrador Sea (since winds are reduced in the vicinity of the storm center). Hence, it was not a lack of storm activity that led to the calm conditions in the Labrador Sea that month, but rather the position of the storm tracks.

Fewer storms (17) occurred during the month of January 1997 (**Figure 4.8b**). They were generally stronger in the subpolar part of the domain and had more organized tracks crossing the Atlantic from southwest to northeast. Some of the storms still veered northward, but only two crossed the Labrador Sea. Although only two storms enter the Irminger Sea, more of the low pressure systems followed a path generally extending from Newfoundland towards the vicinity of Iceland. This in turn tend to draw some cold air

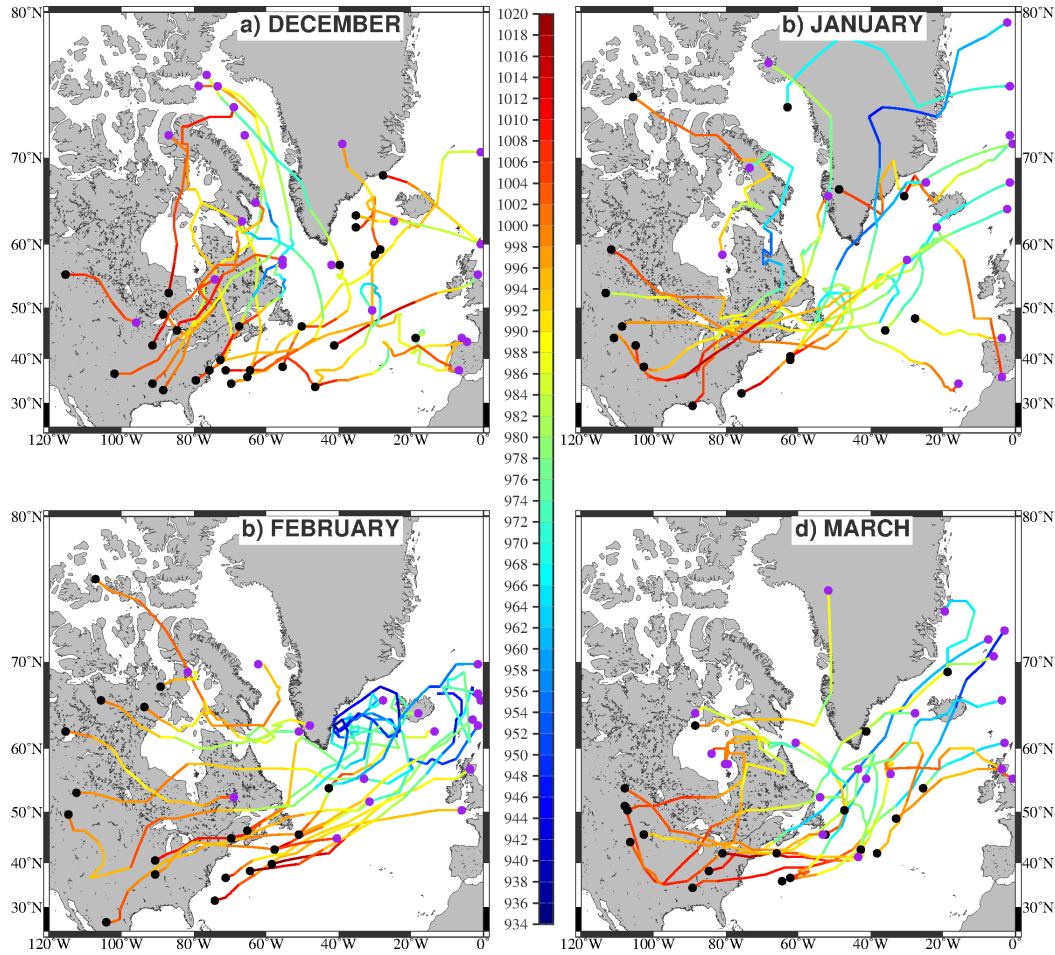


Figure 4.8: Cyclone tracks during December 1996 (top left), January 1997 (top right), February 1997 (bottom left), and March 1997 (bottom right). The tracks are colored by the corresponding sea level pressure (mbar) observed at the center of the system at each position. Black circles show the position at which the storm was first observed, purple circles show the last position of the storm in the domain.

from the Labrador landmass over the Labrador Sea (**Figure 4.6b**), and there were moderately strong heat fluxes over the western part of the basin (**Figure 4.7b**).

Although February 1997 experienced only three more storms than the previous month (20), there was a more clearly defined storm track oriented in the southwest-northeast direction. All of these systems formed south of 50°N, many of them in the Gulf Stream region. A good number of them enter the Irminger Sea where they reached their minimum pressure (in the most extreme case, 940 mb). Of the 7 storms that formed north of 50°N, only two (the two southern-most ones) reached the Irminger Sea. The others crossed the Labrador Sea from west to east before getting distorted by the topography of Greenland. The storms also formed in the very southern part of the domain did not reach the Irminger Sea, but instead left the region by passing south of Iceland. Hence, only the storms that formed in the latitudinal range 50°N – 62°N (7

storms total) reached the typical position of the Icelandic Low and deepened to pressures below 960 mb.

During March 1997, 22 storms were detected, but only one of them formed in the northwestern part of the domain (versus 5 during February). Furthermore, the storms that formed in the Gulf Stream region/eastern US tended to follow a similar southwest to northeast track as seen in February (although not quite as tightly confined). As such, one might have expected to see a similarly deep Icelandic Low in March as the one observed in February. The reason this did not happen is that, whilst multiple storms crossed the Irminger Sea, only a single storm remained in the region and deepened. The other storms traversed the region quickly, limiting their impact on the Labrador Sea.

To better understand what type of atmospheric conditions caused the largest heat fluxes in the Labrador Sea during winter 1996/97, the following methodology is employed: The 6-hourly ERA-Interim data were used to generate a timeseries of turbulent heat flux averaged over the interior Labrador Sea (black box in **Figure 4.9**). High heat flux events are then defined as times when the total turbulent heat flux in this region exceeded 400 W/m^2 . This occurred during 65 6-hr time intervals (a total of approximately 16 days) over the course of the winter. All but two of the high heat flux events took place between mid-January and early-March (**Figure 4.9**, top panel), but there was no statistically significant correlation between the heat flux and the wind speed. This reflects the importance of the air-sea temperature difference, as well as the direction of the wind, in dictating large cooling events. To investigate this further the composite fields of the high heat flux events are analysed (averages of all time periods during winter 1996/97 when the mean heat flux in the Labrador Sea exceeded 400 W/m^2). This reveals the scenario resulting in the strongest air-sea buoyancy fluxes in the Labrador Sea. As seen in **Figure 4.9**, this state is characterized by a region of low pressure situated offshore of the southeast Greenland coast with a central pressure of 984 mb. The wind speeds are elevated in a band around the southeastern/southern side of the low. Importantly, the wind direction in the Labrador Sea is nearly out of the west, i.e., directly off of the pack ice resulting in very cold air streaming over the warm ocean (**Figure 4.9**). The heat fluxes are strongest on the western side of the basin (**Figure 4.9**) with a maximum value $>700 \text{ W/m}^2$ just seaward of the ice edge. It is also worth noting the region of enhanced heat flux to the east of Cape Farewell. This is the signature of westerly tip jets (Moore and Renfrew, 2005).

The storms causing these high heat flux events in **Figure 4.9** are shown in **Figure 4.11** (where the blue trajectories denote the storms in question and the red segments the times when the heat flux exceeded 400 W/m^2 in the Labrador Sea. The high heat flux storms occurred predominantly in January and February (5 and 7 storms, respectively), while in December and March only two storms each resulted in such large fluxes. There seem to be two scenarios that cause high heat loss in the Labrador Sea. The first, when storms progress into or near the southwest Irminger Sea (east of Cape Farewell), and the second when they cross into the Labrador Sea. All of the storms in February, except

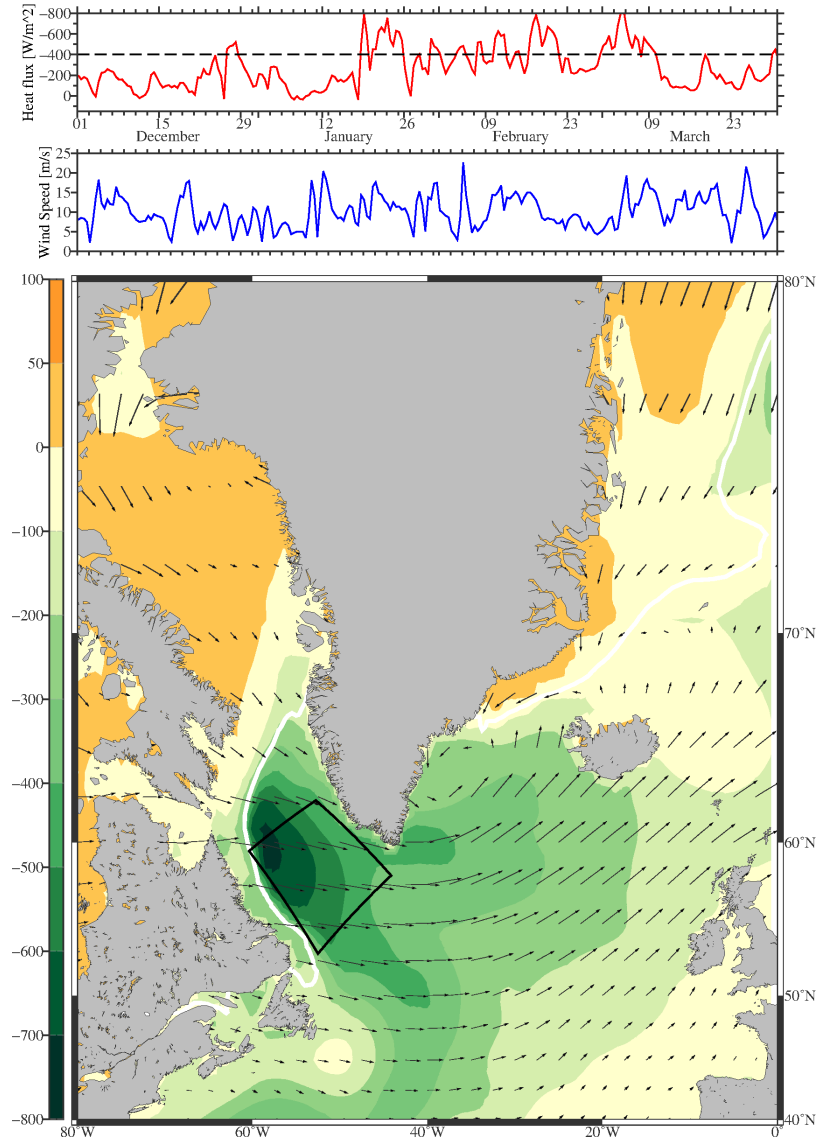


Figure 4.9: Top panel: turbulent heat flux time series of the Labrador Sea with the 400 W/m^2 threshold shown as a dashed line. Below: the corresponding wind speed timeseries for the Labrador Sea. Bottom panel: mean turbulent heat flux field for times when heat flux in the Labrador Sea exceeded 400 W/m^2 (color: W/m^2). The 10 m wind field is shown as vectors (m/s) and the 50% ice edge is shown as the white contour. The black box shows the region over which the turbulent heat flux and wind speeds were averaged for the top two panels.

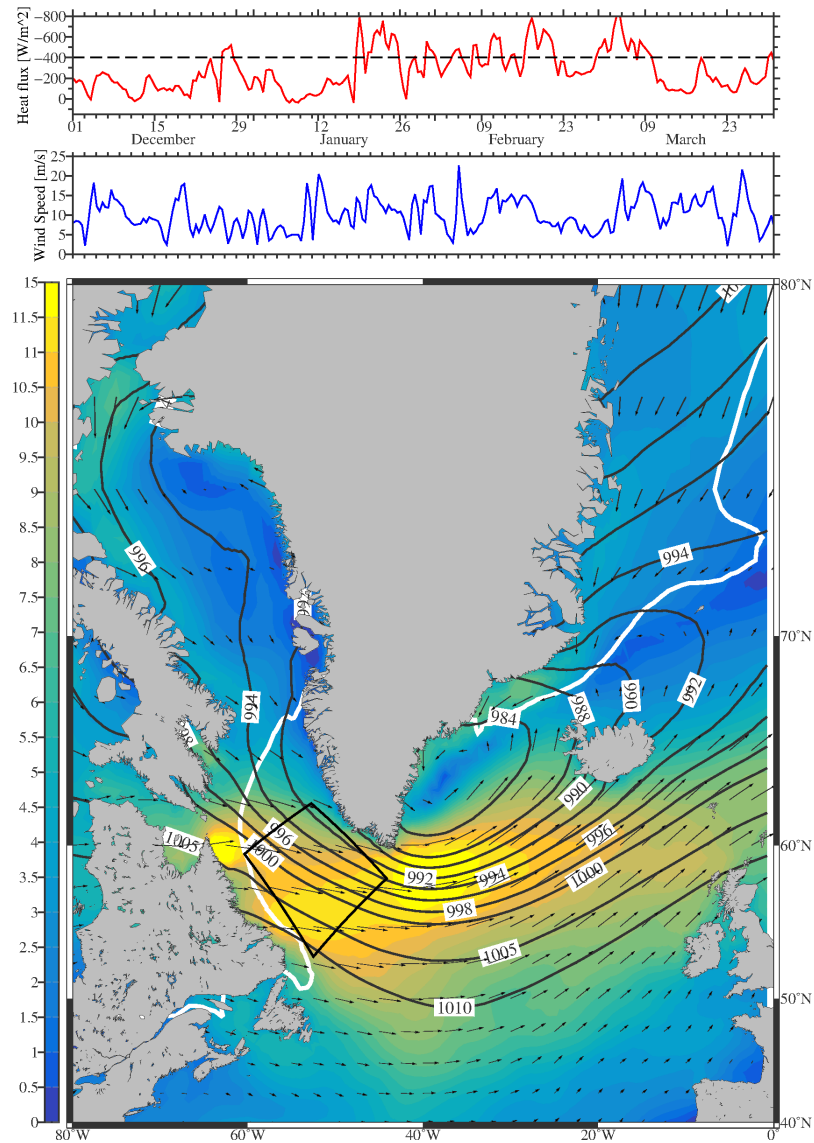


Figure 4.10: Same as **Figure 4.9** but for the mean wind speed field (color: m/s) and the wind direction. Mean sea level pressure is shown as black contours and the 50% ice edge as the white contour.

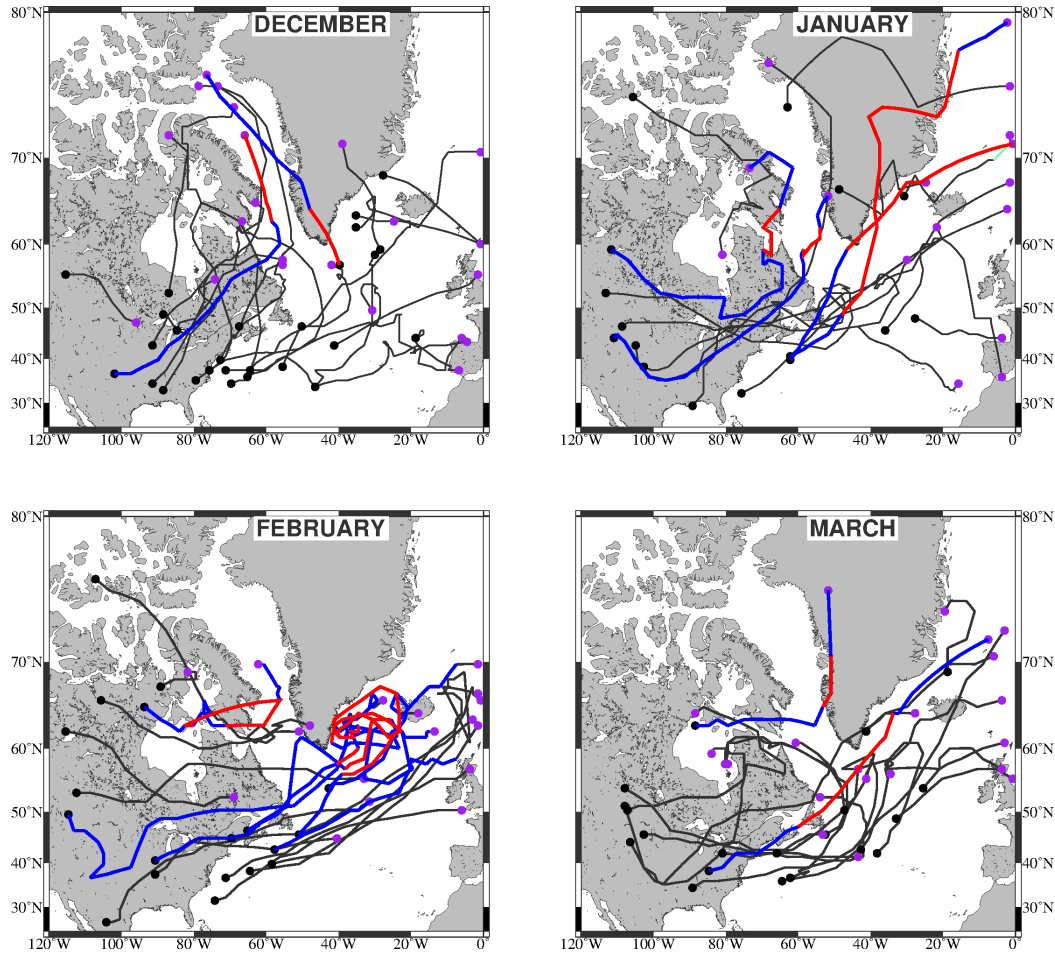


Figure 4.11: Storm tracks of low pressure systems that caused heat fluxes to exceed 400 W/m^2 in the Labrador Sea (blue). The red fragments correspond to the time of high heat fluxes in the Labrador Sea. Grey tracks are storms during which heat fluxes remained below 400 W/m^2 .

for one, followed the former pattern and reversed direction over the Irminger Sea, where they slowed and reached their deepest pressure. The remaining 6 storms followed the latter course. Overall, the Irminger Sea route led to the most extreme heat loss events in the Labrador Sea.

4.4 Impact of Atmospheric forcing on Mixed Layer Variability

4.4.1 Observed mixed layers

The deepest mixed layers, exceeding 1200 m, are found in the western basin, just offshore the 3000 m isobath. A second region of deep mixed layers (around 900 m) is located

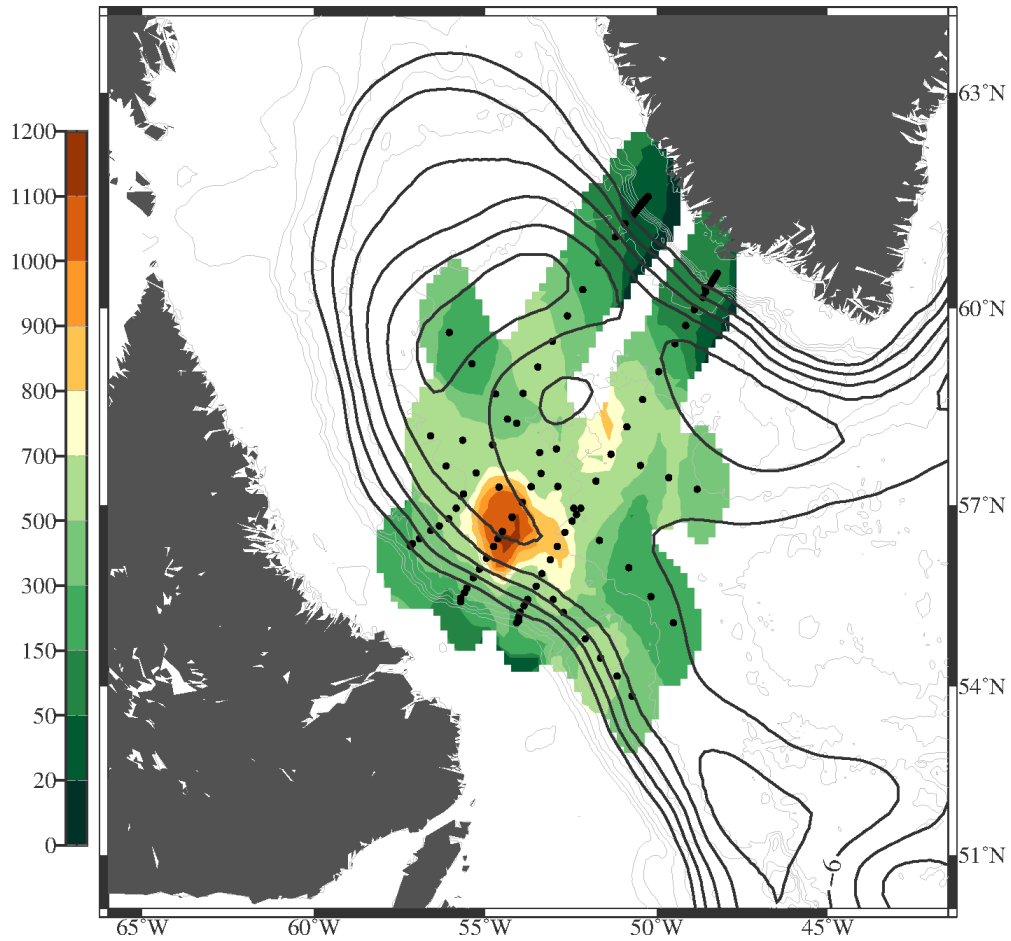


Figure 4.12: Mixed layer depth as observed from the CTD data. The black contours show the streamlines.

in the central basin. The location of the deepest mixed layers in the western basin is consistent with the location of the largest heat fluxes, just south of the ice edge. Mixed layers in the east and south remained shallower than 600 m. Even though the initial stratification is much higher in the boundary currents, mixing to about 900 m was observed in the Labrador Sea current. Convection in this region produced a slightly warmer and saltier class of Labrador Sea Water, which is likely to have entered the DWBC much quicker due to the location of formation (Pickart et al., 2002).

As detailed in **Figure 4.1**, three different regions of the Labrador Sea are considered: the western interior basin (red stations in **Figure 4.1**), the eastern interior basin (yellow stations), and the western boundary current (blue stations). The reason for this is as follows; In Pickart et al. (2002)'s study of the same data set they noted a change in T-S characteristics of the mixed layers between the western boundary current region and the interior. In particular, the remnant Irminger water resided roughly inshore of the 3000 m isobath where the mixed layers tended to be warmer and saltier. Farther

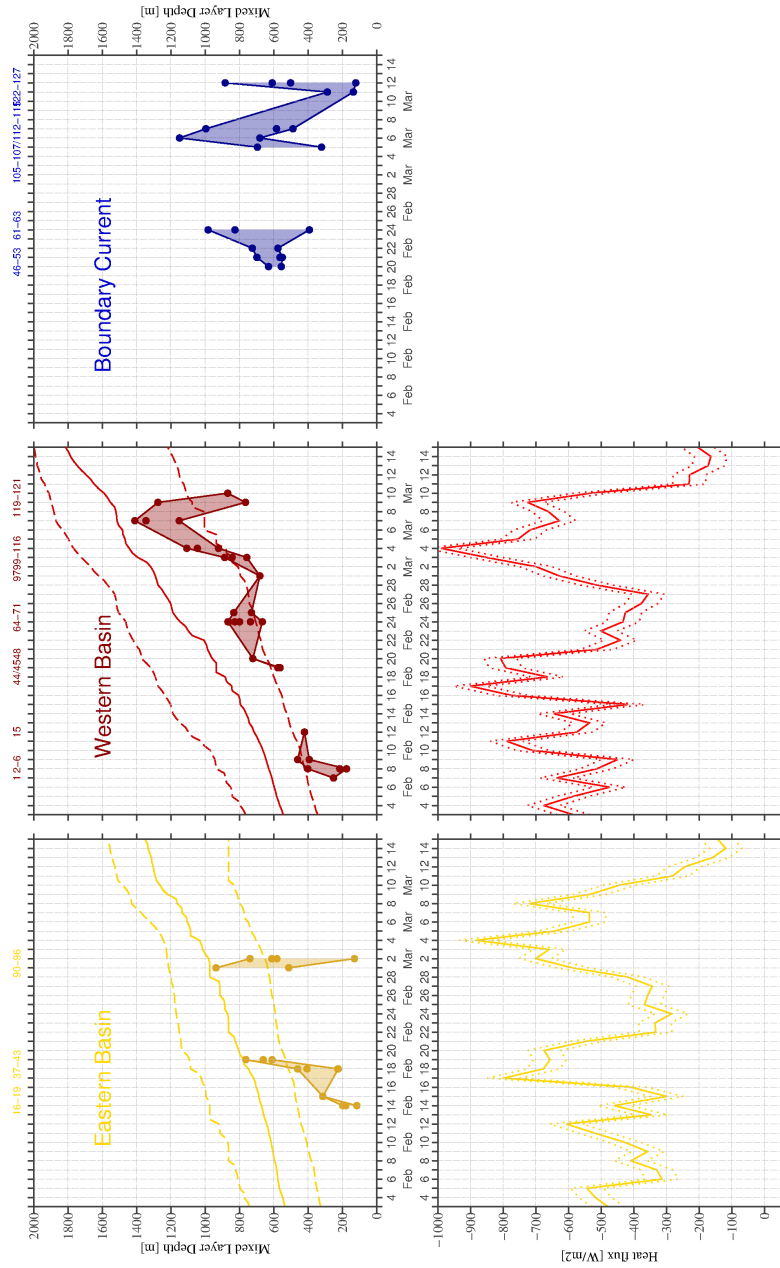


Figure 4.13: The mixed layer depth of each region (top panel). Circles and line fragments show the observed mixed layer depths from the CTD profiles. Mixed layers of stations taken further apart than 7 days are not connected by a line. The numbers at the top show the station number. Solid, thin lines show the predicted mixed layer depth as found in the 2-D PWP mixing model. The bottom panel shows the turbulent heat flux. Dots and line fragments show the mean heat flux half a day before the corresponding station was sampled at the location of the station. The thin, solid line shows the forcing used in the model, the mean turbulent heat flux in the Labrador Sea. Yellow shows mixed layer depth and forcing in the eastern basin, red in the western basin and blue in the western boundary.

offshore, outside of the boundary current system, the ambient stratification is weaker and the circulation is more sluggish (see also streamlines in **Figure 4.12**). The interior basin is divided into a western and eastern side for two reasons. First, the atmospheric forcing varies across the Labrador Sea; as noted above the heat flux is larger on the western half of the basin due largely to the proximity of the ice edge (**Figure 4.7**). Secondly, eddies containing Irminger water are often present on the eastern side of the basin (Lilly et al., 2003), which impacts the stratification of the water column. Stations on the shelf, in the vicinity of the shelfbreak, or on the west Greenland continental slope are not considered because the atmospheric forcing is relatively weak there and mixed layers generally remained shallower than 100 m.

There are clear differences in the mixed layer depths when distinguished geographically (**Figure 4.13**, top panel). For each region the mixed layer depth is plotted as a function of time. When a profile had more than one mixed layer, only the deepest is shown. Typically several stations were occupied in a day, in which case each of the mixed layer depths is plotted. In the western basin, there is a clear trend towards deeper mixed layers as the winter progressed. It is in this region where the deepest mixing occurred, exceeding 1400 m in early-March. Also at this time, the observed daily scatter in mixed layer depth increased.

While there were fewer stations occupied in the eastern basin, and no measurements past the beginning of March, it is nonetheless evident that short time/space-scale variability in mixed layer depth was greater in this region than in the western basin. Some of the observed layers were on the order of 100 – 200 m, while others extended to 800 – 900 m. This variability can be explained in part by the Irminger eddies. As the ship approached the eastern side of the Labrador Sea, warmer, saltier, and shallower layers were occasionally observed that were indicative of such eddies (although this could not be verified because of the relatively coarse station spacing). The mixed layers in the boundary current region also displayed large variations between stations occupied close together in time and space. This might be explained to some degree by deformation of the convective plumes due to winds (Straneo et al., 2002). Furthermore, unlike the western basin, there is no indication of increased mixed layer depths as the season progressed. This is perhaps not surprising because the convected water would be quickly advected to the south, replaced by water from upstream in the boundary current where the atmospheric forcing is not as strong and hence water stronger stratified. Nonetheless, despite the strong currents and greater stratification of the boundary current, deep mixing (to >1100 m) occurred in this region.

4.4.2 Predicted mixed layer depth

To assess the role of the surface buoyancy loss in dictating the observed variation in mixed layer depth, the timeseries of total turbulent heat flux representative of the western and eastern basin (**Figure 4.13**, bottom panel) are used to force the PWP mixing

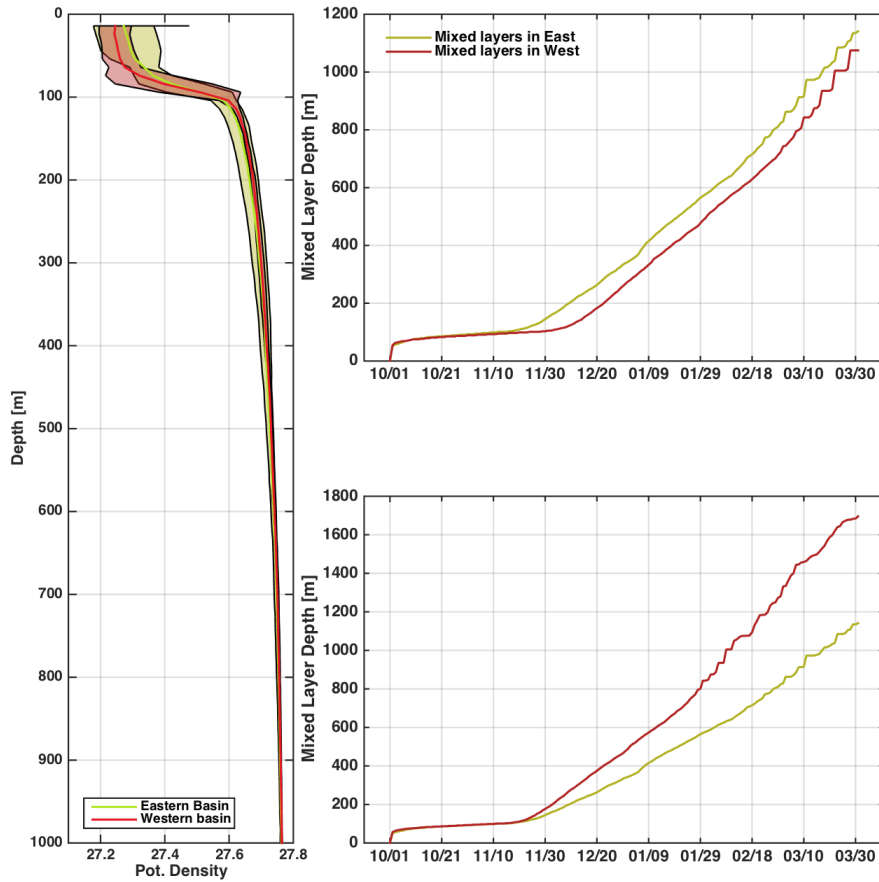


Figure 4.14: Left Panel: The density profile of the eastern basin (yellow) and western basin (red) from the October 1996 AR7W data. Top right panel: the mixed layers for the eastern (yellow) and western (red) basin from PWP when forced with constant forcing of 500 W/m^2 . Bottom right panel: the mixed layers for the eastern (yellow) and western (red) basin from PWP when forced with 500 W/m^2 and 600 W/m^2 , respectively.

model. The model uses initial conditions calculated from the AR7W line in October 1996. This section corresponds geographically to the southern transect occupied across the Labrador Sea during the winter cruise (station 72 - 112, **Figure 4.1**). The stations in the western and eastern basins are averaged together, to create the initial profiles **Figure 4.14**, left panel). The 1-D mixing model was run from October 1996 to the end of March 1997, using these two regional heat flux timeseries and initial profiles. The predicted mixed layers are shown in **Figure 4.13** (top panel) for the time period of the cruise. In light of the uncertainty in the ERA-Interim heat fluxes, three different runs are carried out for each region: one for the computed heat flux (solid line in the figure), one where this value was increased by 50 W/m^2 and one where it was decreased by 50 W/m^2 (these are denoted by the dashed lines in the figure).

Considering the western basin first, during the time period of the cruise there were three pronounced storm events in early-February, mid-February, and early-March. Each

event was stronger than the preceding one. While it is evident that the model overpredicts the observed mixed layer depths, the observations generally fall within the $\pm 50 \text{ W/m}^2$ envelope. When averaging out the scatter of observed mixed layers, the mixed layer depth increases more rapidly after the second storm event; mirrored by the predicted mixed layers.

Whilst the number of days over which the eastern basin was sampled is much less than for the western basin, the comparison between the predicted and observed mixed layer depths is nonetheless insightful. On the eastern side of the Labrador Sea only the latter two storms (in mid-February and early-March) stand out. As noted above, the short time/space variability in observed mixed layer depths in the eastern basin was quite pronounced due to the inhomogeneity of the water column, likely because of Irminger eddies. Considering again the average of observations, there is a modest increase in mixed layer depth over the three week period of measurements. This is consistent with the model prediction, and the deepest mixed layers observed during the two periods of sampling are in line with the PWP value.

The increased scatter of the observed mixed layers in the eastern basin versus the western basin is due to the oceanic preconditioning (i.e., the presence of Irminger rings in the eastern basin). However, the deeper observed mixed layers in the west are the result of the stronger atmospheric forcing on that side of the Labrador Sea. This was assessed by running the PWP model with the same (constant) atmospheric forcing on both initial profiles using 500 W/m^2 (consistent with the average value over the interior Labrador Sea during the 6-week period of the cruise). In this case, the mixed layer depths on the eastern side were in fact deeper than those on the western side (**Figure 4.14**, top right panel). This is because the eastern initial profile has a weaker seasonal pycnocline (from approximately 80 - 100 m, **Figure 4.14**, left panel), which erodes more quickly. Importantly, none of the stations on the eastern side of the 1996 AR7W line were occupied within Irminger eddies (not shown).

One might wonder if the weaker pycnocline in the eastern region was related to the extraordinarily strong convection in the Labrador Sea during the early - to mid-1990s. This is investigated by checking Argo data from more recent winters (2002 – 2011). For profiles measured away from eddies, the eastern basin also has a weaker seasonal pycnocline. This implies that, if it were not for the stronger atmospheric forcing in the west and the presence of Irminger eddies in the east, the mixed layers in the eastern Labrador Sea would be just as deep as those in the western basin. As a final calculation, the PWP model is run with stronger (constant) atmospheric forcing on the western initial profile (stronger by 100 W/m^2 , which is the difference in the mean values of the forcing in the western versus eastern basin, **Figure 4.13**, bottom panel). In this case the maximum predicted mixed layer depth in the western basin was roughly 500 m deeper than for the eastern basin (**Figure 4.14**, bottom right panel), which is consistent with the observations.

While it is reasonable to apply a 1-D mixing model to the two interior basin regions

Table 4.1: Number of intrusions of each class (compensated, temperature, and salinity) found in the 103 mixed layers.

	Total	Compensated	Temperature	Salinity
Number	387	117	137	133
Percentage	100 %	30 %	35.5 %	34.5 %

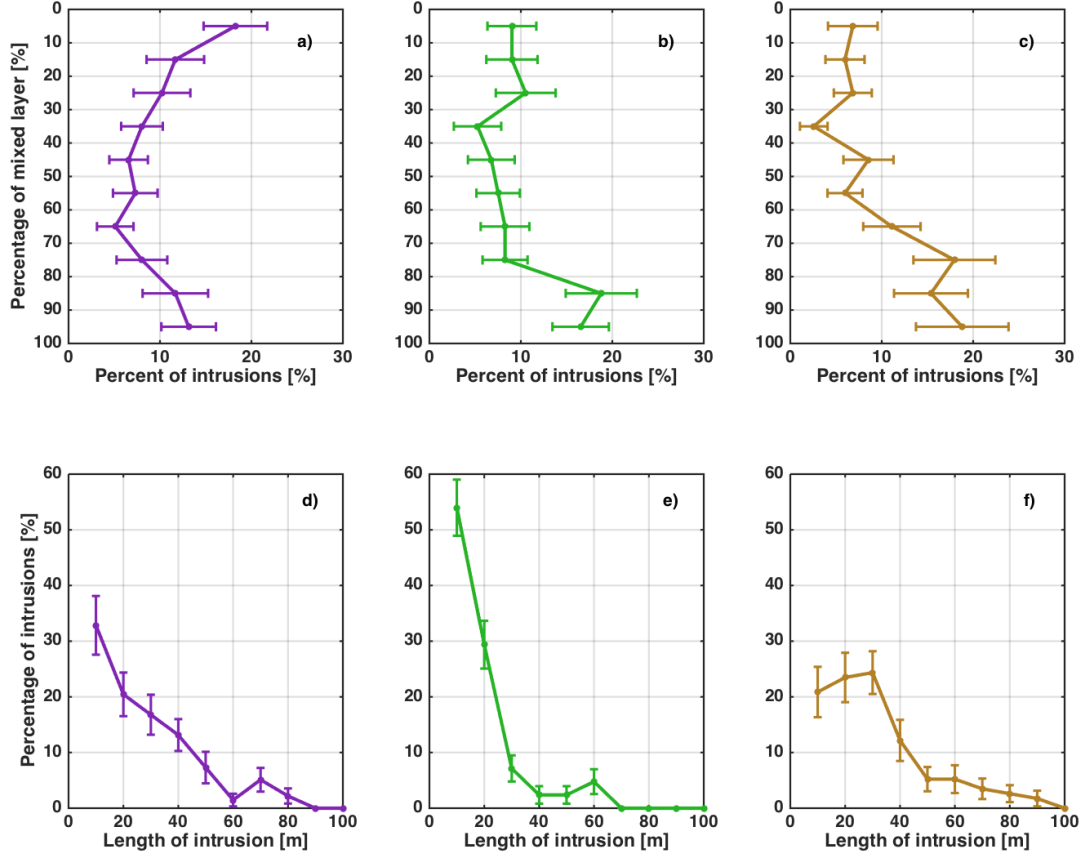


Figure 4.15: Top panels a-c): Percentage of intrusions found at each percentage depth of its mixed layer, a) for temperature intrusions, b) for salinity intrusions, and c) for compensated intrusions. Bottom panels d-f): Percentage of intrusions with a certain length (in m), for d) temperature intrusions, e) salinity intrusions, and f) compensated intrusions.

due to the weak advection there, the boundary current is characterized by speeds as large as 40 -50 cm/s. It is therefore unsurprising that the predicted mixed layer depths displayed no relation to the observed depths in this region (not shown). This is in line with the absence of any trend over time in the observed mixed layers in this region.

4.5 Observed small-scale structure within mixed layers

As noted earlier, none of the observed mixed layers were uniformly mixed. Instead they contained small-scale variations, including significant intrusions. Using the approach outlined in **Section 4.2.3**, a total of 387 intrusions were identified within the 103 mixed layers (**Table 4.1**). Of these, 137 were temperature intrusions (with no significant salinity signal, 35.5%), 133 were salinity intrusions (with no significant temperature signal, 34.5%), and 117 had significant signatures in both temperature and salinity that tended to compensate each other (30%).

On average, 3-4 intrusions were present per profile. Geographically there was no single region of the Labrador Sea where the intrusions were more common; they were observed equally throughout the three regions (boundary current, western basin, and eastern basin). There was also no discernible relationship between the intrusion and the depth at which they occurred. However, there were clear patterns regarding their relative location within the mixed layers. In particular, intrusions occurred more frequently near the base of the mixed layers (**Figure 4.15**, top panels a-c). This is plausible because, during penetrative convection, the sinking water parcels enter the stratified layer below the well-mixed region, which should lead to strong property gradients and mixing. Notably, there is also a higher percentage of temperature intrusions near the top of the mixed layers. This also makes sense as the air-sea heat flux results in cooling of the near surface waters.

Is there a dominant vertical scale associated with the intrusions? To answer this, the frequency with which intrusions of a given length occur is computed (**Figure 4.15**, bottom panels d-f). Overall, there are greater numbers of smaller scale features within the mixed layers, with relatively few intrusions thicker than 50 m. Roughly 80% of all intrusions range between 5 - 35 m (features less than 5 m thick could not be measured). There were, however, clear differences between the types of intrusions. In particular, the percentage of temperature intrusions increased linearly with increasing size, while that for salinity was more exponential (most of the salinity intrusions were ≤ 20 m). By contrast, there was no increase in the number of density compensated intrusions for vertical scales smaller than 30 m.

4.6 Relationship of small-scale structure to storms

How are the occurrence and/or characteristics of the intrusions related to storm activity? As noted earlier, during the time period of the cruise there were three periods that were characterized by high storm activity, i.e., when heat fluxes exceed 400 W/m^2 over the Labrador Sea (**Figure 4.16**, top left panel). The first period in early February was shorter in duration and less intense than the other two, with a maximum heat flux of 600 W/m^2 . The later two periods (mid-February and early-March) had peak heat fluxes

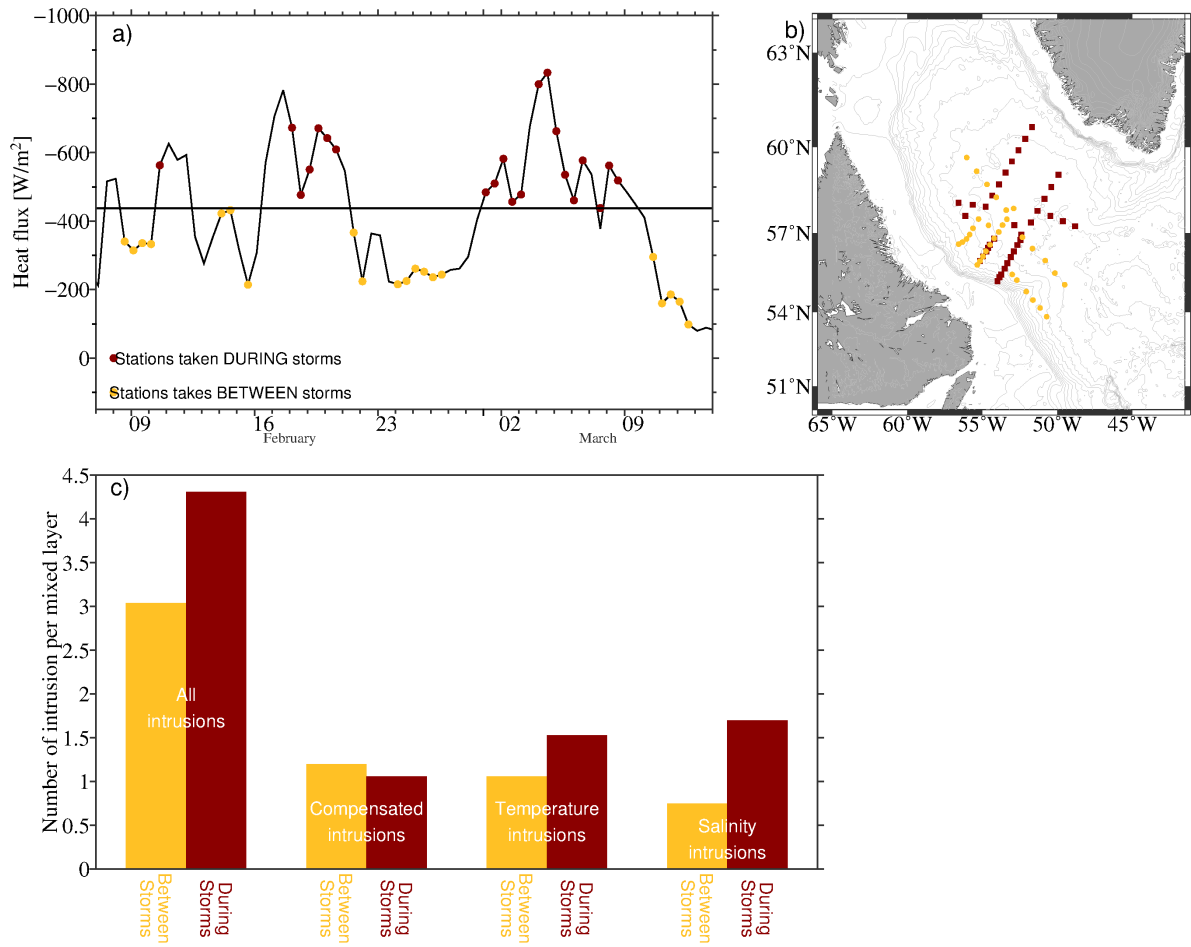


Figure 4.16: Top panels: a) The turbulent heat flux in the Labrador Sea during the time period of the cruise. Yellow dots show the time of stations measured between storms and red dots the time of stations measured during storms. b) The location of the stations measured between storms (yellow) and during storms (red). Bottom panel c): The number of intrusions per mixed layer for stations measured between (yellow) and during (red) storms, for all intrusions, compensated intrusions, temperature intrusions and salinity intrusions (from left to right).

near 800 W/m². Based on this division, each CTD station in our study (75 total) is categorized as "occupied during storms or occupied between storms" (**Figure 4.16**, top panels). All of the stations in the eastern basin were carried out during storms. For the transect that was occupied twice (extending from the boundary current into the western basin), some stations were occupied during storms and some between storms.

When comparing the number of intrusions per mixed layer for stations taken during storms to those occupied between storms, one sees that overall, more intrusions occurred during high storm activity (**Figure 4.16**, bottom panel). However, this is only true for non-compensated intrusions, as there are equal numbers of density compensated intrusions during storms and between storms. This is perhaps reflective of differences in the physical processes that occur during the two phases of convection. During the convective

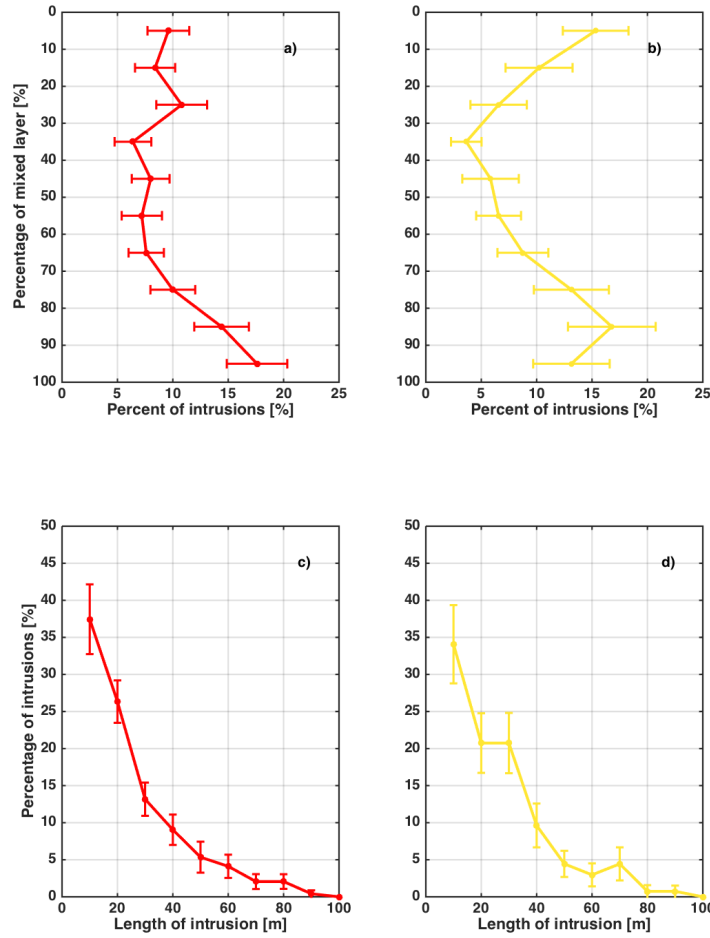


Figure 4.17: Top panels a-b): Percentage of intrusions found at each percentage depth of its mixed layer, a) for intrusions found in mixed layers measured during storms (red), b) for intrusions found in mixed layers measured between storms (yellow). Bottom panels c-d): Percentage of intrusions with a certain length (in m), for c) intrusions found in mixed layers measured during storms, and d) intrusion found in mixed layers measured between storms.

overturning there are strong vertical currents, while during periods of moderate to weak forcing, when restratification commences, lateral motions are more dominant.

There are also differences in the vertical distribution of the intrusions depending on the storm activity (**Figure 4.17**, a-b). During storms there tend to be more intrusions near the base of the mixed layers. As noted above, this is likely because of penetrative convection. At the same time the strong vertical circulation would tend to mix out intrusions higher up in the water column. By contrast, between storms there are just as many intrusions found near the top as there are at the base of the mixed layer (with significantly less intrusions in the middle of the mixed layer). Hence, even though in general there are greater number of intrusions present during periods of strong forcing, more of them are found in the surface layer when forcing abates. This is consistent with

the fact that restratification is greatest, and happens first, in the upper water column.

Finally, there are no significant differences in the vertical scale of the intrusions during storm events versus between storms (**Figure 4.17**, bottom panels c-d).

4.7 Summary and Discussion

Using hydrographic data from a shipboard survey in February - March 1997 in the Labrador Sea, together with atmospheric data from a reanalysis product, the atmospheric forcing and its impact on the variability of the observed mixed layers was investigated. Even though the winter of 1996/97 had a moderate NAO index, mixed layers as deep as 1800 m were observed due to preconditioning of the Labrador Sea during previous years. The early part of the winter (December and January) was uncharacteristically calm and warm with no sign of an Icelandic Low in sea level pressure. Consequently the heat fluxes were relatively low ($100 - 300 \text{ W/m}^2$). In February the atmospheric conditions changed drastically. A deep Icelandic Low developed and strong westerly winds drew cold, dry air over the warmer Labrador Sea, resulting in heat fluxes up to 600 W/m^2 . In March the winds abated to some degree and the heat fluxes moderated, although the signature of the Icelandic Low was still present.

A storm track analysis shed light on the conditions resulting in the highest heat fluxes during the winter of 1996/97. Early in the winter, a significant number of the low pressure systems progressing along the North Atlantic storm track veered into the Labrador Sea, which is not favorable for drawing cold air off of the Canadian continent. As the winter progressed however, the storm tracks became more organized with a direct path into the Irminger Sea. Once in the vicinity east of Cape Farewell, the storms tended to slow down and sometimes backtrack causing the Icelandic Low sea level pressure signature that prevailed during the month. A composite average of the highest heat flux events in the Labrador Sea revealed that this scenario is most favorable for driving convection. Although the storms in March also generally progressed into the Irminger Sea, they traversed the sea quickly and, as such, did not have the chance to impact the Labrador Sea as effectively as the previous month.

The importance of storm tracks to the strength of convection can also be seen in Vage et al. (2009) for the winter of deep convection in 07/08. Storm tracks during this year were more favorable for Westerlies, hence cyclones followed a well-defined track from Canadian continent towards the Irminger Sea, similar to the storms observed here in February. This is important to keep in mind in light of the changing climate that is thought to also result in a change in storm frequency and possible shift in storm tracks. This could drastically alter the convection in the Labrador Sea especially if storm tracks were to shift polewards forcing storms to cross the Labrador Sea and consequently weakening the air-sea fluxes. The high frequency of storms in e.g. Europe during recent years is thought to be due to the presence of a strongly positive NAO

(Alexander et al. 2005). This relationship does not necessarily hold up during other periods with high storm frequency, such as the beginning of the nineteenth-century. This period was also characterized by high storminess but during a time when the NAO index was low and barely ever exceeded +2 with long periods of negative NAO (Matulla et al. 2008). Instead, it was suggested that the ice-pack in the Greenland Sea caused a southward displacement of the North Atlantic storm tracks (Dawson et al. 2005). In particular, the model saw a decrease of storm frequency in their typical locations of the coast of east Greenland but no decrease of the overall storm strength. In other words, a decrease in ice cover in the Labrador Sea could lead to a northward shift of storm tracks, which, in fact, has been observed in models (Bengtsson et al 2005). A different model shows that the growth in storm track activity over north-western Europe has already surpassed the variability of the NAO so that the main effect on the storm tracks is not a change in the sign of the NAO but in the location of the Icelandic Low (Ulbrich and Christoph, 1999). In other words it is likely that the NAO will shift north in a warmer climate. This could lead to a situation where the storm tracks also move north, eventually encounter Greenland which causes them to get trapped in the Labrador Sea, consequently decreasing the air-sea fluxes and convection there. The response of the storm tracks to projected climate warming is amplified especially in this region (Willison et al. 2015)

The uncertainties of how and if storms tracks and individual storms might change in the future leaves important open questions about the future of Labrador Sea convection. To accurately predict the strength of the MOC and changes in climate such fundamental questions need to be addressed. It seems critical to study the atmosphere and ocean together rather than in separate models, as often done for atmospheric models. To explain weak convection in the Labrador Sea it is further important to not only consider the NAO index but also the position of the Icelandic low and the storm tracks. Doing so for past years might led to a deeper insight of the variability in convection strength and LSW formation, which so far is not entirely understood and can not be predicted.

The Labrador basin was divided into three geographical regions: the eastern interior basin, western interior basin, and western boundary current region (shoreward of the 3000 m isobath). The time evolution and variability of the observed mixed layers were different in each of the regions. The deepest mixed layers were found in the western interior, while the station-to-station variability in mixed layer depth was greater in the other two regions. In the eastern interior it was argued that this was due to the intermittent presence of Irminger rings, whose increased stratification would limit convection. The overall trend in mixed layer depth through the winter in the two interior regions was consistent with that predicted by a 1-D mixed layer model using data from the previous fall as the initial condition. By running additional cases with idealized forcing, it was demonstrated that the deeper mixed layers in the west were due to the enhanced heat fluxes on that side of the basin as opposed to oceanic preconditioning.

The small scale variability within the mixed layers was investigated using the ship-board hydrographic data. Three types of intrusions were considered: temperature-only, salinity-only, and joint temperature/salinity intrusions that were largely compensated in density. All three types of intrusions were found to be more common at the base of the mixed layers, likely due to the occurrence of penetrative convection. Enhanced numbers of temperature-only intrusions were also observed near the surface, which is to be expected due to the strong air-sea heat fluxes during winter. During storms there were more non-density compensating intrusions present compared to the periods between storms, and the small scale variability was enhanced near the top of the mixed layer.

Overall the winter analyzed here was characterized as a transition year due to its moderate NAO index. However, considering the individual month the winter was special due to its anormalous calm December and January (with very low heat loss). February on the other hand had the second largest heat loss of all Februaries over the previous 20 years. Hence, this winter can be seen as a sort of case study with December and January representing a calm and warm winter, where as February and March characterize a stormy and cold winter.

Chapter 5

Conclusions and outlook

This study was motivated by the impact that freshwater anomalies can have on the Labrador Sea and by our limited knowledge of freshwater sources and pathways through which this freshwater might reach the region of deep convection in the Labrador Sea. As convection is strongly dependent on air-sea fluxes, it is also essential to gain insight in the impact of storms and storm paths on the convection. It is important to understand how the dynamics of the Labrador Sea might change due to future climate change since the convection here is one of the driving forces of the MOC. With convection being strongly dependent on air-sea fluxes it is also essential to gain insight in the impact of storms and storm paths on the convection.

For this thesis I have utilized available observational data and found that the surface salinities in the Labrador Sea basin have significantly decreased over the last decade, while the salinities and temperatures in the deep ocean have increased. The surface freshening is found to be comparable to the freshening observed during the ‘Great Salinity Anomaly’ but with a different vertical extent. Just like the ‘Great Salinity Anomaly’, the freshening in recent years had the potential to suppress mixing for up to two years. This highlights the importance of freshwater fluxes in the Labrador Sea and the need to understand to what extent the increased ice melt and freshwater content of the Arctic will impact the Labrador Sea. The use of an ocean model made it possible to further investigate freshwater fluxes into the region. For this, Argo data did not prove to be the right tool as they mainly measure the deep basin and not the shallower boundary water. Additionally they are not able to resolve advection due to their uneven distribution in space and time. The Lagrangian view of the Labrador Sea advection showed that the two seasonal freshwater peaks, also seen in previous studies (Schmidt and Send, 2007; Straneo, 2006) and in the Argo data, enter the basin via the eastern boundary. They are the result of the advection of two different water sources via two different pathways. The first peak is due to large fluxes of very fresh coastal water entering the basin via the northeast. It is balanced by almost equally large fluxes of salty water in the southeast. The second, larger peak on the other hand is the result of relatively small freshwater

fluxes from both the inshore and offshore sections of the boundary current as well as from North Atlantic water. This freshwater reaches the basin via both the north and the southeast. Interannual changes in the freshwater advection to the basin were solely due to the inshore water of the EGC.

This implies that the fresh coastal water has a direct impact on the Labrador Sea dynamics and that changes in the properties of the boundary current system, namely the East and West Greenland Currents, will have significant impacts on the Labrador Sea basin. In fact, a warming of the boundary currents, as observed by Rykova et al. (2014), can impact the melting of the Greenland Ice Sheet (Straneo et al., 2010). This in turn is likely to lead to an increase in fresh water inflow into the Labrador Sea and will therefore also affect convection. In order to accurately represent the deep water formation in ocean models and predict the strength of the MOC, it is crucial to represent not only the strength and overall structure of the boundary currents but also the characteristics of the coastal waters and the runoff and ice melt from Greenland. Furthermore, it is not enough to quantify changes in the East and West Greenland currents. Instead, water inshore of the boundary currents, on the shelves and in the fjords, is also significant to the Labrador Sea dynamics. A relative weak freshening of e.g., 0.3 psu here could trigger huge freshwater fluxes to the basin as seen in 1995 for example.

Interestingly, water from Baffin Bay and Hudson Bay does not play an important role in the Labrador Sea dynamics. That is in line with previous observations based on EKE and drifters. However, it is surprising just how little of this water entered the basin in this study. In the case of Hudson Bay, only one trajectory every four years reached the basin. Additionally, very little water entered the basin along the western boundary. The water that did enter the basin here entered in the proximity of a ridge that runs west to east. In this region, hydrographic data has shown large, long lasting, and slow eddies (pers. communication I. Yashavec) that could explain the advection here. However, this advection is governed by the salinities of the EGC inshore and offshore water that, once reaching the Labrador Current, have salinities very similar to each other and are relatively salty. It is surprising that the advection shows no signature of the very fresh coastal water along the Labrador Coast.

It is necessary to further investigate if the freshwater fluxes from Baffin Bay and Hudson Bay really do not matter to the Labrador Sea basin. This could be done with drifters, deployed in the vicinity of the ridge or with gliders that are able to monitor advection in this region. It is crucial to either confirm or eliminate these two water sources from the possible sources of freshwater in the Labrador Sea basin. If, as suggested here by NEMO, we could eliminate this water, we would be able to more confidently predict and observe changes in properties in the main source of water in the basin, the WGC and the water along the Greenland coast. If, on the other hand, Baffin Bay and Hudson Bay and the freshwater from the coast of Canada do play a role, models need to be revisited to ensure they accurately represent this exchange. Furthermore, a more pronounced advection of shelf water to the basin in the west would help explain some of

the discrepancy in the seasonal freshwater increase that, so far, could not be explained purely by eddy fluxes along the eastern side of the basin alone.

In order to better understand the impact of changes in the coastal waters around Greenland, a similar study to the one in Chapter 3 could be set up, using ARIANE to track this water. In particular, particles could be released along the coast and in the fjords and tracked forward to estimate how much of this water reaches the basin. Additionally, the experiment could be started in 1960 to capture the Great Salinity Anomaly. This would help us answer the question of whether the current conditions and increasing freshwater in the Arctic might lead to another, even stronger, ‘Great Salinity Anomaly’ in the future. So far, the freshening has only impacted the surface layer of the Labrador Sea, whilst the ‘Great Salinity Anomaly’ decreased the salinities in the Labrador Sea throughout the entire water column. Observing the Great Salinity Anomaly with ARIANE could result in interesting conclusions about the differences and similarities that this past freshening has to the current situation. We would then be able to draw better conclusions concerning future developments and changes in the convection and the resulting changes in the MOC.

Studies in the past have failed to explain the observed seasonal freshening of the basin by considering only eddy fluxes. This is due to these studies neglecting Ekman transport, which has been shown to play a huge role in advecting water along the eastern basin. In fact, Ekman transport explains about 80% of the variability in advection of the inshore water. Note that we have to keep in mind that the EKE in the model did not agree well with the observed EKE from altimetry. Hence, we should refrain from making assumptions about the role of eddies and the relative importance of Ekman transport versus eddy fluxes. However, winds and the response of the ocean to them are well defined in ocean models and, despite the uncertainties in the eddy fluxes, it is clear that the advection of water along the eastern side of the basin correlates closely to the transport due to wind. Boundary current instabilities and the resulting eddy fluxes are, on the other hand, harder to capture in models. Higher resolution models will be able to resolve smaller features and move further away from having to parameterize eddies. However, it is also necessary to further investigate the boundary currents and their instabilities from observations. This has been proven to be tricky due to their small and fast nature that cannot be resolved with the available data. Higher resolution satellite data would prove useful and would allow tracking and quantifying of eddies in the Labrador Sea. Additionally, surface velocity data could help to distinguish between the role of eddies and Ekman transport in the advection of water to the central Labrador Sea. Furthermore, documenting the seasonal changes in the boundary currents and their impact on the stability of these currents would help us to better understand the relationship between the slope of the isopycnals and the instabilities and growth rates of EKE. This in turn could improve the representation and parametrization in our current climate models and contribute to the development of theoretical models of the boundary

current to investigate mechanisms that govern interannual changes in their stability and its role in sudden increases in the eddy fluxes (e.g., observed in 1997 and 2003 by Lilly et al. (2003); Rykova et al. (2014)). This is something that was not represented well in the NEMO simulation.

Freshwater fluxes are important in the restratification of the basin and in preconditioning it for the convection period in the following winter. Air-sea fluxes, on the other hand, are the driving force through which buoyancy, previously added by freshwater fluxes, is removed and convection triggered. The importance of storms in triggering convection and impacting active mixing was investigated in Chapter 4. Here we saw that storms were only favorable to triggering large heat fluxes when passing through the North Atlantic on a direct track to the Irminger Sea. Potential changes of storm tracks and frequency were discussed in Chapter 4. The models used for investigating changes in storm behaviour in a changing climate suggest a northward shift of storms but a similar frequency. We have seen that this can potentially result in weaker convection in the Labrador Sea. However, these studies are usually done with atmospheric models that do not include ocean circulation, even though the ocean does not only respond to the changes in storm tracks but also influences the storm tracks (Woollings et al., 2012). This results in large uncertainties about changes in storm tracks and storm frequency in a changing climate. Here, future work should include similar studies using ocean-atmosphere coupled models to assess a shift in storm tracks, frequency and magnitude. There is also the possibility to analyze the storm track behavior further by extending this study into more recent years, hence tracking storms for more than one year. This would allow us to conclude on how typical the effect of storm tracks on Labrador Sea convection was in the analyzes of Chapter 4. Furthermore, it would be interesting to extend this to a time slice mode of ERA, there an estimate of the sea surface temperature in the later half of the 21st century is used to force the model.

Additionally, it is worth noting that response of extratropical cyclones to global warming vary significantly with horizontal resolution of the current models, so that, even if the models are well calibrated for current storm tracks, they might not be valid in a warming climate (Willison et al. 2015).

5.1 Outlook

The attempts of this research to explain the observed variability of the Labrador Sea, including the lateral fluxes and the deep mixing, need to be continued, due to the Labrador Seas impact on global circulation and climate. It is still challenging to understand, or even just describe, the dynamics here and the interplay with each other and the Arctic. The available data records are relatively short, if they exist at all and even a 20 year time series is too short to confidently conclude on long term trends. Many factors contribute to the difficulty of understanding the Labrador Sea system: Different time scales, from

seasonal to decadal, play a role here and the ocean has a ‘memory’ of forcing and mixing in previous years. Furthermore, much of the processes here are small scale and dynamic in their position and timescales and observations often struggle to capture such processes. In recent years, new monitoring projects have been initiated (e.g. OSNAP) that will vastly improve our understanding of the year-to-year variability in the Labrador Sea. However, Argo floats and satellite altimetry provide us with year around data and a spatial distribution of measurements that otherwise can not be accomplished. The problem that still has to be solved is the resolution of the satellites and ocean models, which is often too coarse to capture the small scale variability and eddy fluxes that play such an important role in the Labrador Sea. Furthermore, the new insight into the pathways of freshwater are an important first step in a better understanding of the connection between the Arctic outflow and convection. This will enable better predictions of the consequences of increased ice melt on a global scale. However, the pathways have to be verified in the real ocean. Additionally, the vertical extent of the freshwater advection was not addressed here, nor was as an overall estimation of changes in the freshwater budget of the Labrador Sea basin. This would give further insight into the changes that advection and freshwater fluxes might undergo if climate predictions become true.

Appendix A

Freshwater pathways in ORCA-N01

A.1 Freshwater pathways in ORCA-N01

In this Appendix I want to present some of the results from **Chapter 3** done with the NEMO ORCA-N01 run, to highlight the vast changes that resulted from changing the model dynamics in the Labrador Sea.

The namelist shown here lists all parameters used for the creation of the model, including eddy viscosity and diffusivity, runoff etc. A detailed description of these parameters can be found in http://www.nemo-ocean.eu/Media/Files/NEMO_book_V3_4.pdf.

namsbc	Surface Boundary Condition (surface module)
nn_fsbc = 1 ln_ana = .false. ln_flux = .false. ln_blk_clio = .false. ln_blk_core = .true. ln_cpl = .false. ln_apr_dyn = .false. nn_ice = 2 ln_dm2dc = .true. ln_rnf = .true. ln_ssr = .true. nn_fwb = 3	frequency of surface boundary condition computation analytical formulation flux formulation CLIO bulk formulation CORE bulk formulation Coupled formulation Patm gradient added in ocean and ice Eqs. =0 no ice boundary condition, =1 use observed ice-cover, =2 ice-model used daily mean to diurnal cycle on short wave runoffs Sea Surface Restoring on T and/or S FreshWater Budget: =0 unchecked, =1 global mean of e-p-r set to zero at each time step, =2 annual global mean of e-p-r set to zero, =3 global emp set to zero and spread out over erp area
namsbc_rnf	runoffs namelist surface boundary condition
cn_dir = './' ln_rnf_emp = .false. ln_rnf_mouth = .true. rn_hrnf = 10.e0 rn_avt_rnf = 2.e-3 rn_rfact = 1.02e0 ln_rnf_depth = .false. ln_rnf_tem = .false. ln_rnf_sal = .false.	root directory for the location of the runoff files runoffs included into precipitation field (T) or into a file (F) specific treatment at rivers mouths depth over which enhanced vertical mixing is used value of the additional vertical mixing coef. [m2/s] multiplicative factor for runoff read in depth information for runoff read in temperature information for runoff read in salinity information for runoff
namsbc_apr	Atmospheric pressure used as ocean forcing or in bulk
cn_dir = './' ln_ref_apr = .false.	root directory for the location of the bulk files ref. pressure: global mean Patm (T) or a constant (F)

namsbc_ssr	surface boundary condition : sea surface restoring
cn_dir = './'	root directory for the location of the runoff files
nn_sstr = 0	add a retroaction term in the surface heat flux (=1) not (=0)
nn_ssr = 2	add a damping term in the surface freshwater flux (=2) or to SSS only (=1) or no damping term (=0)
rn_dqdt = -40.	magnitude of the retroaction on temperature [W/m ² /K]
rn_deds = -33.333	magnitude of the damping on salinity [mm/day/psu]
ln_ssr_bnd = .true.	flag to bound erp term (associated with nn_ssr=2)
rn_ssr_bnd = 4.e0	ABS(Max/Min) value of the damping erp term [mm/day]
namsbc_alb	albedo parameters
rn_cloud = 0.06	cloud correction to snow and ice albedo
rn_albice = 0.53	albedo of melting ice in the arctic and antarctic
rn_alphd = 0.80	coefficients for linear interpolation used to
rn_alphc = 0.65	compute albedo between two extremes values
rn_alphdi = 0.72	(Pyane, 1972)
namlbc	lateral momentum boundary condition
rn_shlat = 0.	shlat = 0 , free slip 0 < shlat < 2, partial slip shlat = 2 no slip 2 < shlat, strong slip
ln_shlat2d = .true.	Read and use a 2d (point by point) setting
namcla	cross land advection
nn_cla = 0	advection between 2 ocean pts separates by land
namobc	open boundaries parameters
ln_obc_clim = .false.	climatological obc data files (T) or not (F)
ln_vol_cst = .true.	impose the total volume conservation (T) or not (F)
ln_obc_fla = .false.	Flather open boundary condition
nn_obcdta = 1	= 0 the obc data are equal to the initial state = 1 the obc data are read in 'obc.dta' files
cn_obcdta = 'annual'	set to annual if obc datafile hold 1 year of data set to monthly if obc datafile hold 1 month of data
rn_dpein = 1.	damping time scale for inflow at east open boundary
rn_dpwin = 1.	- - - west - -
rn_dpnin = 1.	- - - north - -
rn_dpsin = 1.	- - - south - -
rn_dpeob = 3000.	time relaxation (days) for the east open boundary
rn_dpwob = 15.	- - - west - -
rn_dpnob = 3000.	- - - north - -
rn_dpsob = 15.	- - - south - -

rn_volemp = 1.	! = 0 the total volume change with the surface flux (E-P-R) = 1 the total volume remains constant
namagrif	AGRIF zoom
nn_cln_update = 3 ln_spc_dyn = .true. rn_sponge_tra = 2880. rn_sponge_dyn = 2880.	baroclinic update frequency use 0 as special value for dynamics coefficient for tracer sponge layer [m2/s] coefficient for dynamics sponge layer [m2/s]
nam_tide	tide parameters
ln_tide_obcramp = .false. ln_tide_pot = .false. ln_read_tide_elev = .false. ln_read_tide_trans = .false. ln_compute_tide_trans = .false. ln_read_pot_charge = .false. rdtideramp = 2. nb_harmo = 1 cname(1) = 'M2'	
nambdy	unstructured open boundaries
ln_clim = .false. ln_vol = .false. ln_mask = .false. ln_tides = .false. ln_dyn_fla = .false. ln_tra_frs = .false. ln_dyn_frs = .false. nn_rimwidth = 9 nn_dtactl = 1 nn_volctl = 0	contain 1 (T) or 12 (F) time dumps and be cyclic total volume correction (see volbdy parameter) boundary mask from filbdy_mask (T), boundaries are on edges of domain (F) Apply tidal harmonic forcing with Flather condition Apply Flather condition to velocities Apply FRS condition to temperature and salinity Apply FRS condition to velocities width of the relaxation zone = 0, bdy data are equal to the initial state = 1, bdy data are read in 'bdydata .nc' files = 0, the total water flux across open boundaries is zero = 1, the total volume of the system is conserved
nambdy_tide	tidal forcing at unstructured boundaries
filtide = 'bdytide' tide_cpt = 'M2','S1' tide_speed = 28.984106, 15.000001 ln_tide_date = .false.	file name root of tidal forcing files names of tidal components used phase speeds of tidal components (deg/hour) adjust tidal harmonics for start date of run
nambfr	bottom friction
nn_bfr = 2	type of bottom friction : = 0 : no slip, = 2 : nonlinear friction = 3 : free slip,

rn_bfri1 = 4.e-4 rn_bfri2 = 1.e-3 rn_bfeb2 = 2.5e-3 ln_bfr2d = .false. rn_bfrien = 10.	= 1 : linear friction bottom drag coefficient (linear case) bottom drag coefficient (non linear case) bottom turbulent kinetic energy background (m^2/s^2) horizontal variation of the bottom friction coef multiplying factor of bfr
nambbc	bottom temperature boundary condition
ln_trabbc = .false. nn_geoflx = 0 rn_geoflx_cst = 86.4e-3	Apply a geothermal heating at the ocean bottom geothermal heat flux: = 0 no flux = 1 constant flux = 2 variable flux Constant value of geothermal heat flux [W/m^2]
nambbl	bottom boundary layer scheme
nn_bbl_ldf = 1 nn_bbl_adv = 0 rn_ahtbbl = 1000. rn_gambbl = 10.	diffusive bbl (=1) or not (=0) advective bbl (=1/2) or not (=0) lateral mixing coefficient in the bbl [m^2/s] advective bbl coefficient [s]
nameos	ocean physical parameters
nn_eos = 0 rn_alpha = 2.0e-4 rn_beta = 7.7e-4	type of equation of state and Brunt-Vaisala frequency = 0, UNESCO = 1, linear: $\rho(T) = \rho_{u0} * (1.028 - \alpha * T)$ = 2, linear: $\rho(T,S) = \rho_{u0} * (\beta * S - \alpha * T)$ thermal expansion coefficient (nn_eos= 1 or 2) saline expansion coefficient (nn_eos= 2)
namtra_adv	advection scheme for tracer
ln_traadv_cen2 = .false. ln_traadv_tvd = .true. ln_traadv_muscl = .false. ln_traadv_muscl2 = .false. ln_traadv_ubs = .false. ln_traadv_qck = .false.	2nd order centered scheme TVD scheme MUSCL scheme MUSCL2 scheme + cen2 at boundaries UBS scheme QUICKEST scheme
namtra_ldf	lateral diffusion scheme for tracer
Type of the operator : ln_traldf_lap = .true. ln_traldf_bilap = .false. Direction of action : ln_traldf_level = .false. ln_traldf_hor = .false. ln_traldf_iso = .true. Coefficient	laplacian operator bilaplacian operator iso-level horizontal (geopotential) iso-neutral

rn_aht_0 = 125. rn_ahtb_0 = 0. rn_aeiv_0 = 0.	horizontal eddy diffusivity for tracers [m ² /s] background eddy diffusivity for ldf_iso [m ² /s] eddy induced velocity coefficient [m ² /s]
namtra_dmp ! tracer: T	S newtonian damping
nn_hdmp = -1 nn_zdmp = 0 rn_surf = 50. rn_bot = 360. rn_dep = 800. nn_file = 0	horizontal shape = -1, damping in Med and Red Seas only vertical shape: =0 damping throughout the water column =1 no damping in the mixing layer (kz criteria), =2 no damping in the mixed layer (rho criteria) surface time scale of damping [days] bottom time scale of damping [days] depth of transition between rn_surf and rn_bot [meters] create a damping.coeff NetCDF file (=1) or not (=0)
namdyn_adv	formulation of the momentum advection
ln_dynadv_vec = .true. ln_dynadv_cen2 = .false. ln_dynadv_ubs = .false.	vector form (T) or flux form (F) flux form - 2nd order centered scheme flux form - 3rd order UBS scheme
namdyn_vor	option of physics/algorithm (not control by CPP keys)
ln_dynvor_ene = .false. ln_dynvor_ens = .false. ln_dynvor_mix = .false. ln_dynvor_eeen = .true.	enstrophy conserving scheme energy conserving scheme mixed scheme energy and enstrophy scheme
namdyn_hpg	Hydrostatic pressure gradient option
ln_hpg_zco = .false. ln_hpg_zps = .false. ln_hpg_sco = .true. ln_hpg_hel = .false. ln_hpg_wdj = .false. ln_hpg_djc = .false. ln_hpg_rot = .false. rn_gamma = 0.e0 ln_dynhpg_imp = .true.	z-coordinate - full steps z-coordinate - partial steps (interpolation) s-coordinate (standard jacobian formulation) s-coordinate (helsinki modification) s-coordinate (weighted density jacobian) s-coordinate (Density Jacobian with Cubic polynomial) s-coordinate (ROTated axes scheme) weighting coefficient (wdj scheme) time stepping: semi-implicit time scheme (T) centered time scheme (F)
namdyn_ldf	lateral diffusion on momentum
ln_dynldf_lap = .false. ln_dynldf_bilap = .true. ! Direction of action : ln_dynldf_level = .false. ln_dynldf_hor = .true. ln_dynldf_iso = .false. Coefficient	laplacian operator bilaplacian operator iso-level horizontal (geopotential) iso-neutral

rn_ahm_0.lap = 500. rn_ahmb_0 = 0. rn_ahm_0.blp = -1.25e10	horizontal laplacian eddy viscosity [m2/s] background eddy viscosity for ldf_iso [m2/s] horizontal bilaplacian eddy viscosity [m4/s]
namzdf	vertical physics
rn_avm0 = 1.0e-4 rn_avt0 = 1.0e-5 nn_avb = 0 nn_havtb = 0 ln_zdfevd = .true. nn_evdn = 0 rn_avevd = 10. ln_zdfnpc = .false. nn_npc = 0 nn_npcp = 365 ln_zdfexp = .false. nn_zdfexp = 3	vertical eddy viscosity [m2/s] vertical eddy diffusivity [m2/s] profile for background avt avm (=1) or not (=0) horizontal shape for avtb (=1) not (=0) enhanced vertical diffusion (evd) (T) not (F) evd apply on tracer (=0) on tracer and momentum (=1) evd mixing coefficient [m2/s] Non-Penetrative algorithm (T) or not (F) frequency of application of npc npc control print frequency time-stepping: split-explicit (T) implicit (F) time stepping number of sub-timestep for ln_zdfexp=T
namzdf_ric	richardson number dependent vertical diffusion
rn_rn5.alp = 5. nn_ric = 2	coefficient of the parameterization coefficient of the parameterization
namzdf_tke	turbulent eddy kinetic dependent vertical diffusion
rn_ediff = 0.1 rn_ediss = 0.7 rn_ebb = 60.0 rn_emin = 1.e-6 rn_emin0 = 1.e-4 nn_mxl = 3 nn_pdl = 1 ln_mxl0 = .true. rn_mxl0 = 0.01 ln_lc = .true.	coef. for vertical eddy coef. (avt=rn_ediff*mxl*sqrt(e)) coef. of the Kolmogoroff dissipation coef. of the surface input of tke minimum value of tke [m2/s2] surface minimum value of tke [m2/s2] mixing length: = 0 bounded by distance to surface and bottom = 1 bounded by local vertical scale factor = 2 first vertical derivative of mixing length bounded by 1 = 3 as 2 with distinct dissipative an mixing length scale Prandtl number function of richardson number =1, avt=pdl(Ri)*avm) not (=0, avt=avm) surface mixing length scale = F(wind stress) (T) or not (F) surface buoyancy length scale minimum value Langmuir cell parameterisation (Axell 2002)

rn_lc = 0.15 nn_etau = 1 rn_eft = 0.05 nn_htau = 1	coef. associated to Langmuir cells penetration of tke below the mixed layer (ML) due to internal and inertial waves = 0 no penetration = 1 add a tke source below the ML = 2 add a tke source just at the base of the ML = 3 as = 1 applied on HF part of the stress fraction of surface tke value which penetrates below the ML (nn_etau=1 or 2) type of exponential decrease of tke penetration below the ML = 0 constant 10 m length scale = 1 0.5m at the equator to 30m poleward of 40 degrees
namzdf_kpp	K-Profile Parameterization dependent vertical mixing
ln_kpprimix = .true. rn_difmiw = 1.0e-04 rn_difsiw = 0.1e-04 rn_riinfty = 0.8 rn_difri = 0.0050 rn_bvsqcon = -0.01e-07 rn_difcon = 1. nn_avb = 0 nn_ave = 1	shear instability mixing constant internal wave viscosity [m ² /s] constant internal wave diffusivity [m ² /s] local Richardson Number limit for shear instability maximum shear mixing at Rig = 0 [m ² /s] Brunt-Vaisala squared for maximum convection [1/s ²] maximum mixing in interior convection [m ² /s] horizontal averaged (=1) or not (=0) on avt and amv constant (=0) or profile (=1) background on avt
namzdf_gls	GLS vertical diffusion
rn_emin = 1.e-6 rn_epsmin = 1.e-12 ln_length_lim = .true. rn_clim_galp = 0.53 ln_crban = .true. ln_sigpsi = .true. rn_crban = 100. rn_charn = 70000. nn_tkebc_surf = 1 nn_tkebc_bot = 1 nn_psibc_surf = 1 nn_psibc_bot = 1 nn_stab_func = 2 nn_clos = 1	minimum value of e [m ² /s ²] minimum value of eps [m ² /s ³] limit on the dissipation rate under stable stratification galperin limit Activate or not Craig and Banner 1994 constant for wb tke flux Charnock constant for wb induced roughness length surface tke condition bottom tke condition surface psi condition bottom psi condition stability function (0=Galp, 1= KC94, 2=CanutoA, 3=CanutoB) predefined closure type (0=MY82, 1=k-eps, 2=k-w, 3=Gen)
namzdf_ddm	double diffusive mixing parameterization
rn_avts = 1.e-4	maximum avs (vertical mixing on salinity)

rn_hsbfr = 1.6	heat/salt buoyancy flux ratio
namzdf_tmx	tidal mixing parameterization
rn_htmx = 500.	vertical decay scale for turbulence (meters)
rn_n2min = 1.e-8	threshold of the Brunt-Vaisala frequency (s-1)
rn_tfe = 0.333	tidal dissipation efficiency
rn_me = 0.2	mixing efficiency
ln_tmx_itf = .FALSE.	ITF specific parameterisation
rn_tfe_itf = 1.	ITF tidal dissipation efficiency
namhsb	Heat and salt budgets
ln_diahsb = .false.	check the heat and salt budgets (T) or not (F)

The same number of particles was deployed in the same locations as described in **Section 3.2.2** and the all methods here are the same as described in **Section 3.2**. The time it takes the particle from crossing into the basin and reaching their release position is similar in both model runs, most particles cross within the first one or two month (**Figure A.1**). However, about 10% fewer particles cross into the basin (**Table A.2**). This is a result of the less energetic boundary current and the resulting weaker advection that also causes deeper mixed layers (located in the north and not the west). Exactly 172,765 trajectories crossed into the basin instead of the 198,200 in the ORCA-NO6 model run. However, the proportions are similar, in that most water entered the basin from the south below the surface, very few stayed in the basin or entered the basin below 30 m but arrived at their release point in the surface. Please refer to **Table 3.1** and **Table A.2** for the exact numbers.

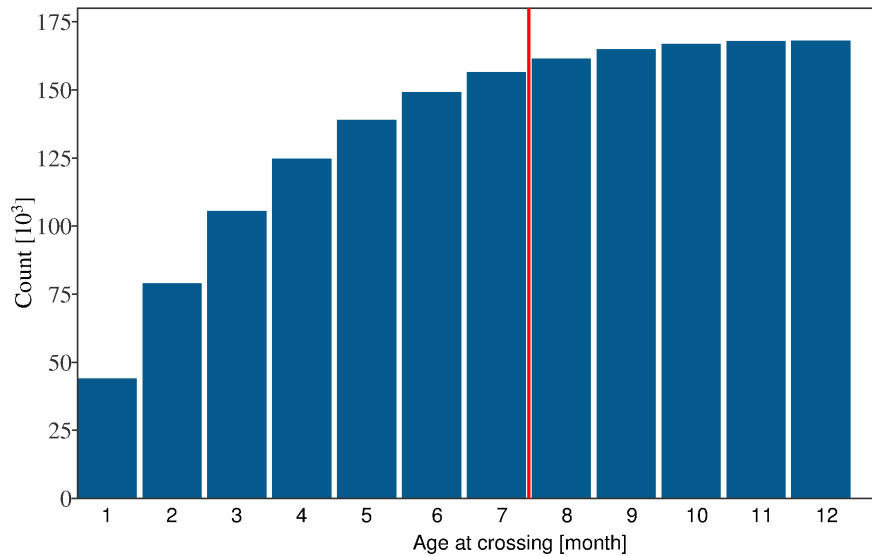


Figure A.1: Number of particles that cross the 2500 m isobath within a certain time after being released. The red line shows the 7 month threshold that is used in this chapter.

Figure A.2: Number of trajectories with different criteria

	Count	% of total
Total	570,240	
Crossings <30 m	172,765	30%
Crossing with in 7 mth	155,371	
• Stay <30 m	122,664	
• Leave top 30 m	33,707	
Crossing later	17,394	3%
• Stay <30 m	13,742	
• Leave top 30 m	3652	
Crossings >30 m	2072	<1%
Enter in south	385,891	67.7 %
• Stay <30 m	32,707	
• Leave top 30 m	353,184	
Stay in basin	9512	1.6%
• Stay <30 m	2104	
• Leave top 30 m	7408	

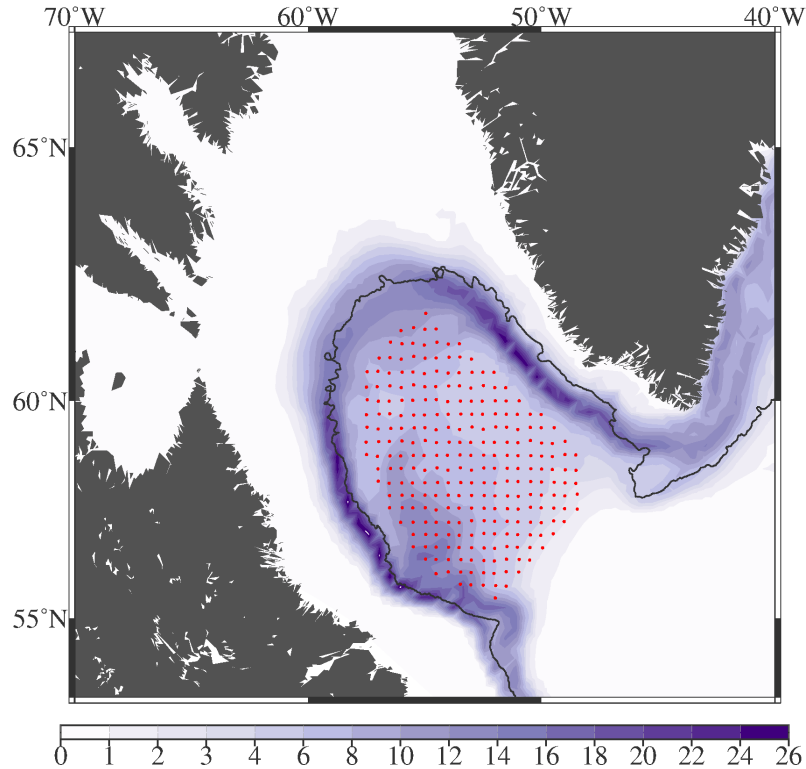


Figure A.3: Percentage of the 198,200 trajectories (that cross into the basin) that pass through each 0.5° longitude \times 0.3° latitude grid point. The black contour shows the 2500 m isobath (i.e. the boundary of the basin). The red dots show the release positions of the particles.

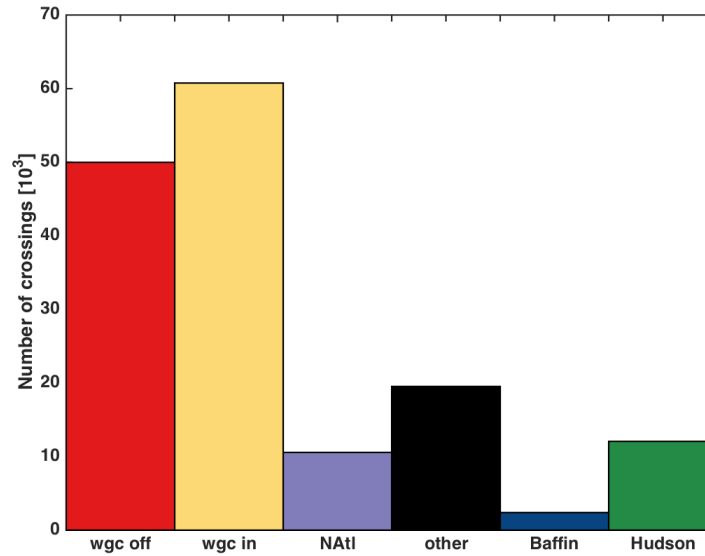


Figure A.4: Number of crossings origination in each of the origin, East Greenland Current offshore (red). East Greenland Current inshore (yellow), other regions in the North Atlantic (purple), unidentified origins (black), Baffin Bay (blue) and Hudson Strait. The five sources are shown in **Figure 3.7**

Particles mainly enter the region via the EGC and then follow the 2500 m isobath around the basin (**Figure A.3**). There seem to be two regions in which particles spread into the basin, on in the northeast corner and a second, stronger one in the southwest. This is different from **Figure 3.14**, where trajectories were concentrated along the east but not the western side of the basin.

In ORCA-N01 water enters the basin mainly Baffin Bay and Hudson Bay (**Figure A.4**). In particular. In ORCA-N06 only 5 particles from Hudson Bay entered the basin, now 7 % of the 172,765 particles from Hudson Bay reach the basin. Additionally, 1.5% of particles originating in Baffin Bay also reach the basin. The EGC is still the dominant source of water advected to the basin but now more inshore than offshore water reaches the basin (35 % and 29%, respectively).

The main pathways of water into the Labrador Sea basin is in the southwest (**Figure A.5**). Only very few particles enter the basin in the southeast and northeast. Additionally, the water entering in the southwest is extremely fresh and freshwater fluxes exceed 0.23 mSv. The freshest water is advected in the far southwest. The water adjacent to the it in the north is also fresh but with salinities of 34.91 compared to the 34.87 to the south of its. The water advected to the basin in the far southwest is especially fresh compared to the water advected just north of it. This is mainly due to the EGC inshore and offshore water compared to which the Hudson Bay and Baffin Bay water are still

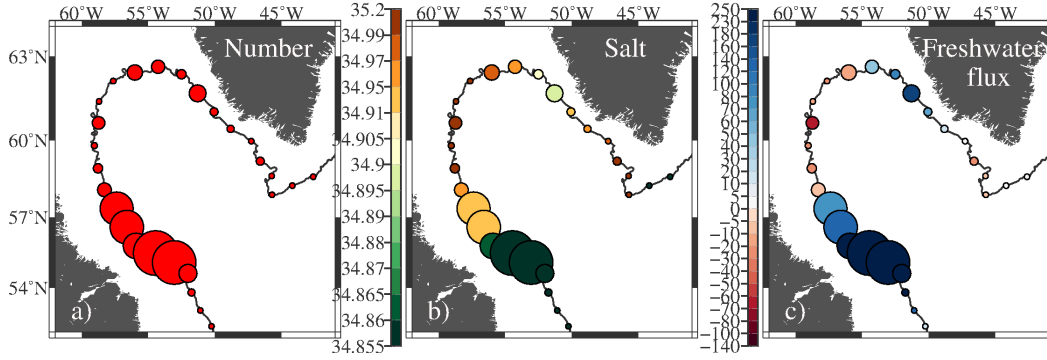


Figure A.5: Number of crossings origination in each of the origin, East Greenland Current offshore (red). East Greenland Current inshore (yellow), other regions in the North Atlantic (purple), unidentified origins (black), Baffin Bay (blue) and Hudson Strait. The five sources are shown in **Figure 3.7**

not very important (**Figure A.6**). The water of unidentified source also contributes to the freshwater fluxes to the basin.

There is no seasonal cycle in the number of crossings that are observed with ORCA-N01. The seasonal salinity of the water entering the basin is opposite to the salinity observed in ORCA-N06, where we saw two period of freshwater entering the basin, on in March and the second in September. Here, using ORCA-N01, the freshest water enters the basin in Jan – Mar. After that salinities increase until September, which is the month with the saltiest water advected to the basin. The speeds with which the particles cross into the basin shows very little variability and is slower than in ORCA-N06. The freshwater fluxes closely mirror the observed salinities since there is no seasonality in the number of crossings. Freshwater is brought to the basin year around with the maximum rate in March and minimum rate in September.

A large year-to-year variability is found in the crossings in ORCA-N01, but the main pathway of water into the basin is in the southwest throughout the entire 14 years. Note that ORCA-N01 is only available until 2007. Two years (2004 and 2005) stand out with many crossings all along the western side. In 2006 a very small number of particles reached the basin.

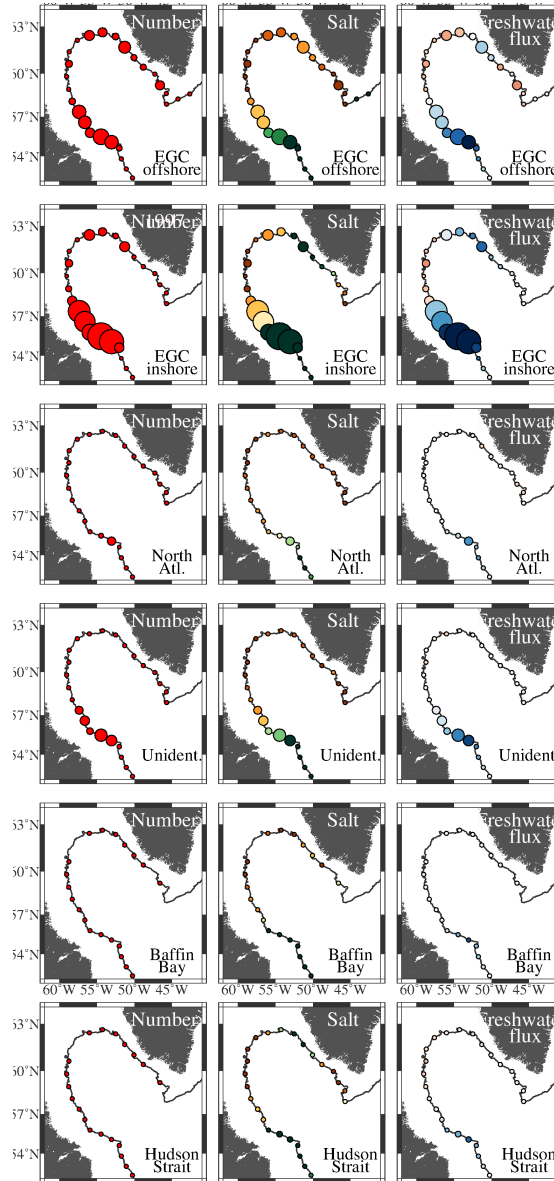


Figure A.6: Number of crossings origination in each of the origin, East Greenland Current offshore (red). East Greenland Current inshore (yellow), other regions in the North Atlantic (purple), unidentified origins (black), Baffin Bay (blue) and Hudson Strait. The five sources are shown in **Figure 3.7**

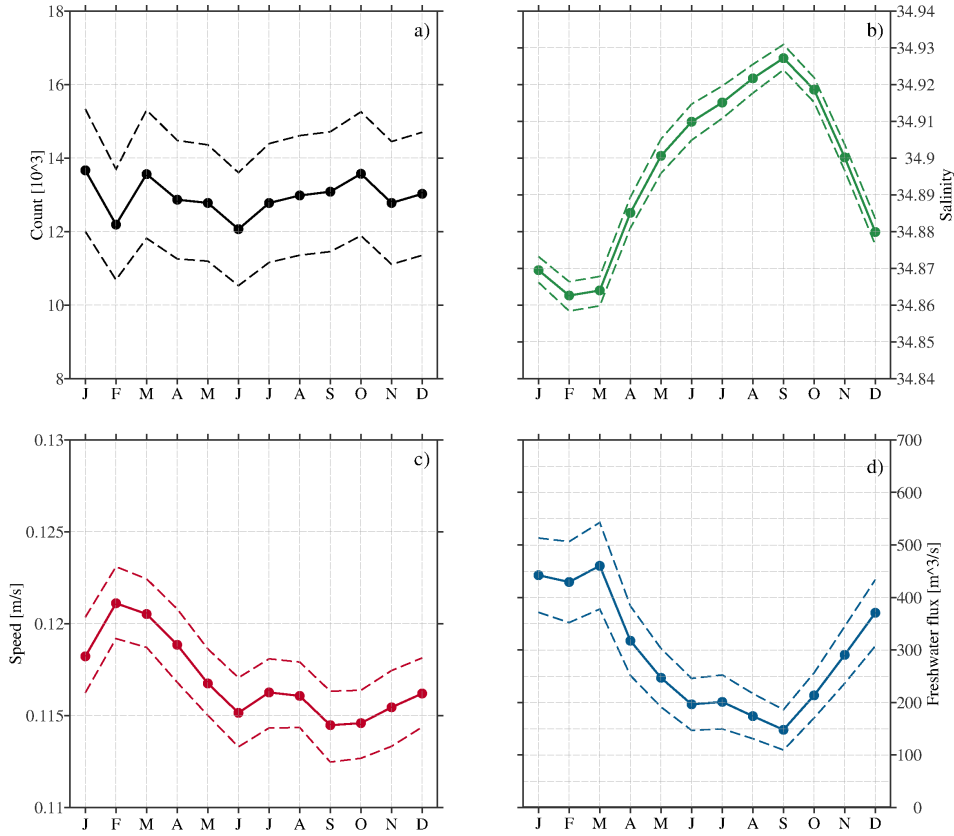


Figure A.7: a) The seasonal cycle of the number of particles crossing the 2500 m isobath (solid line) and the error associated with it, calculated using a Monte Carlo approach (dashed line). b) the seasonal average salinity of the crossing particles (solid line) and the associated error (dashed line). The black horizontal line shows the reference salinity of 34.95 that is used to calculate the freshwater fluxes. c) the average speed with which the particles cross into the basin (solid line) and the associated error (dashed line). d) the accumulated seasonal freshwater flux into the basin (solid line) and the error (dashed line). Positive fluxes show freshwater fluxes into the basin and negative fluxes show fluxes of salty water into the basin.

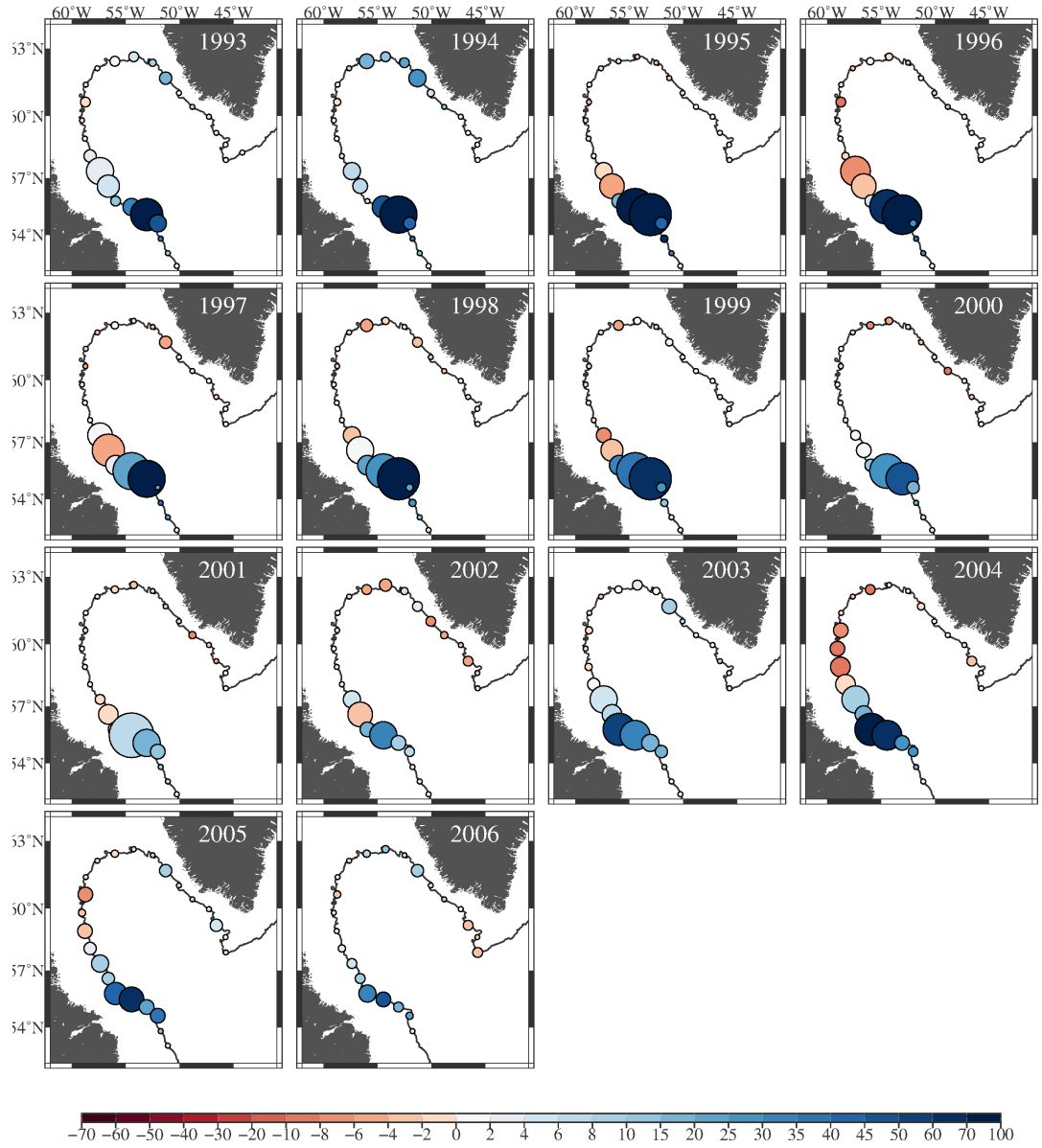


Figure A.8: The relative number of crossings per 50 km boundary section is indicated by the size of the red circles for 1993 – 2012. The color indicates the amount of freshwater brought into the region at each section [m^3/s]

Appendix B

Parameters of ORCA-N06

B.1 Parameters in ORCA-N06

The namelist shown here lists all parameters used for the creation of the model, including eddy viscosity and diffusivity, runoff etc. A detailed description of these parameters can be found in http://www.nemo-ocean.eu/Media/Files/NEMO_book_V3_4.pdf. Parameters not listed here can be found in the parameter table for ORCA-N01 in **Appendix A**.

namsbc	Surface Boundary Condition (surface module)
nn_fsbc = 1 nn_ice_embd = 1 ln_dm2dc = .false. ln_rnf = .true. ln_ssr = .true. nn_fwb = 1	frequency of surface boundary condition computation =0 levitating ice (no mass exchange) =1 levitating ice with mass and salt exchange. No pressure effect =2 embedded sea-ice (salt and mass exchanges, pressure) daily mean to diurnal cycle on short wave runoffs Sea Surface Restoring on T and/or S FreshWater Budget: =0 unchecked =1 global mean of e-p-r set to zero at each time step =2 annual global mean of e-p-r set to zero =3 global emp set to zero and spread out over erp area
namlbc	lateral momentum boundary condition
rn_shlat = 0. ln_shlat2d = .true.	shlat = 0 , free slip 0 ; shlat ; 2, partial slip shlat = 2, no slip 2 ; shlat, strong slip Read and use a 2d (point by point)
nambfr	bottom friction
nn_bfr = 2	type of bottom friction : = 0 : free slip, = 1 : linear friction = 2 : nonlinear friction
nambbc	bottom temperature boundary condition
ln_trabbc = .false. nn_geoflx = 0	Apply a geothermal heating at the ocean bottom geothermal heat flux: = 0 no flux
namtbl	bottom boundary layer scheme
nn_bbl_ldf = 1 nn_bbl_adv = 0 rn_ahttbl = 1000. rn_gamtbl = 10.	diffusive bbl (=1) or not (=0) advective bbl (=1/2) or not (=0) lateral mixing coefficient in the bbl [m ² /s] advective bbl coefficient [s]
namsbc_ssr	surface boundary condition : sea surface restoring
rn_deds = -33.333	magnitude of the damping on salinity [mm/day]
namtra_adv_mle	mixed layer eddy parametrisation (Fox-Kemper param)

ln_mle = .false.	(T) use the Mixed Layer Eddy (MLE) parameterisation
namtra_ldf	lateral diffusion scheme for tracers
ln_traldf_lap = .true. ln_traldf_bilap = .false. ln_traldf_level = .false. ln_traldf_hor = .false. ln_traldf_iso = .true. ln_traldf_grif = .true. rn_aht_0 = 125. rn_ahtb_0 = 0. rn_aeiv_0 = 0. rn_slpmax = 0.01	Operator type: laplacian operator bilaplacian operator Direction of action: iso-level horizontal (geopotential) iso-neutral Griffies parameters use griffies triads horizontal eddy diffusivity for tracers [m ² /s] background eddy diffusivity for ldf_iso [m ² /s] eddy induced velocity coefficient [m ² /s] slope limit
namtra_dmp ! tracer: T	S newtonian damping
ln_tradmp = .false. nn_zdmp = 0 cn_resto = 'resto.nc'	add a damping termn (T) or not (F) vertical shape =0 damping throughout the water column =1 no damping in the mixing layer (kz criteria) =2 no damping in the mixed layer (rho crieria) Name of file containing restoration coefficient field
namdyn_adv	formulation of the momentum advection
ln_dynzad_zts = .true.	Use (T) sub timestepping for vertical momentum advection
nam_vvl	vertical coordinate options
ln_vvl_zstar = .true. ln_vvl_ztilde = .false. ln_vvl_layer = .false. ln_vvl_ztilde_as_zstar = .false. ln_vvl_zstar_at_eqtor = .false. rn_ahe3 = 0.0e0 rn_rst_e3t = 30.e0 rn_lf_cutoff = 5.0e0 rn_zdef_max = 0.9e0 ln_vvl_dbg = .true.	zstar vertical coordinate ztilde vertical coordinate: only high frequency variations full layer vertical coordinate ztilde vertical coordinate emulating zstar ztilde near the equator thickness diffusion coefficient ztilde to zstar restoration timescale [days] cutoff frequency for low-pass filter [days] maximum fractional e3t deformation debug prints (T/F)
namdyn_ldf	lateral diffusion on momentum
ln_dynldf_lap = .false. ln_dynldf_bilap = .true. ln_dynldf_level = .false.	Type of the operator : laplacian operator bilaplacian operator Direction of action : iso-level

ln_dynldf_hor = .true.	horizontal (geopotential)
ln_dynldf_iso = .false.	iso-neutral
	Coefficient
rn_ahm_0_lap = 500.	horizontal laplacian eddy viscosity [m2/s]
rn_ahmb_0 = 0.	background eddy viscosity for ldf_iso [m2/s]
rn_ahm_0_blp = -1.25e10	horizontal bilaplacian eddy viscosity [m4/s]
namzdf	vertical physics
rn_avm0 = 1.0e-4	vertical eddy viscosity [m2/s]
rn_avt0 = 1.0e-5	vertical eddy diffusivity [m2/s]
rn_avevd = 10.	evd mixing coefficient [m2/s]
ln_zdfnpc = .false.	Non-Penetrative Convective algorithm (T) or not (F)
nn_npc = 0	frequency of application of npc
namzdf_tke	turbulent eddy kinetic dependent vertical diffusion
rn_mxl0 = 0.01	surface buoyancy lenght scale minimum value

Bibliography

- Aagaard, K. and E. Carmack, 1989: The role of sea ice and other fresh water in the Arctic circulation. *Journal of Geophysical Research*, **94**, 14,485–14,498.
- Avsic, T., J. Karstensen, U. Send, and J. Fischer, 2006: Interannual variability of newly formed Labrador Sea Water from 1994 to 2005. *Geophysical Research Letters*, **33**, L21 802.
- Bacon, S., A. Marshall, N. Holliday, Y. Aksenov, and S. Dye, 2014: Seasonal variability of the East Greenland Coastal Current. *Journal of Geophysical Research: Oceans*, **10.1002/2013JC009279**, 3967–3987.
- Bacon, S., G. Reverdin, L. Rigor, and H. Smith, 2002: A freshwater jet on the east Greenland shelf. *Journal of Geophysical Research*, **107**.
- Bamber, J., M. van den Broeke, J. Ettema, J. Lenaerts, and E. Rignot, 2012: Recent large increase in freshwater fluxes from Greenland into the North Atlantic. *Geophysical Research Letters*, **39**, L19 501.
- Belkin, I., S. Levitus, J. Antonov, and S.-A. Malmberg, 1998: 'Great Salinity Anomaly' in the North Atlantic. *Progress in Oceanography*, **41**, 1–68.
- Bersch, M., 2002: North Atlantic Oscillation-induced changes of the upper layer circulation in the northern North Atlantic Ocean. *Journal of Geophysical Research*, **107**, C10.
- Blanke, B. and P. Deleclue, 1993: Variability of the tropical atlantic ocean simulated by a general circulation model with two different mixed-layer physics. *Journal of Physical Oceanography*, **23**, 1363–1388.
- Blanke, B. and S. Raynaud, 1997: Kinematics of the Pacific Equatorial Undercurrent: An Eulerian and Lagrangian approach from CM results. *Journal of Physical Oceanography*, **27**, 1038–1053.
- Böning, C., F. Bryan, W. Holland, and R. Doscher, 1996: Deep-water formation and meridional overturning in a high-resolution model of the North Atlantic. *Journal of Physical Oceanography*, **26**, 1142–1164.

- Bower, A., M. Lozier, S. Gary, and C. Boning, 2009: Interior pathways of the North Atlantic meridional overturning circulation. *Nature*, **459**, 243.
- Bracco, A. and J. Pedlosky, 2003: Vortex generation by topography in locally unstable baroclinic flows. *Journal of Physical Oceanography*, **33**, 207–219.
- Brandt, P., A. Funk, L. Czeschel, C. Eden, and C. Böning, 2007: Ventilation and transformation of Labrador Sea Water and its rapid export in the deep Labrador Current. *Journal of Physical Oceanography*, **37**, 946–961.
- Brandt, P., A. Schott, A. Funk, and C. Martins, 2004: Seasonal to interannual variability of the eddy field in the Labrador Sea from satellite altimetry. *Journal of Geophysical Research*, **109**, C02028.
- Brauer, A., G. Haug, P. Dulski, D. Sigman, and J. Negendank, 2008: An abrupt wind shift in western Europe at the onset of the Younger Dryas cold period. *Nature*, **1**, 520–523.
- Chanut, J. and B. Barnier, 2008: Mesoscale Eddies in the Labrador Sea and Their Contribution to Convection and Restratification. *Journal of Physical Oceanography*, **38**, 1617–1643.
- Clarke, M., 1992: Recirculation components to the deep boundary current of the northern North Atlantic. *Progress in Oceanography*, **29**, 283–383.
- Clarke, R., 1977: Transport through the Cape Farewell-Flemish Cap section. *Rapports et Proces-Verbaux des Reunions, Conseil International pour l'Exploration de la Mer*, 120–130.
- Clarke, R., 1983: The formation of Labrador Sea Water. Part I: Large-scale processes. *Journal of Physical Oceanography*, **13**, 1764–1778.
- Cuny, J. and R. Rhines, 2002: Labrador Sea Boundary Currents and the Fate of the Irminger Sea Water. *Journal of Physical Oceanography*, **32**, 627–647.
- Curry, B., C. Lee, B. Petrie, R. Moritz, and R. Kwok, 2014: Multiyear volume, liquid freshwater, and sea ice transport through Davis Strait, 2004–2010. *Journal of Physical Oceanography*, **44**.
- da Silva, A., A. Young, and S. Levitus, 1994: Algorithms and Procedures. *NOAA Atlas NESDIS 6*, **1**, 83.
- Daniault, N., P. Lherminier, and H. Mercier, 2012: Circulation and Transport at the Southeast Tip of Greenland. *Journal of Physical Oceanography*, **41**, 437–457.
- de Jong, M., A. Bower, and H. Furey, 2012: Two years of observations of warm-core anticyclones in the Labrador Sea and their seasonal cycle in heat and salt stratification. *Journal of Physical Oceanography*, **44**, 427–444.

- Dee, D., et al., 2011: The ERA-Interim reanalysis: configuration and performance of data assimilation system. *Quarterly Journal of the Royal Meteorological Society*, **137**, 553–597.
- Dengler, M., F. Schott, C. Eden, P. Brandt, J. Fischer, and R. Zantopp, 2004: Break-up of the Atlantic deep western boundary current into eddies at 8° S. *Letters to Nature*, **432**, 1018–1020.
- Deser, C. and M. Blackmon, 1993: Surface Climate Variations over the North Atlantic Ocean during Winter: 1900 - 1989. *Journal of Climate*, **6**, 1743–1753.
- Dickson, R., J. Lazier, J. Meincke, P. Rhines, and J. Swift, 1996: Long-term coordinated changes in the convective activity of the North Atlantic. *Progress in Oceanography*, **18**, 241–295.
- Dickson, R., J. Meincke, S. Malmberg, and A. Lee, 1988: The 'Great Salinity Anomaly' in the Northern North Atlantic 1968 - 1982. *Progress in Oceanography*, **20**, 103–151.
- Eden, C. and C. Böning, 2002: Sources of Eddy Kinetic Energy in the Labrador Sea. *Journal of Physical Oceanography*, **32**, 3346–3363.
- Emery, W. and R. Thomson, 1997: Data Analysis Methods in Physical Oceanography. *Elsevier*.
- Fichefet, T. and M. M. Maqueda, 1997: Sensitivity of a global sea ice model to the treatment of ice thermodynamics and dynamics. *Journal of Geophysical Research*, **102**, 12,609–12,646.
- Fischer, J. and F. Schott, 2001: Labrador Sea Water tracked by Profiling Floats - From the Boundary Current to the open North Atlantic. *Journal of Physical Oceanography*, **32**, 574–584.
- Fischer, J., F. Schott, and M. Dengler, 2004: Boundary Circulation at the Exit of the Labrador Sea. *Journal of Physical Oceanography*, **34**, 1548–1570.
- Fratantoni, P. and R. Pickart, 1999: The western North Atlantic shelfbreak current system in summer. *Journal of Physical Oceanography*, 2509–2533.
- Gaillard, F., E. Autret, V. Thierry, and P. Galaup, 2009: Quality Control of Large Argo Datasets. *Journal of Atmospheric and Oceanic Technology*, **26**, 337–351.
- Gelderloos, R., F. Straneo, and C. Katsman, 2012: The Mechanism behind the Temporary Shutdown of Deep Convection in the Labrador Sea: Lessons from the Great Salinity Anomaly Year 1968-71. *Journal of Climate*, **25**, 6743–6755.
- Häkkinen, S., 2002: Surface salinity variability in the northern North Atlantic during recent decades. *Journal of Geophysical Research*, **107** (C12), 8003.

- Häkkinen, S. and P. Rhines, 2004: Decline of subpolar North Atlantic Circulation During the 1990s. *Science*, **304**, 555–559.
- Hall, M. and H. Bryden, 1998: Direct estimates and mechanisms of ocean heat transport. *Deep Sea Research Part A*, 339–359.
- Hatun, H., C. Eriksen, and P. Rhines, 2007: Buoyant eddies entering the Labrador Sea observed with Gliders and altimetry. *Journal of Physical Oceanography*, **37**, 2838–2854.
- Hatun, H., A. Sando, H. Drange, B. Hansen, and H. Valdimarsson, 2005: Influence of the Atlantic subpolar gyre on the thermohaline circulation. *Science*, **309**, 1841–1844.
- Holliday, N., A. Meyer, S. Bacon, S. Alderson, and B. de Cuevas, 2007: Retroflection of part of the east Greenland current at Cape Farewell. *Geophysical Research Letters*, **34**, L07 609.
- Houghton, R. and M. Visbeck, 2002: Quasi-decadal salinity fluctuations in the Labrador Sea. *Journal of Physical Oceanography*, **32**, 687–701.
- Hurrell, J., 1995: Decadal trends in the North Atlantic Oscillation regional temperatures and precipitation. *Science*, **269**, 676–679.
- Ikedo, M., 1987: Salt and heat balances in the Labrador Sea using a box model. *Atmosphere - Ocean*, **25**, 197–223.
- Ivchenko, V., N. Wells, D. Aleynik, and A. Shaw, 2012: Variability of heat and salinity content in the North Atlantic in the last decade. *Ocean Science*, **6**, 719–735.
- Jacob, D., H. Goettel, J. Jungclauss, M. Muskulus, R. Podzun, and J. Marotzke, 2005: Slowdown of the thermohaline circulation causes enhanced maritime climate influence and snow over Europe. *Geophysical Research Letters*, **32**, L21 711.
- Jahn, A. and M. Holland, 2013: Implications of Arctic sea ice changes for North Atlantic deep convection and meridional overturning circulation in CCSM4-CMIP5 simulations. *Geophysical Research Letters*, **40** (6), 1206–1211.
- Jones, H. and J. Marshall, 1993: Convection with rotation in a neutral ocean: A study of open ocean deep convection. *Journal of Physical Oceanography*, **23**, 1009–1039.
- Katsman, C., M. Spall, and R. Pickart, 2004: Boundary Current Eddies and Their Role in the Restratification of the Labrador Sea. *Journal of Physical Oceanography*, **34**, 1967–1983.
- Khatriwala, S. and M. Visbeck, 2002: An estimate of eddy-induced circulation in the Labrador Sea. *Geophysical Research Letters*, **27**, 2277–2280.

- Large, W. and S. Yeager, 2004: Diurnal to decadal global forcing for ocean and sea-ice models: The data set and flux climatologies. *NCAR Technical Note, National Center for Atmospheric Research*.
- Latarius, K. and D. Quadfasel, 2010: Seasonal to inter-annual variability of temperature and salinity in the Greenland Sea Gyre: heat and freshwater budgets. *Tellus*, 497–515.
- Lavender, K., R. Davis, and W. Owens, 2002: Observations of Open-Ocean Deep Convection in the Labrador Sea from Subsurface Floats. *Journal of Physical Oceanography*, **32**, 511–526.
- Lavender, K., R. Davis, and W. B. Owens, 2000: Mid-depth recirculation observed in the interior Labrador and Irminger seas by direct velocity measurements. *Nature*, **407**, 66–69.
- Lavender, K., W. Owens, and R.E.Davis, 2005: The mid-depth circulation of the sub-polar North Atlantic Ocean as measured by subsurface floats. *Deep-Sea Research I*, **52**, 767 – 785.
- Lazier, J., 1973: The renewal of Labrador Sea Water. *Deep Sea Research*, **4**, 341–353.
- Lazier, J., 1980: Oceanographic Conditions at Ocean Weather Ship Bravo, 1964 - 1974. *Atmosphere-Ocean*, **18**, 227–238.
- Lazier, J., 1995: The salinity decrease in the Labrador Sea over the past thirty years. *Ocean Observations, National Academy Press, Washington DC*, 295.
- Lazier, J., 2002: .
- Levermann, A., A. Griesel, M. Hofmann, M. Montoya, and S. Rahmstorf, 2005: Dynamic sea level changes following changes in the thermohaline circulation. *Climate Dynamics*, **24**, 347–354.
- Levitus, S., J. Antonov, T. Boyer, and C. Stephens, 2000: Warming of the World Ocean. *Science*, **287**, 5461.2225.
- Lilly, J., P. Rhines, F. Schott, K. Lavender, J. Lazier, U. Send, and E. D’Asaro, 2003: Observraions of the Labrador Sea eddy field. *Progress in Oceaongraphy*, **59**, 75 – 176.
- Madec, G., 2008: NEMO reference manual, ocean dynamic component: NEMO-OPA, Notes du pole de modelisation. *Technical Report, Institute Pierre Simmon Lablace, France*, **27**.
- Manabe, S. and R. Stouffer, 1995: Simulation of abrupt climate change induced by freshwater input to the North Atlantic Ocean. *Nature*, **378**, 165–167.
- Markus, T., J.C.Stroev, and J. Miller, 2009: Recent changes in Arctic sea ice melt onset, freezeup, and melt season length. *Journal of Geophysical Research: Oceans*, **114**, C12024.

- Marsh, R., 2000: Recent variability of the North Atlantic thermohaline circulation inferred from surface heat and freshwater fluxes. *Journal of Climate*, **13**, 3239–3260.
- Marshall, J. and F. Schott, 1998: Open-Ocean Convection: Observations, Theory and Models. *Reviews of Geophysics*, **37**, 1–64.
- Marshall, J., et al., 1998: The Labrador Sea Deep Convection Experiment. *Bulletin of American Meteorology Society*, **797**, 2033–2058.
- Mauritzen, C., 1996: Production of dense overflow waters feeding the North Atlantic across the Greenland-Scotland Ridge. Part I: Evidence for a revised circulation scheme. *Deep-Sea Research I*, **43**, 769–806.
- Mauritzen, C. and S. Häkkinen, 1999: On the relationship between dense water formation and the 'Meridional Overtuning Cell' in the North Atlantic Ocean. *Deep-Sea Research I*, **46**, 877–894.
- Moore, G., R. Pickart, I. Renfrew, and K. Vage, 2014: What causes the location of the air-sea turbulent heat flux maximum over the Labrador Sea? *Geophysical Research Letters*.
- Moore, G. and I. Renfrew, 2002: Open-Ocean Convection: Observations, Theory and Models. *Journal of Climate*, **15**, 2020–2037.
- Moore, G. and I. Renfrew, 2005: Tip Jets and Barrier Winds: A QuickSCAT Climatology of High Wind Speed Events around Greenland. *Journal of Climate*, **18**, 3713–3725.
- Moore, G., I. Renfrew, and R. Pickart, 2013: Multidecadal Mobility of the North Atlantic Oscillation. *Journal of Climate*, **26**, 2453–2466.
- Mortensen, J. and H. Valdimarsson, 1999: Thermohaline changes in the Irminger Sea. *ICES C.M.*, **16**.
- Munk, W. and C. Wunsch, 1998: Abyssal recipes II: Energetics of tidal and wind mixing. *Deep Sea Research, Part I*, **45**, 1977–2010.
- Myers, P., 2005: Impact of freshwater from the Canadian Arctic Archipelago on Labrador Sea Water formation. *Geophysical Research Letters*, **32**, L06 605.
- Myers, P., C. Donnelly, and M. Ribergaard, 2009: Structure and variability of the West Greenland Current in Summer derived from 6 repeat standard sections. *Progress in Oceanography*, **80**, 93–112.
- Myers, R., N.Kulan, and M. Ribergaard, 2007: Irminger Water variability in the West Greenland Current. *Geophysical Research Letters*, **34**, L17 601.

- Mysak, L., D. Manak, and R. Marsden, 1990: Sea-ice anomalies in the Greenland and Labrador Seas during 1901 - 1984 and their relation to interdecadal Arctic climater cycle. *Climate Dynamics*, **5**, 111–133.
- Nikolopoulos, A., R. Pickart, P. Fratantoni, K. Shimada, D. Torres, and E. Jones, 2009: The western Arctic boundary current at 152°W: Structure, variability and transport. *Deep-Sea Research II*, **56**, 1164–1181.
- Palter, J., M. Lozier, and K. Lavender, 2007: How does Labrador Sea Water enter the Deep Western Boundary Current? *Journal of Physical Oceanography*, **38**, 968.
- Pickart, R., 1992: Water mass components of the North Atlantic deep western boundary current. *Deep-Sea Research*, **39**, 1553.
- Pickart, R., G. Moore, A. MacDonald, I. Renfrew, J. Walsh, and W. Kessler, 2009: Seasonal Evolution of Alutian Low Pressure System: Implications for the North Pacific Subpolar Circulation. *Journal of Physical Oceanography*, **39**, 1317–1339.
- Pickart, R. and M. Spall, 2007: Impact of Labrador Sea Convection on the North Atlantic Meridional Overturning Circulation. *Journal of Physical Oceanography*, **37**, 2207–2227.
- Pickart, R., D. Torres, and R. Clarke, 2002: Hydrography of the Labrador Sea during Active Convection. *Journal of Physical Oceanography*, **32**, 428–457.
- Pohlman, H., F. Sienz, and M. Latif, 2006: Influence of the Multidecadal Atlantic Meridional Overturning Circulation Variability on European Climate. *Journal of Climate*, **19**, 6062–6067.
- Prater, M., 2002: Eddies in the Labrador Sea as Observed by Profiling RAFOS Floats and Remote Sensing. *Journal of Physical Oceanography*, **32**, 411–427.
- Prince, J., R. A. Weller, and R. Pinkel, 1986: Seasonal Evolution of Alutian Low Pressure System: Implications for the North Pacific Subpolar Circulation. *Journal of Geophysical Research*, **91**, 8411–8427.
- Renfrew, I., G. Moore, P. Guest, and K. Bumke, 2002: A comparison of surface layer and surface turbulent flux observations over the Labrador Sea with ECMWF analyses and NCEP reanalyses. *Journal of Physical Oceanography*, **32**, 383–400.
- Rhein, M., et al., 2002: Labrador Sea water: Pathways, CFC-inventory, and fromation rates. *Journal of Physical Oceanography*, **32**, 648–665.
- Rhines, P. and J. Lazier, 1995: A 13-year record of convection and climate change in the deep Labrador Sea. *Abstract Report of NOAA Principal Investigator's Meeting, Miami, FL, NOAA*, 50–55.

- Robson, J., D. Hodson, E. Hawkins, and R. Sutton, 2014: Atlantic overturning in decline? *Nature Geoscience*, **7**, 2–3.
- Roemmich, D. and J. Gilson, 2009: The 2004–2008 mean and annual cycle of temperature, salinity and steric height in the global ocean from the Argo Program. *Progress in Oceanography*, 81–100.
- Rykova, T., F. Straneo, and A. Bower, 2014: Seasonal and interannual variability of the West Greenland Current System in the Labrador Sea in 1993 – 2008. *Journal of Geophysical Research: Oceans*, **10.1002/2014JC010386**, 1318–1332.
- Sandstrom, J., 1868: Meteorologische Studien im Schwedischen Hochgebirge. *Goteborgs K. Vetensk. Vitterhetssamhallets Handkl.*, 48.
- Sarafanov, A., A. Falina, P. Lherminier, H. Mercies, A. Sokov, and C. Gourcuff, 2010: Assessing decadal changes in the Deep Western Boundary Current absolute transport southeast of Cape Farewell, Greenland, from hydrography and altimetry. *Journal of Geophysical Research*, **115**, C11003.
- Sathiyamoorthy, S. and G. Moore, 2002: Buoyancy flux at Ocean Weather Station Bravo. *Journal of Physical Oceanography*, **32**, 458–474.
- Schmidt, S., 2008: Upper Labrador Sea Freshwater - Seasonal to Decadal Variability. *Christian-Albrechts-University Kiel*, **PhD. Thesis**.
- Schmidt, S. and U. Send, 2007: Origin and Composition of Seasonal Labrador Sea Freshwater. *Journal of Physical Oceanography*, **37**, 1445–1454.
- Schmittner, A., 2005: Decline of the marine ecosystem caused by a reduction in the Atlantic overturning circulation. *Nature*, **434**, 628–633.
- Schulze, L. and R. Pickart, 2012: Seasonal variation of upwelling in the Alaskan Beaufort Sea: Impact of sea ice cover. *Journal of Geophysical Research*, **117**, C06022.
- Serreze, M., R. Carse, and R. Barry, 1997: Icelandic low cyclone activity: Climatological features, linkage with the NAO, and relationships with recent changes in the Northern Hemisphere circulation. *Journal of Climate*, **10**, 453–464.
- Smeed, D., et al., 2013: Observed decline of the Atlantic Meridional Overturning Circulation 2004 to 2012. *Ocean Science Discussion*, **10**, 1619–1645.
- Smethie, W., R. Fine, A. Putzka, and E. Jones, 2000: Deep Water using chlorofluorocarbons. *Journal of Geophysical Research*, **105**, 297.
- Smith, S. and F. Dobson, 1984: The heat budget at Ocean Weather Station Bravo. *Atmosphere-Ocean*, **22**, 1–22.
- Spall, M. and R. Pickart, 2003: Wind-Driven Recirculation and Exchange in the Labrador and Irminger Seas. *Journal of Physical Oceanography*, **33**, 1829–1845.

- Spall, M., R. Pickart, P. Fratantoni, and A. Plueddemann, 2008: Western Arctic Shelfbreak eddies: Formation and Transport. *Journal of Physical Oceanography*, **38**, 1644–1914.
- Speer, K., H.-J. Isemer, and A. Biastoch, 1995: Water mass formation from revised COADS data. *Journal of Physical Oceanography*, **25**, 2444–2457.
- Stommel, H. and A. Arons, 1960a: On the abyssal circulation of the world ocean - I Stationary planetary flow patterns on a sphere. *Deep-Sea Research*, **6**, 140–154.
- Stommel, H. and A. Arons, 1960b: On the abyssal circulation of the world ocean - II. An idealized model of the circulation pattern and amplitude in oceanic basins. *Deep-Sea Research*, **6**, 217–233.
- Stramma, L., D. Kieke, M. Rhein, F. Schott, I. Yashayaev, and K. Koltermann, 2004: Deep water changes at the western boundary of the subpolar North Atlantic during 1996 to 2001. *Deep-Sea Research: Part I*, **51** (8), 1033–1056.
- Straneo, F., 2006: Heat and Freshwater Transport through the Central Labrador Sea. *Journal of Physical Oceanography*, **36**, 606–628.
- Straneo, F., G. Hamilton, D. Sutherland, L. Stearns, F. Davidson, M. Hammill, G. Stenson, and A. Rosing-Asvid, 2010: Rapid Circulation of warm subtropical waters in a major glacial fjord of East Greenland. *Nature Geoscience*, **3**, 182–186.
- Straneo, F., M. Kawase, and R. Pickart, 2002: Effects of Wind on Convection in Strongly and Weakly Baroclinic Flows with Application to the Labrador Sea. *Journal of Physical Oceanography*, **32**, 2603–2618.
- Straneo, F. and F. Saucier, 2008: The outflow from Hudson Strait and its contribution to the Labrador Current. *Deep-Sea Research*, **55**, 926–946.
- Talley, L. and M. McCartney, 1982: Distribution and Circulation of Labrador Sea Water. *Journal of Physical Oceanography*, **12**, 1189–1205.
- Toggweiler, J. and B. Samuels, 1993: Is the magnitude of the deep outflow from the Atlantic Ocean actually governed by Southern Hemisphere winds? *The Global Carbon Cycle, NATO ASI Series, Series I*, edited by M. Heimann, Springer, New York, 333–366.
- Trenberth, K. and J. Caron, 2001: Estimates of meridional atmosphere and ocean heat transports. *Journal of Climate*, **14**, 3433–3443.
- Vage, K., et al., 2008: Surprising return of deep convection to the subpolar North Atlantic Ocean in winter 2007–2008. *Nature*, **2**, 67–72.
- Wang, J., L. Mysak, and R. Ingram, 1994: Interannual variability of sea-ice cover in Hudson Bay, Baffin Bay and the Labrador Sea. *Atmosphere-Ocean*, **32**, 421–447.

- Weaver, A., S. Aura, and P. Myers, 1994: Interdecadal variability in an idealized model of the North Atlantic. *Journal of Geophysical Research*, **99**, 12,412–12,441.
- Willis, J., D. Roemmich, and B. Cornuelle, 2004: Interannual variability in upper ocean heat content, temperature, and thermosteric expansion on global scale. *Journal of Geophysical Research*, **109**, C12036.
- Woollings, T., J. Gregory, J. Pinto, M. Reyers, and D. Brayshaw, 2012: Response of the North Atlantic storm tracks to climate change shaped by ocean - atmosphere coupling. *Nature Geoscience*, **5**, 313–317.
- Worthington, L., 1976: On the North Atlantic Circulation. *The John Hopkins Oceanographic Studies, The John Hopkins University Press*, **6**, 110.
- Yashayaev, I., 2007: Hydrographic changes in the Labrador Sea, 1960-2005. *Progress in Oceanography*, **73**, 242–276.
- Yashayaev, I. and J. Loder, 2009: Enhanced production of Labrador Sea Water in 2008. *Geophysical Research Letters*, **36**, L01606.
- Zhang, X., J. Walsh, J. Zhang, U. Bhatt, and M. Ikeda, 2004: Climatology and interannual variability of Arctic cyclone activity: 1948-2002. *Journal of Climate*, **17**, 2300–2317.
- Zimmermann, S., T. McKee, R. Pickart, and W. S. Jr., 2000: KNORR 147 leg V hydrographic data report: Labrador Sea Deep Convection Experiment. *Tech Report WHOI-2000-05, Woods Hole Oceanographic Institution, Woods Hole, MA*, 92.